

**A measurement of the  $\tau$  polarisation  
in  $e^+e^-$  interactions produced at LEP**

Dissertation présentée en vue de l'obtention du grade de Docteur en Sciences

**Véronique Lefébure**

Promoteur: D<sup>r</sup> D. Bertrand

Septembre 1997

# Errata

Véronique Lefébure  
September 1997

## 1. Introduction

Page 2, equation (1.5):

$$\mathcal{A}_{f,e} \equiv \frac{|g_{\mathbf{L}}^{f,e}|^2 - |g_{\mathbf{R}}^{f,e}|^2}{|g_{\mathbf{R}}^{f,e}|^2 + |g_{\mathbf{L}}^{f,e}|^2}$$

## 2. Electroweak interactions

Page 6, table 2.2: The upper bound values quoted for the neutrino masses are the ones corresponding to the 1994 world-averages. The 1996 values are  $0.17 \text{ MeV}/c^2$  and  $24 \text{ MeV}/c^2$  respectively for  $m_{\nu_\mu}$  and  $m_{\nu_\tau}$ .

Page 9, equation (2.8): (minus sign)

$$J_\mu^0 = \sum_f \bar{f} \gamma_\mu \frac{(g_v^f - g_a^f \gamma_5)}{2} f$$

Page 9, equation (2.9):

$$J_\mu^0 = \sum_f \bar{f} \gamma_\mu \left\{ g_{\mathbf{L}}^f \frac{(1 - \gamma_5)}{2} + g_{\mathbf{R}}^f \frac{(1 + \gamma_5)}{2} \right\} f$$

Pages 11 and 16:

$$\text{Re}\chi(s)$$

Page 23, equation (2.47):

$$\frac{d\Gamma}{\Gamma dx_l} = \frac{1}{3} \left\{ (5 - 9x_l^2 + 4x_l^3) + \langle \mathcal{P}_\tau \rangle (1 - 9x_l^2 + 8x_l^3) \right\} .$$

Page 23, equation (2.49):

$$\Delta \langle \mathcal{P}_\tau \rangle = \frac{1}{\sqrt{N_i}} \left( \int \frac{g_i^2}{f_i - \langle \mathcal{P}_\tau \rangle g_i} \right)^{-\frac{1}{2}}$$

## 3. Selection of the inclusive one-prong $\tau$ decay modes

Page 53, line 32 (minus sign)

“... or only one charged particle to which at least *two* VD signals had been associated.”

## 5. Identification of the exclusive one-prong $\tau$ decay modes

Page 79, line 33

“the squared angle ... had to be *larger* than  $10 \text{ degrees}^2 \text{ GeV}$ .”

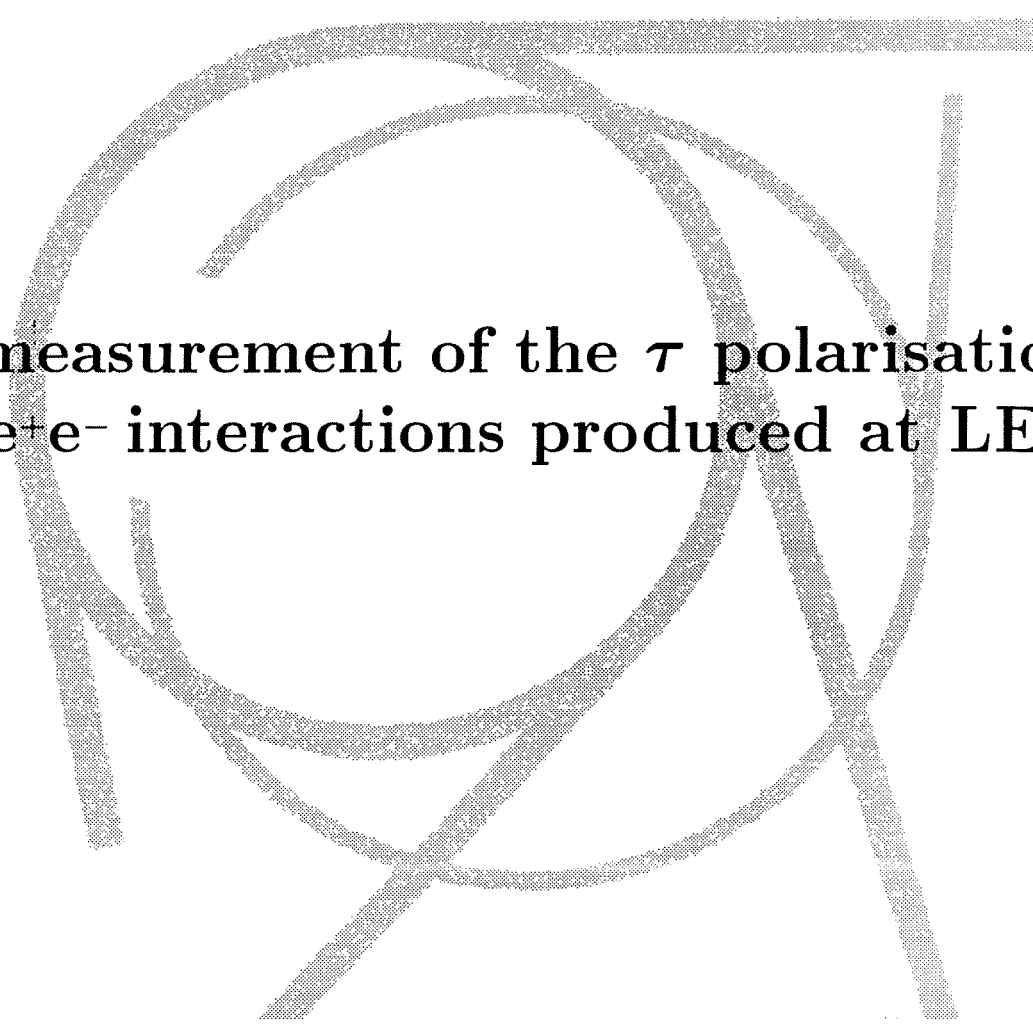
Page 82, line 15

“... because of the important Lorentz boost *and* the larger mass of the kaon. ”





Université Libre de Bruxelles  
Faculté des Sciences

A large, stylized logo for LEP (Large Electron-Positron collider) is centered in the background. It features a circular path with two intersecting lines, representing the collider's structure.

**A measurement of the  $\tau$  polarisation  
in  $e^+e^-$  interactions produced at LEP**

Dissertation présentée en vue de l'obtention du grade de Docteur en Sciences

**Véronique Lefébure**

Promoteur: D<sup>r</sup> D. Bertrand

Septembre 1997

---

<sup>0</sup>Cette thèse de doctorat a été réalisée avec le soutien du Fonds pour la Formation à la Recherche dans l'Industrie et l'Agriculture (F.R.I.A.).

# Contents

<b>1</b>	<b>Introduction</b>	<b>1</b>
<b>2</b>	<b>Electroweak interactions</b>	<b>5</b>
2.1	The Standard Model . . . . .	5
2.2	Neutral current interactions: $e^+e^- \rightarrow f\bar{f}$ . . . . .	9
2.2.1	Cross-section . . . . .	11
2.2.2	Forward-backward charge asymmetry . . . . .	13
2.2.3	Polarisation . . . . .	16
2.2.4	Left-right asymmetry . . . . .	18
2.3	Charged current interactions: $\tau$ physics . . . . .	18
2.3.1	The $\tau$ decay and the Michel parameters . . . . .	20
2.3.2	The $\tau$ decay as a polarimeter . . . . .	21
<b>3</b>	<b>Experimental setup and methods</b>	<b>25</b>
3.1	The Large Electron Positron collider at CERN . . . . .	25
3.2	The DELPHI detector and its performance . . . . .	27
3.2.1	Tracking system . . . . .	29
3.2.2	Calorimetry . . . . .	35
3.2.3	Muon detectors . . . . .	37
3.2.4	Data acquisition system . . . . .	39
3.2.5	Luminosity measurement . . . . .	40
3.3	Data simulation technique . . . . .	40
3.4	The neural network technique . . . . .	41
3.4.1	The neuron . . . . .	41
3.4.2	The feed-forward neural network . . . . .	43
3.4.3	The SNNS package . . . . .	45
<b>4</b>	<b>Selection of the inclusive one-prong <math>\tau</math> decay modes</b>	<b>46</b>
4.1	Data sample description . . . . .	46
4.2	Selection of the $e^+e^- \rightarrow \tau^+\tau^-$ interactions . . . . .	51
4.2.1	Reconstruction of the event topology . . . . .	51
4.2.2	Calibration of the HPC energy . . . . .	54
4.2.3	Selection criteria . . . . .	55
4.3	Background study . . . . .	61
4.3.1	Cosmic ray background study . . . . .	61
4.3.2	Bhabha background study . . . . .	61
4.4	Selection efficiencies and purity of the selected samples . . . . .	62
4.4.1	Efficiencies . . . . .	62
4.4.2	Purities . . . . .	63

4.4.3	Comparison between real and simulated data . . . . .	64
4.5	Selection of the inclusive one-prong $\tau$ decay modes . . . . .	65
4.6	Study of the systematic effects . . . . .	70
4.7	Summary . . . . .	72
<b>5</b>	<b>Identification of the exclusive one-prong <math>\tau</math> decay modes</b>	<b>73</b>
5.1	The set of discriminant variables . . . . .	74
5.1.1	Electron identification . . . . .	74
5.1.2	Muon identification . . . . .	77
5.1.3	Hadron identification . . . . .	79
5.1.4	Summary . . . . .	82
5.2	Test-samples . . . . .	83
5.2.1	Re-calibration of some variables . . . . .	83
5.2.2	Selection criteria for the test-samples . . . . .	88
5.3	Performances of the neural network classification . . . . .	93
5.3.1	Neural network architecture and training . . . . .	93
5.3.2	Neural network performances . . . . .	97
5.4	Summary . . . . .	106
<b>6</b>	<b>Measurement of the <math>\tau</math> polarisation</b>	<b>107</b>
6.1	Method for the experimental measurement of the $\tau$ polarisation . . . . .	107
6.2	Results . . . . .	114
6.3	Study of the systematic effects . . . . .	121
6.4	Introduction of the Michel parameters and $h_{\nu\tau}$ in the $\langle\mathcal{P}_\tau\rangle$ measurement . . . . .	129
<b>7</b>	<b>Discussion of the results</b>	<b>133</b>
7.1	Combination of the 93, 94 and 95 results . . . . .	133
7.2	Determination of the coupling constants of the Z boson . . . . .	134
7.3	Test of lepton universality for weak neutral current interactions . . . . .	137
7.4	Test of the V–A structure of the charged current in $\tau$ decays . . . . .	137
<b>8</b>	<b>Conclusions</b>	<b>141</b>
<b>A</b>		<b>145</b>
A.1	The simple perceptron . . . . .	145
A.2	The multi-layer perceptron . . . . .	147

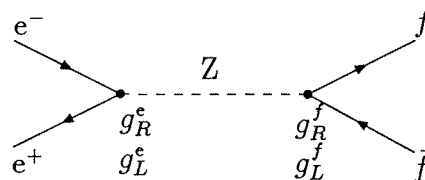
# Chapter 1

## Introduction

The Standard Model was elaborated in the sixties for the description of the electro-weak interactions. Based on symmetry and gauge invariance arguments, it offers a complete formalism which unifies the well known electromagnetic processes and the weak interactions for which it predicts the existence of the massive  $Z$ ,  $W^+$  and  $W^-$  bosons as mediators of the weak charged and neutral currents. Despite the fact that the Standard Model is not a complete theory since it depends on several parameters such as the fermion masses, the number of fermion families and the mixing angle  $\sin^2 \theta_w$ , it describes with a remarkable precision the experimental results obtained in the electro-weak domain. In particular, the LEP collider (Large Electron Positron collider), in operation at CERN since 1989, provides a unique facility to test lots of the model predictions. Between 1990 and 1995, some 20 million  $Z$  bosons were created through the interactions  $e^+e^- \rightarrow Z$ . The  $Z$  boson decays into a pair of fermions  $f\bar{f}$  which can be neutrinos ( $f = \nu_e, \nu_\mu$  or  $\nu_\tau$ ), leptons ( $f = e^-, \mu^-$  or  $\tau^-$ ) or quarks ( $f = u, d', c, s'$  or  $b'$ ).

The analysis of the  $Z$  decays allows the measurement of  $f\bar{f}$  production cross-sections and asymmetries which leads to a precise determination of the parameters of the Standard Model directly accessible at these energies such as the number of fermion families and the  $Z$  coupling constants. On the basis of these results, limits can be put on other parameters such as the top quark and Higgs boson masses.

At the peak of the  $Z$  resonance, the  $e^+e^- \rightarrow f\bar{f}$  interaction is dominated by the  $Z$   $s$ -channel exchange shown on the following Feynman diagram:



where  $g_R^f$  and  $g_L^f$  are the coupling constants of the  $Z$  boson to the right-handed (R) and left-handed (L) fermion component respectively ( $f = f_R + f_L$ ).



For fermions of electric charge  $Q^f$  and weak isospin  $I_3^f$ , the coupling constants are given by

$$\begin{aligned} g_R^f &= -Q^f \sin^2 \theta_w, \\ g_L^f &= I_3^f - Q^f \sin^2 \theta_w. \end{aligned} \quad (1.1)$$

The cross-section  $\sigma_{f\bar{f}}$  of the process is proportional to  $|g_R^f|^2 + |g_L^f|^2$ . The Standard Model predicts that the Z boson couples with different strengths to fermions of opposite helicities ( $g_R^f \neq g_L^f$ ). Consequently, the Z boson produced in  $e^+e^-$  interactions is expected to be polarised. It is this particular aspect of the interaction which makes the object of this thesis.

For interactions with unpolarised beams, the Z polarisation  $\mathcal{P}_Z$  is defined as

$$\mathcal{P}_Z = \frac{|g_R^e|^2 - |g_L^e|^2}{|g_R^e|^2 + |g_L^e|^2} \quad (1.2)$$

Due to the conservation of angular momentum, a non-zero  $\mathcal{P}_Z$  leads to a variation of the cross-section  $\sigma_{f\bar{f}}$  as a function of the angle  $\theta_f$  of emission of the produced fermion with respect to the incident electron. The forward-backward charge asymmetry is given by:

$$A_{FB} = \frac{3 |g_R^e|^2 - |g_L^e|^2}{4 |g_R^e|^2 + |g_L^e|^2} \frac{|g_R^f|^2 - |g_L^f|^2}{|g_R^f|^2 + |g_L^f|^2} \quad (1.3)$$

The produced fermion is polarised and its longitudinal polarisation is a function of  $\theta_f$ :

$$\mathcal{P}_f(\cos \theta_f) = - \frac{(1 + \cos^2 \theta_f) \mathcal{A}_f + 2 \cos \theta_f \mathcal{A}_e}{(1 + \cos^2 \theta_f) + 2 \cos \theta_f \mathcal{A}_f \mathcal{A}_e}. \quad (1.4)$$

where

$$\mathcal{A}_{f,e} \equiv \frac{|g_R^{f,e}|^2 - |g_L^{f,e}|^2}{|g_R^{f,e}|^2 + |g_L^{f,e}|^2} = \frac{2g_v^{f,e} g_a^{f,e}}{|g_v^{f,e}|^2 + |g_a^{f,e}|^2} = \frac{2g_v^{f,e}/g_a^{f,e}}{1 + (g_v^{f,e}/g_a^{f,e})^2} \quad (1.5)$$

$$\stackrel{\text{lept. univ.}}{=} \frac{2(1 - 4 \sin^2 \theta_w)}{1 + (1 - 4 \sin^2 \theta_w)^2}$$

The average fermion polarisation is

$$\langle \mathcal{P}_f \rangle = \frac{|g_R^f|^2 - |g_L^f|^2}{|g_R^f|^2 + |g_L^f|^2} \quad (1.6)$$

In order to determine the Standard Model parameter  $\sin^2 \theta_w$  via (1.5), we performed the measurement of the angular dependence of the  $\tau$  polarisation  $\mathcal{P}_\tau(\cos \theta_\tau)$ . The  $\tau$  lepton is the only fermion which decays within the detector, providing the possibility to determine statistically its helicity state via the analysis of the kinematical spectra of its decay products. That measurement allows an independent determination of  $\mathcal{A}_e$  and  $\mathcal{A}_\tau$ , and gives the opportunity to test the hypothesis of lepton universality (i.e. is  $g_{R(L)}^e$  identical to  $g_{R(L)}^\tau$  ?). The precision obtained on  $\sin^2 \theta_w$  is a factor five better than the corresponding result deduced from the  $A_{FB}$  measurement and it is much less sensitive to the centre-of-mass energy of the  $e^+e^-$  system, and hence to radiation effects. A more detailed theoretical introduction is given in Chapter 2.

Our analysis was based on the experimental data recorded during the years 1993, 1994 and 1995 (i.e. about 125000  $\tau^+\tau^-$  pairs) by the DELPHI detector described in Chapter 3. It proceeded in four steps:

1.- Selection of the  $e^+e^- \rightarrow \tau^+\tau^-$  interactions

The final states  $\tau^+\tau^-$  were isolated from the other Z decay modes and from background processes (four-fermion  $e^+e^- \rightarrow f\bar{f}f'\bar{f}'$  interactions, cosmic rays, ...) by applying kinematical and topological criteria. The  $e^+e^- \rightarrow \tau^+\tau^-$  interactions present a relatively clean signal at LEP energies. They are characterised by a multiplicity of 2 to 10 charged particles produced together with neutral particles in two collimated jets which are emitted back to back from the interaction region and have missing energy due to the production of two or more undetected neutrinos. This signature is quite different from the one of the hadronic Z decays which have a mean charged multiplicity of 20 particles emitted in wide jets, and from  $e^+e^-$  and  $\mu^+\mu^-$  channels where the two final state particles have an energy equal or close to the beam energy (see Chapter 4, sections 4.1 and 4.2).

2.- Selection of the  $\tau \rightarrow 1\text{-prong}$  decay modes

The present analysis used the 85% of  $\tau$  decays where only one primary charged particle ("1-prong") is produced. The selection of these events was performed taking account of the influence of secondary particles, in particular electrons produced in photon conversions, which increase the apparent multiplicity of charged particles. Our analysis allowed a relatively precise measurement of the topological  $\tau$  decay branching ratio  $B(\tau \rightarrow 1\text{-prong})$  (see Chapter 4, section 4.5).

3.- Identification of the  $\tau$  decay modes

For the polarisation measurement, the  $\tau$  decay modes need to be identified. The majority of the 1-prong decay channels are of the following types:

$$\begin{array}{ll}
 \text{leptonic decays:} & \tau^- \rightarrow e^- \bar{\nu}_e \nu_\tau \quad ; \\
 & \tau^- \rightarrow \mu^- \bar{\nu}_\mu \nu_\tau \quad ; \\
 \text{semi-leptonic decays:} & \tau^- \rightarrow h^- \nu_\tau \quad ; \\
 & \tau^- \rightarrow h^- \pi^0 \nu_\tau \quad ; \\
 & \tau^- \rightarrow h^- \pi^0 \pi^0 \nu_\tau \quad ;
 \end{array}$$

where  $h$  is a charged pion or kaon. The  $\pi^0$ 's decay in 99% of the cases into two photons ( $\pi^0 \rightarrow \gamma\gamma$ ). All the above five channels were analysed. The neural network technique was chosen for the identification of the three semi-leptonic decay modes. It was well suited to handle the various sources of photon misidentification correlated to the detection of the electromagnetic activity: photon conversions, merging of electromagnetic showers, loss of information in the dead detector zones, overlapping of neutral electromagnetic showers with showers originating from charged particles, production of secondary photons. The technique was extended for the simultaneous identification of the leptonic decay modes. Simulated events were used for the training of the neural networks and the estimation of the migration matrices (see Chapter 5).

The measurement of the  $\tau$  polarisation was performed by adjusting to the experimental distributions of the relevant kinematical variables, the corresponding distributions obtained for simulated events for which the polarisation could be varied (see Chapter 6). The measurement was performed for six regions covering the  $\theta_\tau$  range retained for the analysis ( $43^\circ < \theta_\tau < 137^\circ$ ) where optimal conditions were assured for the reconstruction of the needed information. The quantities  $\mathcal{A}_e$  and  $\mathcal{A}_\tau$  were extracted from a fit of the function (1.4) to the six experimental measurements. In addition the exclusive 1-*prong*  $\tau$  decay branching ratios could also be determined. The measurements were realised assuming a pure V–A structure of the charged current describing the  $\tau$  decay. A preliminary measurement of the  $\nu_\tau$  helicity  $h_{\nu_\tau}$  and of the Michel parameters, was performed in view of a test of the validity of that assumption.

All physics results are summarised in Chapter 7. They are discussed in the frame of the Standard Model and compared to the results of other measurements.

# Chapter 2

## Electroweak interactions

The large variety of matter of which the Universe is composed can be described, on the basis of symmetry arguments, as being built from various combinations of a limited number of elementary constituents assumed to be point-like: the fermions (spin- $\frac{1}{2}$  particles). They interact with one another by exchanging intermediate bosons (spin-1 or spin-2) (see table 2.1). The possible role of one or more fundamental scalars (spin-0) called the Higgs bosons, has still to be verified.

According to the present modelling of these interaction processes, the matter constituents are grouped in three families, each one composed of two leptons and two quarks, and of their anti-particles (table 2.2) <sup>1</sup>. Some of them have been known for a long time (the electron was discovered in 1897 by J.J. Thomson), while others, though eagerly searched by the physicists in order to confirm their theories, were directly observed only quite recently (the top quark was found at the Fermi National Laboratory in 1995 [1]).

Each intermediate boson is the vector of one of the four fundamental interactions (table 2.1):

- **the gravitation force:** massive particles ( $m \neq 0$ ), as well as massless energetic particles, are submitted to the gravitational attraction mediated by the so-called hypothetical graviton;
- **the electromagnetic force:** electrically charged particles ( $Q \neq 0$ ), as well as particles endowed with a magnetic or electric dipole moment, interact electromagnetically through the exchange of a **photon**;
- **the weak force:** all particles are submitted to the weak interaction to which the  $Z$  and  $W^\pm$  bosons are associated;
- **the strong force:** particles endowed with a colour charge ( $C \neq 0$ ) exchange **gluons**, the mediators of the strong interaction.

At the end of the sixties, the description of the electromagnetic and weak interactions were successfully unified in a single although incomplete model: the Standard Model.

### 2.1 The Standard Model

The Standard Model [3] is the theory proposed in 1967-1968 by S.L. Glashow, S. Weinberg and A. Salam to describe in a unified way the electromagnetic and the weak interactions of the

---

<sup>1</sup>Theories exist that imply in addition the existence of “supersymmetric-particles”. Such objects are searched for by present (and future) experiments, but this subject is beyond the scope of this work and will not be discussed here.

Interaction	Intermediate boson	Spin ( $\hbar$ )	Mass (GeV/c <sup>2</sup> )
gravitational	graviton	2	zero (theoretical value)
electromagnetic	photon ( $\gamma$ )	1	0 ( $< 3 \times 10^{-36}$ )
weak (N.C.)	$Z$	1	$91.187 \pm 0.007$
(C.C.)	$W^+, W^-$	1	$80.22 \pm 0.26$
strong	gluons (g)	1	zero (theoretical value)

Table 2.1: The four types of interactions and the corresponding intermediate bosons. The mass values are extracted from reference [2]. The initials N.C. and C.C. stand for Neutral Current and Charged Current respectively.

Fermion families			Elec. charge $Q_f (e)$	colour $C_f$
1	2	3		
<b>leptons (anti-leptons)</b>				
e-neutrino $\nu_e$ ( $\bar{\nu}_e$ ) $m_{\nu_e} < 5.1 \text{ eV}/c^2$	$\mu$ -neutrino $\nu_\mu$ ( $\bar{\nu}_\mu$ ) $m_{\nu_\mu} < 0.27 \text{ MeV}/c^2$	$\tau$ -neutrino $\nu_\tau$ ( $\bar{\nu}_\tau$ ) $m_{\nu_\tau} < 31 \text{ MeV}/c^2$	0 (0)	0
electron $e^-$ ( $e^+$ ) $m_e = 0.511 \text{ MeV}/c^2$	muon $\mu^-$ ( $\mu^+$ ) $m_\mu = 105.6 \text{ MeV}/c^2$	tau $\tau^-$ ( $\tau^+$ ) $m_\tau = 1777.1 \text{ MeV}/c^2$	-1 (1)	0
<b>quarks (anti-quarks)</b>				
up $u$ ( $\bar{u}$ ) $m_u \simeq 5 \text{ MeV}/c^2$	charm $c$ ( $\bar{c}$ ) $m_c \simeq 1.3 \text{ GeV}/c^2$	top $t$ ( $\bar{t}$ ) $m_t \simeq 174 \text{ GeV}/c^2$	2/3 (-2/3)	$\neq 0$
down $d'$ ( $\bar{d}'$ ) $m_{d'} \simeq 10 \text{ MeV}/c^2$	strange $s'$ ( $\bar{s}'$ ) $m_{s'} \simeq 200 \text{ MeV}/c^2$	bottom $b'$ ( $\bar{b}'$ ) $m_{b'} \simeq 4.3 \text{ GeV}/c^2$	-1/3 (1/3)	$\neq 0$

Table 2.2: The three families of elementary particles and anti-particles, with their corresponding electric charge  $Q_f$  in units of  $e \simeq 1.6 \times 10^{-19} \text{ C}$ . The column colour indicates whether the (anti-) fermions have a colour charge. The mass values  $m_f$  are extracted from reference [2].

fermions. This standard electroweak model is based on the gauge group

$$SU(2)_I \times U(1)_Y$$

of weak isospin I and weak hypercharge Y, with massless gauge bosons represented by 4-vector fields noted  $W_\mu^i$  ( $i = 1, 2, 3$ ) and  $B_\mu$ , and gauge coupling constants  $g$  and  $g'$ :  $g$  is unique for  $SU(2)$ , and for  $U(1)$ ,  $g'$  is the same for all fermions in the hypothesis of *lepton universality*. The associated Lagrangian is of the form

$$\mathcal{L} = g\mathbf{J}_\mu \cdot \mathbf{W}_\mu + g'J_\mu^Y B_\mu$$

where  $\mathbf{J}_\mu$  and  $J^Y$  are respectively the isospin and hypercharge currents.

While gauge symmetry is needed for renormalisability, masses for the gauge bosons need to be introduced. This can be done through the mechanism of spontaneous symmetry breaking [4], which leads to the following Lagrangian for the electroweak interaction:

$$\begin{aligned} \mathcal{L}_{int} = & -\frac{g}{\sqrt{2}} \left( J_\mu^- W_\mu^- + J_\mu^+ W_\mu^+ \right) & ] \text{ weak C.C. interaction} \\ & -\frac{g}{\cos \theta_w} J_\mu^0 Z_\mu & ] \text{ weak N.C. interaction} \\ & -(-|e|)J_\mu^{em} A_\mu & ] \text{ electromagnetic N.C. interaction} \end{aligned} \quad (2.1)$$

where:

- $e = g'g/\sqrt{g^2 + g'^2} = g \sin \theta_w$  is the absolute value of the electron electric charge ;
- $\theta_w \equiv \tan^{-1}(g'/g)$  is the weak mixing angle entering in the definition of the fields associated to the neutral intermediate vector bosons Z and  $\gamma$ :

$$\begin{aligned} Z_\mu &= W_\mu^0 \cos \theta_w - B_\mu \sin \theta_w , \\ A_\mu &= W_\mu^0 \sin \theta_w + B_\mu \cos \theta_w ; \end{aligned}$$

- $W_\mu^\pm = (W_\mu^1 \pm iW_\mu^2)/\sqrt{2}$  are the fields associated to the charged vector bosons  $W^\pm$  ;
- $J_\mu^\pm$ ,  $J_\mu^0$ ,  $J_\mu^{em}$  are respectively the weak charged (C.C.) and neutral (N.C.) currents, and the neutral electromagnetic current. Their fermionic parts are explicitly given below (equations 2.2 to 2.5 ).

The first major success of the theory was the discovery of the existence of weak neutral currents made in 1973 at CERN in the Gargamelle bubble-chamber experiment of neutrino scattering on nucleons [5].

The photon ( $A_\mu$ ) was already known to be massless, while the masses of the other three intermediate bosons,  $W^\pm$  and Z, were predicted by the theory to be:

$$M_W = gv/2 \text{ and } M_Z = v\sqrt{g^2 + g'^2}/2$$

The Z and the  $W^\pm$  were indeed discovered at the CERN  $p\bar{p}$  collider in 1983 [6]. The factor  $v$  represents the vacuum expectation value of the Higgs scalar field resulting from the symmetry breaking. The *Minimal* Standard Model considered here involves only one such physical Higgs particle.

For the first family, the currents  $J_\mu^\pm$ ,  $J_\mu^0$  and  $J_\mu^{em}$  are expressed by (they are similar for the second and third families):

$$J_\mu^- = \bar{e} \gamma_\mu \frac{(1-\gamma_5)}{2} \nu_e + \bar{d}' \gamma_\mu \frac{(1-\gamma_5)}{2} u \quad (2.2)$$

$$J_\mu^+ = \bar{\nu}_e \gamma_\mu \frac{(1-\gamma_5)}{2} e + \bar{u} \gamma_\mu \frac{(1-\gamma_5)}{2} d' \quad (2.3)$$

$$\begin{aligned} J_\mu^0 &= I_3^{\nu_e} \bar{\nu}_e \gamma_\mu \frac{(1-\gamma_5)}{2} \nu_e + I_3^e \bar{e} \gamma_\mu \frac{(1-\gamma_5)}{2} e \\ &+ I_3^u \bar{u} \gamma_\mu \frac{(1-\gamma_5)}{2} u + I_3^{d'} \bar{d}' \gamma_\mu \frac{(1-\gamma_5)}{2} d' \\ &- \sin^2 \theta_w J_\mu^{em} \end{aligned} \quad (2.4)$$

$$J_\mu^{em} = Q_e \bar{e} \gamma_\mu e + Q_u \bar{u} \gamma_\mu u + Q_{d'} \bar{d}' \gamma_\mu d' \quad (2.5)$$

where:

- $e$ ,  $\nu_e$ ,  $u$  and  $d'$  are respectively the spinors of the electron and electron-neutrino leptons, and of the up and down<sup>2</sup> quarks. The spinors can be expressed in terms of their right-handed (R) and left-handed (L) components:

$$e = e_L + e_R, \quad e_L = \frac{(1-\gamma_5)}{2} e, \quad e_R = \frac{(1+\gamma_5)}{2} e,$$

$$\nu_e = \nu_{eL}, \quad \nu_{eL} = \frac{(1-\gamma_5)}{2} \nu_e, \quad \nu_{eR} = 0,$$

$$u = u_L + u_R, \quad u_L = \frac{(1-\gamma_5)}{2} u, \quad u_R = \frac{(1+\gamma_5)}{2} u,$$

$$d' = d'_L + d'_R, \quad d'_L = \frac{(1-\gamma_5)}{2} d', \quad d'_R = \frac{(1+\gamma_5)}{2} d'.$$

- the  $\gamma_\mu$  ( $\mu = 0, 4$ ) are the Dirac gamma-matrices,  $\gamma_5 = -i\gamma_0\gamma_1\gamma_2\gamma_3$  ( $\gamma_5^2 = 1$ ).
- $I_3^f$  is the third component of the weak isospin of fermion  $f$ :  $+1/2$  for  $u$  and  $\nu_e$ ,  $-1/2$  for  $d'$  and  $e$ . To the right-handed component of the fermions corresponds a vanishing weak isospin ( $I = 0$ ), as indicated by the expression of the charged current which involves only left-handed fermions.

The vector  $g_v^f$  and axial  $g_a^f$  coupling constants of the Z boson to the fermion  $f$  are given by:

$$g_v^f = I_3^f - 2Q_f \sin^2 \theta_w \quad (2.6)$$

$$g_a^f = I_3^f \quad (2.7)$$

---

<sup>2</sup>The quark mass eigenstates are not the same as the weak eigenstates [7]. By convention, the three charge 2/3 quarks ( $u$ ,  $c$ , and  $t$ ) are unmixed, and all the mixing is expressed in terms of a  $3 \times 3$  unitary matrix  $V$  operating on the charge -1/3 quarks ( $d$ ,  $s$ ,  $b$ ):

$$\begin{pmatrix} d' \\ s' \\ b' \end{pmatrix} = \begin{pmatrix} V_{ud} & V_{us} & V_{ub} \\ V_{cd} & V_{cs} & V_{cb} \\ V_{td} & V_{ts} & V_{tb} \end{pmatrix} \begin{pmatrix} d \\ s \\ b \end{pmatrix}.$$

The  $V$  matrix elements are estimated experimentally. The diagonal elements are close to 1, and  $V_{us}$  and  $V_{cd}$  amount to about 0.2 only.

so that (2.4) can be rewritten

$$J_\mu^0 = \sum_f \bar{f} \gamma_\mu \frac{(g_v^f + g_a^f \gamma_5)}{2} f \quad (2.8)$$

or equivalently:

$$\begin{aligned} J_\mu^0 &= \sum_f \bar{f} \gamma_\mu \left\{ g_R^f \frac{(1 - \gamma_5)}{2} + g_L^f \frac{(1 + \gamma_5)}{2} \right\} f \\ &= \sum_f \left\{ g_L^f \bar{f}_L \gamma_\mu f_L + g_R^f \bar{f}_R \gamma_\mu f_R \right\} \end{aligned} \quad (2.9)$$

where  $g_R^f$  and  $g_L^f$  are the coupling constants of the Z boson to the right (R) and left (L) -handed states of the fermion f:

$$g_L^f = (g_v^f + g_a^f)/2 = I_3^f - Q_f \sin^2 \theta_w \quad (2.10)$$

$$g_R^f = (g_v^f - g_a^f)/2 = -Q_f \sin^2 \theta_w . \quad (2.11)$$

Note that in (2.9),  $f_L$  ( $f_R$ ) represents a left- (right-) handed incoming fermion or a right- (left-) handed outgoing anti-fermion,  $\bar{f}_L$  ( $\bar{f}_R$ ) represents a left- (right-) handed outgoing fermion, or a right- (left-) handed incoming anti-fermion also noted by  $\bar{f}_R$  ( $\bar{f}_L$ ).

The number of fermion families is not fixed by the Standard Model but was found to be 3: it has been determined at LEP to be  $2.991 \pm 0.016$  [8] by fitting the theoretical Z resonance lineshape (2.14) to the real data. However, one (or more) additional generation with a corresponding massive neutrino ( $m_\nu > 0.5 M_Z$ ) is not excluded by this measurement.

The quantities  $g$ ,  $g'$  and  $v$  are three free parameters of the Standard Model as are the fermion masses (and the Higgs mass for higher order calculations). They need to be fixed in order to obtain quantitative predictions of physical observables such as interaction cross-sections or decay branching ratios of unstable particles. They can be indirectly determined by measuring for example the electron electric charge  $-e$  (or the fine structure constant  $\alpha = e^2/2hc$ ), the Fermi constant  $G_\mu$  ( $G_\mu/\sqrt{2} = g^2/8M_W^2$ ) and the mass of the Z (or W) boson  $M_Z$  ( $M_W$ ). Alternatively,  $\sin^2 \theta_w$  can be measured through several methods which will be described in the next section.

The Standard Model assumes that there exists no mixing between leptons, and attributes identical values to the coupling constants for leptons of different generations. This hypothesis of *lepton universality* has also to be verified by experimental measurements.

## 2.2 Neutral current interactions: $e^+e^- \rightarrow f\bar{f}$

In the framework of the Standard Model, the electron-positron interaction is described by the s-channel exchange of a photon or that of a Z intermediate boson according to the Feynman diagram of figure 2.1.a .

A fermion-anti-fermion pair  $f\bar{f}$  is produced, where  $f$  represents any fermion of table 2.2 having a mass  $m_f$  smaller than or equal to one half of the centre-of-mass energy  $E_{cm}$  of the electron-positron system. Neutrino pairs are of course not produced through the electromagnetic interaction as they have no electric charge. Electron-positron pairs are also produced through the t-channel diagram of figure 2.1.b which interferes with the s-channel one. The Feynman diagrams of background processes where four fermions are produced in the final state, are represented on figure 2.2. In chapter 4 it is described how they represent a contamination source for the selection of Z decays.



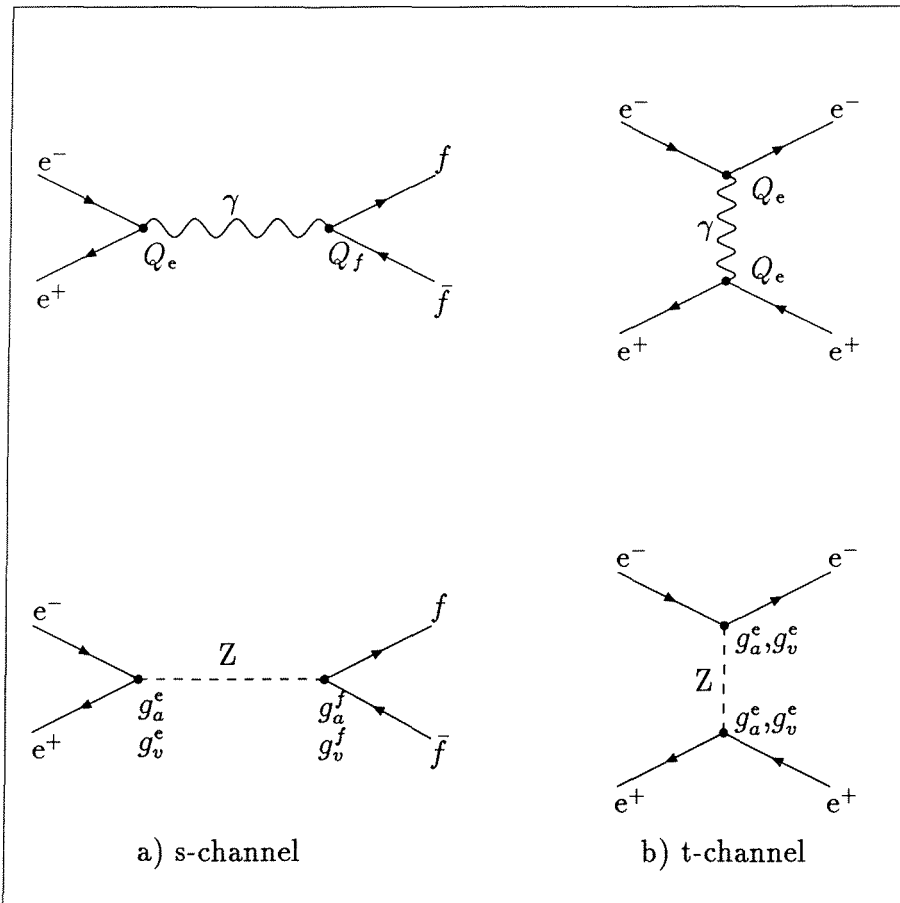


Figure 2.1: *Lowest order Feynman diagrams for  $e^+e^-$  interaction.*

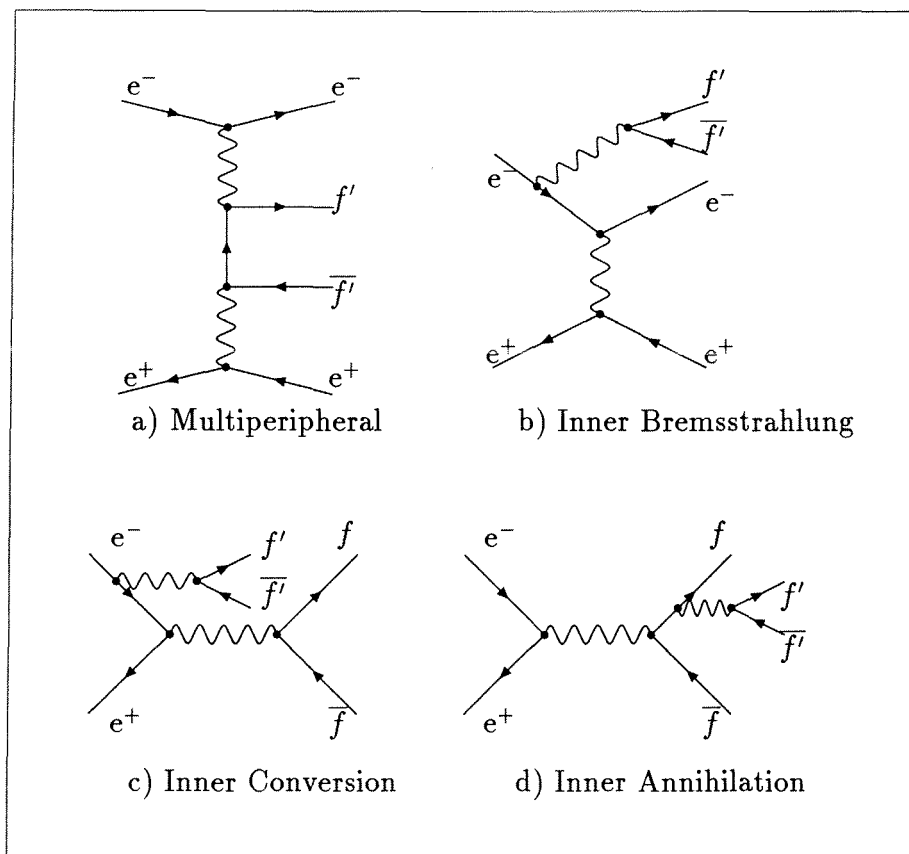


Figure 2.2: *Feynman diagrams of the four-fermion processes*

## 2.2.1 Cross-section

The total cross-section of the  $e^+e^- \rightarrow f\bar{f}$  process  $\sigma_{f\bar{f}}$ , is the sum of the weak and the electromagnetic interactions contributions and of their interference:

$$\sigma_{f\bar{f}} = \sigma_{f\bar{f}}^{\gamma \text{ exchange}} + \sigma_{f\bar{f}}^{\text{Z exchange}} + \sigma_{f\bar{f}}^{\gamma\text{-Z interference}}$$

The differential cross-section of the process,  $\frac{d\sigma_{f\bar{f}}^0}{d\Omega}$ , computed at the Born level (i.e. at the first significant order of the perturbative development) is given by:

$$\frac{d\sigma_{f\bar{f}}^0(s)}{d\Omega} = \frac{\alpha^2}{4s} N_C^f \sqrt{1 - 4\mu_f} \cdot \left\{ G_1(s)(1 + \cos^2 \theta) + 4\mu_f G_2(s)(1 - \cos^2 \theta) + \sqrt{1 - 4\mu_f} G_3(s) 2 \cos \theta \right\} \quad (2.12)$$

where  $\theta$  is the angle between the incident electron and the outgoing fermion directions measured in the centre-of-mass system,  $N_C^f$  is the colour factor (1 for leptons and 3 for quarks),  $\alpha$  is the fine structure constant ( $\sim 1/137$ ) and  $\mu_f = m_f^2/s$  is the square of the fermion reduced mass [9]. This cross-section is seen to be a function of:

- $s = E_{cm}^2$  ;
- the coupling constants of the Z and the photon to the electron and to the fermion  $f$  through the functions  $G_i(s)$ :

$$\begin{aligned} G_1(s) &= \underbrace{Q_e^2 Q_f^2}_{\gamma \text{ exchange}} + 2 \underbrace{g_v^e g_v^f Q_e Q_f Re_\chi(s)}_{\gamma\text{-Z interference}} + \underbrace{(g_v^{e2} + g_a^{e2})(g_v^{f2} + g_a^{f2} - 4\mu_f g_a^{f2}) |\chi(s)|^2}_{\text{Z exchange}} \\ G_2(s) &= \underbrace{Q_e^2 Q_f^2}_{\gamma \text{ exchange}} + 2 \underbrace{g_v^e g_v^f Q_e Q_f Re_\chi(s)}_{\gamma\text{-Z interference}} + \underbrace{(g_v^{e2} + g_a^{e2}) g_v^{f2} |\chi(s)|^2}_{\text{Z exchange}} \\ G_3(s) &= \underbrace{2 g_a^e g_a^f Q_e Q_f Re_\chi(s)}_{\gamma\text{-Z interference}} + \underbrace{4 g_v^e g_a^e g_v^f g_a^f |\chi(s)|^2}_{\text{Z exchange}} \end{aligned}$$

where the Z boson propagator  $\chi(s)$  is given by:

$$\chi(s) \simeq \frac{s}{s - M_Z^2 + i s \Gamma_Z / M_Z} \quad (2.13)$$

with  $M_Z$  and  $\Gamma_Z$  being the Z mass and width:

$$\Gamma_Z = \sum_f N_C^f \frac{\alpha}{3} M_Z \sqrt{1 - 4\mu_f} (g_v^{f2}(1 + 2\mu_f) + g_a^{f2}(1 - 4\mu_f)) \quad (2.14)$$

The form of the Z propagator presented in equation (2.13) takes into account the corrections due to an energy dependent  $\Gamma_Z$  ( $s\Gamma_Z/M_Z$  factor) which results from the increase of the available phase-space domain with increasing centre-of-mass energy.

In the following discussions the fermion masses will be neglected ( $\mu_f \sim 0$ ).

As can be seen on figure 2.3, the electromagnetic interaction dominates at small centre-of-mass energies ( $s < M_Z^2$ ), while it is negligible around the Z resonance ( $s \sim M_Z^2$ ). The interference term is very small and at maximum a few tenths of the total cross-section in absolute value. It changes from negative to positive sign at  $E_{cm} = M_Z$  (figure 2.3.b).

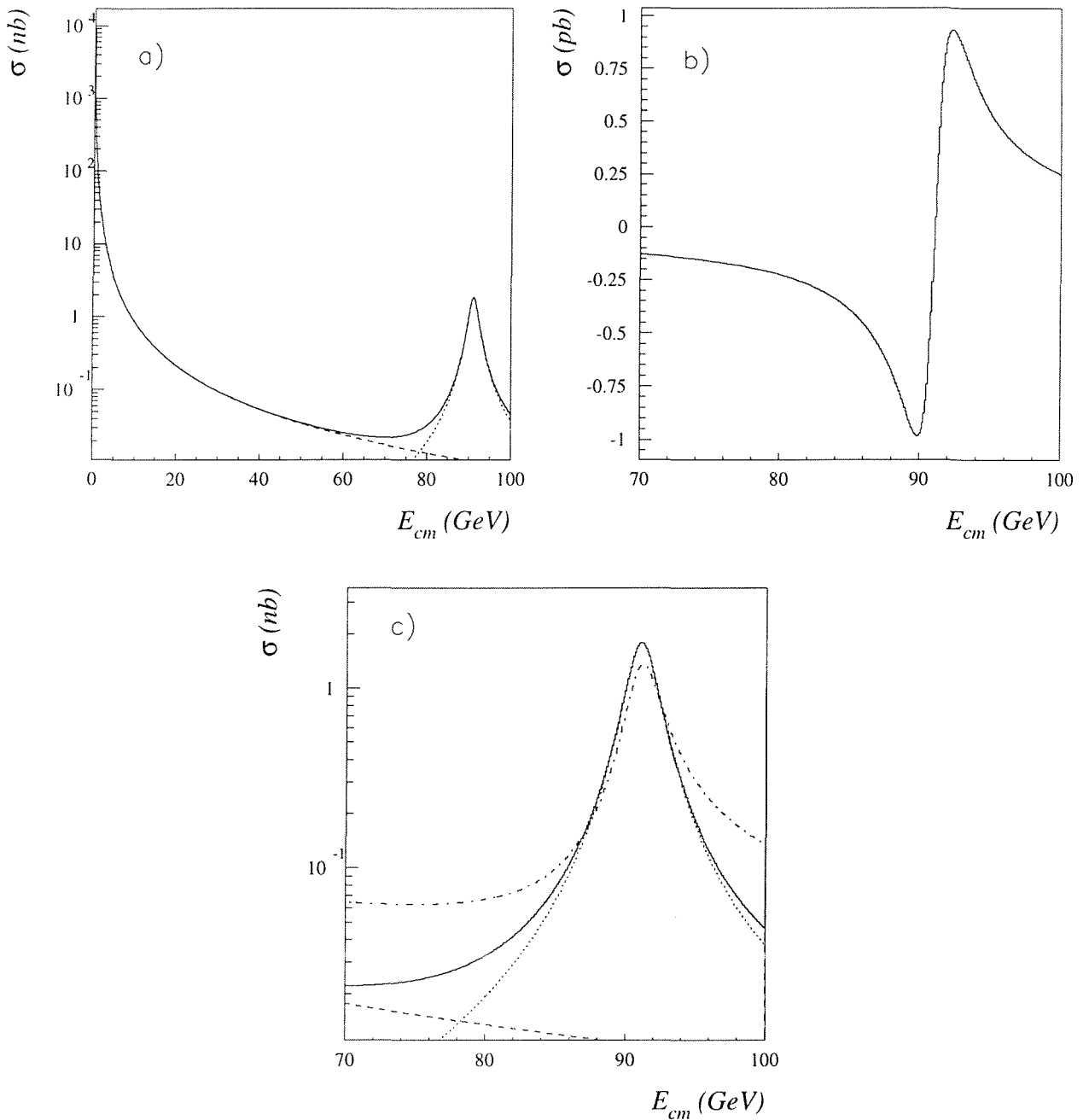


Figure 2.3: Born-level  $e^+e^- \rightarrow \gamma, Z \rightarrow l\bar{l}$  cross-section ( $l = e^-, \mu^-, \tau^-$ ). On plots a) and c) the solid line represents the total cross-section, the dashed and the dotted lines are respectively the  $\gamma$  and  $Z$  exchange contributions (logarithmic scale). Plot b) shows the interference term  $\gamma$ - $Z$  (linear scale). The cross-section corrected for the initial state radiation (computed using formula 2.15) is presented as a point-dash line on plot c). The following inputs were used:  $\alpha = 1/137$ ,  $M_Z = 91.17 \text{ GeV}/c^2$ ,  $\sin^2 \theta_w = 0.229$ ,  $\Gamma_Z = 2.481 \text{ GeV}$ .

## Radiative corrections

Additional Feynman diagrams contribute to the total cross-section of the  $e^+e^-$  interaction. The second order corrections can be divided into two classes: the ‘‘QED’’ and the ‘‘Weak’’ corrections. Some examples of the corresponding diagrams are represented in figure 2.4. The QED corrections include the initial (ISR) and final (FSR) state radiation, i.e. the emission of a real photon by the incident or by the produced fermion or anti-fermion (figure 2.4.a). In the case of an ISR, the  $e^+e^-$  centre-of-mass energy is decreased and the total cross-section of the process is then affected. The ISR effect, which is the dominant radiative correction, can be parameterised by an integral of the type:

$$\sigma_{f\bar{f}} = \int_0^{v_{max}} dv \rho(v) \sigma_{f\bar{f}}^0(s(1-v)) \quad , \quad (2.15)$$

where the function  $\rho(v)$ , given in reference [10], is the probability function for a photon to be emitted with a fraction  $v$  of the initial centre-of-mass energy squared  $s$ . The upper bound of the integral,  $v_{max} < 1$ , results from the fact that the remaining energy  $\sqrt{s'} = \sqrt{s(1-v)}$  has to be greater or equal to the total mass of the produced  $f\bar{f}$  fermion pair. This parameterisation of the ISR correction does not take into account possible ISR-FSR interference. The ISR effect on the production cross-section is shown on figure 2.3.c; it induces a 75% reduction of the cross-section at  $E_{cm} = M_Z$ .

The diagrams of the type of the ones presented in figure 2.4.b lead to a renormalisation of the fine structure constant:  $\alpha^{-1}(M_Z^2) \sim 128$ .

The effect of the propagator (or ‘oblique’) corrections (figure 2.4.c) and of the boxes diagrams (figure 2.4.d) represent negligible corrections.

## The Z boson decay modes

The Z bosons produce pairs of fermions  $f\bar{f}$  with the branching ratios given below [2]:

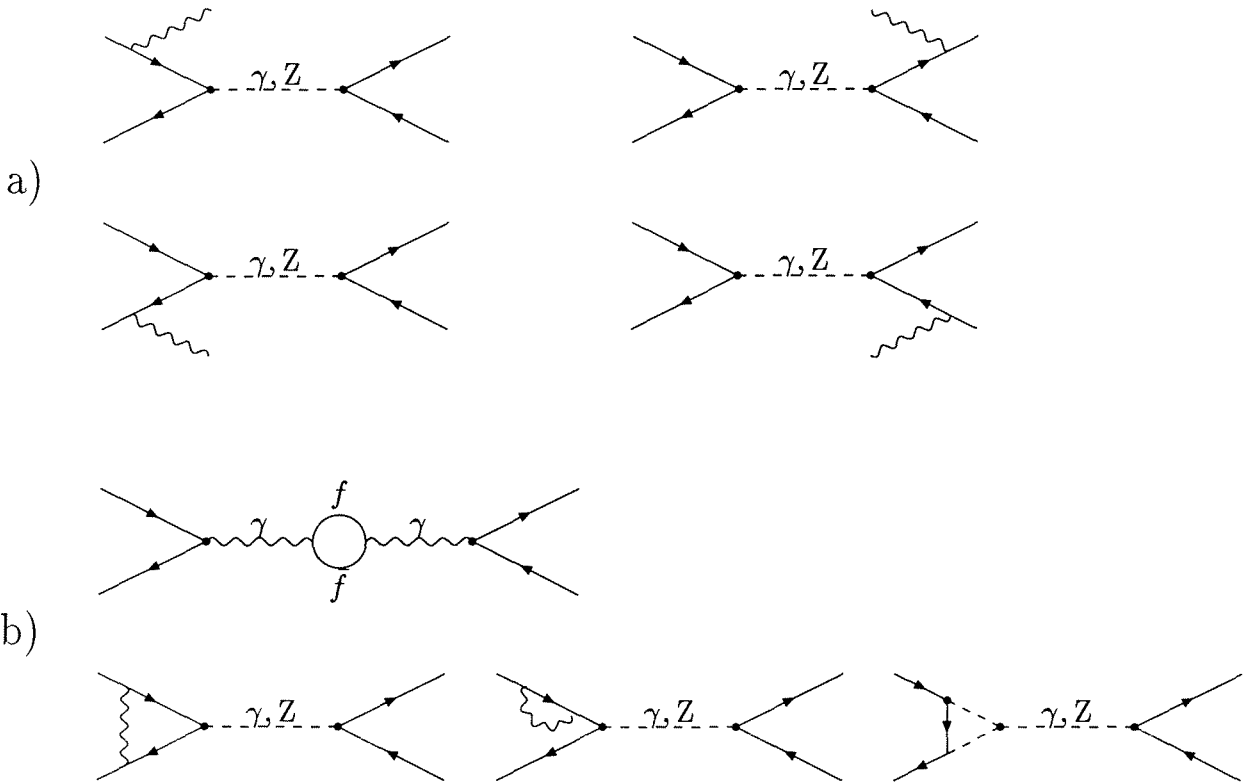
$$\begin{aligned} f\bar{f} = q\bar{q} & : (69.90 \pm 0.15)\% , \\ f\bar{f} = \nu_i\bar{\nu}_i & : (20.01 \pm 0.16)\% \quad (i = e, \mu, \text{ or } \tau) , \\ f\bar{f} = e^+e^- & : (3.366 \pm 0.008)\% , \\ f\bar{f} = \mu^+\mu^- & : (3.367 \pm 0.013)\% , \\ f\bar{f} = \tau^+\tau^- & : (3.360 \pm 0.006)\% . \end{aligned}$$

In the Z boson centre-of-mass system, the two fermions are emitted exactly back-to-back with an energy of half the centre-of-mass energy each, except when a FSR occurs, in which case their directions are no longer collinear because of momentum and energy conservation. In the case of quark pair production, hadronisation occurs: as soon as created, while going away from one another, the two quarks interact together by exchanging gluons. These gluons materialise into additional quarks which in turn emit gluons. This process of hadronisation results in the production of linked states of quarks: mesons (quark – anti-quark) and baryons (3 quarks) which share the initial quarks energy and are emitted in 2 (or less frequently 3 or 4) jets.

## 2.2.2 Forward-backward charge asymmetry

From equation (2.12) it is seen that the fermion production is asymmetric with respect to the forward ( $\cos\theta > 0$ ) and backward ( $\cos\theta < 0$ ) directions because of the weak interaction contribution which lead to the production of a polarised Z boson. A measurement of this

# QED



# WEAK

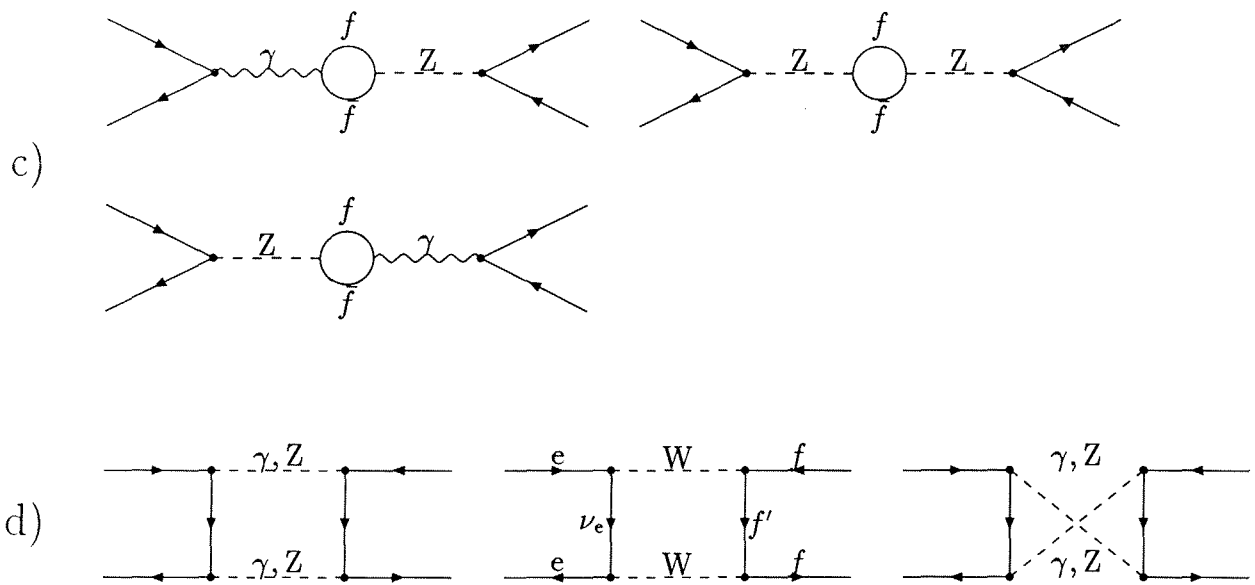


Figure 2.4: Examples of second order Feynman diagram for  $e^+e^-$  interaction.

asymmetry,  $A_{FB}^f$ , defined by

$$A_{FB}^f = \frac{\int_1^0 \frac{d\sigma_{ff}}{d\cos\theta} d\cos\theta - \int_0^{-1} \frac{d\sigma_{ff}}{d\cos\theta} d\cos\theta}{\int_1^{-1} \frac{d\sigma_{ff}}{d\cos\theta} d\cos\theta}, \quad (2.16)$$

allows the determination of the product of the Z coupling constants to the fermions: at  $s = M_Z^2$ , the following relation holds when the photon exchange is neglected:

$$A_{FB}^f \simeq \frac{3}{4} \frac{2g_v^e g_a^e}{g_v^{e2} + g_a^{e2}} \frac{2g_v^f g_a^f}{g_v^{f2} + g_a^{f2}} \quad (2.17)$$

Figure 2.5 shows the  $A_{FB}^f$  dependence on  $s$  and the effect of the ISR corrections.

In the special case of  $e^+e^- \rightarrow e^+e^-$  Bhabha scattering, the presence of the t-channel leads to a high forward asymmetry of the produced electron which is not taken into account here.

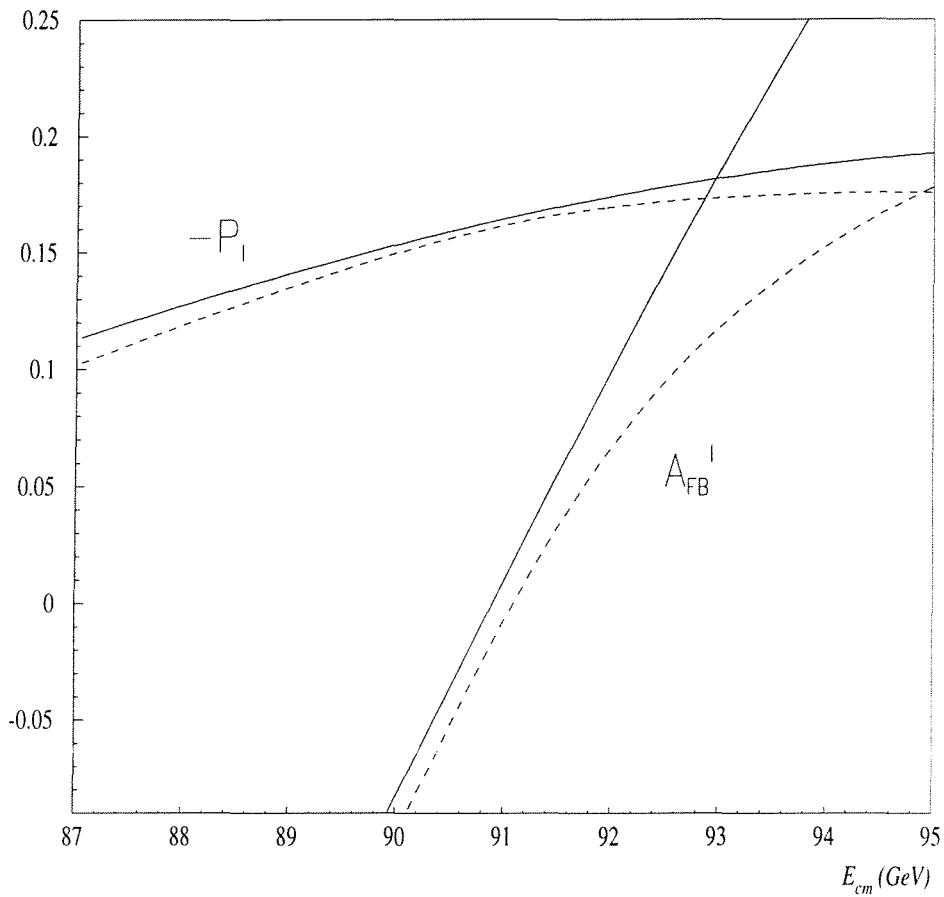


Figure 2.5: Mean polarisation  $\langle \mathcal{P}_l \rangle$  and forward-backward asymmetry  $A_{FB}^l$  as a function of  $E_{cm}$  for  $l = e^-, \mu^-, \tau^-$ . The solid lines represent the Born-level values. The ISR corrections were introduced in the computation of the dashed curves. The following inputs were used:  $\alpha = 1/137$ ,  $M_Z = 91.17 \text{ GeV}/c^2$ ,  $\sin^2 \theta_w = 0.229$ ,  $\Gamma_Z = 2.481 \text{ GeV}$ .

### 2.2.3 Polarisation

Following the Standard Model expression (2.9) and (2.5) of the neutral weak and electromagnetic currents  $J_\mu^0$  and  $J_\mu^{em}$ , the four possible helicity configurations of  $f\bar{f}$  pair production in  $e^+e^-$  interactions are:

$$e_L^- e_R^+ \rightarrow f_L \bar{f}_R \quad (2.18)$$

$$e_L^- e_R^+ \rightarrow f_R \bar{f}_L \quad (2.19)$$

$$e_R^- e_L^+ \rightarrow f_L \bar{f}_R \quad (2.20)$$

$$e_R^- e_L^+ \rightarrow f_R \bar{f}_L \quad (2.21)$$

( $f \neq \nu_e, \nu_\mu, \nu_\tau$  in the case of a photon exchange, and for the Z exchange, only (2.18) and (2.20) are valid when  $f = \nu_e, \nu_\mu, \text{ or } \nu_\tau$ ).

The Standard Model predicts that the Z boson couples differently to the right and to the left components of fermions (equations 2.10 and 2.11). Consequently, the Z boson and the produced fermions are polarised, and the fermion polarisation presents a dependence with respect to the fermion emission direction as explained below.

The differential production cross-section given by equation (2.12) can be parameterised in function of the produced fermion helicity state  $p$  ( $p = +1$  for a right-handed fermion,  $p = -1$  for a left-handed fermion) using  $g_p^f = 1/2(g_v^f - pg_a^f)$  with  $g_{+1}^f = g_R^f$  and  $g_{-1}^f = g_L^f$  in the limit of massless particles:

$$\frac{d\sigma_{f\bar{f}}^0(s, \cos \theta; p)}{d \cos \theta} = \frac{\pi \alpha^2}{2s} \left\{ \begin{aligned} & F_0(s) (1 + \cos^2 \theta) + F_1(s) 2 \cos \theta \\ & - p (F_2(s) (1 + \cos^2 \theta) + F_3(s) 2 \cos \theta) \end{aligned} \right\} \quad (2.22)$$

where the form-factors  $F_i(s)$  are:

$$\begin{aligned} F_0(s) &= Q_e^2 Q_f^2 + 2 g_v^e g_v^f Q_e Q_f \text{Re}_\chi(s) + (g_v^{e2} + g_a^{e2}) (g_v^{f2} + g_a^{f2}) |\chi(s)|^2 \\ F_1(s) &= 2 g_a^e g_a^f Q_e Q_f \text{Re}_\chi(s) + 4 g_v^e g_a^e g_v^f g_a^f |\chi(s)|^2 \\ F_2(s) &= 2 g_v^e g_a^f Q_e Q_f \text{Re}_\chi(s) + 2 (g_v^{e2} + g_a^{e2}) g_v^f g_a^f |\chi(s)|^2 \\ F_3(s) &= 2 g_a^e g_v^f Q_e Q_f \text{Re}_\chi(s) + 2 (g_v^{f2} + g_a^{f2}) g_v^e g_a^e |\chi(s)|^2 \end{aligned}$$

The fermion mean polarisation  $\langle \mathcal{P}_f \rangle$  and its angular dependence are defined by:

$$\langle \mathcal{P}_f(s) \rangle = \frac{\sigma_{f\bar{f}}^0(s; p = +1) - \sigma_{f\bar{f}}^0(s; p = -1)}{\sigma_{f\bar{f}}^0(s; p = +1) + \sigma_{f\bar{f}}^0(s; p = -1)} \quad (2.23)$$

$$= - \frac{F_2(s)}{F_0(s)} \quad (2.24)$$

$$\mathcal{P}_f(s, \cos \theta) = - \frac{(1 + \cos^2 \theta) F_2(s) + 2 \cos \theta F_3(s)}{(1 + \cos^2 \theta) F_0(s) + 2 \cos \theta F_1(s)} \quad (2.25)$$

$$(2.26)$$

and, at the peak of the Z resonance, neglecting the  $\gamma$  exchange:

$$\langle \mathcal{P}_f(s = M_Z^2) \rangle \simeq - \frac{2g_v^f g_a^f}{g_v^{f2} + g_a^{f2}} = \frac{g_R^{f2} - g_L^{f2}}{g_R^{f2} + g_L^{f2}} \quad (2.27)$$

$$\mathcal{P}_f(s = M_Z^2, \cos \theta) \simeq - \frac{(1 + \cos^2 \theta) \mathcal{A}_f + 2 \cos \theta \mathcal{A}_e}{(1 + \cos^2 \theta) + 2 \cos \theta \mathcal{A}_f \mathcal{A}_e} \quad (2.28)$$

with:

$$\mathcal{A}_i = \frac{2g_v^i g_a^i}{g_v^{i2} + g_a^{i2}} \quad (2.29)$$

The anti-fermion  $\bar{f}$  is always produced with an helicity opposite to that of the fermion (in the massless limit), so that:

$$\langle \mathcal{P}_{\bar{f}} \rangle = -\langle \mathcal{P}_f \rangle \quad (2.30)$$

The measurement of the mean polarisation of the fermion ( $\langle \mathcal{P}_f \rangle$ ) is another method allowing the determination the Z coupling constants  $g_R^f$  and  $g_L^f$  (or  $g_v^f$  and  $g_a^f$ ), leading to a better precision on the determination of  $\sin^2 \theta_w$  than the measurement of  $A_{FB}^f$  (2.17). Indeed, for the charged leptons ( $f = l = e^-, \mu^-, \tau^-$ ):

$$\mathcal{A}_l = \frac{2(1 - 4 \sin^2 \theta_w)}{1 + (1 - 4 \sin^2 \theta_w)^2} \approx -2 + 8 \sin^2 \theta_w \quad (2.31)$$

so that:

$$\langle \mathcal{P}_l \rangle = -\mathcal{A}_l \quad \Rightarrow \quad \Delta \sin^2 \theta_w \approx \frac{\Delta \langle \mathcal{P}_l \rangle}{8}$$

while

$$A_{FB}^l = \frac{3}{4} \mathcal{A}_e \mathcal{A}_l \quad \Rightarrow \quad \Delta \sin^2 \theta_w \approx \frac{\Delta A_{FB}^l}{1.6} \quad (\text{for } \sin^2 \theta_w = 0.233)$$

For a similar statistical precision, the error obtained on the  $\sin^2 \theta_w$  measurement by the determination of  $\langle \mathcal{P}_l \rangle$  is a factor  $\sim 5$  smaller than by the evaluation of  $A_{FB}^l$ .

Moreover, as can be seen on figure 2.5,  $\langle \mathcal{P}_l \rangle$  is less dependent on the  $e^+e^-$  centre-of-mass energy than is  $A_{FB}^l$  and consequently less sensitive to the initial state radiation effects.

In addition, the measurement of  $\mathcal{P}_l(\cos \theta)$  leads to an independent determination of  $\mathcal{A}_l$  and  $\mathcal{A}_e$ . Furthermore, it offers the possibility to test the lepton universality hypothesis.

Since the helicity of the final state lepton is determined by a statistical analysis of the kinematical spectra of its decay products (as detailed in the next section), at LEP energies, the measurement of  $\langle \mathcal{P}_l \rangle$  and  $\mathcal{P}_l(\cos \theta)$  is only feasible for  $l = \tau^-$  as the  $\tau$  is the only lepton to decay inside the detector volume. (For quark pair final states, the issue is complicated by their hadronisation).

Note that if the centre-of-mass energy  $E_{cm}$  of the  $e^+e^-$  system is not exactly equal to the Z boson mass (due to ISR or experimental conditions), what is actually measured is

$$\mathcal{P}_f(s, \cos \theta) \simeq \frac{(1 + \cos^2 \theta) \langle \mathcal{P}_f \rangle + 2 \cos \theta \mathcal{P}_Z}{(1 + \cos^2 \theta) + 2 \cos \theta \langle \mathcal{P}_f \rangle + \mathcal{P}_Z} \quad (2.32)$$

where  $\langle \mathcal{P}_f \rangle$  and  $\mathcal{P}_Z$  are respectively the mean fermion polarisation and the Z boson polarisation for  $E_{cm} = \sqrt{s}$ . They need to be corrected for the contribution of the photon exchange and for the radiation effects in order to have a correct determination of the quantities  $\mathcal{A}_f$  and  $\mathcal{A}_e$  at  $s = M_Z^2$  (see Chapter 7).



## 2.2.4 Left-right asymmetry

An interesting experiment, which is not realised at LEP but is at the SLAC Linear Collider (SLC), is the production of  $e^+e^- \rightarrow f\bar{f}$  interactions using polarised electron beams [11]. The SLC collider is able to accelerate electrons with 80% longitudinal polarisation (known with a precision of  $\pm 0.67\%$ ) at a rate of 120Hz, with the possibility of reversing the spin at each pulse. By a simple counting method,  $\mathcal{A}_e$  can be determined by measuring the left-right asymmetry  $A_{LR}$  defined as the normalised difference of the interaction cross-sections ( $\sigma_R^{obs}$  and  $\sigma_L^{obs}$ ) observed for the two different helicity states of the beam:

$$A_{LR} = \frac{\sigma_L^{obs} - \sigma_R^{obs}}{\sigma_L^{obs} + \sigma_R^{obs}} = P_{beam} \mathcal{A}_e \quad (2.33)$$

where  $P_{beam}$  is the beam polarisation. All final states of the  $e^+e^-$  interactions can be used for that measurement, leading to a low statistical error on the result.

## 2.3 Charged current interactions: $\tau$ physics

In 1971, four years before the first observations of the  $\tau$  lepton at the SPEAR  $e^+e^-$  storage ring [12], many of the  $\tau$  properties were described and quantified by Y.S.Tsai [13]. The mass of the  $\tau$  lepton allows it to decay not only into lighter leptons through purely leptonic decay modes:

$$\begin{aligned} \tau^- &\rightarrow e^- \bar{\nu}_e \nu_\tau, \\ \tau^- &\rightarrow \mu^- \bar{\nu}_\mu \nu_\tau, \end{aligned}$$

but also to light mesons, for example:

$$\begin{aligned} \tau^- &\rightarrow \pi^- / K^- / K^* \nu_\tau, \\ \tau^- &\rightarrow \pi^- / K^- \pi^0 \nu_\tau, \\ \tau^- &\rightarrow \pi^- / K^- K^0 \nu_\tau, \\ \tau^- &\rightarrow \pi^- / K^- \pi^0 \pi^0 \nu_\tau, \\ \tau^- &\rightarrow \pi^- \pi^+ \pi^- \nu_\tau, \\ \tau^- &\rightarrow \pi^- \pi^+ \pi^- \pi^0 \nu_\tau, \\ \tau^- &\rightarrow \pi^- \pi^+ \pi^- \pi^+ \pi^- \nu_\tau, \end{aligned}$$

( $\tau^+$  decay modes are charge conjugates of the upper modes). The  $\tau$  lepton has a lifetime of  $291fs$  [2]. The values of the main exclusive 1-prong  $\tau$  decay mode branching fractions and of the inclusive 1-prong ( $B_1$ ), 3-prong ( $B_3$ ) and 5-prong ( $B_5$ ) branching ratios are given in table 2.3. They correspond to the present world averages given in reference [2].

The Standard Model describes the  $\tau$  decay as a weak charged current interaction (2.2) or (2.3). For example, the leptonic decay mode ( $\tau^- \rightarrow l \bar{\nu}_l \nu_\tau$ ,  $l = e^-, \mu^-$ ) corresponds to the Feynman diagram of figure 2.6. In section 2.3.1, the general  $\tau$  decay matrix element is developed and the Michel parameters are introduced: they allow to test the pure V-A structure of the charged current. Section 2.3.2 describes how the  $\tau$  decay is used as a polarimeter in  $e^+e^-$  interactions.

$\tau$ decay mode	Branching ratio (%)
exclusive decay modes:	
$\tau^- \rightarrow e^- \bar{\nu}_e \nu_\tau$	$17.83 \pm 0.08$
$\tau^- \rightarrow \mu^- \bar{\nu}_\mu \nu_\tau$	$17.35 \pm 0.10$
$\tau^- \rightarrow \pi^- \nu_\tau$	$11.31 \pm 0.15$
$\tau^- \rightarrow K^- \nu_\tau$	$0.71 \pm 0.05$
$\tau^- \rightarrow (\rho^- \nu_\tau \rightarrow) \pi^- \pi^0 \nu_\tau$	$25.24 \pm 0.16$
$\tau^- \rightarrow K^- \pi^0 \nu_\tau$	$0.52 \pm 0.05$
$\tau^- \rightarrow (a_1^- \nu_\tau \rightarrow) \pi^- \pi^0 \pi^0 \nu_\tau$	$9.27 \pm 0.14$
...	
or inclusively:	
$\tau^- \rightarrow$ incl. 1-prong	$85.53 \pm 0.14$
$\tau^- \rightarrow$ incl. 3-prong	$14.36 \pm 0.14$
$\tau^- \rightarrow$ incl. 5-prong	$0.097 \pm 0.007$

Table 2.3: World average of the  $\tau$  branching ratios for the main 1-prong exclusive decay modes and the inclusive 1-prong, 3-prong and 5-prong modes.

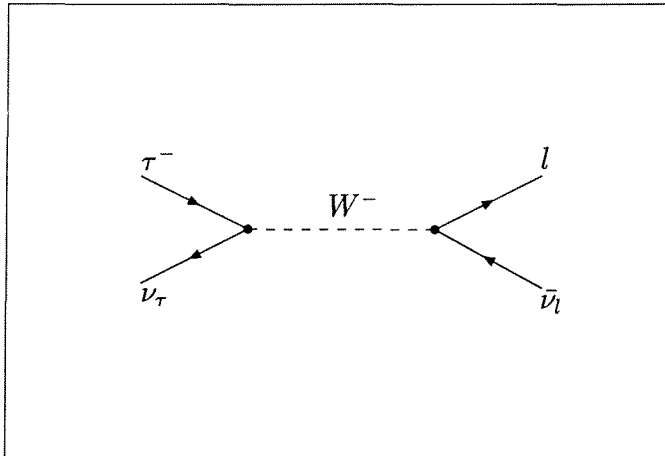


Figure 2.6: First order Feynman diagram for the leptonic decay of the  $\tau$  lepton ( $l = e^-, \mu^-$ ).

### 2.3.1 The $\tau$ decay and the Michel parameters

The Standard Model V–A structure of the charged weak current can be tested in the context of the  $\tau$  decay. In the case of the leptonic decay modes  $\tau \rightarrow l\nu_l\nu_\tau$ , the associated most general four-fermion point-interaction matrix element can be written as follows:

$$\mathcal{M} \propto \sum_{\gamma=S,V,T} \sum_{i,j=L,R} g_{ij}^\gamma \langle \bar{l}_i | \Gamma^\gamma | (\nu_l)_m \rangle \langle (\bar{\nu}_\tau)_n | \Gamma_\gamma | \tau_j \rangle, \quad (2.34)$$

where  $\gamma$  labels the type of interaction:  $\Gamma^S, \Gamma^V, \Gamma^T$  for scalar, vectorial and tensorial respectively, the indices  $i$  and  $j$  indicate the helicity state of the leptons  $l$  and  $\tau$  ( $R$  and  $L$  represent respectively the right- and left-handed states) and the neutrinos helicity  $m$  and  $n$  are fixed by the  $\gamma, i, j$  combination. If the possibility of the existence of a vector boson carrying a chiral charge is excluded ( $g_{LL}^T = 0$  and  $g_{RR}^T = 0$ ) [14], the  $g_{ij}^\gamma$  represent 10 complex coupling constants. In the frame of the Standard Model, all of them are zero except  $g_{LL}^V$  which is equal to 1.

The Michel parameters  $\rho, \eta, \delta$  and  $\xi$  are combinations of the  $g_{ij}^\gamma$  [15]:

$$\rho = \frac{3}{4} - \frac{3}{4} \left( |g_{RL}^V|^2 + |g_{LR}^V|^2 + 2|g_{RL}^T|^2 + 2|g_{LR}^T|^2 + \mathcal{R}e(g_{RL}^S g_{RL}^{T*} + g_{LR}^S g_{LR}^{T*}) \right) \quad (2.35)$$

$$\xi = -\frac{1}{4} \left( |g_{RR}^S|^2 + |g_{LR}^S|^2 - |g_{RL}^S|^2 - |g_{LL}^S|^2 \right) + 5 \left( |g_{LR}^T|^2 - |g_{RL}^T|^2 \right) - \left( |g_{RR}^V|^2 - 3|g_{LR}^V|^2 - |g_{LL}^V|^2 + 3|g_{RL}^V|^2 \right) + 4\mathcal{R}e(g_{RL}^S g_{RL}^{T*} - g_{LR}^S g_{LR}^{T*}) \quad (2.36)$$

$$\delta = \frac{1}{\xi} \left( -\frac{3}{16} \left( |g_{RR}^S|^2 + |g_{LR}^S|^2 - |g_{RL}^S|^2 - |g_{LL}^S|^2 \right) - \frac{3}{4} \left( |g_{RR}^V|^2 - |g_{LL}^V|^2 \right) + \frac{3}{4} \left( |g_{RL}^T|^2 - |g_{LR}^T|^2 \right) + \frac{3}{4} \mathcal{R}e(g_{RL}^S g_{RL}^{T*} - g_{LR}^S g_{LR}^{T*}) \right) \quad (2.37)$$

$$\eta = \frac{1}{2} \mathcal{R}e \left( 6g_{RL}^V g_{LR}^{T*} + 6g_{LR}^V g_{RL}^{T*} + g_{RR}^S g_{LL}^{V*} + g_{RL}^S g_{LR}^{V*} + g_{LR}^S g_{RL}^{V*} + g_{LL}^S g_{RR}^{V*} \right) \quad (2.38)$$

The Standard Model values of the  $\rho, \eta, \delta$  and  $\xi$  parameters are respectively  $\frac{3}{4}, 0, \frac{3}{4}$  and 1. In case where the lepton universality would not hold for the charged weak current, the parameters could have different values for the electron and the muon ( $\rho_e \neq \rho_\mu, \dots$ ).

The Michel parameters appear in the following parameterisation of the distribution of the reduced energy  $x_l = E_l/E_\tau$  of the final state charged lepton  $l$  ( $l = e$  or  $\mu$ ) (see equation 2.47):

$$\begin{aligned} \frac{d\Gamma}{\Gamma dx_l} &= f_l(x_l) - \langle \mathcal{P}_\tau \rangle g_l(x_l) \\ &= f_c(x_l) + \rho_l f_\rho(x_l) + \eta_l f_\eta(x_l) - \langle \mathcal{P}_\tau \rangle \xi_l (g_c(x_l) + \delta_l g_\delta(x_l)) \end{aligned} \quad (2.39)$$

where:

$$\begin{aligned}
f_c(x_l) &= 2 - 6x_l^2 + 4x_l^3, \\
f_\rho(x_l) &= \frac{4}{9} (-1 + 9x_l^2 - 8x_l^3), \\
f_\eta(x_l) &= 12 \frac{m_l}{m_\tau} (1 - x_l^2), \\
g_c(x_l) &= -\frac{2}{3} + 4x_l - 6x_l^2 + \frac{8}{3}x_l^3, \\
g_\delta(x_l) &= \frac{4}{9}(1 - 12x_l + 27x_l^2 - 16x_l^3).
\end{aligned}$$

and  $\langle \mathcal{P}_\tau \rangle$  is the  $\tau$  mean polarisation (see section 2.3.2).

The parameters can be extracted from a fit to real data of the correlated spectra of the energy of the  $\tau$  decay products,  $\frac{d^2\Gamma}{\Gamma dx_i dx_j}$ , allowing at the same time the measurement of  $\langle \mathcal{P}_\tau \rangle$ :

$$\begin{aligned}
\frac{d^2\Gamma}{\Gamma dx_i dx_j} &= f_i(x_i)f_j(x_j) + g_i(x_i)g_j(x_j) \\
&\quad - \langle \mathcal{P}_\tau \rangle (g_i(x_i)f_j(x_j) + f_i(x_i)g_j(x_j)).
\end{aligned} \tag{2.40}$$

Any deviation of the parameters from their Standard Model values would indicate new physics. However, the parameter  $\rho$  can be equal to 3/4 and still allow non-Standard physics. Indeed,

$$|g_{RL}^V|^2 + |g_{LR}^V|^2 + 2|g_{RL}^T|^2 + 2|g_{LR}^T|^2 = -\mathcal{R}e(g_{RL}^S g_{RL}^{T*} + g_{LR}^S g_{LR}^{T*})$$

is a solution. If  $g_{LR}^T$  and  $g_{RL}^T$  vanish, it suffices that  $g_{LR}^V$  and  $g_{RL}^V$  be also zero. All other couplings are arbitrary and in particular, a pure V+A coupling is possible ( $g_{RR}^V \neq 0$ ). The measurement of  $\xi$  allows to remove the ambiguity: in case of pure V+A coupling,  $\xi$  equals -1. On the other hand, if  $\rho$  equals 3/4 and there is simultaneous scalar and tensor couplings, a mixing of V+A and V-A interactions is allowed ( $g_{RL}^V \neq 0$  or  $g_{LR}^V \neq 0$ ).

The  $\eta_l$  parameter is practically impossible to measure in the case of  $l = e$  because of the highly suppressive factor  $m_e/m_\tau$  which appears in the expression of  $f_\eta(x_l)$ . The measurement of  $\eta_\mu$  is feasible but still only efficient for low energy muons. The observation of  $\eta_\mu$  being non-zero would indicate that there exists at least two different couplings (V and T, or S and V) implying charged leptons of opposite chiralities which would result in a non-maximal parity and charge conjugation violation. If the V-A interaction is dominant, then the second coupling would be of the scalar- (or Higgs-) type ( $g_{RR}^S \neq 0$ ).

### 2.3.2 The $\tau$ decay as a polarimeter

In the  $\tau$  centre-of-mass system, the  $\tau$  decay products are emitted with a preferred direction with respect to the  $\tau$  spin to ensure conservation of the total angular momentum. Figure 2.7 shows the clearest case of  $\tau^- \rightarrow \pi^- \nu_\tau$ . As the neutrino is left-handed (its helicity  $h_{\nu_\tau}$  equals -1) and the pion has spin 0, the pion is preferably produced in the direction parallel ( $1 + \cos \theta^*$ ) or anti-parallel ( $1 - \cos \theta^*$ ) to the  $\tau$  spin depending whether the  $\tau^-$  is right-handed or left-handed

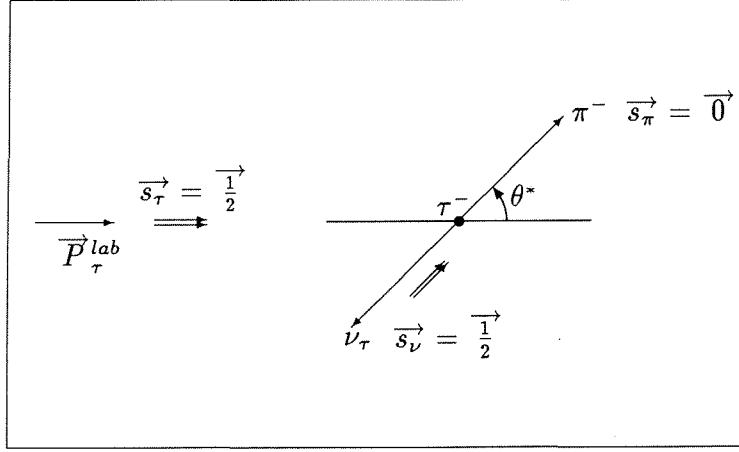


Figure 2.7:  $\tau^- \rightarrow \pi^- \nu_\tau$  decay description in the  $\tau^-$  decay frame. This is an example for the decay of a right-handed  $\tau$  ( $h_\tau = +1$ );  $\vec{P}_\tau^{lab}$  indicates the  $\tau$  flight direction in the laboratory frame and  $\vec{s}_\tau$  is its spin vector. The double-arrows indicate the directions of the spin-vectors.

in the laboratory frame. Consequently, the angular spectrum of the pion is of the form:

$$\begin{aligned}
 \frac{d\Gamma}{\Gamma d\cos\theta^*} &= \frac{1}{2} \frac{1}{|g_R^\tau|^2 + |g_L^\tau|^2} ( |g_R^\tau|^2(1 + \cos\theta^*) + |g_L^\tau|^2(1 - \cos\theta^*) ) \\
 &= \frac{1}{2} ( 1 + \langle \mathcal{P}_{\tau^-} \rangle \cos\theta^* ) \\
 &\equiv \frac{1}{2} ( 1 - h_{\nu_\tau} \langle \mathcal{P}_{\tau^-} \rangle \cos\theta^* )
 \end{aligned} \tag{2.41}$$

where  $\theta^*$  is the angle between the direction of the  $\pi^-$  momentum and the  $\tau^-$  spin direction, measured in the  $\tau^-$  rest-frame. In the case of the  $\tau^+$  decay, a right-handed anti-neutrino is produced. The  $\pi^+$  is then emitted preferably in the direction anti-parallel ( $1 - \cos\theta^*$ ) or parallel ( $1 + \cos\theta^*$ ) to the  $\tau^+$  spin depending whether the  $\tau^+$  is right-handed or left-handed ( $\theta^*$  is the angle between the  $\pi^+$  momentum and the  $\tau^+$  spin direction, measured in the  $\tau^+$  rest-frame). Since a left-handed  $\tau^+$  is produced when the  $\tau^-$  is right-handed, the  $\pi^+$  angular spectrum is identical to the  $\pi^-$  spectrum (2.41).

The pion decay angle  $\theta^*$  in the  $\tau$  rest-frame is directly related to its energy  $E_\pi$  and the  $\tau$  energy  $E_\tau$  measured in the laboratory system:

$$\cos\theta^* = \frac{2E_\pi m_\tau^2 - E_\tau(m_\tau^2 + m_\pi^2)}{(m_\tau^2 - m_\pi^2)\sqrt{E_\tau^2 - m_\tau^2}} \simeq 2x_\pi - 1, \quad x_\pi = \frac{E_\pi}{E_\tau}, \tag{2.42}$$

where the ratios  $\frac{m_\pi^2}{m_\tau^2}$  and  $\frac{m_\tau^2}{E_\tau^2}$  are neglected.

Using (2.42), the relation (2.41) becomes:

$$\frac{d\Gamma}{\Gamma dx_\pi} = 1 - h_{\nu_\tau} \langle \mathcal{P}_\tau \rangle (2x_\pi - 1), \tag{2.43}$$

where  $\pi$  is either  $\pi^+$  or  $\pi^-$  and  $\langle \mathcal{P}_{\tau^-} \rangle$  is denoted  $\langle \mathcal{P}_\tau \rangle$ . Both  $\tau$  decays can be used for the measurement of  $\langle \mathcal{P}_\tau \rangle$  which is given by the slope of the pion reduced energy spectrum. Note that if the Standard Model value  $h_{\nu_\tau} = -1$  is not assumed, what is actually measured is the product  $-h_{\nu_\tau} \langle \mathcal{P}_\tau \rangle$ .

In the case of the  $\tau$  decay into a spin-1 hadron like  $h = \rho$  or  $a_1$ ,  $h$  can have helicity 0 or  $\pm 1$ . The sensitivity to  $\langle \mathcal{P}_\tau \rangle$  of  $\frac{d\Gamma}{\Gamma dx_h}$  is reduced by a factor  $\alpha_h = \frac{m_\tau^2 - 2m_h^2}{m_\tau^2 + 2m_h^2}$ , where  $m_h$  is the hadron mass:  $\alpha_\rho \approx 0.46$ ,  $\alpha_{a_1} \approx 0.12$ . The angular spectrum of the hadron is then:

$$\frac{d\Gamma}{\Gamma dx_h} = \frac{1}{2} (1 - \alpha_h h_{\nu_\tau} \langle \mathcal{P}_\tau \rangle \cos \theta^*) \quad (2.44)$$

with

$$\cos \theta^* = \frac{2x_h - 1 - (m_h/m_\tau)^2}{1 - (m_h/m_\tau)^2}, \quad x_h = \frac{E_h}{E_\tau} \quad (2.45)$$

The sensitivity to  $\langle \mathcal{P}_\tau \rangle$  can be increased if information about the hadron helicity state is deduced from the decay distribution of the hadronic system. For example, in the case of a  $\rho$  decay ( $\rho^\pm \rightarrow \pi^\pm \pi^0$ ), the decay angle  $\psi$  of the charged pion is given by:

$$\cos \psi = \frac{m_h}{\sqrt{m_h^2 - 4m_\pi^2}} \frac{E_\pi - E_{\pi^0}}{|\vec{p}_\pi + \vec{p}_{\pi^0}|} \quad (2.46)$$

where  $E_\pi$  ( $E_{\pi^0}$ ) and  $\vec{p}_\pi$  ( $\vec{p}_{\pi^0}$ ) are respectively the energy and the momentum vector of the charged (neutral) pion measured in the laboratory frame. A two-dimensional decay spectrum  $W(\cos \theta^*, \cos \psi; \langle \mathcal{P}_\tau \rangle)$  [16] is then used to determine  $\langle \mathcal{P}_\tau \rangle$  with an increased sensitivity (see table 2.4).

The leptonic  $\tau$  decay mode, being a 3-body decay, leads also to a less sensitive distribution:

$$\frac{d\Gamma}{\Gamma dx_l} = \frac{1}{3} \{ (5 - 9x_l^2 + 4x_l^3) - \langle \mathcal{P}_\tau \rangle (1 - 9x_l^2 + 8x_l^3) \} . \quad (2.47)$$

According to the  $\tau$  decay mode  $i$ , the information on  $\langle \mathcal{P}_\tau \rangle$  is thus contained in a 1 or 2 dimensional distribution of the form:

$$W_i(\vec{x}_i) = f_i(\vec{x}_i) - \langle \mathcal{P}_\tau \rangle g_i(\vec{x}_i) \quad (2.48)$$

where  $\vec{x}_i$  is the set of the relevant variable(s) for the considered channel  $i$ , and the functions  $f_i$  and  $g_i$  satisfy the following conditions:  $\int_0^1 f_i(\vec{x}) d\vec{x} = 1$ ,  $\int_0^1 g_i(\vec{x}) d\vec{x} = 0$ ,  $f_i \geq 0$  and  $|g_i| \leq f_i$ . Each decay channel offers a different sensitivity  $S_i$  to  $\langle \mathcal{P}_\tau \rangle$ , the  $\tau \rightarrow \pi \nu_\tau$  mode being the most sensitive (table 2.4).

In ideal conditions (i.e. no detector effects, no radiative corrections, pure samples selected with a 100% efficiency), the error on the measurement of  $\langle \mathcal{P}_\tau \rangle$  obtained from a fit of the distribution (2.48) to a set of  $N_i$  measurements is asymptotically equal to:

$$\Delta \langle \mathcal{P}_\tau \rangle = \frac{1}{\sqrt{N_i}} \left( \int \frac{g_i^2}{f_i + \langle \mathcal{P}_\tau \rangle g_i} \right)^{-\frac{1}{2}} \equiv \frac{1}{S_i \sqrt{N_i}} , \quad (2.49)$$

so that the weight of a given decay channel  $\tau \rightarrow X_i \nu_\tau$  of branching ratio  $Br_i$  used for the  $\langle \mathcal{P}_\tau \rangle$  determination is  $w_i = S_i^2 Br_i$  (table 2.4) [17]. Evidently, it is very interesting to include a maximum of  $\tau$  final states into the  $\langle \mathcal{P}_\tau \rangle$  measurement since it results in a smaller error  $\Delta \langle \mathcal{P}_\tau \rangle$  ( $N_\tau$  is the number of  $\tau$  decays):

$$\Delta \langle \mathcal{P}_\tau \rangle = \left( \sum_i \frac{1}{(\Delta \langle \mathcal{P}_\tau \rangle)_i^2} \right)^{-\frac{1}{2}} = \left( \sum_i w_i N_\tau \right)^{-\frac{1}{2}} . \quad (2.50)$$

$\tau$ decay mode $i$	Sensitivity $S_i$	Relative weight $w_i/w_\tau$
$\tau \rightarrow \pi\nu_\tau$	0.6	1.
$\tau \rightarrow \rho\nu_\tau$	0.49 (0.26)	1.6
$\tau \rightarrow a_1\nu_\tau$	0.23 (0.10)	0.1
$\tau \rightarrow e\nu_e\nu_\tau$	0.22	0.2
$\tau \rightarrow \mu\nu_\mu\nu_\tau$	0.22	0.2

Table 2.4: Sensitivity to  $\langle\mathcal{P}_\tau\rangle$  and relative weight in the  $\langle\mathcal{P}_\tau\rangle$  measurement for different  $\tau$  decay modes. For the  $\rho$  and  $a_1$  channels, the sensitivity values given in brackets correspond to the 1-dimensional spectrum (2.44).

# Chapter 3

## Experimental setup and methods

The  $e^+e^- \rightarrow \tau^+\tau^-$  interactions studied in the present work have been produced in the collision of electron and positron beams at CERN, the European Laboratory for Particle Physics. The particle beams are accelerated in several steps up to an energy of 20 GeV, by a series of linear and circular pre-accelerators. They are then injected into the LEP storage ring, the Large Electron Positron collider, operating since 1989, where their nominal energy of about 45 GeV is reached and where the collisions are produced in four equidistant interaction points equipped with detectors: ALEPH, DELPHI, L3 and OPAL. The present analysis is based on data recorded by the DELPHI detector during the years 1993, 1994 and 1995.

In the following, some information about the collider and the beam injection and acceleration systems are given (section 3.1). More details can be found in reference [18].

The DELPHI detector is then presented (section 3.2) together with the data acquisition system, the luminosity measurement and the procedures of data reconstruction and calibration. Also simulated data are used in the present work. The simulation algorithm, based on the Monte Carlo method, is described in section 3.3. The neural network analysis technique, used for our analysis, is explained in section 3.4.

### 3.1 The Large Electron Positron collider at CERN

The LEP collider is a very large machine located on the CERN site on the French-Swiss border near Geneva. It is built at a depth of 100 to 150 metres inside a tunnel of 26.7 km of circumference. The plane of the tunnel is inclined by 1.4% to ensure that all underground caverns and the main part of the tunnel are located in solid rock.

The electron and positron beams are generated by an electron gun (atomic electrons are isolated using an electric field) and a positron converter (electrons are accelerated on a tungsten target where bremsstrahlung photons are produced and converted into electron-positron pairs separated by a magnetic field).

The acceleration of the beams and their injection into the LEP machine proceeds in several steps (see figure 3.1). The beams are first accelerated by two linear accelerators LIL (LEP injector Linac) to an energy of respectively 200 MeV and 600 MeV and are then stored in a 600 MeV Electron-Positron Accumulator (EPA), which injects the particles into the CERN Proton Synchrotron (PS) operating as a 3.5 GeV synchrotron. From the PS, the beams are injected into the Super Proton Synchrotron (SPS), which operates as a 20 GeV injector for LEP where the beams reach finally their nominal energy of 45 GeV (Phase I from 1989 to 1995) or up to  $\simeq 90$  GeV (Phase II starting end of 1995). The decision to use the two already existing CERN proton synchrotrons (the SPS and the PS) and all the infrastructure associated with



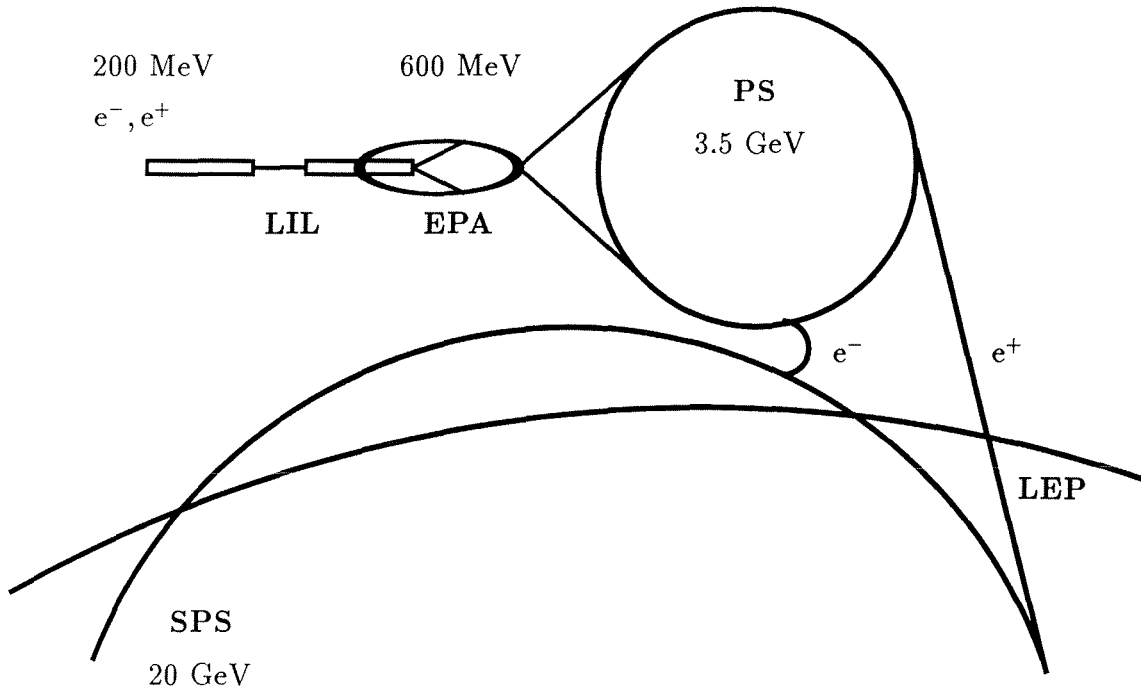


Figure 3.1: Schematic view of the LEP injection chain, which consists of a two stage injector linac (LIL), the Electron Positron Accumulator (EPA), the Proton Synchrotron (PS) and the Super Proton Synchrotron (SPS).

them, resulted in significant economies both in cost and in construction time.

The electromagnetic beam guide field system of LEP consists of dipoles, quadrupoles, sextupoles, rotated quadrupoles, and finally electrostatic dipole deflectors. Both electron and positron beams are circulating inside the same vacuum chamber on an octagonal trajectory with rounded corners. The electrons and positrons are bent in the piecewise circular trajectory by strings of dipole magnets. Thanks to the large LEP radius, the bending field of these dipoles is relatively low (about 0.1 T) so that the amount of synchrotron radiation is reduced. The quadrupole magnets, which produce fields varying linearly with the transverse position, act as magnetic lenses and focus the beam to be comfortably contained within the vacuum chamber. The sextupoles produce a field which is quadratic in transverse displacement. They are used to compensate the dependence of the focusing strength of the quadrupoles on the beam energy.

Each beam is made of four equidistant particle bunches of about 15 mm long<sup>1</sup> which cross, at eight points during each revolution, the particle bunches of the beam circulating in the opposite direction. During LEP injection and acceleration of the beams to their nominal energy, electrostatic separators, installed at the eight crossing points, allow to separate vertically the two beam trajectory in order to avoid beam-beam effects and loss of the beams. After acceleration, the beams are oriented so that they collide in the four equidistant interaction regions situated in the centre of the four LEP detectors. The particle bunches must be tightly focused to very small dimensions in the centre of each detector in order to increase the luminosity  $\mathcal{L}$  of

<sup>1</sup>This was the situation up to 1995. Afterwards, each bunch was made of several packets of particles, in order to increase the luminosity.

the collider which determines the interaction rate  $dN/dt$ :

$$dN/dt = \mathcal{L} \cdot \sigma_{e^+e^-}$$

for a given interaction cross-section  $\sigma_{e^+e^-}$ . This is accomplished by a set of superconducting quadrupoles with very strong field gradients that focus the transverse beam dimensions to about  $10 \mu\text{m}$  and  $250 \mu\text{m}$  in the vertical and horizontal planes respectively. Typically, particles circulate about 12 hours inside the collider. During this time each of the  $10^{12}$  particles in the beams will have traversed the complete 26.67 km of the LEP vacuum chamber about 500 million times (the revolution period is  $88 \mu\text{s}$ ). In order to minimise particle losses due to collisions with residual gas molecules, the whole vacuum chamber must be pumped down to very low pressures. The achieved static pressure for LEP is  $8 \times 10^{-12}$  Torr whereas in the presence of beam the pressure rises to about  $10^{-9}$  Torr. This pressure rise is due to gas desorption from the inner vacuum-chamber wall, provoked by the synchrotron radiation of the circulating beams. The beam-pipe is a few millimetres thick and is essentially made of aluminium covered with lead cladding. At the level of the detectors, the beam-pipe diameter is reduced from 160 mm to 120 mm to allow a better reconstruction of the interaction vertex, and, for reason of transparency to particles, the beam-pipe is built here in beryllium (for DELPHI), thin-walled aluminium or carbon-fibre composites.

The luminosity  $\mathcal{L}$  is proportional to:

$$\mathcal{L} \propto \frac{N_{e^+}N_{e^-}bf}{A} \quad (\text{cm}^{-2}\text{s}^{-1})$$

when each of the  $b$  particle bunches contains  $N_{e^-}$  ( $N_{e^+}$ ) electrons (positrons) and collides with the opposite bunch through a transverse section of  $A \text{ cm}^2$  and at a frequency of  $f \text{ s}^{-1}$ . The luminosity is determined experimentally as described in section 3.2.5. During phase I of LEP running where the centre-of-mass energy of the  $e^+e^-$  system corresponded to the  $Z$  resonance domain, typical instantaneous luminosities of the order of  $10^{31} \text{ cm}^{-2}\text{s}^{-1}$  were reached, corresponding to a  $Z$  production rate of the order of 1 Hz.

Background sources originating from the beams and reaching the detectors, are of different types. Electrons or positrons occupying the transverse tails of the bunches can collide with the beam-pipe wall and interact with the material, producing background particles. Photons from the beam synchrotron radiation produce a counting rate of the order of 5 to 150 per beam cross-over (BCO) (i.e. every  $22 \mu\text{s}$ , 45 kHz). Finally, these synchrotron radiation photons often collide into the collimator setup, leading to the production of  $e^+e^-$  or  $\mu^+\mu^-$  pairs emitted in a direction parallel to the beams, which are detected by the forward parts of the detectors at a rate of about 0.02 per BCO. These important background rates demand the development of efficient logic for the trigger decision by the detector data acquisition system.

## 3.2 The DELPHI detector and its performance

The DELPHI detector is centred on the eighth LEP collision point. This “DEtector with Lepton, Photon and Hadron Identification” is designed to provide high granularity, allowing an efficient particle identification. It is built of co-axial cylindrical detection modules surrounding the beam-pipe and is closed by two endcaps of similar detection systems in order to assure a maximum solid angle coverage around the interaction region (see figure 3.2). Its components are described in detail in reference [19]. The detector has been operating since 1989 and has been constantly upgraded since then. These developments are summarised in reference [20] where the detector performance is reviewed as well.

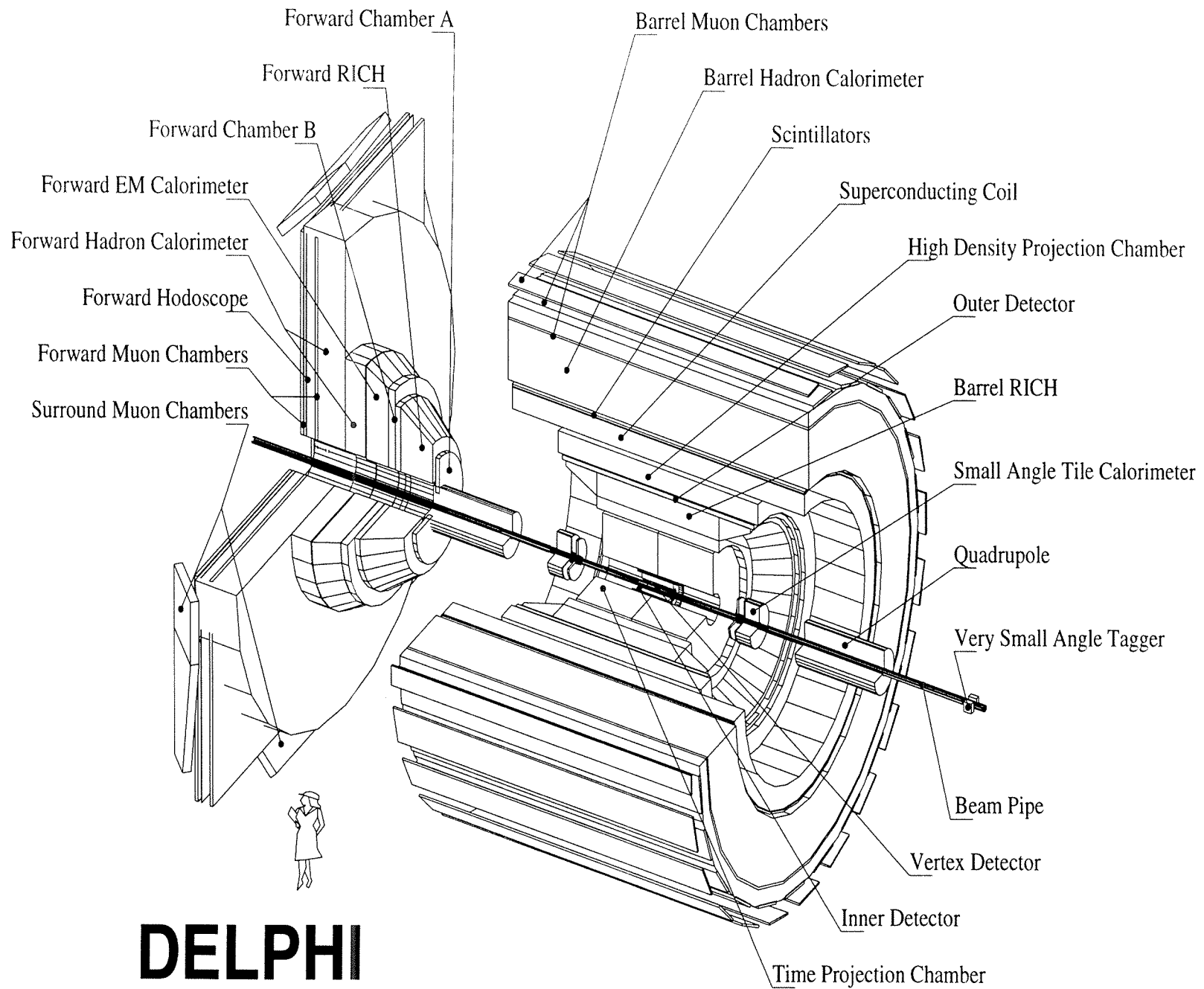


Figure 3.2: Schematic view of the DELPHI detector

In the standard DELPHI coordinate system, the geometrical centre of the detector is taken as the origin,  $z$  is measured along the electron beam direction, the  $x$ -axis is pointing towards the centre of the LEP ring and  $y$  point upwards. In polar coordinates,  $R$  is measured in the  $xy$  plane where the azimuthal angle  $\phi$  is measured with respect to the  $x$ -axis. The polar angle  $\theta$  refers to the  $z$ -axis. Our analysis is limited to events produced inside the barrel (central) region of the detector ( $43^\circ < \theta < 137^\circ$ ) which is completely covered by all central tracking devices, calorimeters and muon detectors and where the trigger efficiency is consistent with 100%, so that optimal conditions are met for the estimation of the physical quantities needed for the measurement of the  $\tau$  polarisation.

In the following sections, a review<sup>2</sup> is given of the DELPHI barrel detector modules which were directly relevant to our analysis, and of the performance for the reconstruction of the different physical quantities such as particle momentum and electromagnetic or hadronic energy depositions. This reconstruction is performed by DELANA, the DELPHI reconstruction program [21] which treats the raw data (the electronic signals provided by each detector submodules) and records the treated information on the Data Summary Tapes (DST). Our analysis used the refined reconstruction of electron radiations and photon conversions and the information on  $\pi^0$ 's extracted from the study of the electromagnetic showers, provided by the ELEPHANT package (ELEctron Photon ANalysis Tool) [22] as explained in what follows. Also results from the MUFLAG package [23] described below, are exploited in our analysis (see Chapter 5). Both ELEPHANT and MUFLAG analysis are performed after the DST production. In the last sections, the DELPHI data acquisition system and the luminosity measurement are briefly described.

### 3.2.1 Tracking system

The tracking of charged particles (i.e. the reconstruction in the detector volume of the particle trajectories) is done using the information provided by four tracking detectors placed in a 1.23 T homogeneous magnetic field parallel to the beam axis produced by a superconducting solenoid. From the curvature of its reconstructed track both the charge and the momentum of a charged particle can be determined.

The main tracking device of DELPHI is the **Time Projection Chamber (TPC)**. It consists of a large gas chamber with inner and outer radius of respectively 30 cm and 120 cm and a total length of 3 m (see figure 3.3). It is submitted to an electric field parallel to the beam axis, generated by a cathode plane at  $\theta = 90^\circ$  and 2 anode planes forming the end-plates of the chamber and divided into 6 azimuthal sectors, each with 192 sense wires and 16 circular pad rows with constant spacing. The detector provides up to 16 space points per particle trajectory (for  $40 \text{ cm} < R < 110 \text{ cm}$  and  $39^\circ < \theta < 141^\circ$ ) with information on the  $z$  coordinate deduced from the drift time of the ionisation electrons. At least 3 pad rows are crossed for polar angles of  $20^\circ < \theta < 160^\circ$ . The dead space between the pads of adjacent end-plate sectors corresponds to 4% of the  $xy$  plane. Because of the action of the magnetic field, the minimum momentum required for a charged particle produced at the interaction point to reach the TPC is 0.09 GeV/c (0.14 GeV/c) at  $\theta = 90^\circ$  (at  $\theta = 40^\circ$ ). Below 0.36 GeV/c (0.56 GeV/c), the particle curls inside the TPC. The single point precision for tracks from  $Z \rightarrow \mu^+\mu^-$  decays is 250  $\mu\text{m}$  in the  $R\phi$  plane and 880  $\mu\text{m}$  in the  $Rz$  plane. The two-point resolution is about 1 cm in both directions.

The 192 sense wires of the TPC provide information about the energy lost by a charged particle due to ionisation of the gas ( $dE/dX$ ). This measurement (together with the corresponding

---

<sup>2</sup>Most of the informations are extracted from reference [20]

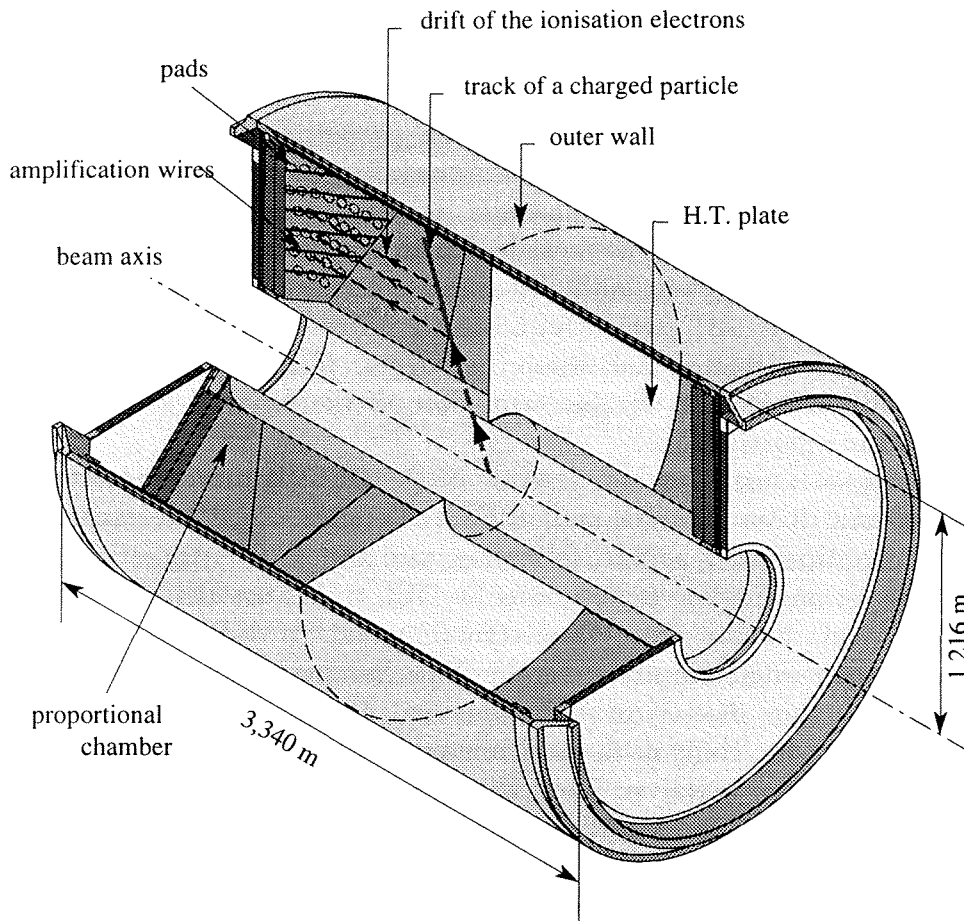


Figure 3.3: *Schematic view of the TPC*

experimental error and the momentum estimation of the ionising particle) allows to attribute a mass probability to the particle. The  $dE/dX$  measurement is deduced from a truncated average of the  $dE/dX$  measurements provided by the sense wires. For several reasons, some sense wire signals are indeed rejected: signals below the electronic threshold (about 8%), signals too close in time to be correctly separated (this requirement corresponds, for tracks orthogonal to the drift direction, to a separation of at least 2 cm), signals incompatible with the ionisation of a single particle. A minimum of 30 contributing signals is required to obtain a reliable  $dE/dX$  measurement: in the barrel region, this happens for 61% to 97% of the particles depending on the track multiplicity. The precision on the  $dE/dX$  measurement is 5.5% for isolated particles and of the order of 7.5% for particles in jets. The value of the Fermi plateau, normalised to the minimum ionising particle, is found to be 1.52 units.

For a higher tracking precision in the region of the interaction point, two tracking devices are present at smaller radii:

**The Vertex Detector (VD):** it is made of three cylindrical layers of silicon strip detectors at average radii of 6.3 cm, 9.0 cm and 10.9 cm (see figure 3.4). It provides a single hit precision of  $7.6 \mu\text{m}$  in  $R\phi$ . The inner and outer layers of the VD cover respectively the polar angle ranges of  $27^\circ < \theta < 153^\circ$  and  $44^\circ < \theta < 136^\circ$ . Each layer covers the full azimuthal angle in 24 sectors with a 10% overlap between adjacent sectors, which consist of four modules of 6 cm along the  $z$ -axis. At the beginning of 1994, the first and third layers were equipped with double-sided silicon detectors, having strips orthogonal to each other on opposite sides, giving measurements also in the  $z$  direction, with a single hit precision in  $z$  of  $9 \mu\text{m}$  to  $32 \mu\text{m}$  depending on the incidence angle of the particle. Information from the VD provides precise coordinates on the trajectory of charged particles which are used for vertex reconstruction and lifetime measurements.

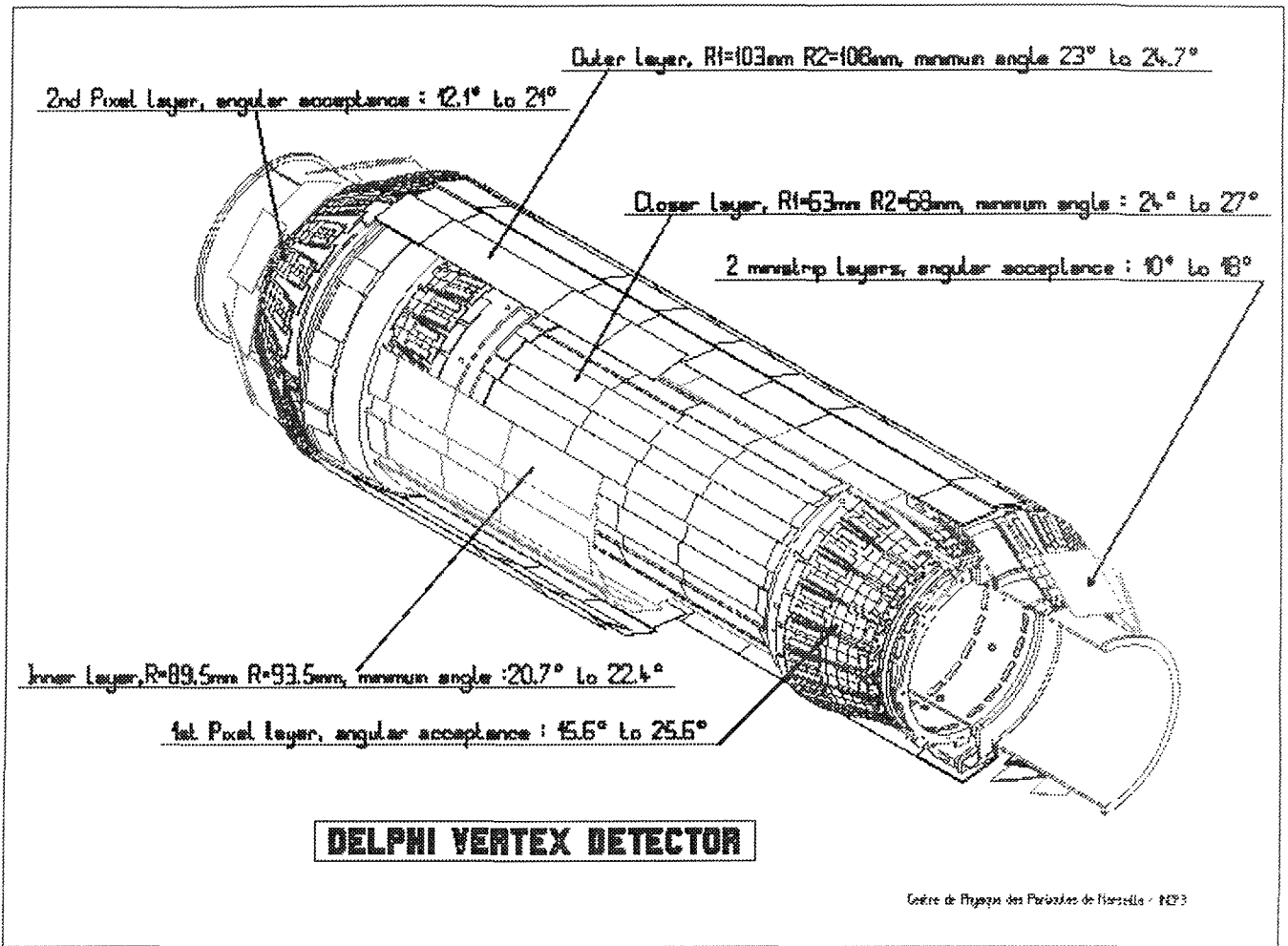


Figure 3.4: Schematic view of the VD

The **Inner Detector (ID)**: it gives a supplementary information in the region between the VD and the TPC: it has inner and outer radii of 12 cm and 28 cm and consists of an 11 cm deep inner drift chamber with jet-chamber geometry built in 24 azimuthal sectors, and five surrounding MWPC layers (Multi-Wire Proportional Chambers) with sense wires spaced by about 8 mm giving  $Rz$  information and allowing to resolve the left/right ambiguities inherent in the jet-chamber. The ID provides up to 24  $R\phi$  points per track, at least 10 for  $23^\circ < \theta < 157^\circ$  ( $15^\circ < \theta < 165^\circ$  since the beginning of 1995 when a new longer ID was installed). The MWPC layers cover the range of  $30^\circ < \theta < 150^\circ$ . In 1995 they were replaced by five cylindrical layers of straw tube detectors, no longer providing any  $z$  measurement. The precisions of the parameters of the local track element in  $Z \rightarrow \mu^+\mu^-$  events are  $\sigma(R\phi) = 50 \mu\text{m}$  and  $\sigma(\phi) = 1.5 \text{ mrad}$ . Tracks separated by less than 1 mm cannot be disentangled. The  $z$  precision from a single MWPC layer for an isolated track varies from 0.5 mm to 1 mm depending on  $\theta$ .

The barrel tracking system is completed by the **Outer Detector (OD)** consisting of five layers of drift tubes with full azimuthal coverage, located between radii of 197 cm and 206 cm, operated in the limited streamer mode. The active length of the OD corresponds to polar angles of  $42^\circ < \theta < 138^\circ$  and provides a single point precision of  $\sigma(R\phi) = 110 \mu\text{m}$  and  $\sigma(z) = 3.5 \text{ cm}$ .

The volume between the TPC and the OD is occupied by the Ring Imaging Cherenkov Detectors (RICH) providing information about the mass of charged hadrons of known momentum;

the RICH was not used in this analysis.

### **Momentum precision:**

In the barrel region of the detector, the momentum of charged particles is deduced from the curvature of the track reconstructed by DELANA from the signals provided by the VD, ID, TPC and OD. First the TPC track segments are extrapolated inwards and outwards to form candidate strings of track elements with the ID and OD. In the dead zones of the TPC, only ID and OD track elements are connected. In a second step, all strings of track elements are passed through a track fitting processor which accounts for multiple scattering and energy loss in the material between the sensitive detector parts. The fitted track is then extrapolated towards the VD where signals can be associated to the track and a second fit is performed using the VD information. When information is available from the four tracking modules, the obtained momentum precision for 45.6 GeV/c muons is:  $\sigma(1/p) = 0.6 \times 10^{-3}(\text{GeV}/c)^{-1}$ . It decreases to  $\sigma(1/p) = 1.1 \times 10^{-3}(\text{GeV}/c)^{-1}$  when no VD information is included in the track reconstruction. The precision for lower momenta is estimated using simulated data (see section 3.3). It is stable in function of the polar angle for tracks located in the barrel where the precision is of the order of 0.7% to 1.4% for momenta increasing from 0.5 GeV/c to 12 GeV/c, and deteriorates in the forward region (see figures 3.5).

### **Beam-spot reconstruction**

The collision region of the electron and positron beams, also called beam-spot, is reconstructed for every  $\sim 200$  recorded hadronic Z decays. A vertex common to the 200 events is fitted using all tracks of all events to which at least two VD signals have been associated by DELANA. The horizontal ( $x$ ) and vertical ( $y$ ) positions of the beam-spot are determined as well as the spread along  $z$ . The primary vertex can be re-estimated event by event for hadronic decays because of the high track multiplicity, but for low multiplicity events (such as leptonic Z decays), the beam-spot position has to be used as primary interaction vertex for the computation of track impact parameters for example.

### **Reconstruction of photons converted in front of the TPC:**

In the barrel region of the detector, about 7% of the photons convert in front of the TPC (see figure 3.6 from [22]), creating visible  $e^+e^-$  pairs, and thus increasing the apparent charged particle multiplicity of the events. One of the tasks of ELEPHANT is the reconstruction of the converted photons and the estimation of their energies and directions. The procedure is the following: assuming that the electron-positron opening angle is zero, each track is searched for a point where the tangent to the track, in the  $R\phi$  plane, is pointing to the interaction point. If the point is not compatible with the interaction point itself, the track is kept as an electron (positron) candidate. When two particles of opposite charge present a compatible conversion point, several conditions are required on the corresponding conversion radius, on the opening angles and on the presence of associated signals at smaller radii, for the charged particle pair to be identified as a photon conversion. Also single tracks satisfying tighter criteria, can be interpreted as being issued from a photon conversion (the second track can have been lost in the beam-pipe or by reconstruction inefficiencies). These are called "Singles".

From simulation, the reconstructed converted photons are found to have an energy precision of  $\pm 1.2\%$  ( $\pm 12\%$  for "Singles" for which a mean energy correction is applied for the unseen lepton), an angular precision of  $\pm 1.5$  mrad in  $\theta$  and  $\phi$ , and a precision on the conversion radius of  $\pm 5$  mm. The identification efficiency decreases with increasing momentum since the track curvature decreases and the conversion point tends to be compatible with the interaction point. Figure 3.7 shows the distribution of the conversion points for simulated events.

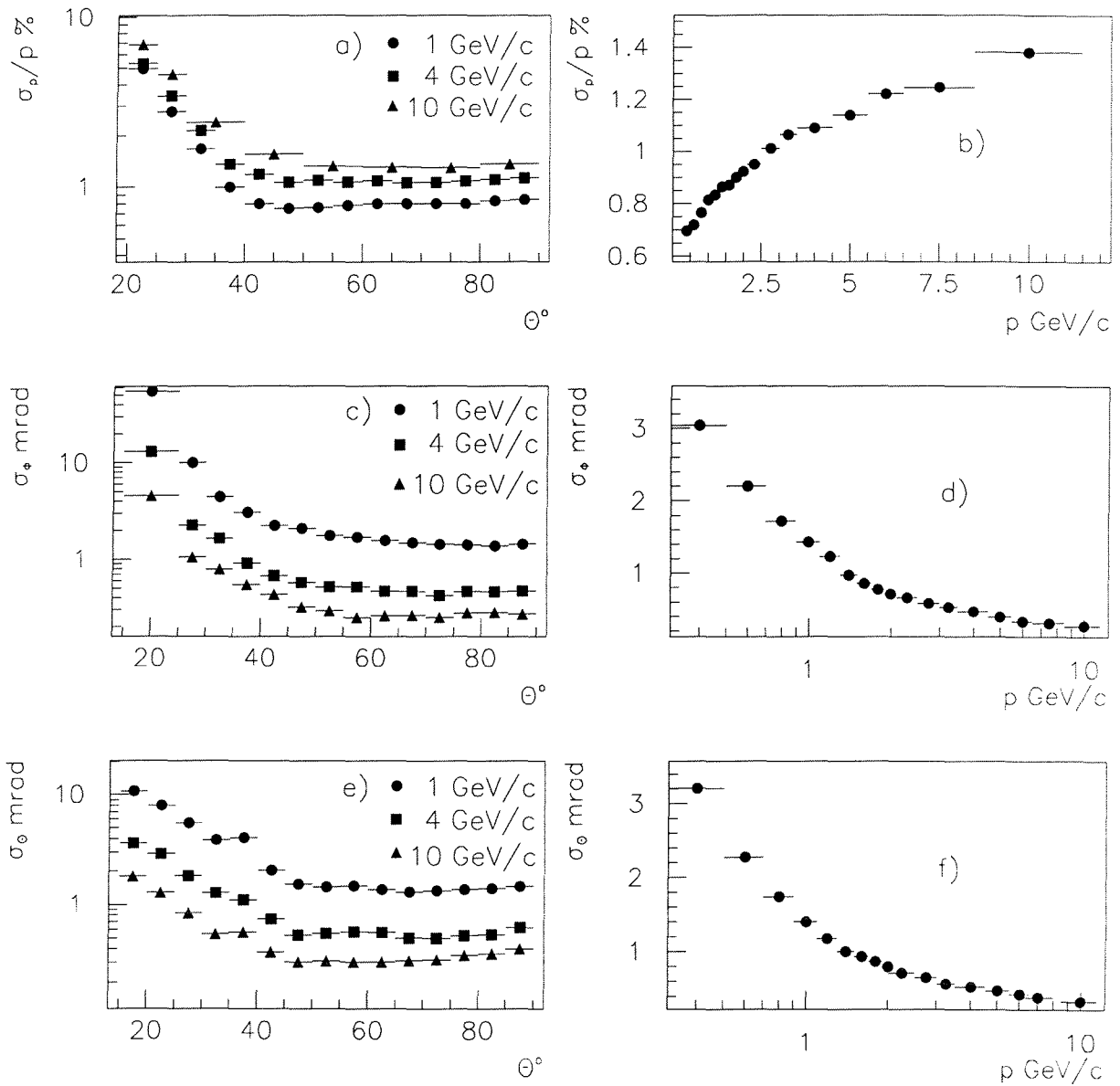


Figure 3.5: Track parameter precisions estimated by comparing simulated and reconstructed parameters: momentum (a,b), azimuthal angle (c,d) and polar angle (e,f) precision as a function of the polar angle  $\theta$  (first column), and of the momentum for barrel tracks (second column). (From reference [20]).



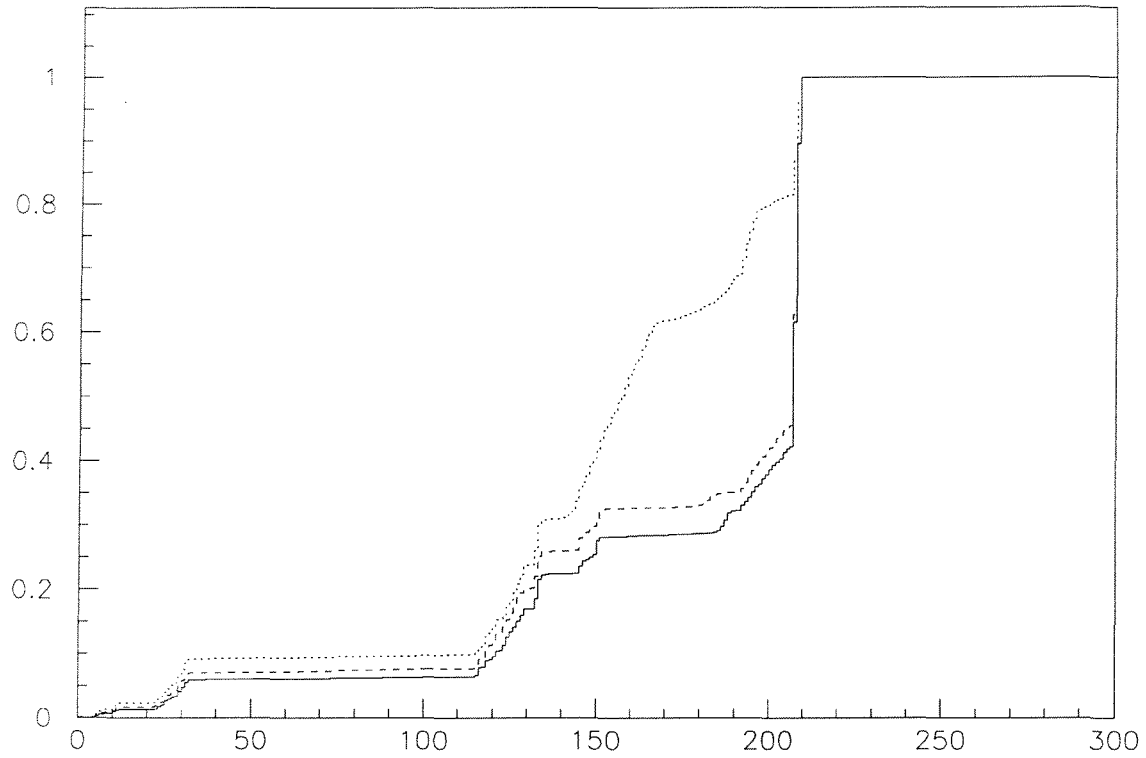


Figure 3.6: Accumulated photon conversion probability as a function of the conversion radius (given in cm), for simulated events (solid line: photon direction in the interval  $0.1 < |\cos \theta| < 0.2$ ; dashed line:  $0.5 < |\cos \theta| < 0.6$ ; dotted line:  $0.65 < |\cos \theta| < 0.75$ ).

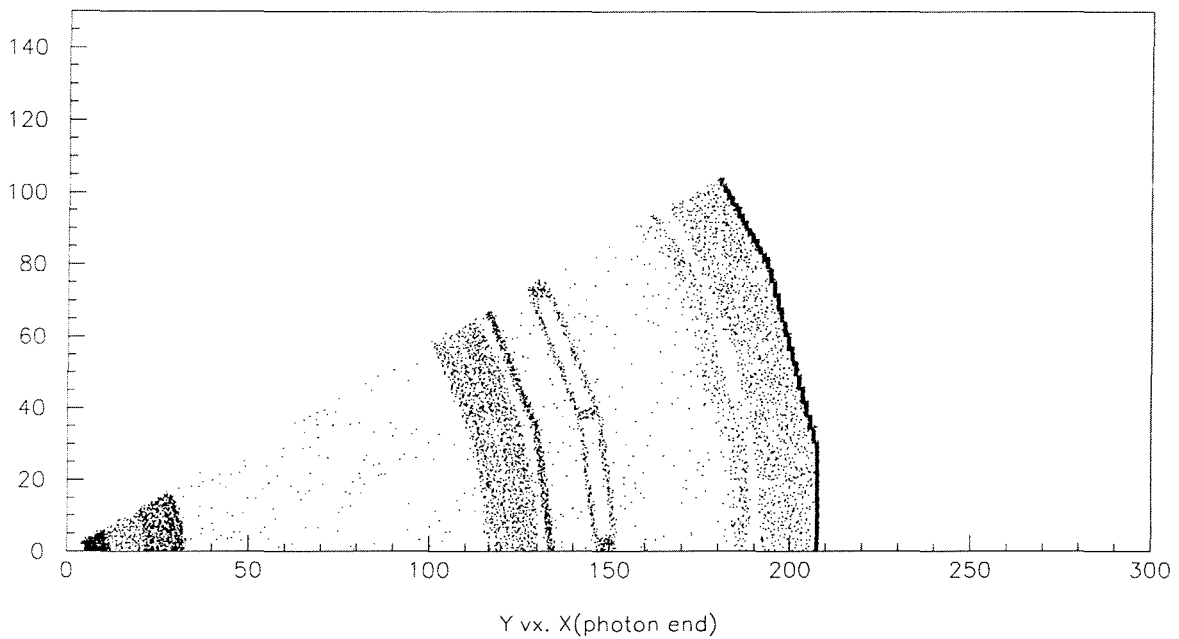


Figure 3.7: Photon conversion points for simulated events, in the  $x - y$  plane ( $\text{cm} \times \text{cm}$ ) for  $8 \text{ cm} < |z| < 115 \text{ cm}$ , i.e. neither in the  $z = 0$  plane nor in the end-cap plates of the detector.

### 3.2.2 Calorimetry

An electromagnetic calorimeter is installed between the solenoid and the OD for the measurement of electron and photon energies. Surrounding the magnet, a hadron calorimeter is built, made of iron in order to absorb hadrons. Active detection layers embedded in the material provide information on the incident particle energy. The hadron calorimeter constitutes at the same time the return yoke of the magnet.

The electromagnetic calorimeter is a **High density Projection Chamber (HPC)**. It is composed of six juxtaposed rings consisting of 24 modules covering the  $2\pi$  azimuthal angle. Each module is made of 40 alternated layers of lead wires which serve as converter material and generate the electric drift field for the layers of gas which act as small TPC's. The HPC has an inner radius of 208 cm (covering the polar angle range of  $38^\circ < \theta < 142^\circ$  with a  $1^\circ$  dead zone at the level of each module boundary, every  $15^\circ$  in azimuth and at  $67^\circ$  and  $113^\circ$  in polar angle) and an outer radius of 260 cm, which corresponds to a total converter thickness of  $18/\sin \theta$  radiation lengths. In each module there are 128 pads arranged in 9 rows (see figure 3.8). In the row closest to the beam-pipe, the pads are 2 cm wide, increasing to 8 cm wide in the last row. The charge of each pad is sampled in 256 time slots, providing a very high granularity in  $z$  (3.5 mm). Between the third and fourth rows, scintillator arrays are installed to provide a fast trigger signal.

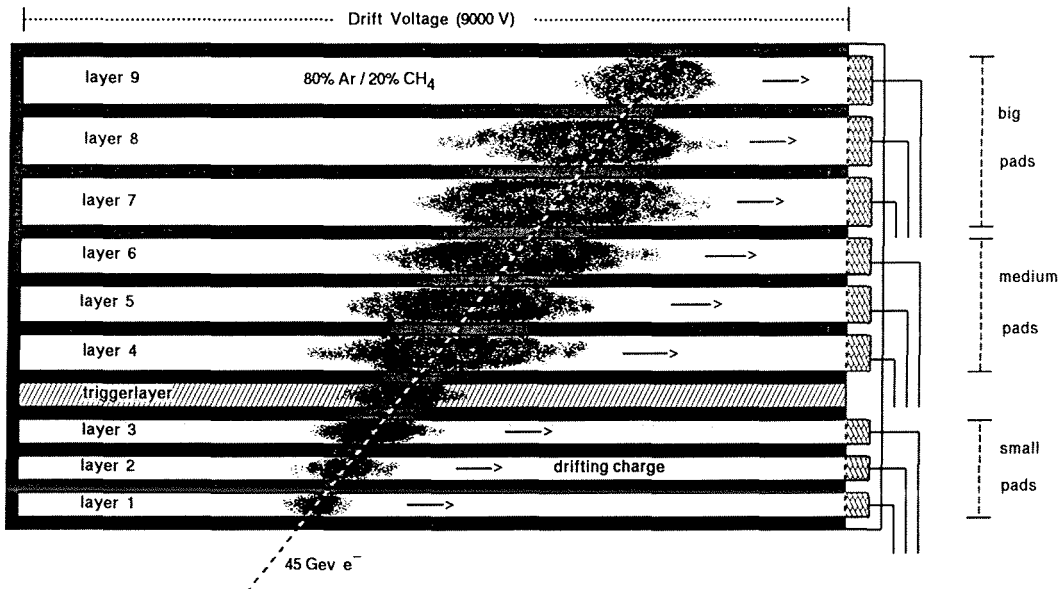


Figure 3.8: *Example of the electromagnetic shower development in a single HPC module*

When crossing the HPC material, electrons and photons lose their energy by producing electromagnetic showers. The electrons of the showers ionise the gas contained between the lead layers and the corresponding collected charge allows, after calibration, to determine the energy of the initial electron or photon. Hadrons and muons, which are minimum ionising particles, lose a very small amount of their energy when crossing the HPC.

The first DELANA reconstruction step at the HPC level, is the clustering of the information from each single HPC pad, taking care of suppressing the fluctuation effect of slow electrons curling in the magnetic field and rejecting the energy depositions due to radioactive alpha decays occurring in the lead converter. This is done by applying thresholds and performing

detailed pattern recognition on the clusters. The clusters are then grouped into showers by looking for local maxima of charge deposition, after a projection, along the direction pointing to the interaction point, of each cluster charge, onto the surface corresponding to the third HPC layer ( $R = 217$  cm). The internal shower direction and reference point (centre of gravity) are then calculated. Further analysis of the longitudinal and transverse shower profiles performed by the ELEPHANT package provides additional rejection of noises.

In the second stage of the DELANA pattern recognition, each track of charged particle is extrapolated into the HPC. If it points to a HPC shower, this one is associated to the track. Showers which are not associated to any track are considered to originate from neutral particles.

The energy calibration is performed using  $Z \rightarrow e^+e^-$  decays or  $\pi^0 \rightarrow \gamma\gamma$  decays for lower energy showers. For 45 GeV electrons, the HPC  $\theta$  and energy resolutions are respectively 0.6 mrad and 6.5%, and the  $\phi$  resolution is found to be 3.1 mrad, most of the imprecision being due to the uncertainty on the electron track extrapolation from the TPC through the material of the RICH into the OD and the HPC: electrons passing through material lose energy by radiating soft and hard photons and their trajectories are no longer perfect helix, but spirals with decreasing radius of curvature. To determine the energy precision of less energetic showers, the  $\pi^0$  mass is reconstructed from the precisely measured kinematic parameters of a photon converted in front of the TPC, and a photon seen as a neutral shower in the HPC. This is done for  $\pi^0$  energies between 0.5 GeV and 15 GeV. The precision on the shower energy is found to be  $31\%/E^{0.44} \oplus 2.7\%$ , for the energy  $E$  expressed in GeV. The study of the reconstructed  $\pi^0$  mass in function of the shower energy allows in addition to observe and correct for non-linearities of the HPC response.

#### Electron radiation reconstruction:

The ELEPHANT package looks for photons radiated by electrons in front of the TPC. In case of such energy loss, the momentum of the electron determined from the TPC track curvature is under-estimated. ELEPHANT provides a better estimation of the electron momentum at the production vertex by identifying radiated photons and correcting the electron energy taking into account the photon energy. The procedure is simple: for electron candidates (i.e. charged particles for which the energy loss  $dE/dX$ , and/or the associated HPC energy deposit are compatible with the electron hypothesis:  $dE/dX$  corresponding to the Fermi plateau, and an electromagnetic energy deposit equal to the particle momentum), a point is searched for on the track extrapolation towards small radii, at which the tangent to the track points to a neutral shower in the HPC. That shower is considered as being produced by a photon radiated by the charged particle. The momentum-vector of the charged particle, estimated at the production vertex, is computed from the momentum of the particle as measured in the TPC, to which the momentum of the radiated photon is added.

#### Reconstruction of photons converted behind the TPC:

In the barrel region of the detector, about  $42\%/\sin\theta$  of the photons convert before reaching the HPC<sup>3</sup>. About 7% of the photons convert in front of the TPC, and can be identified by ELEPHANT as explained above. Photon conversions in the outer wall of the TPC or in the RICH are reconstructed using the OD track element to find pair of opposite charge particles that can each be linked to a HPC shower and that are compatible with a photon conversion topology.

---

<sup>3</sup>Around 80% of them occur for photons traversing the end-plates of the RICH, in front of the outermost HPC rings:  $38^\circ < \theta < 49^\circ$  and  $131^\circ < \theta < 142^\circ$

### $\pi^0$ identification:

For  $\pi^0$ 's of energy higher than 6 GeV, the opening angle of the two decay photons is generally smaller than  $2^\circ$ . In such conditions, both photon showers are most often merged into one single shower by the HPC pattern recognition described above. The ELEPHANT package provides a refined shower reconstruction algorithm which allows to extract a more precise structure of the electromagnetic shower and to recognise the possible presence of two maxima of energy deposition. Such reconstructed  $\pi^0$ 's are called "merged"  $\pi^0$ 's (see figure 3.9). For the identification of  $\pi^0$ 's a minimum of  $0.08 \text{ GeV}/c^2$  is required for the invariant mass of the two photons. Also photons converting just at the entrance of the HPC lead to similar two-peak topologies, but the solenoidal magnetic field separates the two showers in the  $\phi$  direction, so that about 60% of these contaminating cases can be rejected by requiring that the separation in  $\theta$  between the showers be greater than 10 times their separation in  $\phi$ .

The identification efficiency of this procedure lies between 10% and 20% only, depending on the  $\pi^0$  energy, with the maximum efficiency observed around 16 GeV.

The **Hadron Calorimeter (HCAL)** is constituted by the 5 cm thick iron plates of the magnet return yoke separated by 20 planes of 18 mm wide limited streamer tubes. The HCAL is made of 24 sectors covering the full azimuthal angle and the polar angle range of  $42.6^\circ < \theta < 137.4^\circ$ . The energy precision for hadronic showers reconstructed within  $52^\circ < \theta < 128^\circ$  is:  $\sigma(E)/E = 0.21 \oplus 1.12/\sqrt{E}$  for  $E$  expressed in GeV.

### 3.2.3 Muon detectors

Installed as the outermost detection modules, the drift chambers of the **Muon Chambers (MUC)** detect the passage of minimum ionising particles which have not been stopped by the HPC nor by the HCAL, namely muons of momentum above  $3 \text{ GeV}/c$ . Also hadrons traversing the HCAL sector boundaries, or charged particles of external origin, such as cosmic ray particles, are detected by the MUC, as well as possibly punch-through particles from the HCAL hadronic showers. The MUC is made of a barrel part, the **MUon Barrel detection chambers (MUB)**, and a forward-backward part, the **MUon Forward detection chambers (MUF)**. In 1994, the **Surrounding Muon Chambers (SMC)**, based on limited streamer tubes, were installed in order to cover the gap between the MUF and the MUB.

The MUB consists of two layers of drift chambers operating in the proportional mode: the first one, inserted into the return yoke after 90 cm of iron, is made of 24 modules containing three staggered set of drift chambers<sup>4</sup>; the second layer is placed outside, after a further 20 cm thickness of iron and is made of two staggered sets of drift chambers. Each drift chamber module has an active length of 3.65 m. Four signals per crossing muon are typically recorded by the MUB, with an accuracy of 2 mm in  $R\phi$  and 80 mm in  $z$ . The MUB covers the polar angle range of  $53^\circ < \theta < 127^\circ$  while the two layers of the MUF drift chambers, operating in the limited streamer mode, cover regions lying between  $20^\circ$  and  $45^\circ$ , and between  $135^\circ$  and  $160^\circ$ .

#### Muon identification

The MUFLAG package makes use of the estimated goodness of MUC signals association to extrapolated tracks to flag muon candidates as "very loose", "loose", "standard" or "tight" depending whether the  $\chi^2$  of the agreement of the track extrapolation with the signal hits satisfies looser or more stringent conditions [23]. This is based on the fact that signals induced by hadronic showers and decays in flight of charged kaons ( $K^- \rightarrow \mu^- \nu_\mu$ ) give in general larger

<sup>4</sup>The outer of the three drift chamber sets is not read out but is foreseen as spare because of the site inaccessibility.

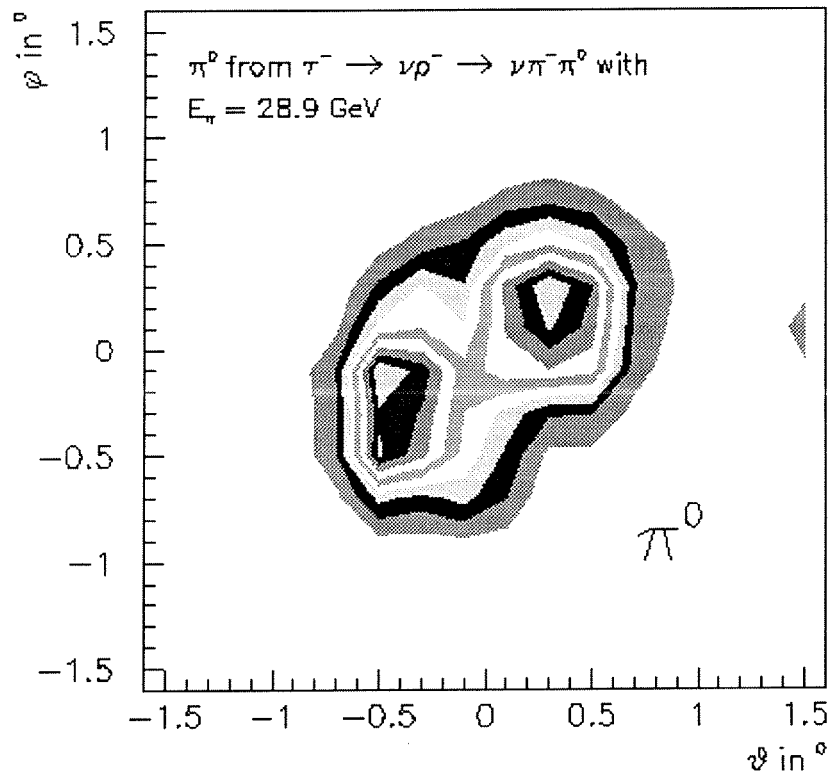
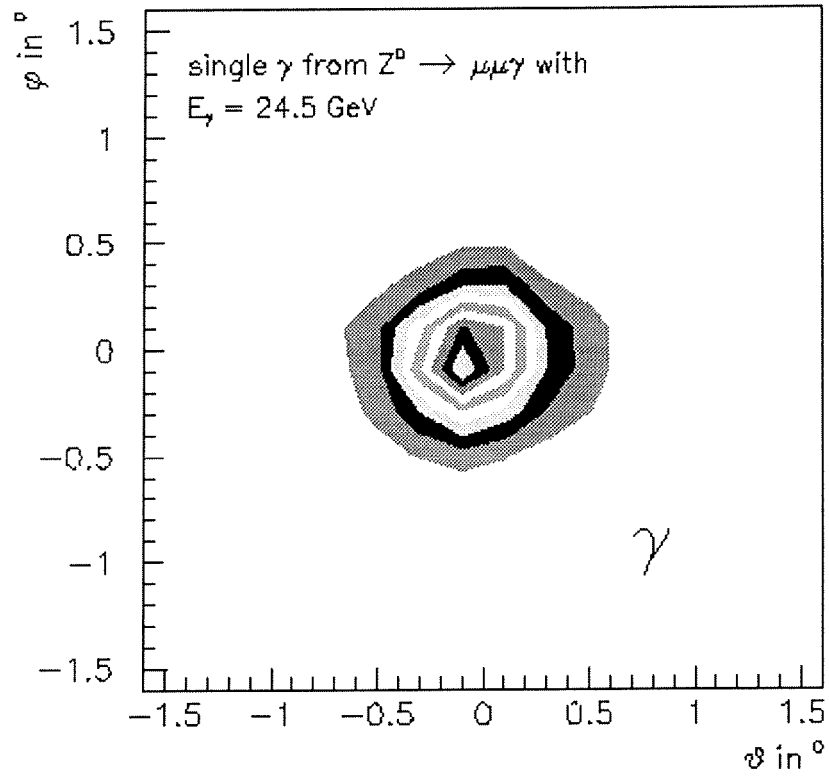


Figure 3.9: Structure of the electromagnetic showers produced respectively by a single photon (upper figure) and by a "merged"  $\pi^0$  (lower figure).

deviations from the track extrapolation in position and direction than those expected from the multiple Coulomb scattering of a primary muon of the same momentum. "Standard" and "tight" tags require among others that at least one associated signal has been recorded in the external layer of the muon chambers. The efficiencies and misidentification probabilities (in %) obtained by MUFLAG are respectively  $95.9 \pm 0.1$  and  $5.4 \pm 0.2$  for the very loose tag,  $94.8 \pm 0.1$  and  $1.5 \pm 0.1$  for the loose tag,  $86.1 \pm 0.2$  and  $0.7 \pm 0.1$  for the standard tag, and  $76.0 \pm 0.2$  and  $0.4 \pm 0.1$  for the tight tag. The SMC information was not yet included in the data treatment for the 1994 and 1995 data samples.

### 3.2.4 Data acquisition system

As mentioned at the end of section 3.1, the Data Acquisition System (DAS) needs a trigger decision logic that allows to cope with the high background rates while being 100% efficient for recording  $e^+e^-$  interactions. The DELPHI trigger system and the determination of the trigger efficiency from the data are described in detail in reference [24]. Here are the main DELPHI trigger features:

The trigger system consists of four successive decision levels T1, T2, T3 and T4. The first levels T1 and T2 are synchronous with the BCO signal (every  $22 \mu\text{s}$ ) and use the information provided, for T1, by the fast detector modules such as the ID, the OD, the MUB, the HPC scintillator plane or the forward tracking detectors, and for T2, by the TPC, HPC and MUF. The T1 decision is taken  $3.5 \mu\text{s}$  after the BCO. If it is negative, the detector module counters are re-initialised and ready for the next BCO with no loss of data. If T1 is positive, the next BCO is lost since the T2 decision is available  $35.5 \mu\text{s}$  after T1. The dead-time introduced is typically 3% of which 2% is due to T1 and 1% to T2, for a mean readout time of 3 ms per event. The total dead time of DELPHI is of the order of 14%<sup>5</sup>. In order to reduce the effect of the internal noise of some detector modules, coincidence of signals from different modules are used (logical AND) in the decision procedure, and T2 is the results of an OR-ing of several conditions such as the presence of a signal in the TPC, OD.OR.HPC, ID.OR.(MUB.AND.HCAL), ... T3 and T4 are software filters performed asynchronously with the BCO. Thanks to T3, which uses the same logic as T2 but with more detailed information, the background level is halved and the data logging rate is kept below 2 Hz. T4 was implemented in 1994 in order to reject about half of the background events remaining after T3.

The overlapping geometrical acceptance of the different detectors provides substantial redundancy between the different trigger conditions. This feature of the DELPHI trigger ensures high and stable efficiency over long running period, and makes it possible to determine both the trigger efficiency and its maximal error with good precision. The global trigger efficiency for electron and muon pairs is consistent with 100% at the level of  $10^{-4}$  for polar angles between  $20^\circ$  and  $160^\circ$ . Due to their high final state multiplicity, hadronic Z decays are triggered with an efficiency hardly distinguishable from 100% over nearly the full solid angle. Since the  $\tau^+\tau^-$  final state can be regarded, from the topological point of view, as a mixture of the hadronic and other leptonic final states ( $e^+e^-$ ,  $\mu^+\mu^-$ ), the trigger efficiency for  $\tau^+\tau^-$  events is expected to be also very close to 100% [24].

During data acquisition, the Slow Control system controls the operation of the detector, reporting significant changes in the detector running conditions such as chamber pressures, temperatures, and voltage values, or deficient detector submodules. These parameters are

---

<sup>5</sup>1.5% due to initial setting up of the detectors at the beginning of each new beam fill, 1% for DAS internal checking, 2% for DAS stopped due to the LEP machine background being too high, 7% for DAS stopped due to DAS software crashes and 3% due to T1 and T2 dead time.

recorded on the central database and are necessary for the offline data analysis by DELANA, and for simulations.

The average Z event size is about 150 kbytes. At the Z peak energy, the data sample comprises typically 15% of Z decays, 30% Bhabha t-channel events and 55%  $\gamma\gamma$  events, cosmic rays and background events (see Chapter 4). After the reconstruction of the events by DELANA, some 40% of the triggers are retained on the DST (a simple filter is used to reject non ambiguous background events using the processed information obtained by DELANA [25]) and at this stage, the average size of a hadronic event is reduced to 60 kbytes. The summarised information recorded on the DST tapes is still detailed enough to allow a re-processing of the data by software packages such as ELEPHANT and MUFLAG.

### 3.2.5 Luminosity measurement

The LEP luminosity is estimated by each of the four detectors at the corresponding collision point and is in each case integrated over the data taking periods. The luminosity is measured by counting the number of events of a process with a clear experimental signature, with high statistics and with a cross-section which can be calculated theoretically with high precision. The Bhabha scatterings  $e^+e^- \rightarrow e^+e^-$  present a very large cross-section for electrons produced in the very forward directions with respect to the incident beam. The process is dominated by the t-channel photon exchange which is calculable from the Quantum Electro-Dynamics (QED) theory with a precision of 0.11 % [26]. The Bhabha scattering interactions are thus used for the luminosity determination. Special calorimeters are installed very close to the beam-pipe for the detection and identification of these events. Before 1994, the absolute luminosity was measured in DELPHI by the Small Angle Tagger (SAT) covering the polar angles between 43 mrad and 135 mrad. It was replaced in 1994 by the Small angle Tile Calorimeter (STIC) of larger acceptance (29 mrad to 185 mrad). A second calorimeter, the Very Small Angle Tagger (VSAT), is used for the measurement of the relative luminosity at different beam energies.

The cross-section  $\sigma_{vis}$  of Bhabha scattering is calculated for the given acceptance of the calorimeter (SAT or STIC), and the number of detected scatterings  $N_{Bhabha}$  is corrected for backgrounds, trigger efficiency and contribution from the s-channel Z exchange. The overall experimental precision on the obtained integrated luminosity, given by the ratio  $N_{Bhabha}/\sigma_{vis}$ , was, for 1994, 0.09%, with the main sources of uncertainty coming from the determination of the interaction point (0.06%) and the acceptance of the detector (0.04%).

## 3.3 Data simulation technique

Simulated events are used for physics analysis where selection criteria have to be chosen, and selection efficiencies and background levels have to be evaluated (see Chapters 4), but also for statistical procedures such as neural network trainings (see Chapter 5) or for fits to experimental distributions for the determination of physical parameters (see Chapter 6).

The simulated data have to reproduce as closely as possible the real data recorded by the detector, and produced with statistics large enough compared to the real data statistics in order to reduce statistical fluctuations (the MONTE CARLO method, based on probabilities, is used).

The DELPHI Simulation (DELSIM) [27] is done in two steps:

- the generation of the primary physics process: it is performed by dedicated programs such as JETSET [28] for the  $e^+e^- \rightarrow q\bar{q}$  interactions, BABAMC [29] for  $e^+e^- \rightarrow e^+e^-$ ,

DYMU3 [30] for  $e^+e^- \rightarrow \mu^+\mu^-$ , KORALZ [31] for  $e^+e^- \rightarrow \tau^+\tau^-$ , and DIAG36 [32] for four fermions final states  $e^+e^- \rightarrow f^+f^-f^+f^-$ . The Standard Model is used for the theoretical predictions, using the most recent measurements of its parameters.

- the simulation of the detector response to the passage of the final state particles through each detection module: this is done taking into account the effect of the solenoidal magnetic field, the secondary interactions of the particles with the detector material (multiple scattering, photoelectric effects, emission of delta rays, bremsstrahlung, annihilation of positrons, photon conversions, Compton scattering, nuclear interactions) and the possible particle decays. A very detailed description of the material layers and of the sensitive components of the detector are needed here as well as for the data reconstruction by DELANA. It is stored in the database. When a particle crosses the sensitive volume of a detector, the relevant information is stored to compute the detector response in the form of electronic signals, requiring the information about all parameters (gas pressure, temperature, ...) and possible inefficiencies (dead submodules) of each detector module.

The generated data are then passed through the DELANA reconstruction program and the analysis packages (ELEPHANT, MUFLAG) in the same way as for the real events, and recorded on DST tapes.

## 3.4 The neural network technique

As explained in section 2.3.2, our analysis relies on the correct identification of the  $\tau$  decay products. This identification can only be performed on the basis of the kinematical and ionisation informations recorded by the DELPHI detector. This kind of classification problem with criteria depending on correlated variables, is well adapted to discriminant analysis. In particular, the neural network technique with a feed forward architecture gives, as will be shown in Chapter 5, competitive or better results than more classical methods.

In this section a general introduction is given on the subject of the neural network technique, starting from the first simple model of neuron by McCulloch and Pitts, ending with the multi-layer feed-forward neural network used in Chapter 5. More complete information can be found in [33]. In Appendix A, it is explained why the simple neural network (or *perceptron*) is not sufficient for the resolution of non linearly separable problems.

The terms *neuron* and *neural networks* are used in this domain because the technique was inspired by the knowledge coming from neurosciences and not because it would really reproduce the processes occurring in the brain, which are enormously more complex, far from being completely understood and artificially reproducible.

### 3.4.1 The neuron

A biological neural cell (or *neuron*) can be seen as made of a cell body equipped with dendrites which act as receivers, and one axon which acts as the cell transmitter (see figure 3.10). The junction regions between axons and dendrites (or axons and the cell body itself) are called synapses. The neural network of the brain consists of a net of about  $10^{11}$  neurons which receive signals from other neurons through complex chemical processes. The effect of the signals is to raise or to lower the electrical potential inside the cell body. When this potential reaches some threshold, the cell fires: a pulse (or *action potential*) is sent to the connected neurons down the cell axon.



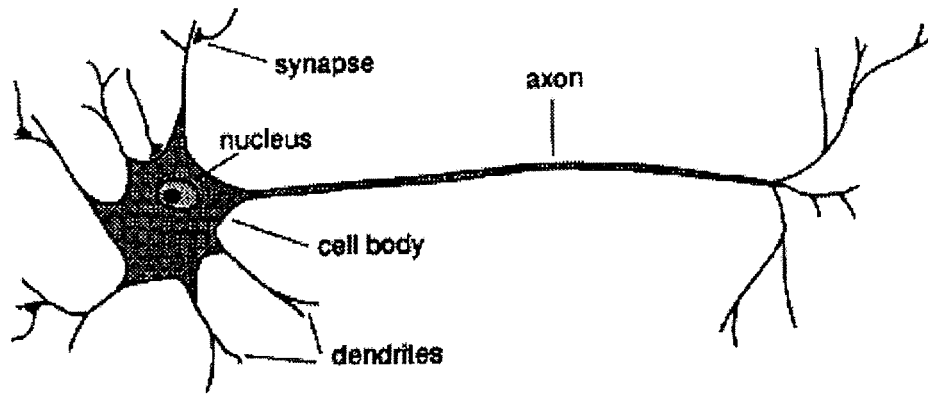


Figure 3.10: Schematic representation of a neuron cell.

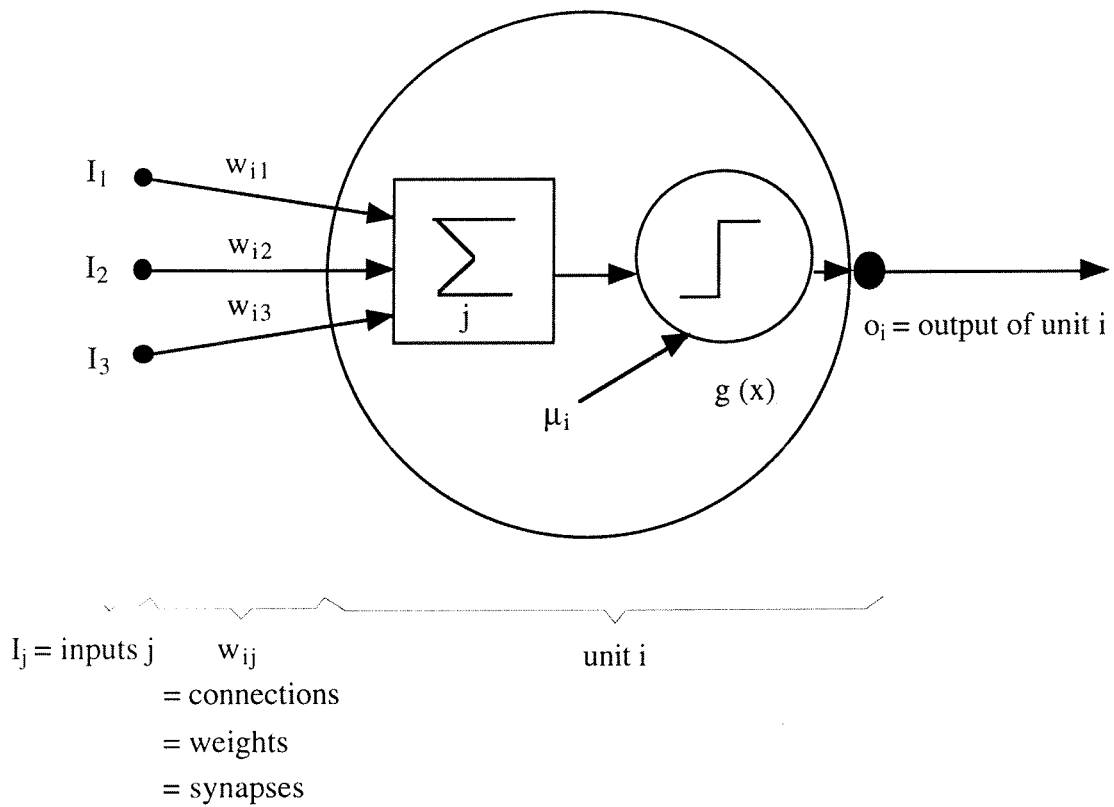


Figure 3.11: Schematic representation of the threshold unit.

This mechanism was simplified and modelled in 1943 by McCulloch and Pitts as a **binary threshold unit** (see figure 3.11) [34].

The unit  $i$  (or neuron  $i$ ) computes a weighted sum of its  $N$  input values  $I_j$  ( $j = 1$  to  $N$ ) and it produces an output variable  $o_i$  which is 1 or 0 according to whether this sum is above or below a certain threshold (or *bias*)  $\mu_i$ :

$$o_i = g\left(\sum_{j=1}^N w_{ij}I_j - \mu_i\right) \quad (3.1)$$

The *state* or *activation* of unit  $i$ ,  $o_i$ , is 1 or 0 when the *activation* (or *transfer* or *gain*) function  $g(x)$  is the step function  $\theta(x)$  :

$$\theta(x) = \begin{cases} 0 & x \leq 0 \\ 1 & x > 0. \end{cases} \quad (3.2)$$

Also the sign function  $sgn(x)$  can be used. The output is then  $\pm 1$ :

$$sgn(x) = \begin{cases} -1 & x \leq 0 \\ 1 & x > 0. \end{cases} \quad (3.3)$$

The strength of the connection (or *link* or *synapse*) between the input  $I_j$  and unit  $i$  is represented by the weight  $w_{ij}$  which is a real number. The weight is positive or negative when the link is respectively excitatory or inhibitory. A zero value for  $w_{ij}$  corresponds to no connection between unit  $i$  and input  $I_j$ .

### 3.4.2 The feed-forward neural network

In feed-forward neural networks, the units are organised into layers and all units of a given layer is connected to each unit of the next layer (as on figure 3.12). The connections are unidirectional. The weights associated to the connections can be determined using a learning algorithm. This is an iterative approach in which the appropriate weights  $w_{ij}$  are adjusted by successive improvements from an arbitrary starting point. The learning process can be supervised or un-supervised.

In the un-supervised case, the learning goal is not defined *a priori*. Patterns<sup>6</sup> are submitted to the neural network which has to recognise and create “by itself” the different categories to which the patterns belong. The only available information lies in the correlations of the input data. No “correct” example is shown to the network as it is the case for the supervised learning.

The supervised learning is developed in what follows, since it was used for the classification of the  $\tau$  decay modes in Chapter 5.

For the supervised learning, a set of  $p$  *training* patterns is used for which the desired neural network output  $t_i^\lambda$  ( $\lambda = 1, p$ ;  $i = 1, C$ ) is known. The  $t_i^\lambda$  are called the *target* values and  $C$  represents the number of classes into which the patterns have to be classified.

Starting from an arbitrary set of weights and thresholds, the outputs  $o_i^\lambda$  are computed for all training patterns and compared to the desired outputs  $t_i^\lambda$ . The weights and the thresholds are then iteratively modified in order to get closer and closer to the target values. It can be shown that, if there exists a set of weights allowing to obtain the desired network outputs, then it can be found by a simple learning rule.

---

<sup>6</sup>A pattern is an event. It is defined by its coordinates in an N-dimensional hyperspace, where N corresponds to the number of inputs of the neural network.

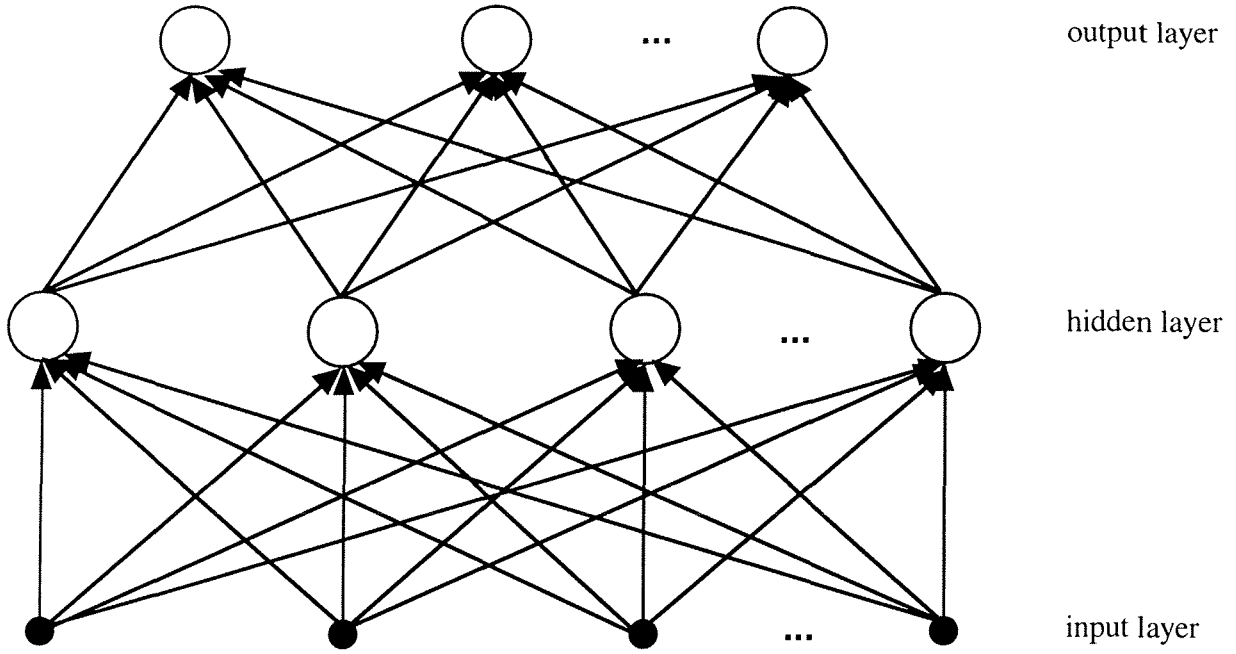


Figure 3.12: Example of a feed forward neural network with one hidden layer and full connection between the units.

After the training, the performances of the neural network are estimated using a set of testing patterns, independent of the training patterns, so that the generalisation power of the network can be evaluated when applied to cases previously unseen.

The performances of a neural network can be measured by the estimation of a *cost* or *energy* or *error* function  $E(\vec{w})$ , where  $\vec{w}$  represents the set of weights  $w_{lm}$ . For a neural network with  $N$  inputs, one hidden layer with  $H$  hidden units, and  $C$  output units,  $E(\vec{w})$  is defined as:

$$E(\vec{w}) = \frac{1}{2} \sum_{i,\lambda} (t_i^\lambda - o_i^\lambda)^2 \quad (3.4)$$

$$= \frac{1}{2} \sum_{i,\lambda} \left( t_i^\lambda - g \left( \sum_h w_{ih} g \left( \sum_k w_{hk} I_k \right) \right) \right)^2, \quad (3.5)$$

$$\begin{aligned} \text{with } i &= 1 \text{ to } C, \\ \lambda &= 1 \text{ to } p, \\ k &= 1 \text{ to } N, \\ h &= 1 \text{ to } H \end{aligned}$$

(3.6)

The learning rule has to define how to modify the weights  $w_{lm}$  in order to decrease  $E$ . The usual gradient descent algorithm suggests changing each  $w_{lm}$  by an amount  $\Delta w_{lm}$  proportional to the gradient of  $E$  at the present location. This is the “back-propagation” learning function:

$$w'_{lm} = w_{lm} + \Delta w_{lm} \quad (3.7)$$

with

$$\Delta w_{lm} = -\eta \frac{\partial E}{\partial w_{lm}}, \quad (3.8)$$

The errors  $\Delta w_{lm}$  are propagated backwards through the connections of the neural network in order to correct the weights appropriately. The process is repeated during several cycles (or epochs) until the total error function has reached a minimum. To avoid converging to a local minimum, the training patterns should be presented to the network in a random order with respect to their class.

The factor  $\eta$  is called the learning factor. A large value of  $\eta$  ( $\eta \sim 1$ ) allows to find quickly the global minimum of  $E(\vec{w})$ , but smaller values of  $\eta$  ( $\eta \sim 0.01$ ) lead to a more precise determination of the minimum.

In order to have more sensitivity, the logistic function is usually used as gain function:

$$g(x) = \frac{1}{1 + e^{-2x}}. \quad (3.9)$$

This allows to get continuous-valued output values:  $o_i \in ]0, 1[$ .

### 3.4.3 The SNNS package

The SNNS [35] package (Stuttgart Neural Network Simulator) was used for the analysis presented in Chapter 5. It is an interactive interface developed at the University of Stuttgart since 1989. It allows to create neural networks quickly and easily. Files containing the learning or testing patterns are provided by the users. During the training of the networks, the SNNS program can display the instantaneous value of the error function. It creates output files containing the network weight and threshold values, and the output activations for all presented patterns, for the estimation by the user of the classification efficiencies.

# Chapter 4

## Selection of the inclusive one-prong $\tau$ decay modes

The data recorded by the DELPHI detector during electron-positron beam collisions do not only result from the detection of particles produced by the interaction itself, but also from background processes. The data corresponding to the  $e^+e^- \rightarrow \tau^+\tau^-$  final states, have to be disentangled from the other interactions in a way that satisfies at the same time high selection efficiency of the interesting signal and high purity of the selected sample, i.e. a minimal contamination from background sources.

For the measurement of the  $\tau$  polarisation and of the Michel parameters, a special effort has been done to minimise the selection correlation between both  $\tau$ 's produced in the  $e^+e^-$  interaction, and to obtain a maximal efficiency everywhere in the phase-space domain available to the  $\tau$  decay products, while keeping the background contamination at an acceptable level.

Section 4.1 gives a description of the recorded data content. The chosen set of optimised  $e^+e^- \rightarrow \tau^+\tau^-$  selection criteria is then detailed in section 4.2, followed by the background study (section 4.3), and the evaluation of the selection efficiencies and purities (section 4.4). In section 4.5, the inclusive 1-prong  $\tau$  decay final states are isolated and the corresponding branching ratio is estimated as a cross-check of the validity of the proposed selection procedure. The systematic effects are studied in section 4.6.

### 4.1 Data sample description

The following analysis is based on the data recorded by the DELPHI detector during years 1993, 1994 and 1995 and on the corresponding simulated data. It was required that the analysed data be collected during periods of correct running conditions (see section 3.2.4) for the VD, TPC, HPC, MUB and HCAL modules in order to guaranty a good and uniform quality of the recorded information. The corresponding integrated luminosities  $\mathcal{L}_{int}$  are given in table 4.1 for each year, together with the respective centre-of-mass energy  $E_{cm}$  of the  $e^+e^-$  system. The *peak* energy ( $P$ ) corresponds to the energy the closest to the maximum of the Z boson resonance.

Position w.r.t. the peak $P$	1993		1994		1995	
	$E_{cm}$ (GeV)	$\mathcal{L}_{int}$ (nb $^{-1}$ )	$E_{cm}$ (GeV)	$\mathcal{L}_{int}$ (nb $^{-1}$ )	$E_{cm}$ (GeV)	$\mathcal{L}_{int}$ (nb $^{-1}$ )
$P - 2$ GeV	89.43	$9209 \pm 7$			89.44	$7999 \pm 8$
$P$	91.22	$13851 \pm 7$	91.20	$39983 \pm 27$	91.28	$8544 \pm 8$
	91.30	$518 \pm 5$			91.37	$4313 \pm 6$
$P + 2$ GeV	93.02	$9563 \pm 7$			92.97	$8282 \pm 8$

Table 4.1: Centre-of-mass energy  $E_{cm}$  and integrated luminosity  $\mathcal{L}_{int}$  for the 1993, 1994 and 1995 data samples, with the corresponding experimental errors. The relative theoretical error on  $\mathcal{L}_{int}$  is 0.11%

Most of the recorded events are of the following types:

- **hadronic events:**  $e^+e^- \rightarrow q\bar{q}$ . They represent 70% of the Z boson decays, i.e. more than 2 millions events for the 70 pb $^{-1}$  integrated luminosity on the Z resonance peak, which was approximately available for this analysis (see table 4.1). They are characterised by an average multiplicity of 20 charged particles in the final state [36] produced in general in two widely spread jets after hadronisation of the created quark pair  $q\bar{q}$ . A typical hadronic event is shown on figure 4.1a.
- **leptonic events:**  $e^+e^- \rightarrow l\bar{l}$ ,  $l = e^-, \mu^-, \tau^-, \nu_e, \nu_\mu, \nu_\tau$ . They constitute the remaining 30% of the Z boson decay modes. Since neutrinos are neutral stable leptons, they only interact weakly with the matter and are thus not detectable. The identification of one photon only in the whole detection volume can be the indication of a neutrino pair production with an initial state radiation. Other leptonic channels share equally about 10% of the Z boson width (3.3% for each lepton family). The two leptons are produced back-to-back with an energy of half the centre-of-mass energy, except in case of radiative events. Their nature is determined from the following signatures:
  - **Bhabha events:**  $e^+e^- \rightarrow e^+e^-$ . The electrons generate electromagnetic showers in the HPC where they lose the whole of their energy. Bhabha events are thus characterised by the presence of two high energy charged particles stopped in the HPC where the energy depositions are equal to the particle momenta. Being very light, the electrons often radiate bremsstrahlung photons producing additional electromagnetic showers. As introduced in section 2.2, the t-channel  $e^+e^-$  production interferes with the s-channel Z decay to  $e^+e^-$  pairs and modifies both the  $e^+e^-$  production cross-section and its dependence on the electron emission direction, so that, with regard to the other lepton channels, the electron polar angle spectrum is distorted towards the very forward directions. An example of a Bhabha event is displayed on figure 4.1b.
  - **dimuon events:**  $e^+e^- \rightarrow \mu^+\mu^-$ . At the LEP centre-of-mass energies, the muons are minimum ionising particles. They pass through the whole detector, losing a negligible amount of energy in the HPC and producing a signal in the MUB or MUF. An example of a dimuon event is displayed on figure 4.1c.
  - **$\tau^+\tau^-$  events:**  $e^+e^- \rightarrow \tau^+\tau^-$ . With a momentum of about 45 GeV/c, the  $\tau$  leptons have a mean flight distance of 2 mm inside the beam-pipe where they decay into two back-to-back low multiplicity jets, each one containing 1 or 2 neutrinos and 1 to 5 highly collimated charged particles often accompanied by one or several neutral

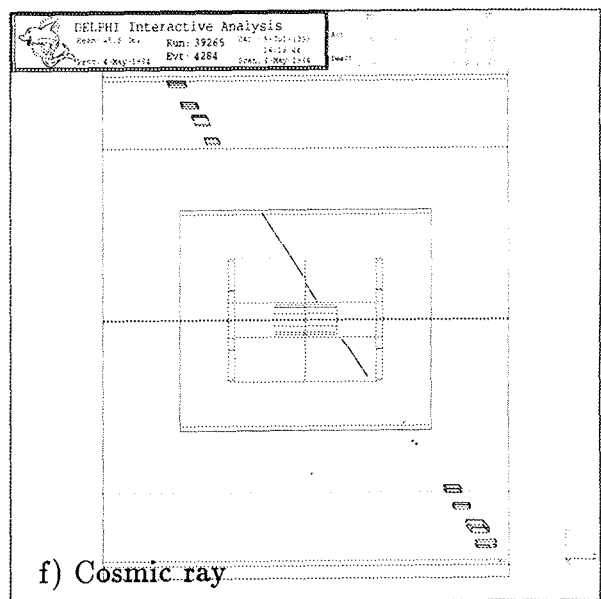
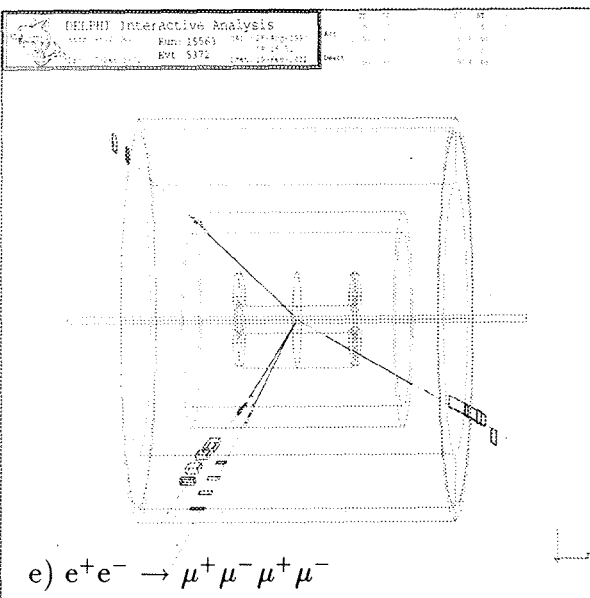
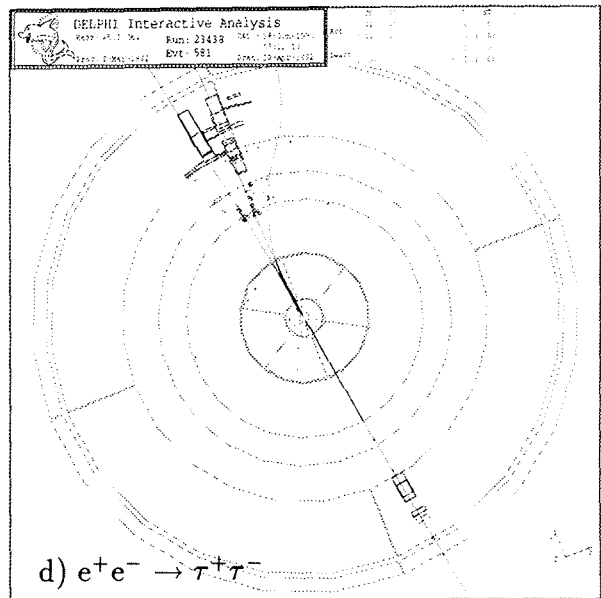
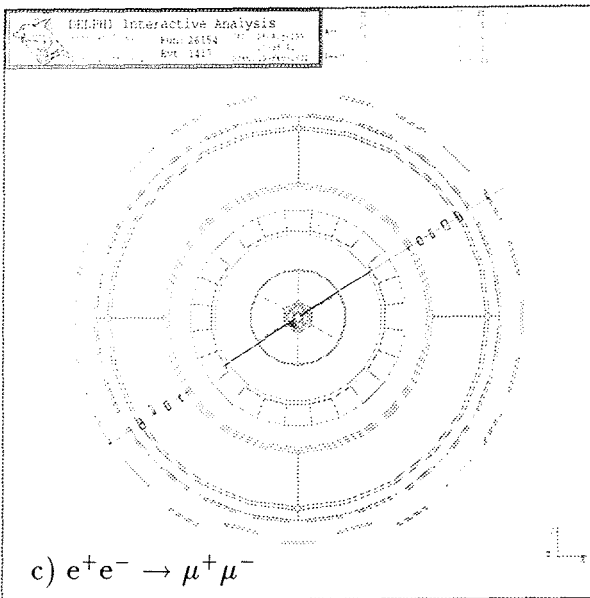
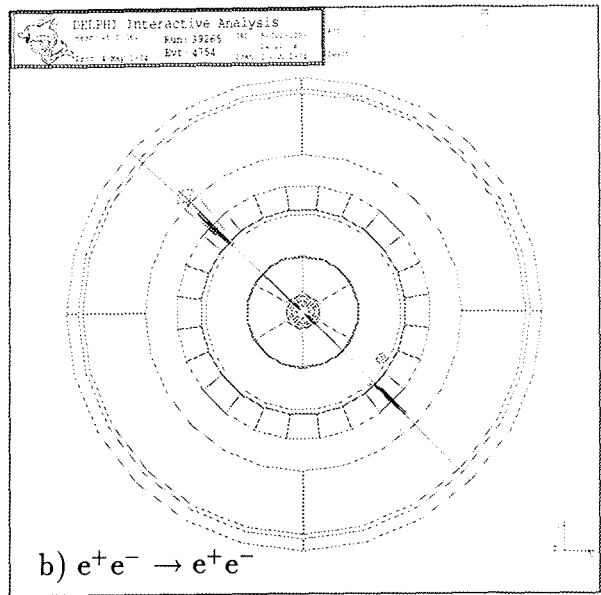
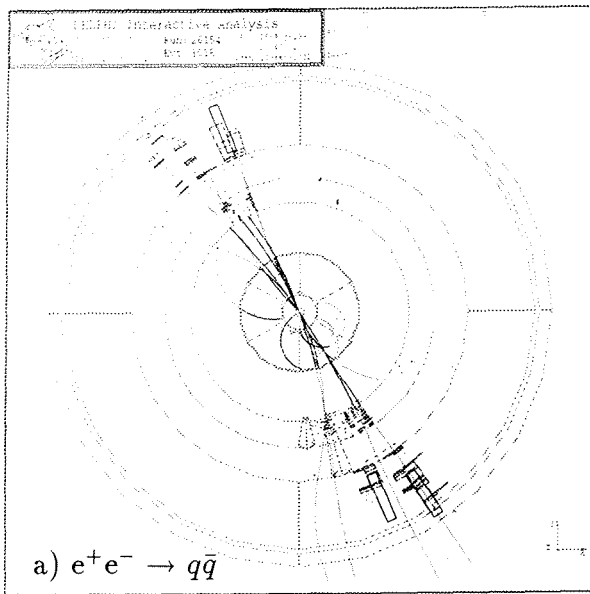


Figure 4.1: Display of typical events recorded by the DELPHI detector.

pions or kaons. Whatever the  $\tau$  decay mode, the  $\tau^+\tau^-$  events can be efficiently distinguished from the other leptonic events due to the missing energy and momentum taken away by the undetected neutrino(s) and to the acollinear decay products. An example of a  $\tau^+\tau^-$  event is displayed on figure 4.1d.

- **four-fermion (4f) events:**  $e^+e^- \rightarrow f\bar{f}f'\bar{f}'$ , with  $f$  and  $f' = e^-, \mu^-, \tau^-, q$ . They can be produced through the four Feynman diagrams presented on figure 2.2. The  $\gamma\gamma$  (or *multiperipheral*)  $e^+e^- \rightarrow e^+e^-\gamma\gamma \rightarrow e^+e^-f'\bar{f}'$  interactions dominate the total 4f production with a cross-section of the order of 100 nb at LEP energies. The two electrons retain most of their initial momentum and fly away nearly back-to-back along the beam-pipe, while a small fraction of energy is transmitted to the produced fermions which are emitted predominantly at small polar angles. Such events are then most often not detected. The other three processes (*inner bremsstrahlung*, *conversion* and *annihilation*) have a cross-section of the order of 1 pb and are characterised by the presence of a pair of low momentum and low invariant mass fermions accompanied by a third charged particle, emitted in the direction opposite to the one of the fourth fermion, which has an energy close to half the centre-of-mass energy. An example of a four-fermion event is displayed on figure 4.1e.
- **cosmic rays:** these are mainly muons traversing the detector randomly in space and time at a rate of about 3 detected muons per second [37]. The track of a cosmic muon is similar to the tracks of two oppositely charged muons of equal energy which would have been produced inside the detector and emitted in opposite directions: they have a common origin and curvature in the  $R\phi$  plane. However, the tracks of cosmic rays cross the beam-spot zone only accidentally. An example of a cosmic event is displayed on figure 4.1f.
- **synchrotron radiation and parallel muons:** The electrons accelerated inside LEP lose energy by synchrotron radiation. The photons emitted in this process can be detected in the forward/backward detector modules. When they cross the collimator material, they can also convert into  $e^+e^-$  pairs which are stopped in the material, or into  $\mu^+\mu^-$  pairs which can reach the detector and be identified by the MUF [38].
- **beam-gas events and beam-beam-pipe events:** it happens that the beam electrons interact with the residual gas present in the beam-pipe, or with the matter of the beam-pipe itself. Together with the cosmic rays, they represent approximately 20% of the recorded events, but are easily identified since they are similar to fixed-target experiments where all produced particles are highly boosted along the direction of the incident electron.
- **random noise of the sub-detector electronics:** such noises are highly suppressed by the T2 trigger decision (see section 3.2.4) where correlations between different subdetectors are used.

In order to decrease the amount of data to be handled, non-ambiguous *hadronic* events were separated from the *leptonic* event candidates on the basis of the number of reconstructed tracks of charged particles as described in references [25] and [39] and the same treatment was applied to the simulated events before further analysis: events with more than 12 tracks were rejected. The present work concerns a total of 1.7 million *leptonic* candidates of which about 20% are  $e^+e^- \rightarrow l\bar{l}$  interactions.



The Monte Carlo technique is used for the simulation of  $e^+e^- \rightarrow e^+e^-, \mu^+\mu^-, \tau^+\tau^-, q\bar{q}, e^+e^-e^+e^-, e^+e^-\mu^+\mu^-$  and  $e^+e^-\tau^+\tau^-$  interactions (see Chapter 3.3). The details of the simulated events statistics used in this analysis to perform the selection of  $\tau^+\tau^-$  event candidates (section 4.2.3) are given in table 4.2. For the Bhabha's, both the s-channel and the t-channel interactions (and their interference) were generated, but in the limited solid angle of  $37^\circ < \theta < 143^\circ$ . Since the t-channel effects on the production cross-section and on the kinematic spectra depend on the centre-of-mass energy, simulation of Bhabha events is needed for the 3 energy points P-2, P and P+2. It has been checked that, for the other  $e^+e^-$  interaction types, the distributions of the kinematical and topological variables used in the following analysis do not significantly depend on the centre-of-mass energy. For the 4f final states, the event generation has been done for a truncated final phase-space domain<sup>1</sup> corresponding to the highly reduced cross-sections given in table 4.2.

In all chapters, the following convention is applied, unless specified otherwise, for the presentation of the data in the distributions:

- dots with error bars correspond to real data,
- the histogram corresponding to the sum of the simulated events is delimited by a solid line,
  - the white area of the histogram corresponds to the  $\tau^+\tau^-$  events,
  - the single-hatched surface corresponds to the dimuons events,
  - the double-hatched surface corresponds to the Bhabha events,
  - hadronic events are represented by the tight-hatched area,
  - the dotted-line delimits the histogram corresponding to the  $e^+e^- \rightarrow e^+e^-\mu^+\mu^-$ ,  $e^+e^- \rightarrow e^+e^-\tau^+\tau^-$  and  $e^+e^- \rightarrow e^+e^-e^+e^-$  events.

---

<sup>1</sup>For the  $e^+e^-\mu^+\mu^-$  and  $e^+e^-\tau^+\tau^-$  final states, the generation has been done requiring that: at least two charged particles are produced with an energy larger than 0.1 GeV and  $\theta > 10^\circ$ , that the total energy visible in the detector is at least 7 GeV, and that the invariant mass of the final state  $e^+e^-$  system is greater than 0.1 GeV/c<sup>2</sup>. The final state phase-space was similarly truncated for the generation of  $e^+e^-e^+e^-$  events.

Physical process	Number of generated events		
	93	94	95
$e^+e^- \rightarrow \tau^+\tau^-$	649975	1286587	726262
$e^+e^- \rightarrow e^+e^-(P-2)$	94294	-	31877
$e^+e^- \rightarrow e^+e^-(P)$	119432	119885	33503
$e^+e^- \rightarrow e^+e^-(P+2)$	118783	-	33075
$e^+e^- \rightarrow \mu^+\mu^-$	217225	293645	219641
$e^+e^- \rightarrow q\bar{q}$	853134	93 sample	93 sample
$e^+e^- \rightarrow e^+e^-\mu^+\mu^-$	94 sample	36363	94 sample
$e^+e^- \rightarrow e^+e^-\tau^+\tau^-$	94 sample	35386	94 sample
$e^+e^- \rightarrow e^+e^-e^+e^-$	94 sample	132322	94 sample
	Generated cross-section (nb)		
$e^+e^- \rightarrow e^+e^-\mu^+\mu^-$	-	0.3267	-
$e^+e^- \rightarrow e^+e^-\tau^+\tau^-$	-	0.1145	-
$e^+e^- \rightarrow e^+e^-e^+e^-$	-	3.406	-

Table 4.2: *Simulated events statistics and generated cross-section for the four-fermion final states.*

## 4.2 Selection of the $e^+e^- \rightarrow \tau^+\tau^-$ interactions

On the basis of the topological and kinematical characteristics given in the previous section for the various type of events, the  $e^+e^- \rightarrow \tau^+\tau^-$  interactions were isolated from the other leptonic events by applying a set of selection criteria based on kinematical variables. The choice of the variables and of the cut values was based on the analysis of the distributions obtained for the simulated events in order to take into account detector effects (secondary interactions of the particles with the detector material, detection dead zones, threshold effects, noise) and reconstruction imperfections (pattern recognition, track search efficiencies, geometrical imprecisions).

Before describing the  $e^+e^- \rightarrow \tau^+\tau^-$  selection criteria (section 4.2.3), a section is devoted to the determination of the event topology (section 4.2.1). In section 4.2.2 we show that a re-calibration of the HPC energy was seriously needed for the simulated events of the 94 and 95 processings.

### 4.2.1 Reconstruction of the event topology

Since the selection of  $\tau^+\tau^-$  events was partially based on the number of charged particles and on their kinematical properties (momentum and direction), some requirements regarding their impact parameters<sup>2</sup>  $|R_{imp}|$  and  $|Z_{imp}|$  and the length of their tracks<sup>3</sup> were imposed in order to assure that:

- the momentum and polar and azimuthal angles could be properly measured:

$$\text{Track length} \geq 30 \text{ cm}$$

<sup>2</sup>The impact parameters of a track are the distances between the track or its extrapolation and the interaction vertex at the point of nearest approach measured separately in the  $R\phi$  plane ( $R_{imp}$ ) and along the  $z$ -axis ( $Z_{imp}$ ).

<sup>3</sup>The length of a track is the length of the curve between the first and the last reconstructed points in the tracking detectors.

- each charged particle can be a direct product of the  $e^+e^-$  interaction or of the  $\tau$  decay and not a cosmic ray or a secondary particle such as an electron or a positron arising from photon conversions and which would not have been identified by the ELEPHANT package (see section 3.2.2):

$$|R_{imp}| \leq 5 \text{ cm} \quad \text{and} \quad |Z_{imp}| \leq 10 \text{ cm} .$$

Particles which did not fulfil these requirements were not counted as charged  $\tau$  decay products; their possible associated calorimetric showers were treated in the same way as signals from neutral particles in order to take into account the corresponding energies.

In order to attribute the final state charged and neutral particles to each  $\tau$  in the case of possible  $\tau^+\tau^-$  production, the thrust  $T$  and the thrust axis  $\vec{t}$  were computed for each event according to the following definition: the thrust axis is the unit vector  $\vec{t}$  which maximises the quantity  $T$  defined as:

$$T = \frac{\sum_j |\vec{p}_j \cdot \vec{t}|}{\sum_j |\vec{p}_j|}$$

where  $\vec{p}_j$  is the momentum of particle  $j$ . The sums are performed on all charged particles of the event, satisfying the track quality criteria. (The thrust  $T$  is 1 for two exactly collinear momenta and decreases to 1/2 for an isotropic distribution of the momentum vectors.) The space was then divided into two hemispheres according to the plane containing the geometrical centre of the detector and transverse to the thrust axis. All particles detected in a same hemisphere were assumed to be the decay products of the same  $\tau$  since the Lorentz boost from the  $\tau$  rest-frame to the laboratory frame is very high. The *leading track* in hemisphere  $i$  ( $i = 1, 2$ ) was defined as the charged particle having the highest momentum. Its momentum, polar angle, impact parameters and associated electromagnetic energy are respectively noted  $p_i$ ,  $\theta_i$ ,  $R_{imp,i}$ ,  $Z_{imp,i}$ , and  $E_{em,i}$ . To assure optimal reconstruction conditions of these variables and other physical quantities, the analysis was limited to the barrel region of the detector: it was required that the polar angle  $\theta_i$  of at least one of the two leading tracks was in the interval  $[43^\circ, 137^\circ]$ . Also, events with no detected charged particle in one hemisphere were rejected.

## Photon conversions

Some electrons<sup>4</sup> from photon conversions (which were not identified by ELEPHANT) still survived the track quality cuts and increased the apparent number of charged products in the event. This was a problem since our goal is the selection of 1-*prong*  $\tau$  decays which often contain  $\pi^0$ 's which decay into photon pairs. An over-estimation of the number of charged particles results in a decrease in the selection efficiency. Moreover, as explained in the next section, Bhabha and dimuon events were rejected by selection criteria applied only to 1-1 topologies (i.e. events where only one charged particle was detected in each hemisphere). If, because of conversion electrons, Bhabha (or dimuon) events are not identified as 1-1 topology events, they are not submitted to the criteria dedicated to the 1-1 topologies and the residual background level of the  $\tau^+\tau^-$  sample increases. As more than 98% of the conversions occur after the VD (see section 3.2.1), surviving conversion electrons are most often not associated to a VD signal. This fact was used to try to identify such electrons: in case of a photon conversion in an actual 1-*prong* hemisphere, three charged particles are in principle detected of which most probably only one has a VD signal associated to the extrapolation of its track, the other two being of opposite charges and having an invariant mass close to zero, the photon mass. When selecting

<sup>4</sup>When speaking about photon conversions, we use the word *electrons*, for both electrons and positrons.

tracks with  $45^\circ < \theta < 135^\circ$  (and rejecting background with cuts 2, 5, 7 and 8 described in the next section), the ratios of real to simulated number of charged particle trajectories starting inside and outside the VD were respectively found to be  $0.994 \pm 0.003$ , compatible with 1, and  $1.36 \pm 0.02$ . This indicated a  $\sim 36\% \pm 2\%$  deficit in the simulation of tracks originating from photon conversions in the limit where all tracks not associated to a VD signal are issued from photon conversions<sup>5</sup>. The deficit is in fact more important since some tracks can present no associated VD signal because of VD response or reconstruction imperfections. It was consequently necessary to try to be as insensitive as possible to these surviving conversion electrons in order not to bias the selection efficiencies since they are evaluated on the basis of the simulation (see section 4.4).

A track actually originating from the interaction point can present no associated VD signal, either because of VD or tracking inefficiencies, or, as it is mostly the case for electrons, when the curvature of its trajectory is modified because of the emission of a hard bremsstrahlung photon after the particle has passed through the VD. The trajectory extrapolation to the VD is then no longer pointing to the VD hits. In order to confirm that the observed disagreement was indeed caused by photon conversions and not by an incorrect simulation of the VD response or by a tracking problem, converted photon candidates were selected in the following way:  $\tau$  decays were selected for which three tracks were reconstructed but only one had at least two associated signals in the VD, the other two tracks being an electron-positron pair candidate for which the total electric charge  $Q_{e^+e^-}$  and the invariant mass  $M_{e^+e^-}$  were computed. As can be seen on figure 4.2,a),  $Q_{e^+e^-}$  is equal to 0 in 77% of the cases. This rejects the hypothesis that the observed discrepancy would only be due to an incorrect VD response simulation, since, in that case, the selected events being  $\tau \rightarrow 3$  charged particles decays, the fraction of events with  $Q_{e^+e^-} = 0$  would be  $2/3$ . This observation, together with the fact that the distributions concentrate around the value 0 for the pull of the energy loss for the electron mass hypothesis<sup>6</sup> (figure 4.2,e) ) tends to confirm that the charged particles giving no hit in the VD were electrons originating from photon conversions. Clear cases of photon conversions are identified by the ELEPHANT package. We are left here with conversions where probably one or both tracks of the  $e^+e^-$  pair were badly reconstructed, leading to a wrong estimation of the invariant mass of the electron pair,  $M_{e^+e^-} \neq 0$  (figure 4.2,b) ).

Considering these observations, an event of topology 1-1 was defined as an event where, in each hemisphere, there was either only one charged particle, or only one charged particle to which at least one VD signal had been associated. That particle was called the *main* charged particle and could be different from the *leading* one. Simulated Bhabha's were found to present one single charged particle in each hemisphere in  $(96.29 \pm 0.04)\%$  of cases, while  $(99.84 \pm 0.01)\%$  satisfied this new 1-1 topology definition. For simulated dimuons, where bremsstrahlung is less probable, the proportion increased from  $(98.89 \pm 0.04)\%$  to  $(99.87 \pm 0.02)\%$ . For simulated 1-1 (non 1-1)  $\tau^+\tau^-$  events, the proportion increased from  $(89.86 \pm 0.05)\%$  ( $(2.39 \pm 0.04)\%$ ) to  $(97.53 \pm 0.03)\%$  ( $(9.24 \pm 0.08)\%$ ). Note that the Dalitz decay of the  $\pi^0$ 's,  $\pi^0 \rightarrow e^+e^-\gamma$ , which occur in 1.2% of the  $\pi^0$  decays instead of the  $\pi^0 \rightarrow \gamma\gamma$  channel, also contribute to the migration of the event topology to higher multiplicities in charged particles.

<sup>5</sup>An independent study of photon conversion simulation has been performed using radiative dimuons events  $e^+e^- \rightarrow \mu^+\mu^-\gamma$ . Conversions with both one or two reconstructed electrons were used. A factor of  $34\% \pm 9\%$  was found [40] which is compatible with our estimation.

<sup>6</sup>The pull of the energy loss for the electron mass hypothesis,  $Pull(dE/dx)_e$ , is defined as the difference between the measured energy loss per unit length and the expected value for an electron of the same momentum, divided by the error on the measurement.

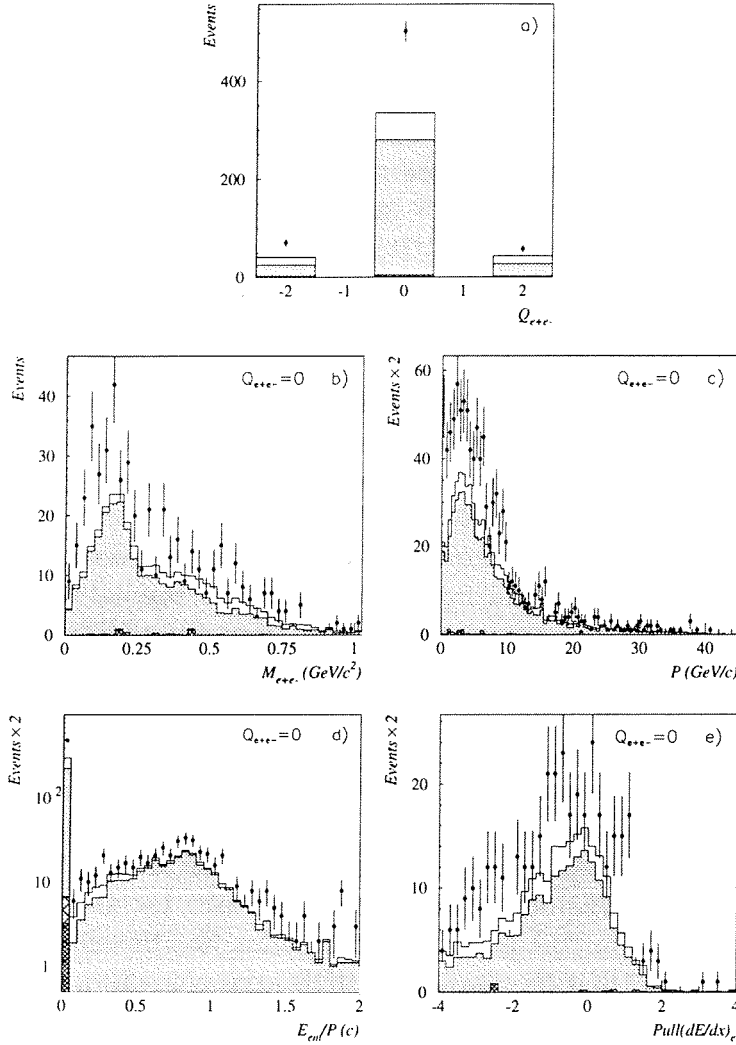


Figure 4.2: a) Total electric charge of the electron pair candidates  $Q_{e^+e^-}$ . For the pairs having a zero total charge: b) invariant mass  $M_{e^+e^-}$ , c) momentum  $p$ , d) electromagnetic to momentum ratio  $E_{em}/p$ , and e) energy loss pull for the electron hypothesis,  $Pull(dE/dx)_e$ , of the  $e^\pm$  candidates. The points with error bars represent the real data, the solid line is the total Monte Carlo prediction according to the convention given at the end of section 4.1, except that the true 1-prong (non 1-prong)  $\tau$  decays are represented by the plain grey (white) areas.

## 4.2.2 Calibration of the HPC energy

The calibration of the HPC energy was found to be quite bad for the simulated events of the 94 and 95 processings. Figure 4.3 shows the electromagnetic energy associated to the leading tracks of events satisfying the cuts 1, 2, 7 and 8 described below (section 4.2.3). The smooth curve represents the simulated data before any correction, and the histogram (solid line) corresponds to the re-calibrated simulated data. The calibration was done in a way that a better agreement was found between the experimental and the simulated distributions for both the energy of the electrons produced in  $e^+e^- \rightarrow e^+e^-$  (i.e. energies of the order of 45 GeV), and the mass of  $\pi^0$ 's computed from the photon energies (i.e. the full range of energies between 1 GeV and 45 GeV) (see reference [40]). A scaling factor of  $1.014 \pm 0.002$ ,  $1.041 \pm 0.002$  and  $1.030 \pm 0.003$  was applied for the 93, 94 and 95 simulations respectively. Also a random smearing of the energies was necessary. A significant improvement is observed but the agreement with the real data (points with error bars) is not perfect. Consequently, a conservative systematic error due

to the calibration of the HPC energy was estimated for all the measurements presented in this work.

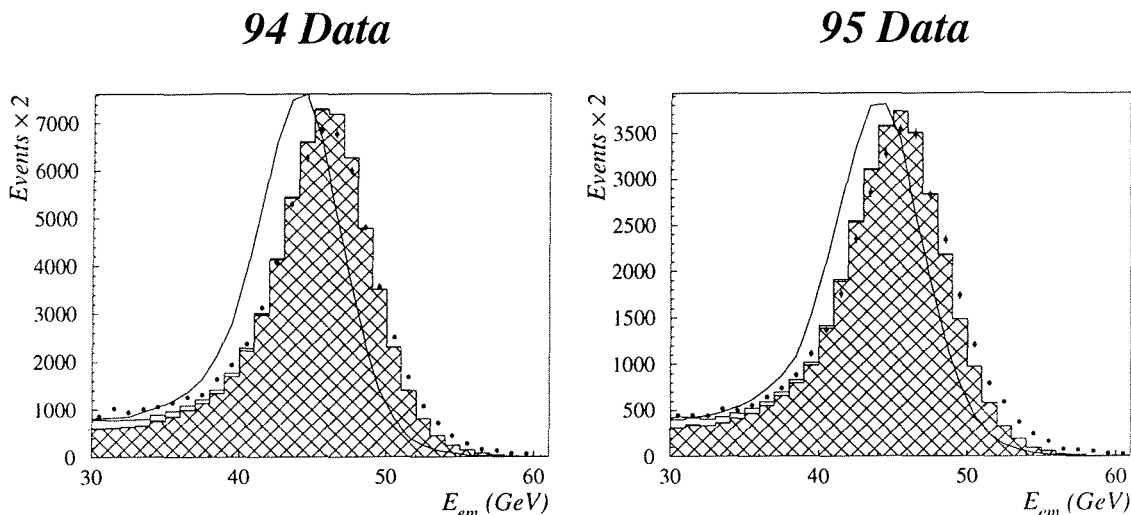
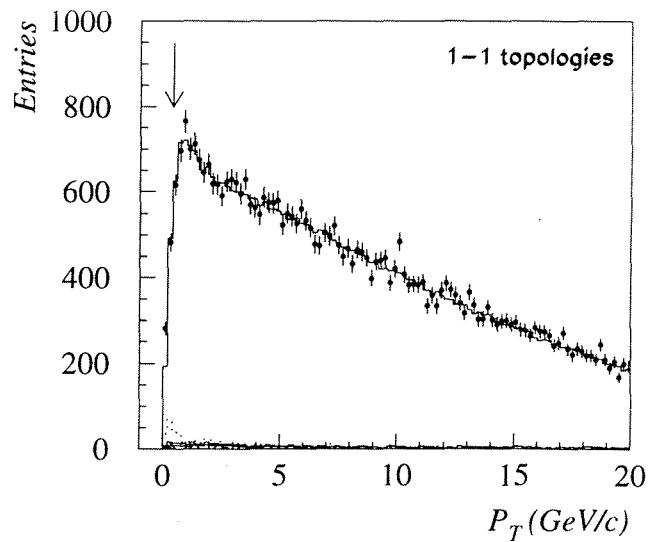
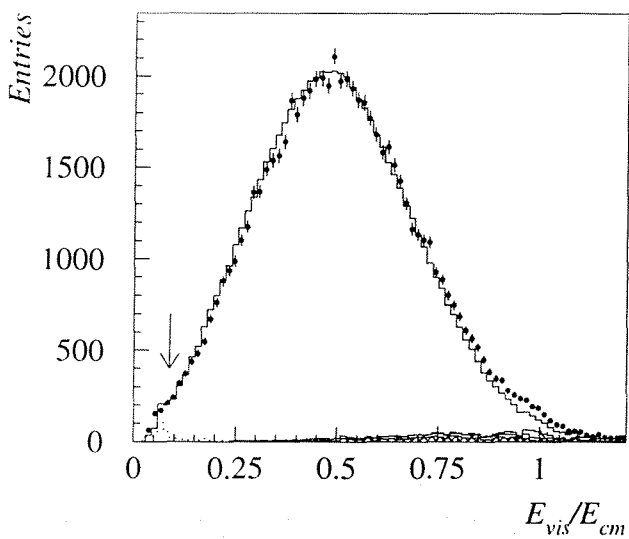
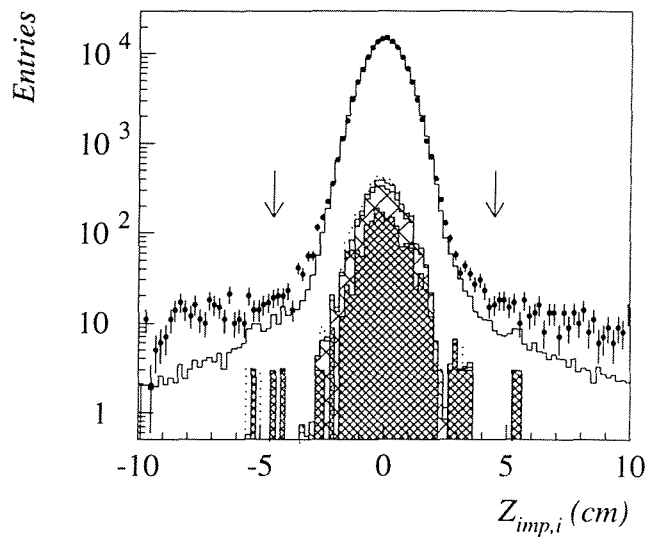
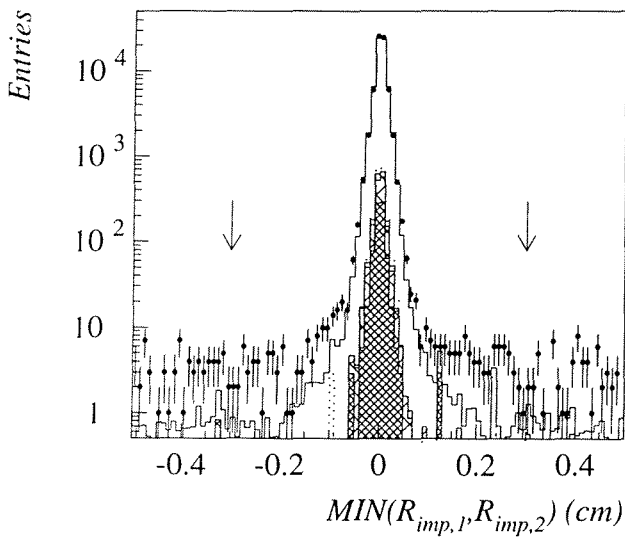
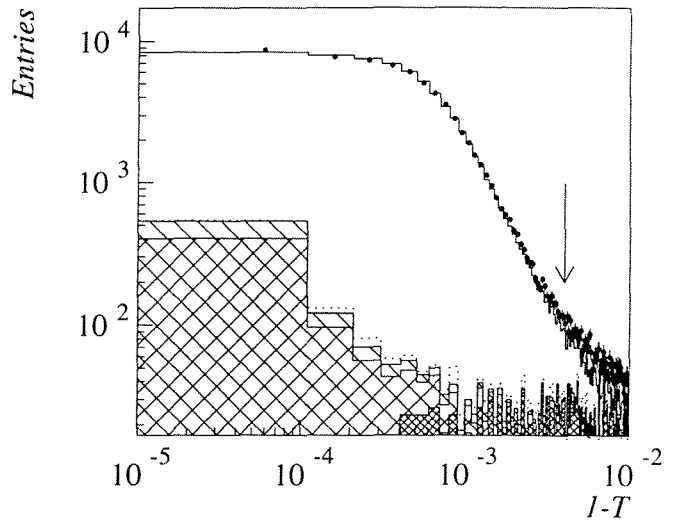
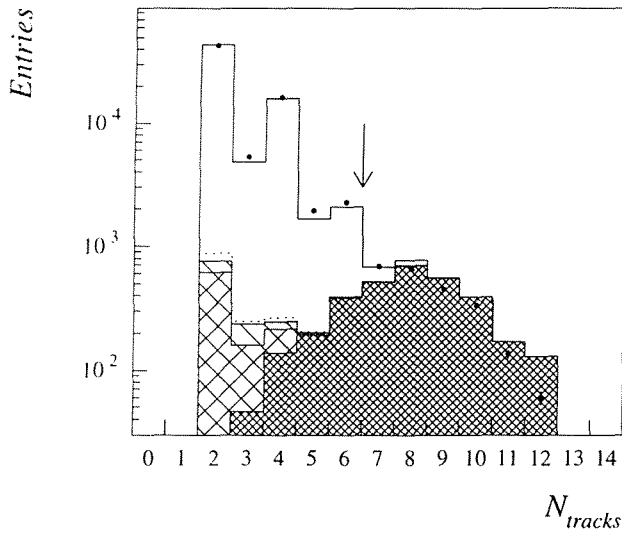


Figure 4.3: *Re-calibration of the HPC energy for the 94 and 95 processings: distributions of the associated electromagnetic energy ( $E_{em}$ ) for the leading tracks of preselected events. The smooth curve represent the simulated data before the re-calibration.*

### 4.2.3 Selection criteria

Here follows the list of the  $\tau^+\tau^-$  selection criteria defined to reject the various background sources. A particular effort was devoted to retain the largest possible domain of the phase space of the  $\tau$  decay products. This concerns mainly the pion decay mode  $\tau \rightarrow \pi\nu_\tau$  which is the most sensitive channel for the  $\tau$  polarisation measurement (see section 2.2.3). For that reason, the variables used for the rejection of the Bhabha's and dimuon events, i.e. the rejection of highly energetic particles, have been specially chosen to avoid rejecting energetic pions produced in  $\tau$  decays. In addition, those cuts were applied exclusively to the 1-1 topologies (see the adopted definition in the previous section), where the Bhabha and dimuon contamination is expected to be concentrated, so that  $\tau \rightarrow \pi\nu_\tau$  decay modes present in non-1-1 topologies were preserved. Also, an attempt was made to avoid selection criteria implying a correlation between the two  $\tau$ 's.

The distributions of the variables used in the selection procedure are shown on figure 4.4 for the real data and the simulation (the convention introduced at the end of section 4.1 is used). For each plot, all cuts have been applied except the one relative to the displayed variable and an arrow indicates the cut value. The data correspond to the whole sample (resulting from the 1993, 1994 and 1995 runs) as a satisfactory agreement with the simulation was observed for each year separately. Simulated events were normalised to the respective integrated luminosities given in table 4.1 multiplied by the production cross-sections given in tables 4.3 and 4.2. The  $\tau^+\tau^-$  cross-sections of table 4.3 were computed by ZFIT-TER [41] on the basis of the world-average measures of  $M_Z$ ,  $M_{top}$ ,  $M_{Higgs}$  presented at the ICHEP96 Conference [42]:  $M_Z = (91.186 \pm 0.002) \text{ GeV}/c^2$ ,  $M_{top} = (175 \pm 6) \text{ GeV}/c^2$  and  $M_{Higgs} = (300_{-240}^{+700}) \text{ GeV}/c^2$ . Some scaling factors had to be introduced to take into account the centre-of-mass dependence of the t-channel contribution for Bhabha events, as explained in the next section. The ratio  $\sigma_{\mu^+\mu^-}/\sigma_{\tau^+\tau^-}$  is in fact very slightly greater than 1 because of the



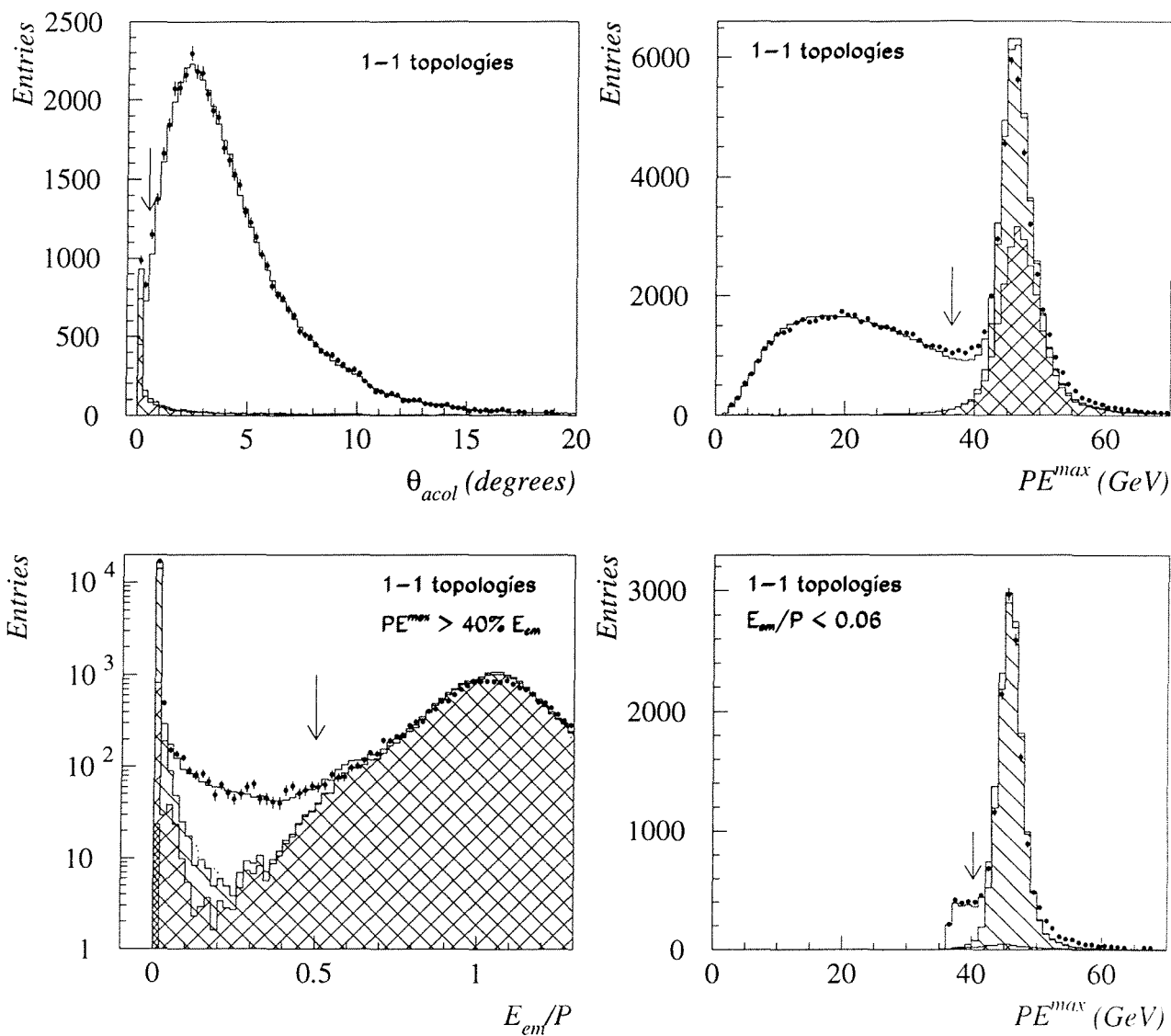


Figure 4.4: Distributions of the selection cut variables (93, 94 and 95 data). For each plot, all cuts have been applied except the one related to the displayed variable. Arrows indicate the cut values. The normalisation of the simulated events is done as described in the text. The representation of the data follows the convention given at the end of section 4.1. The excess of events in the distributions of the impact parameters  $R_{imp}$  and  $Z_{imp}$  are attributed to cosmic rays.



reduced phase-space available to the more massive  $\tau$ 's. This effect is negligible at the present level of precision.

The successive signal ( $\tau^+\tau^-$  events) and background (non- $\tau^+\tau^-$  events) reduction factors corresponding to each selection cut are given in table 4.4 for the 1993 simulated data.

$E_{cm}$ (GeV)	$\sigma_{\tau^+\tau^-}$	$\sigma_{e^+e^-}/\sigma_{\tau^+\tau^-}$	$\sigma_{\mu^+\mu^-}/\sigma_{\tau^+\tau^-}$	$\sigma_{q\bar{q}}/\sigma_{\tau^+\tau^-}$
89.43	0.490	1.72	1.	20.778
89.44	0.493	1.72	1.	20.778
91.20	1.475	1.14	1.	20.778
91.22	1.477	1.14	1.	20.778
91.28	1.480	1.14	1.	20.778
91.30	1.479	1.14	1.	20.778
91.37	1.473	1.14	1.	20.778
92.97	0.701	0.993	1.	20.778
93.02	0.684	0.993	1.	20.778

Table 4.3: *ZFITTER*  $\tau^+\tau^-$  cross-section  $\sigma_{\tau^+\tau^-}$  (nb) and relative cross-sections  $\sigma_i/\sigma_{\tau^+\tau^-}$  of other processes, used for comparison between measurements and simulation predictions. In spite the assumed leptonic universality, the ratios given for the Bhabhas differ from 1 because of the contribution from the *t*-channel; those numbers are computed for the produced electron being emitted in the solid angle  $43^\circ < \theta < 137^\circ$ . The error on the cross-sections due to the model parameters uncertainty is 1 pb.

In the following, selection criteria are presented which reject first the residual hadronic events present in the *leptonic* data samples, then the Bhabha and dimuon events, and finally the  $\gamma\gamma$  events and cosmic rays.

### Rejection of the hadronic events

Hadronic events were rejected by requiring the maximum number of tracks in the event  $N_{tracks}$  to be 6, and the thrust  $T$  to be greater than 0.996:

$$\text{Cut 1} \quad N_{tracks} \leq 6$$

$$\text{Cut 2} \quad T > 0.996$$

### Rejection of the Bhabha and dimuons events

The following cuts were applied to reconstructed events of 1-1 topology. In non-radiative Bhabha and dimuon events, the two final state leptons are emitted in exactly opposite directions. This is not the case in 1-1  $\tau^+\tau^-$  events where the neutrinos, and often neutral pions as well, carry a part of the momentum so that the two charged decay products present acollinear momentum-vectors. The acollinearity angle  $\theta_{acol}$  is defined as  $180^\circ$  minus the angle between the momentum-vectors  $\vec{p}_1$  and  $\vec{p}_2$  of the two leading tracks of the event. Bhabha and dimuon events were rejected by asking a minimum acollinearity of half a degree:

$$\text{Cut 3} \quad \theta_{acol} > 0.5^\circ \quad \text{for 1-1 topologies}$$

This criterium is not sufficient to reject radiative Bhabha or dimuon events (see table 4.4). The aim of the following procedure was to identify such events. If the radiation takes place in

the final state, the charged energy in at least one hemisphere is still of the order of half the centre-of-mass energy  $E_{cm}$ . The variable  $PE^{max}$  was computed as the maximum of  $p_1, p_2, E_1^{1deg}$  and  $E_2^{1deg}$  where  $p_i$  is the momentum of the leading particle of hemisphere  $i$ , and  $E_i^{1deg}$  is the sum of the electromagnetic energy associated to all charged particles of hemisphere  $i$  and to all neutrals contained in a cone of 1 degree half-opening angle around the main charged particle (to take into account radiated photons which have not been identified by the ELEPHANT algorithm.) As can be seen on figure 4.4, the distribution of  $PE^{max}$  is peaked at 45 GeV (i.e.  $\sim$  the beam energy) for Bhabha or dimuon events. In this case, the event was rejected if the ratio  $E_{em}/P$  of the electromagnetic energy associated to the particle to its momentum was larger than 0.5 (it was then an electron candidate) or if the particle entered the HPC within 1 degree of one of its  $\phi$  cracks. When the ratio  $E_{em}/P$  was smaller than 0.06, the event was a dimuon candidate and was rejected if  $PE^{max}$  was larger than 44% of  $E_{cm}$ .

#### Cut 4

*for 1-1 topologies*

When  $PE^{max} > 0.40 \times E_{cm}$ , the event is rejected if:

$$\begin{aligned} E_{em}/P &> 0.5 \\ \text{or } E_{em}/P &< 0.06 \text{ and } PE^{max} > 0.44 \times E_{cm} \\ \text{or } |\phi - \phi^{crack}| &< 1 \text{ degree} \end{aligned}$$

#### Rejection of the four-fermion events

Since the two highly energetic final state electrons from  $\gamma\gamma$  events remain inside the beam pipe (they are sometimes detected in the very-forward calorimeters), such events were rejected by imposing a minimum visible energy in the event. The visible energy  $E_{vis}$  is the sum of the energy of all charged particles and of the electromagnetic energy of all neutral particles, without taking into account energy deposits recorded by the very forward calorimeters (SAT, VSAT or STIC). Events are accepted when  $E_{vis}$  is larger than 9% of  $E_{cm}$ :

#### Cut 5

$$E_{vis} > 0.09 \times E_{cm}$$

For 1-1 events, an additional condition was applied on  $P_T$ , the total charged particle momentum projected on the  $R\phi$  plane, which is very small for  $\gamma\gamma$  events and was chosen to be greater than 0.4 GeV/c for  $\tau^+\tau^-$  candidates:

#### Cut 6

$$P_T > 0.4 \text{ GeV}/c$$

*for 1-1 topologies*

Since the fermion-pair  $f'\bar{f}'$  produced by the four-fermion interaction are not emitted in back-to-back directions, a large fraction of four-fermion events were also rejected by the thrust cut (Cut 2).

#### Rejection of the cosmic rays

Cosmic rays cross the detector randomly in space. The two reconstructed tracks have a uniform  $Z_{imp}$  distribution. On the other hand, as they result from a unique particle, the point of closest approach to the interaction point is the same for the two hemisphere, leading to a correlation between the impact parameters  $R_{imp,1}$  and  $R_{imp,2}$  seen in the diagonal region of the  $R_{imp,1}$  versus  $R_{imp,2}$  plane (see figure 4.5). Consequently, the following cuts were applied using the impact parameters of the main track of each hemisphere:

#### Cut 7

$$MAX(|Z_{imp,1}|, |Z_{imp,2}|) \leq 4.5 \text{ cm}$$

#### Cut 8

$$MIN(|R_{imp,1}|, |R_{imp,2}|) \leq 0.3 \text{ cm}$$

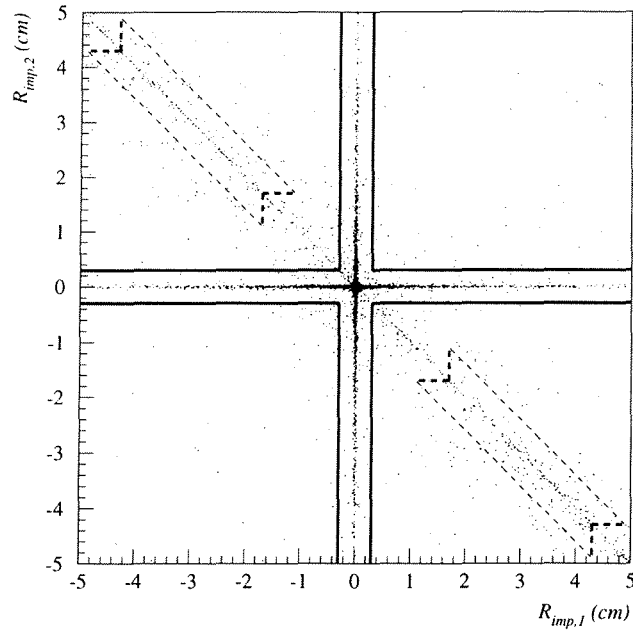


Figure 4.5: Distribution of the impact parameter  $R_{imp}$  for the two main tracks of real events. The solid line indicates the accepted zone according to cut 8, and the regions delimited by the dashed lines correspond to the areas used for cosmic ray background estimation as described later in section 4.3.1.

Final state:	$\tau^+\tau^-$	$e^+e^-$ (P-2)	$e^+e^-$ (P)	$e^+e^-$ (P+2)	$\mu^+\mu^-$	$q\bar{q}$	$e^+e^-\mu^+\mu^-$	$e^+e^-\tau^+\tau^-$	$e^+e^-e^+e^-$
Cut:									
0) $N_{tracks}$ , barrel	61.91	76.08	80.43	81.30	63.33	2.32	21.15	17.79	3.49
1) $N_{tracks} \leq 6$	61.52	76.08	80.43	81.30	63.33	0.416	21.15	17.23	3.49
2) $Thrust$	59.26	72.27	77.77	77.15	61.70	0.033	1.90	2.27	0.26
3) $\theta_{acoi}$	58.50	23.71	24.04	41.56	12.85	0.033	1.52	2.24	0.25
4) $PE^{max}, E_{em}/P$	55.54	0.60	0.55	0.74	0.19	0.033	1.30	2.14	0.25
5) $E_{vis}$	55.30	0.60	0.55	0.74	0.19	0.033	1.12	1.92	0.07
6) $P_T$	54.80	0.59	0.55	0.73	0.18	0.033	0.79	1.92	0.05
7) $Z_{imp,i}$	54.62	0.59	0.54	0.73	0.18	0.032	0.79	1.91	0.05
8) $R_{imp,i}$	54.55	0.58	0.54	0.72	0.18	0.032	0.79	1.91	0.05

Table 4.4: Effects of the selection criteria on the leptonic samples of simulated signal and background events for the 93 processing: percentage of generated events selected after the successive application of each criterium. Cut 0) corresponds to the request of having at least one track in each hemisphere, and one of the two leading tracks emitted in the barrel region of the detector. The last two cuts are assigned to reject the cosmic ray background and do essentially not affect the event categories displayed in this table. For the  $e^+e^- \rightarrow e^+e^-$  channel, the values have to be multiplied by the scaling factors of table 4.6.

## 4.3 Background study

### 4.3.1 Cosmic ray background study

Cosmic ray contamination is evaluated by counting the number of real events satisfying all cuts except cut 8 on impact parameter  $R_{imp}$  which is transformed to the acceptance corresponding to the regions delimited by the dashed-line contour drawn on figure 4.5. The total number of events found in these two regions was normalised to the area corresponding to the intersection of the retained surface (the cross) and the diagonal region of the plane  $R_{imp,1} \times R_{imp,2}$ . It was taken as an estimation of the total number of cosmic ray contained in the selected data sample. The results are given in table 4.5 for each year and each centre-of-mass energy.

$E_{cm}$	1993	1994	1995
$P - 2$	$4.7 \pm 0.9$	-	$1.8 \pm 0.6$
$P$	$7.2 \pm 1.1$	$16.3 \pm 1.6$	$3.5 \pm 0.8$
$P + 2$	$3.5 \pm 0.8$	-	$1.7 \pm 0.5$

Table 4.5: *Evaluated number of cosmic rays contaminating the selected samples.*

### 4.3.2 Bhabha background study

The percentages of Bhabha contamination given in table 4.7 have to be scaled since the Bhabha events are not simulated for the whole solid angle  $4\pi$ . The scaling factor was determined by fitting the simulated distribution of  $E_{rad} = 2\sqrt{(E_1^{30deg})^2 + (E_2^{30deg})^2}/E_{cm}$  to the real distributions. The variable  $E_i^{30deg}$  was evaluated by summing the energy of all electromagnetic showers produced in a cone of  $30^\circ$  half opening angle around the main particle of each hemisphere. The distribution (figure 4.6) was obtained after applying cuts 1, 2, 7 and 8 and the simulated events were normalised to the product of the integrated luminosities (table 4.1) and the cross-sections (tables 4.3 and 4.2); for the Bhabha's, a preliminary factor of 0.739 (correct on peak) was applied. The fits were performed for each year and each centre-of-mass energy separately, on the  $E_{rad}$  range where Bhabha events dominate, namely  $[0.8, 1.7]$  ( $[0.5, 1.5]$ ) when the thrust axis is not (is) pointing within one degree of a HPC module boundary where some energy can be lost. The results are given in table 4.6 and have been used in figure 4.4.

	Scaling factors
93 $P - 2$	$0.894 \pm 0.007$
93 $P$	$0.739 \pm 0.007$
93 $P + 2$	$0.754 \pm 0.007$
94 $P$	$0.747 \pm 0.010$
95 $P - 2$	$0.909 \pm 0.007$
95 $P$	$0.739 \pm 0.007$
95 $P + 2$	$0.805 \pm 0.015$

Table 4.6: *Evaluated scaling factors to be applied to the selection efficiencies of the  $e^+e^- \rightarrow e^+e^-$  channel given in tables 4.4 and 4.7.*

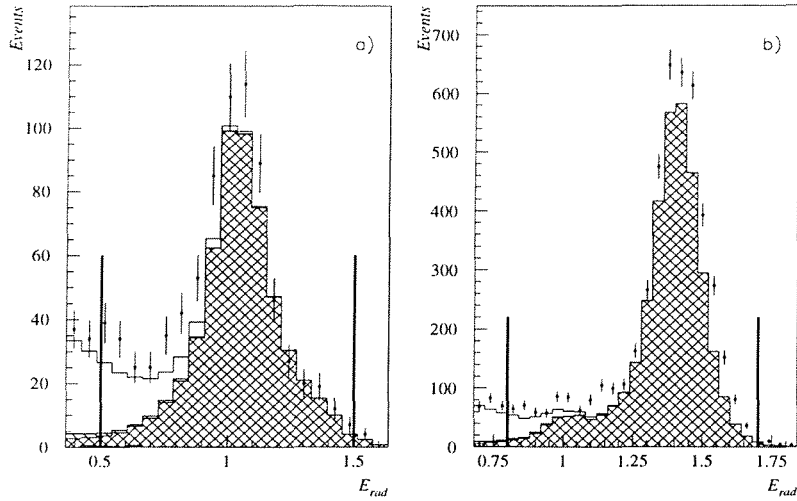


Figure 4.6: Distributions of  $E_{rad}$  used for adjusting the Bhabha background level as described in section 4.3.2 ( $P - 2$ , 93 data). Plot a) and b) correspond respectively to events where the thrust axis is or is not pointing to an HPC module boundary region. The plots are given before the adjustment which was performed on the ranges limited by the vertical lines.

## 4.4 Selection efficiencies and purity of the selected samples

In this section, the selection efficiencies and purities, estimated on the basis of the simulated data, are given separately for the three processings 93, 94 and 95 and the agreement with the real data is estimated.

### 4.4.1 Efficiencies

The selection efficiencies estimated using the simulated events are given in table 4.7 for 1993, 1994 and 1995 simulations of the different interaction types, together with the number of real selected events. The values for the different years differ slightly but significantly with respect to the statistical errors. This is due to the different states of the DELPHI detector (the VD was upgraded in 1994) and to differences in the calibration of the detection modules, in particular to the HPC energy calibration. Since the cut values for the selection (and the requirement of the association of at least 2 VD signals to the track for the definition of the event topology) are identical for the three years of data taking, differences in the selection performances from year to year are expected. The important point is that, for each data sample (93, 94 and 95), the simulation reproduces correctly the experimental measurements, and that the physics results are compatible for all samples. This is carefully checked in section 4.4.3, 4.5 and 4.6.

	93	94	95
Simulated interaction	Percentage of selected events		
$e^+e^- \rightarrow \tau^+\tau^-$	$54.55 \pm 0.07$	$55.12 \pm 0.04$	$55.30 \pm 0.08$
$e^+e^- \rightarrow e^+e^-(P-2)$	$0.58 \pm 0.02$	-	$0.85 \pm 0.05$
$e^+e^- \rightarrow e^+e^-(P)$	$0.54 \pm 0.02$	$0.84 \pm 0.03$	$0.75 \pm 0.05$
$e^+e^- \rightarrow e^+e^-(P+2)$	$0.72 \pm 0.02$	-	$0.95 \pm 0.05$
$e^+e^- \rightarrow \mu^+\mu^-$	$0.18 \pm 0.01$	$0.20 \pm 0.01$	$0.21 \pm 0.01$
$e^+e^- \rightarrow q\bar{q}$	$0.032 \pm 0.003$	-	-
$e^+e^- \rightarrow e^+e^-\mu^+\mu^-$	-	$0.79 \pm 0.05$	-
$e^+e^- \rightarrow e^+e^-\tau^+\tau^-$	-	$1.91 \pm 0.07$	-
$e^+e^- \rightarrow e^+e^-e^+e^-$	-	$0.05 \pm 0.01$	-
Real data	Number of selected events		
$P-2$	2540	-	2328
$P$	12033	33789	10925
$P+2$	3665	-	3316

Table 4.7: *Effect of the  $\tau^+\tau^-$  selection criteria on the simulated data and the final number of selected events for the real data. For the  $e^+e^- \rightarrow e^+e^-$  channel, the values have to be multiplied by the scaling factors of table 4.6.*

#### 4.4.2 Purities

The purity of the selected samples and the residual background levels were estimated for each centre-of-mass energy ( $i = 1, 2, 3$  for  $P-2, P, P+2$ ) using the selection efficiencies  $\epsilon_i^l$  of each interaction type  $l$  (table 4.7) scaled according to the factors  $f_i^l$  of table 4.6, the integrated luminosities  $\mathcal{L}_{int,i}$  (table 4.1), the production cross-sections  $\sigma_i^l$  (table 4.3) and the estimated cosmic background contamination  $C_i$  (table 4.5). The proportions  $P_i^l$  of events of type  $l$  contained in the samples are calculated using the formulae:

$$P_i^l = \frac{\mathcal{L}_{int,i} \sigma_i^l \epsilon_i^l f_i^l}{C_i + \mathcal{L}_{int,i} \sum_l \sigma_i^l \epsilon_i^l f_i^l},$$

$$P_i^{Cosmics} = \frac{C_i}{C_i + \mathcal{L}_{int,i} \sum_l \sigma_i^l \epsilon_i^l f_i^l},$$

and are given in table 4.8: the second column corresponds to the purity of the sample ( $P_i^{\tau^+\tau^-}$ ) and the next columns give the residual background levels ( $P_i^l, l \neq \tau^+\tau^-$ ).

The contamination level of the four-fermion processes are greater at the off-peak points  $P-2$  and  $P+2$  because their production cross-sections do not follow the Z resonance shape and are quasi-constant on the centre-of-mass energy range  $[P-2, P+2]$ . The same observation can be done concerning the cosmic ray background because the rate of cosmic particles crossing the detector is of course independent on the beam energy. For the  $e^+e^- \rightarrow e^+e^-$  background, the t-channel affects the contamination level in two opposite ways: at  $P-2$  it increases a lot the

$e^+e^-$  production cross-section but it distorts the polar angle spectrum of the emitted electrons towards the forward-backward directions which are not in the geometrical acceptance of this selection. At  $P + 2$ , the effects are reversed, and, in addition, the bremsstrahlung being more important than at lower energies, the acollinearity cut is less efficient (see table 4.4).

	Interaction type ( $l$ )							Cosmics
	$\tau^+\tau^-$	$e^+e^-$	$\mu^+\mu^-$	$q\bar{q}$	$e^+e^-\mu^+\mu^-$	$e^+e^-\tau^+\tau^-$	$e^+e^-e^+e^-$	
93 ( $P - 2$ )	$94.63 \pm 0.03$	1.48	0.36	1.11	0.91	0.77	0.55	0.18
93 ( $P$ )	$96.87 \pm 0.01$	0.80	0.37	1.14	0.31	0.26	0.19	0.06
93 ( $P + 2$ )	$95.87 \pm 0.02$	0.91	0.37	1.13	0.66	0.56	0.40	0.09
94 ( $P$ )	$96.46 \pm 0.01$	1.26	0.36	1.12	0.30	0.26	0.18	0.05
95 ( $P - 2$ )	$94.09 \pm 0.03$	2.16	0.40	1.09	0.89	0.76	0.53	0.08
95 ( $P$ )	$96.59 \pm 0.01$	1.10	0.41	1.12	0.30	0.26	0.18	0.03
95 ( $P + 2$ )	$95.62 \pm 0.02$	1.25	0.41	1.11	0.63	0.54	0.38	0.05

Table 4.8: *Composition of the selected samples (%)* .

#### 4.4.3 Comparison between real and simulated data

Using the ZFITTER cross-section values of table 4.3 and the generated four-fermion cross-section of table 4.2, the agreement between the number of observed events  $N_{real}$  and the normalised number of simulated events  $N_{pred}$ , can be quantified by evaluating the ratio

$$R = (N_{real} - \sum_i C_i) / N_{pred}$$

where  $N_{pred}$  is given by:

$$N_{pred} = \sum_i \mathcal{L}_{int,i} \sum_l \sigma_i^l \epsilon_i^l f_i^l$$

The obtained values of the ratio  $R$  are:

$$0.997 \pm 0.008 (stat) \pm 0.003 (syst) \text{ for 93 data,}$$

$$1.004 \pm 0.006 (stat) \pm 0.003 (syst) \text{ for 94 data,}$$

$$1.002 \pm 0.008 (stat) \pm 0.003 (syst) \text{ for 95 data.}$$

where the first errors are taking into account the limited real and simulated statistics, and the second ones are the systematic errors due to the selection procedure. The systematic errors were estimated as explained in section 4.6. The normalisation appears to be good for the three data samples. Taking the systematic errors as fully correlated between the three years, the averaged ratio  $R$  for the three years amounts to  $R = 1.002 \pm 0.004 (stat) \pm 0.003 (syst)$ .

## 4.5 Selection of the inclusive one-prong $\tau$ decay modes

In the previous section we have obtained a  $e^+e^- \rightarrow \tau^+\tau^-$  sample with a selection efficiency and purity of around 55% and 96.5% respectively.

The next step is to isolate the  $\tau$  decay final states involving one single charged particle of whatever nature:  $\tau \rightarrow e\nu\nu, \mu\nu\nu, \pi/K(n\pi^0, K^0)\nu$  ( $n \geq 0$ ), from the decay modes producing three or five charged particles, which represent about 15% of the  $\tau$  decay channels.

As explained in detail in section 4.2.1, simply rejecting final states in which more than one charged particle has been detected presents two weak points. First, this procedure would imply a loss of decays involving  $\pi^0$ 's. Indeed, as soon as produced, the  $\pi^0$ 's decay into two photons which can convert into electron pairs before or inside the tracking detectors, resulting in a migration of the charged particle multiplicity of the decay to higher values. The second point is more important: the photon conversion rate in the real data was observed to be higher than in the simulation. The selection efficiency would then be over-estimated. Consequently,  $\tau$  decay candidates were selected as  $\tau \rightarrow 1\text{-prong}$  decays when there was at the maximum 1 track with at least two associated VD hits. The numbers of reconstructed tracks per hemisphere are displayed on figure 4.7 for the three data samples 93, 94 and 95. The world-average of the inclusive  $1\text{-prong}$   $\tau$  branching ratio  $B(\tau \rightarrow 1\text{-prong}) = 85.53\% \pm 0.14\%$  [2] was used and the normalisation of the simulated data was done using the integrated luminosity. The plain grey (white) areas of the histograms represent simulated  $\tau \rightarrow 1\text{-prong}$  ( $\tau \rightarrow > 1\text{-prong}$ ) decays. In the histograms of the first line, the first bin ("1Tr") gives the number of  $\tau$  decay candidates where only one track has been reconstructed. A slight excess of simulated data was observed in that bin because of migrations to higher multiplicities due to photon conversions not correctly simulated or not identified by ELEPHANT with the same efficiency for real and simulated data. Boxes named "0" to "4" give the numbers of tracks having at least 2 associated VD signals (= "VD-tracks") for decays with more than one reconstructed track. The histograms of the following lines give the number of non VD-tracks per decay, for decays with more than one track and respectively 0, 1, 2 or 3 VD-tracks. The deficits of simulated events are attributed to the photon conversions not correctly simulated. However it cannot be excluded that there could be more migrations in real data than in simulation, of 3-prongs decays, from 3 VD-tracks to 2 VD-tracks. In section 4.6 we try to estimate the systematic errors due to the photon conversions and to the contamination of the 3-prongs decays possibly incorrectly simulated.

The efficiencies of the  $1\text{-prong}$  decay selection evaluated on the basis of the simulation after  $\tau^+\tau^-$  selection are given in table 4.9 for exclusive and inclusive  $\tau$  decay modes: in column A is the fraction of decays presenting only 1 charged particle, in column B the fraction of decays where only one charged particle was associated to at least 2 VD signals. Column C corresponds to the criterium adopted here: 0 or 1 track having at least 2 associated VD signals. The last column gives the correction factors  $f_i^{conv}$  which have to be applied to the values  $\epsilon_i$  of column C ( $i=e, \mu, \pi/K, \rho, a_1$ ) in order to take into account the factor  $1.36 \pm 0.02$  which was the estimation made in section 4.2.1 of the excess of unidentified photon conversions in the real data with respect to the simulated data. The  $1\text{-prong}$  inefficiencies  $1 - \epsilon_i$  are due to the migration of the  $1\text{-prong}$  decays to higher multiplicities due to photon conversions. They have to be corrected by the factor  $f_i^{conv}$  given by:

$$f_i^{conv} = \frac{1 - (1 - \epsilon_i) \cdot 1.36}{\epsilon_i}$$

The global  $1\text{-prong}$   $\tau$  decay selection efficiencies ( $\epsilon^{\tau\tau} \times 1\text{-prong}$  selection efficiency  $\epsilon_i$ ) are given in table 4.10 for the 93, 94 and 95 simulations together with the number of real candidates for each centre-of-mass energy. They also have to be corrected by the factors  $f_i^{conv}$ .



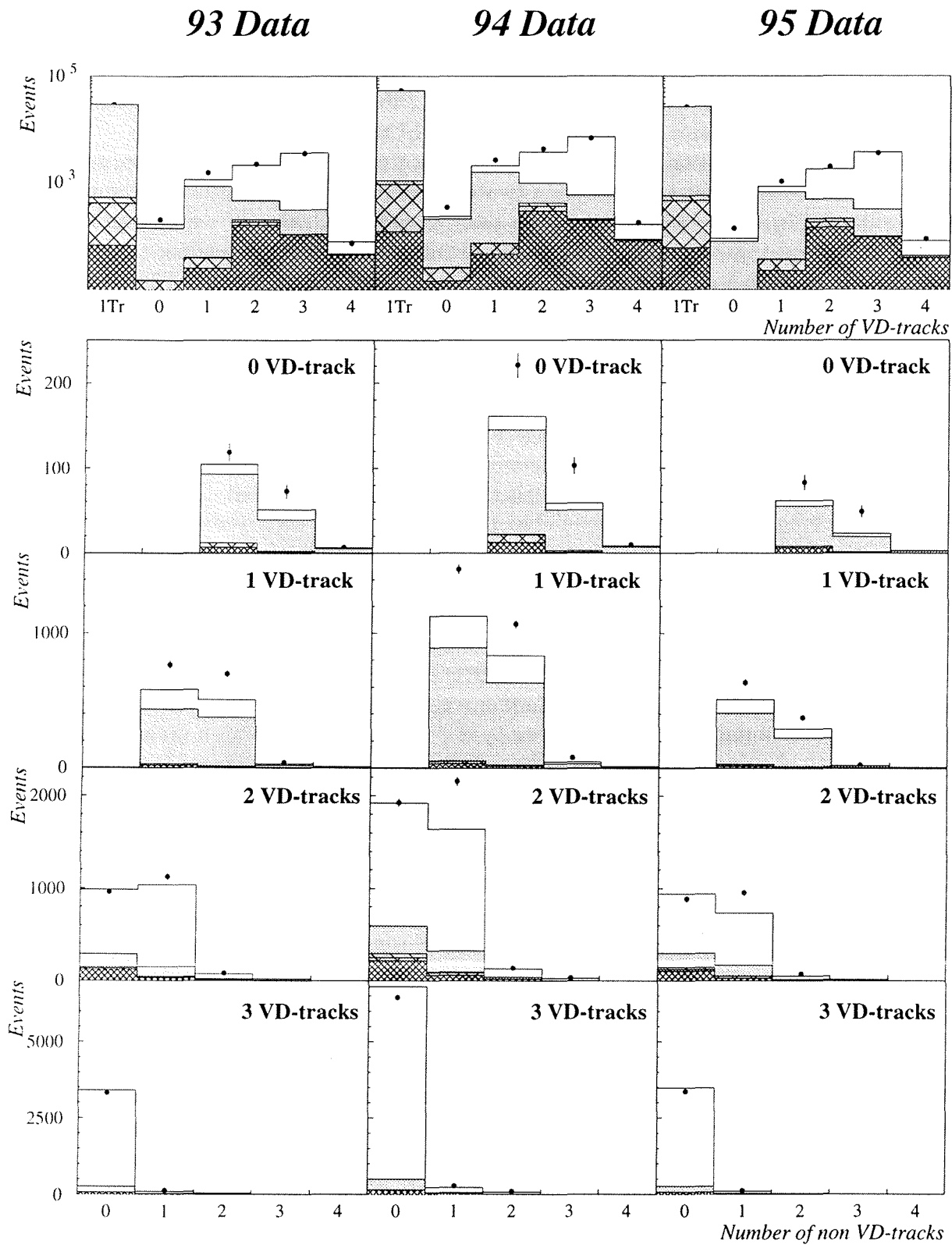


Figure 4.7: Distributions of the number of VD-tracks and non VD-tracks per hemisphere, for  $\tau$  decay candidates.

$\tau$ decay mode (%)	1-prong sel. eff. after $\tau^+\tau^-$ selection			$f_i^{conv}$ (%)
	A	B	C	
$\tau \rightarrow e\nu\nu$	$99.20 \pm 0.03$	$92.71 \pm 0.07$	$99.92 \pm 0.01$	$99.971 \pm 0.002$
$\tau \rightarrow \mu\nu\nu$	$99.77 \pm 0.01$	$97.11 \pm 0.05$	$99.95 \pm 0.01$	$99.982 \pm 0.001$
$\tau \rightarrow \pi\nu$	$98.79 \pm 0.04$	$95.76 \pm 0.07$	$99.90 \pm 0.01$	$99.964 \pm 0.002$
$\tau \rightarrow \pi\pi^0\nu$	$93.51 \pm 0.06$	$93.50 \pm 0.06$	$98.06 \pm 0.03$	$99.287 \pm 0.004$
$\tau \rightarrow \pi 2\pi^0\nu$	$89.21 \pm 0.13$	$91.59 \pm 0.11$	$96.48 \pm 0.08$	$98.686 \pm 0.007$
$\tau \rightarrow$ 1-prong	$96.75 \pm 0.03$	$94.07 \pm 0.03$	$98.80 \pm 0.01$	
$\tau \rightarrow >$ 1-prong	$2.56 \pm 0.05$	$7.65 \pm 0.08$	$8.33 \pm 0.06$	

Table 4.9: 1-prong  $\tau$  decay selection efficiencies after  $\tau^+\tau^-$  selection, estimated from 93 Monte Carlo simulation (%). In column A (B) decays with only 1 charged particle (with only 1 charged particle to which at least 2 VD signals were associated) are selected. Column C corresponds to the 1-prong selection criterium adopted here: not more than 1 track having 2 or more associated VD signals. The last column gives the correction factors to be applied to the values of column C to take into account the discrepancy between experimental and simulated data concerning the photon conversions.

In table 4.10, the global efficiencies of the selection of the inclusive 1-prong  $\tau$  decays estimated using the world-averages of the exclusive  $\tau$  decay branching ratios, are given. Table 4.11 gives the purity and the level of backgrounds of the selected sample of 1-prong decay candidates, for the three years.

	1993	1994	1995
Simulation			
$\tau$ decay mode	Global 1-prong sel. efficiency		
$\tau \rightarrow e\nu\nu$	$52.18 \pm 0.10$	$52.88 \pm 0.07$	$53.04 \pm 0.10$
$\tau \rightarrow \mu\nu\nu$	$56.12 \pm 0.10$	$56.52 \pm 0.07$	$56.52 \pm 0.10$
$\tau \rightarrow \pi\nu$	$52.03 \pm 0.13$	$52.37 \pm 0.09$	$52.40 \pm 0.12$
$\tau \rightarrow \pi\pi^0\nu$	$53.34 \pm 0.09$	$53.53 \pm 0.06$	$53.62 \pm 0.08$
$\tau \rightarrow \pi 2\pi^0\nu$	$52.84 \pm 0.15$	$52.65 \pm 0.11$	$53.00 \pm 0.14$
$\tau \rightarrow$ 1-prong	$53.34 \pm 0.05$	$53.67 \pm 0.03$	$53.79 \pm 0.04$
$\tau \rightarrow >$ 1-prong	$4.82 \pm 0.05$	$3.77 \pm 0.03$	$3.28 \pm 0.04$
Real data			
$E_{cm}$	Number of selected 1-prong $\tau$ decays		
$P - 2$	4315	-	3882
$P$	20209	56288	18101
$P + 2$	6186	-	5521

Table 4.10: 1-prong  $\tau$  decay global selection efficiencies (%), estimated from Monte Carlo simulation, and number of real 1-prong  $\tau$  decay selected candidates.

Process	93			94	95		
	$P - 2$	$P$	$P + 2$	$P$	$P - 2$	$P$	$P + 2$
	Percentage of the selected sample						
$\tau \rightarrow 1\text{-prong}$	94.19 $\pm 0.04$	96.16 $\pm 0.01$	95.70 $\pm 0.01$	96.06 $\pm 0.01$	93.95 $\pm 0.03$	96.33 $\pm 0.01$	95.40 $\pm 0.02$
$\tau \rightarrow > 1\text{-prong}$	1.34	1.50	1.42	1.18	0.97	1.05	1.00
$e^+e^- \rightarrow e^+e^-$	1.60	0.89	1.02	1.38	2.32	1.19	1.42
$e^+e^- \rightarrow \mu^+\mu^-$	0.36	0.38	0.37	0.32	0.38	0.39	0.39
$e^+e^- \rightarrow q\bar{q}$	0.31	0.32	0.32	0.32	0.31	0.32	0.32
$e^+e^- \rightarrow e^+e^-\mu^+\mu^-$	0.68	0.23	0.50	0.23	0.68	0.23	0.49
$e^+e^- \rightarrow e^+e^-\tau^+\tau^-$	0.70	0.24	0.51	0.24	0.70	0.24	0.50
$e^+e^- \rightarrow e^+e^-e^+e^-$	0.59	0.20	0.43	0.20	0.59	0.20	0.42
Cosmic rays	0.21	0.07	0.11	0.06	0.09	0.04	0.06

Table 4.11: Composition of the selected samples of 1-prong  $\tau$  decay candidates.

As a verification of the validity of the present 1-prong  $\tau$  decay selection procedure, the 1-prong  $\tau$  decay branching ratio  $B_1$  was extracted via the relation:

$$B_1 = \frac{\epsilon_{>1\text{-prong}} - \text{Br } \epsilon_{>1\text{-prong}}^{\tau\tau}}{\text{Br } \Delta\epsilon^{\tau\tau} - \Delta\epsilon} ,$$

where

$$\text{Br} = \frac{1}{2} \frac{N_{1\text{-prong}}^{\text{Real}} - N_{1\text{-prong}}^{\text{Back}}}{N_{\tau\tau}^{\text{Real}} - N_{\tau\tau}^{\text{Back}}} ,$$

$$\Delta\epsilon^{\tau\tau} = \epsilon_{1\text{-prong}}^{\tau\tau} - \epsilon_{>1\text{-prong}}^{\tau\tau} ,$$

$$\Delta\epsilon = \epsilon_{1\text{-prong}} - \epsilon_{>1\text{-prong}} ,$$

and  $\epsilon_{1\text{-prong}}^{\tau\tau}$  ( $\epsilon_{>1\text{-prong}}^{\tau\tau}$ ) is the probability to select 1-prong (non-1-prong)  $\tau$  decays at the level of the  $\tau^+\tau^-$  selection,  $\epsilon_{1\text{-prong}}$  ( $\epsilon_{>1\text{-prong}}$ ) is the probability to select 1-prong (non-1-prong)  $\tau$  decays at the level of the 1-prong decay selection, corrected for the conversion deficit in the simulation (see section 4.5 and table 4.9),  $N_{1\text{-prong}}^{\text{Real}}$  ( $N_{\tau\tau}^{\text{Real}}$ ) is the number of selected 1-prong ( $\tau^+\tau^-$ ) candidates and  $N_{1\text{-prong}}^{\text{back}}$  ( $N_{\tau\tau}^{\text{back}}$ ) is the number of selected non- $\tau$  decay final states in the sample of 1-prong  $\tau$  decay ( $\tau^+\tau^-$  final state) candidates. The results are:

$$85.61\% \pm 0.19\% (\text{stat}) \pm 0.08\% (\text{syst}) \text{ for 93 data,}$$

$$85.20\% \pm 0.14\% (\text{stat}) \pm 0.10\% (\text{syst}) \text{ for 94 data,}$$

$$85.12\% \pm 0.21\% (\text{stat}) \pm 0.10\% (\text{syst}) \text{ for 95 data.}$$

The systematic errors are estimated in section 4.6. The combined result is:

$$B_1 = 85.30\% \pm 0.10\% (\text{stat}) \pm 0.09\% (\text{syst}),$$

which is in agreement with the world-averaged value [2] of  $85.53\% \pm 0.14\%$  ( $\text{stat} + \text{syst}$ ).

This analysis leads to the distributions given in figure 4.8 where a good agreement is observed between data and simulation for the momentum, polar and azimuthal angle of the selected 1-prong decay product. Part of the Bhabha contamination accumulates around the  $90^\circ$  crack of the HPC which is rejected in the analysis of the next chapters.

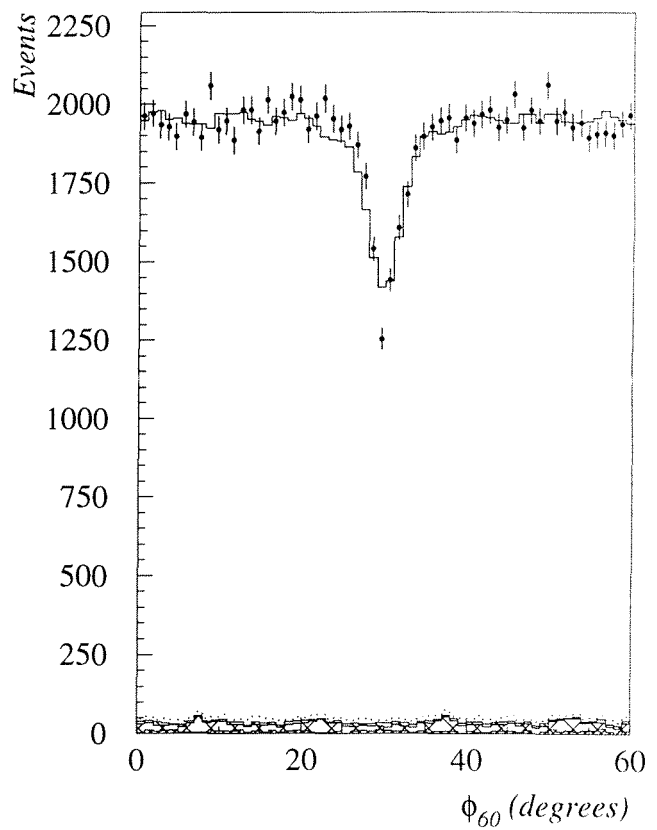
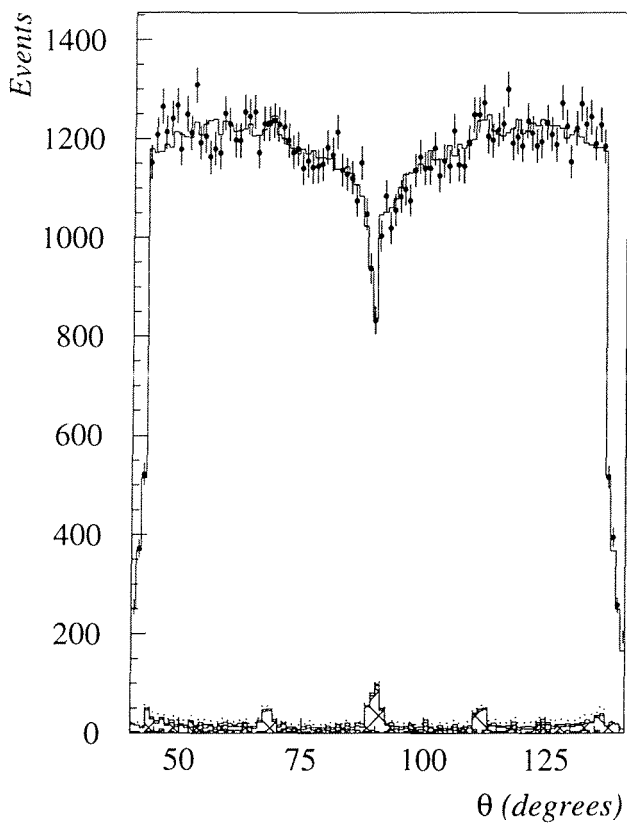
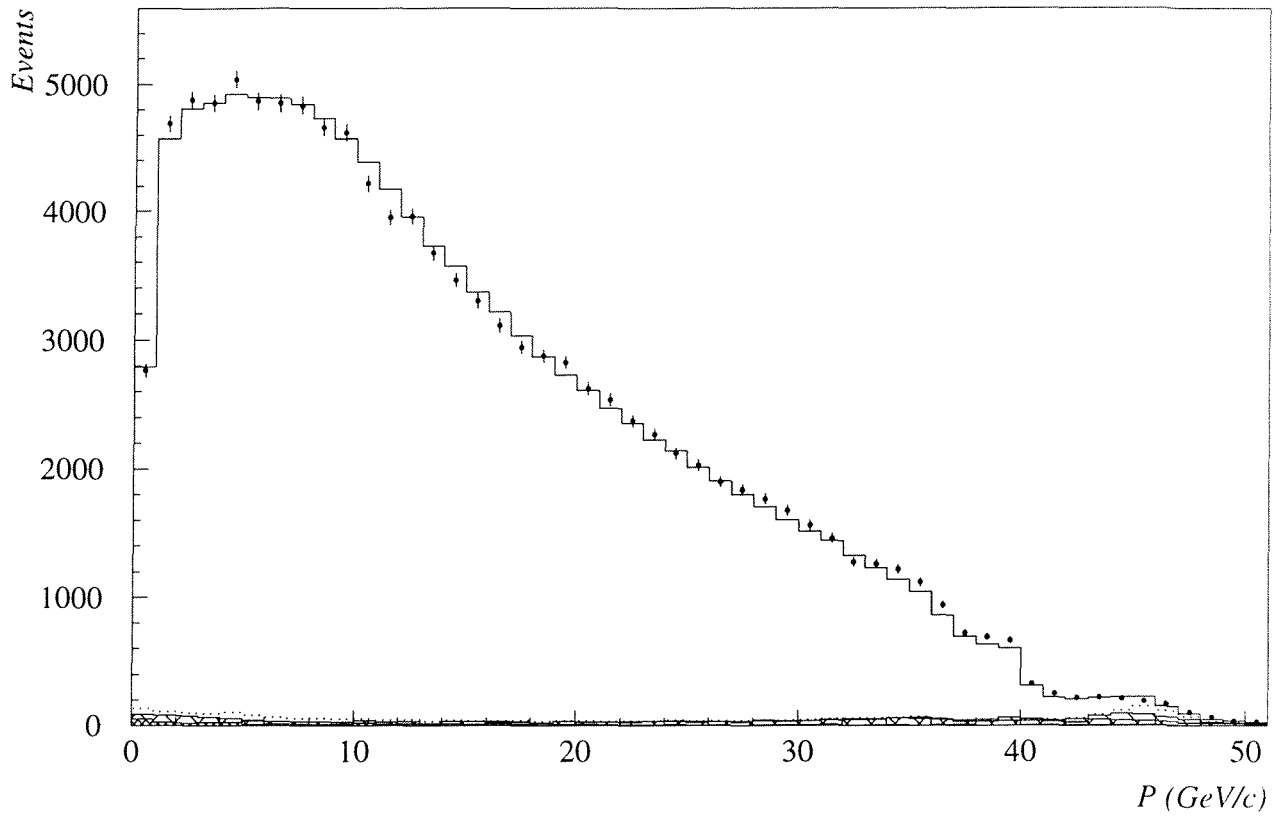


Figure 4.8: Distribution of the momentum ( $P$ ), polar angle ( $\theta$ ) and azimuthal angle modulo 60 degrees ( $\phi_{60}$ ) of the selected 1-prong  $\tau$  decay product for the 93, 94 and 95 samples.

## 4.6 Study of the systematic effects

The systematic effects due to the imperfect reproduction of the experimental distributions by the simulation are evaluated by varying the selection cut values: the corresponding variations of the ratios  $R$  and  $B_1$  respectively, were taken as systematic errors and were summed up quadratically. The cut values were varied to a lower and an upper value as specified in tables 4.13 and 4.14. It was checked that the statistical error variation was in each case at least a factor two smaller than the corresponding systematic error except for the cut on the number of tracks where it was found to be between 50% and 80% of the corresponding systematic error on  $R$ .

At the bottom of the tables are given the effects of the uncertainty on the cosmic ray background and on the scaling factors of table 4.6 for the Bhabha background estimation. Since the calibration of the HPC energy influences mainly the level of contamination from Bhabha events, the scaling factors were varied by plus and minus twice their error.

In order to have an estimation of the systematic error due to the simulation of the VD response, the definition of the 1-1 topology and the 1-prong selection criteria were varied by requiring a minimum of one associated VD signal instead of two. Table 4.12 gives the selection efficiencies in each case (“1 VD-hit” and “2 VD-hits”) for the 1-prong and  $> 1$ -prong  $\tau$  decays at the level of the  $\tau^+\tau^-$  selection ( $\epsilon_{1\text{-prong}}^{\tau\tau}, \epsilon_{>1\text{-prong}}^{\tau\tau}$ ) and the 1-prong selection ( $\epsilon_{1\text{-prong}}, \epsilon_{>1\text{-prong}}$ ), together with the corresponding measurements of  $R$  and  $B_1$ . Half the deviation from the results was taken as a systematic error.

The effect on the results due to the uncertainty on the factor  $1.36 \pm 0.02$  which corrects the simulation data for the photon conversion deficit, was found to be negligible.

Selection efficiency (%)		1 VD-hit		2 VD-hits	
		$\tau^+\tau^-$	1-prong	$\tau^+\tau^-$	1-prong
93 data	$\tau \rightarrow 1\text{-prong}$	54.03	53.28	53.99	53.34
	$\tau \rightarrow > 1\text{-prong}$	57.95	3.88	57.86	4.82
94 data	$\tau \rightarrow 1\text{-prong}$	54.47	53.62	54.46	53.67
	$\tau \rightarrow > 1\text{-prong}$	58.90	3.42	58.87	3.77
95 data	$\tau \rightarrow 1\text{-prong}$	54.61	53.75	54.60	53.79
	$\tau \rightarrow > 1\text{-prong}$	58.99	2.91	58.95	3.28
		$R$	$B_1$	$R$	$B_1$
93 data		0.9996	85.51 %	0.9973	85.61 %
94 data		1.0049	85.06 %	1.0041	85.20 %
95 data		1.0024	85.15 %	1.0021	85.12 %

Table 4.12: Study of the systematic effects on the measurement of  $R$  and  $B_1$ , due to the simulation of the VD response.

Cut	Cut value variation	$\Delta R (\times 10^{-3})$		
		1993	1994	1995
1	$N_{tracks} \leq 5$ or 7	1.2	1.2	1.5
2	$T > 0.9955$ or 0.9965	1.4	1.0	0.9
3	$\theta_{acol} > 0.4^\circ$ or $0.6^\circ$	0.6	0.6	0.4
4	$PE^{max} > 39\%$ or 41%	0.3	0.7	1.5
4	$PE^{max} < 43\%$ or 45% ( $E_{em}/P < 0.06$ )	0.4	0.06	0.04
5	$E_{vis}/E_{cm} > 11\%$ or 7%	0.1	0.1	0.8
6	$P_T > 0.3$ GeV/c or 0.5 GeV/c	0.2	0.2	0.1
7	$ Z_{imp,i}  \leq 4$ cm or 5 cm	0.2	0.4	0.4
8	$ R_{imp,i}  \leq 0.2$ cm or 0.4 cm	0.6	0.4	0.7
Background uncertainty				
Cosmic rays		0.09	0.05	0.07
Bhabha		0.18	0.32	0.29
cross-section		1.0	0.7	1.0
Integrated luminosity		1.3	1.3	1.4
VD response		1.2	0.4	0.2
total		2.9	2.5	3.2

Table 4.13: Systematic effects study on the ratio  $R$  of the numbers of observed to simulated selected events.

Cut	Cut value variation	$\Delta B_1$		
		1993	1994	1995
1	$N_{tracks} \leq 5$ or 7	0.042	0.061	0.076
2	$T > 0.9955$ or 0.9965	0.019	0.018	0.001
3	$\theta_{acol} > 0.4^\circ$ or $0.6^\circ$	0.010	0.011	0.007
4	$PE^{max} > 39\%$ or 41%	0.005	0.011	0.026
4	$PE^{max} < 43\%$ or 45% ( $E_{em}/P < 0.06$ )	0.007	0.001	0.001
5	$E_{vis}/E_{cm} > 11\%$ or 7%	0.002	0.004	0.015
6	$P_T > 0.3$ GeV/c or 0.5 GeV/c	0.018	0.014	0.006
7	$ Z_{imp,i}  \leq 4$ cm or 5 cm	0.004	0.007	0.002
8	$ R_{imp,i}  \leq 0.2$ cm or 0.4 cm	0.013	0.005	0.007
Background uncertainty				
Cosmic rays		0.001	0.001	0.001
Bhabha		0.002	0.003	0.002
cross-section		0.001	0.0005	0.001
Integrated luminosity		0.001	0.001	0.001
VD response		0.05	0.07	0.02
total		0.08	0.10	0.10

Table 4.14: Systematic effects study on the inclusive 1-prong  $\tau$  branching ratio  $B_1$ . The values are absolute errors expressed in %.

## 4.7 Summary

A set of selection criteria has been presented in order to identify  $e^+e^- \rightarrow \tau^+\tau^-$  interactions among a sample of 1.7 million low multiplicity real events recorded during years 1993, 1994 and 1995 by the DELPHI detector at  $e^+e^-$  centre-of-mass energies close to the Z resonance peak. Events simulated by the Monte Carlo technique have been used in order to choose optimal cut variables and cut values, and to estimate selection efficiencies and purities. Special attention has been put on minimising the loss of  $\tau$  decay products in the high energy domain of the phase space where background from  $e^+e^- \rightarrow e^+e^-$  and  $e^+e^- \rightarrow \mu^+\mu^-$  events is most significant. The set of selection variables has been carefully chosen in order to avoid as much as possible introduction of a selection correlation between the two  $\tau$ 's produced in the  $e^+e^-$  interactions. Selection efficiencies and sample purities of the order of 55% (i.e.  $\sim 88\%$  within the geometrical acceptance region) and 96.5% respectively have been reached. Background contamination and systematic effects have been carefully studied. A good agreement between simulation and real data has been observed: the ratio of the number of selected events in both samples has been estimated to:

$$1.002 \pm 0.004 (stat) \pm 0.003 (syst).$$

The 1-prong  $\tau$  decay candidates have been isolated after a precise analysis of the influence of photon conversions on the reconstructed charged particle multiplicity. They have been selected with an efficiency and purity of the order of 99% and 96% respectively. The evaluated inclusive 1-prong  $\tau$  decay branching ratio obtained was:

$$B_1 = 85.30\% \pm 0.10\%(stat) \pm 0.09\%(syst).$$

This is in good agreement with the world-average measurement, confirming the validity of the present selection procedure.

# Chapter 5

## Identification of the exclusive one-prong $\tau$ decay modes

The  $\tau$  polarisation  $\mathcal{P}_\tau$  is measured by analysing the energy spectra of the  $\tau$  decay products (see section 2.3.2). This implies that the  $\tau$  decay final state has to be identified in order to distinguish on one side the leptonic from the semileptonic decay modes, and on the other side, to gain a maximum sensitivity amongst the hadronic states. In the present analysis, we have limited ourself the 1-prong  $\tau$  decay modes<sup>1</sup> which were selected as described in the previous chapter. We present here a procedure for the classification of the 1-prong  $\tau$  decay channels into the following exclusive channels:

- Class 1:  $\tau \rightarrow e\nu_e\nu_\tau$ ,
- Class 2:  $\tau \rightarrow \mu\nu_\mu\nu_\tau$ ,
- Class 3:  $\tau \rightarrow \pi/K\nu_\tau$ ,
- Class 4:  $\tau \rightarrow \rho\nu_\tau \rightarrow \pi\pi^0\nu_\tau$ ,
- Class 5:  $\tau \rightarrow a_1\nu_\tau \rightarrow \pi\pi^0\pi^0\nu_\tau$ .

We have chosen to use the neural network technique to perform that classification (see section 3.4). The choice of this technique was motivated by the fact that the identification of the hadronic  $\tau$  decay modes (Classes 3, 4 and 5), which is mainly a problem of  $\pi^0$  identification, was hindered by the experimental difficulties of the correct reconstruction of the electromagnetic showers in the DELPHI detector, leading to a poor selection efficiency of these final states when using classical identification methods based on the application of cuts on kinematical variables. The neural network technique was then also applied for the identification of the leptonic decays (Classes 1 and 2), although it is not more efficient than classical analysis in that domain. In this way, a homogeneous analysis was performed, allowing to separate the five classes at the same time and to determine a unique complete migration matrix.

In section 5.1 the set of discriminant variables, used as inputs for the neural networks, is presented. After the training of the neural networks, the classification efficiencies (migration matrices) were estimated on the basis of simulated data (section 5.3). For that reason, it was carefully checked that the simulated distributions of the relevant variables were in good agreement with the experimental distributions: test-samples of events were selected for that purpose (section 5.2). The performances of the trained neural networks are given in section 5.3 and compared with classical selection methods.

---

<sup>1</sup>The 1-prong  $\tau$  decay modes correspond to the  $\tau$  decay channels producing only one primary charged particle in the final state, i.e. after the decay of the possible intermediate resonance such as the  $\rho$  or the  $a_1$  mesons. Note that the  $a_1$  decays with equal probability into a 1-prong final state ( $\pi^\pm\pi^0\pi^0$ ) and a 3-prong final state ( $\pi^\pm\pi^\pm\pi^\mp$ ).



## 5.1 The set of discriminant variables

To perform the classification proposed above, a set of the discriminant variables, to be fed as inputs into the neural networks, was chosen on the basis of the nature of the final state charged particle to be identified (electron, muon or pion<sup>2</sup>). Also the characteristics of the  $\rho$  and  $a_1$  resonances were used to differentiate the three hadronic decay modes (classes 3, 4 and 5).

### 5.1.1 Electron identification

The main particularity of the electron is that it loses the whole of its energy in the electromagnetic calorimeter since it is a light charged lepton, presenting a high bremsstrahlung probability. The electromagnetic energy associated to an electron should then be equal, within the measurement errors, to its momentum. This is not the case for the heavier muon and pion or kaon, which lose a very small fraction of their energy in the HPC.

The variable relevant to this point is the pull of  $E_{em}/p$ :

$$\Pi_{E_{em}/p} = \frac{\frac{E_{em}}{p} - 1}{\sigma(E_{em}/p)}, \quad (5.1)$$

where  $E_{em}$  and  $p$  are respectively the associated electromagnetic energy and the momentum of the particle, and  $\sigma(E_{em}/p)$  is the experimental error on the measurement of  $E_{em}/p$ .

Figures 5.1, a) to f) show the distributions of  $E_{em}/p$  and of  $\Pi_{E_{em}/p}$  for simulated  $\tau$  decays through respectively the electron (e), the muon ( $\mu$ ) and the hadronic ( $\pi/K n\pi^0$ ,  $n \geq 0$ ) channels<sup>3</sup>.

Two other variables are introduced in order to deal with the following two ambiguous cases where a large amount of electromagnetic energy can be associated to the track of a particle which is not an electron:

- Case A: The electromagnetic shower of a  $\pi^0$  produced by a secondary hadronic interaction of a charged hadron with the detector material (the HPC lead for example), can sometimes be associated to the track of the hadron.
- Case B: The electromagnetic shower of a  $\pi^0$  produced by the  $\tau$  decay through the  $\tau \rightarrow hn\pi^0\nu_\tau$  channel ( $n > 0$ ), can sometimes be associated to the track of the hadron  $h$ .

In case A, it is observed that the associated electromagnetic shower is mostly developed in the deepest layers of the HPC (i.e. at larger radii) while showers generated by electrons start within the first HPC layer. As can be seen on figure 5.2, a), the following variable,  $A_{em}$ , discriminates efficiently between electrons and pions:

$$A_{em} = \frac{[(\sin^2 \theta - \cos^2 \theta) \cdot \sum_{l=1}^4 E_{em}^l] - [\sum_{l=5}^9 E_{em}^l]}{\sum_{l=1}^9 E_{em}^l}, \quad (5.2)$$

where  $E_{em}^l$  is the electromagnetic energy deposited in layer  $l$  of the HPC, and  $\theta$  is the polar angle of the particle track. The  $\theta$  correction in the definition of  $A_{em}$  takes into account the angular dependence of the energy deposition.

<sup>2</sup>The kaons are treated in the same way as the pions. Despite their different masses, the same variables can be used for their classification, leading to similar efficiencies.

<sup>3</sup>The distribution of  $E_{em}/p$  is expected to be centred on 1 for electrons. However a slight shift towards smaller values is observed, probably due to the different treatments which were applied by the ELEPHANT package to the HPC energy and the momentum of the electron candidates, in addition to the recalibration of the HPC energy still needed, presented in section 4.2.1. No attempt was made to correct for that shift, since the same behaviour is observed for the experimental data, and since the variable is anyway normalised between 0 and 1 for the neural network analysis (see section 5.3).

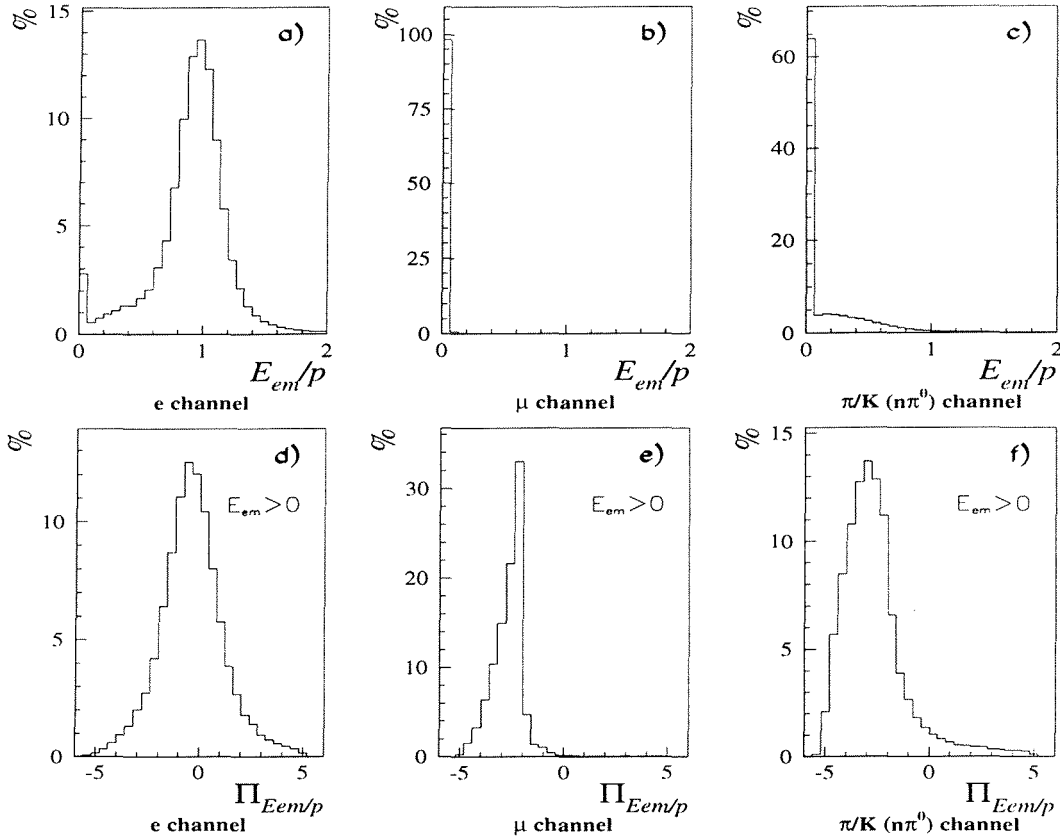


Figure 5.1: Simulated distributions of  $E_{em}/p$  and  $\Pi_{E_{em}/p}$  for a) and d) electrons, b) and e) muons, c) and f) hadrons ( $\pi$  or  $K$ ) produced in  $\tau$  decays. Only particles with  $E_{em} > 0$  enter the histograms in d), e) and f).

In case B, the electromagnetic shower associated to the track of the hadron is a superposition of the showers generated by the photons coming from  $\pi^0$ 's which are  $\tau$  decay products, – the shower profile is then similar to the one of an electron –, and from  $\pi^0$ 's which are produced in a secondary hadronic interaction – the shower profile is then the one of case A. Figure 5.2, b) and c) give the distributions of  $A_{em}$  and of  $\Pi_{E_{em}/p}$  respectively for electrons, and for pions produced by the  $\rho$  or  $a_1$  resonance when no isolated neutral particle was detected in addition to the charged pion. The variable  $A_{em}$  is not efficient in this case.

The measure of the energy loss  $dE/dX$  provided by the TPC gives an information independent of the electromagnetic energy measurement, which allows also a good separation between electrons and hadrons (produced with or without  $\pi^0$ 's). The pull with respect to the electron mass hypothesis is used (see figure 5.2, d) ):

$$\Pi_{dE/dX} = \frac{dE/dX^{meas} - dE/dX^e}{\sigma(dE/dX^{meas})},$$

where  $dE/dX^{meas}$  is the measured energy loss,  $dE/dX^e$  is the expected energy loss for an electron, and  $\sigma(dE/dX^{meas})$  is the experimental error on the measurement of  $dE/dX^{meas}$ . The value of  $dE/dX^e$  is quasi independent of the momentum of the particle because, above 0.5 GeV/c, the electron is on the Fermi plateau of the energy loss curve.

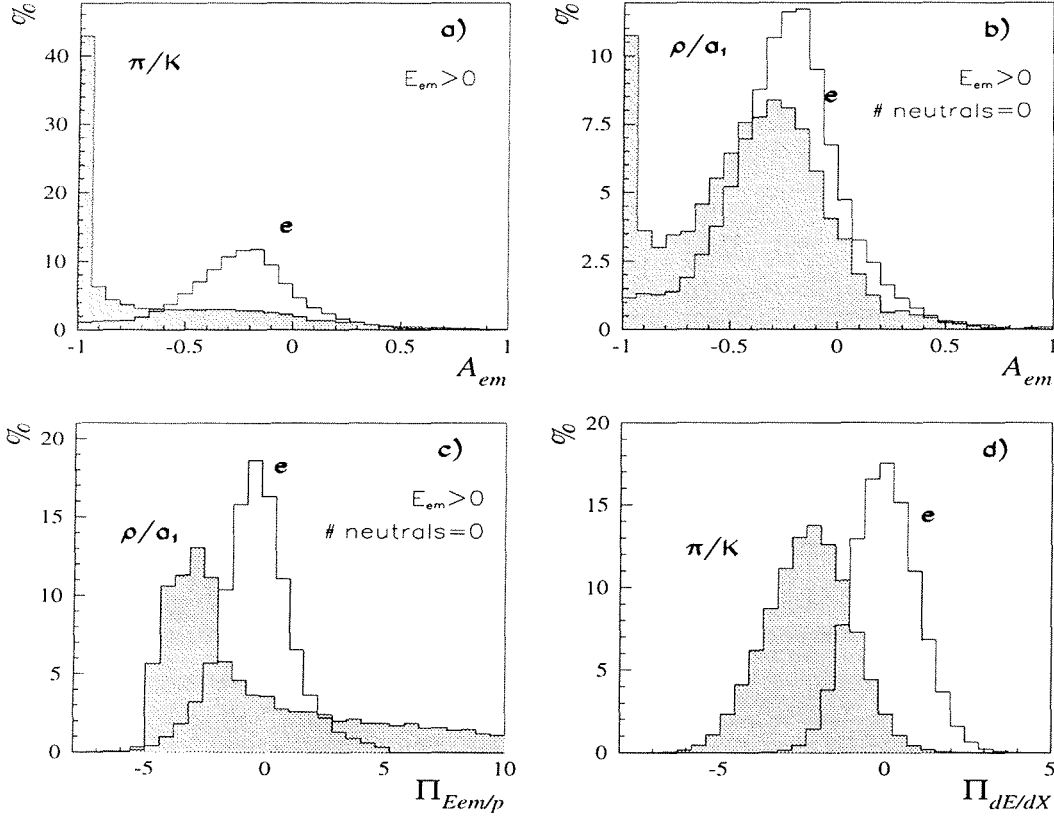


Figure 5.2: Simulated distributions of a) and b)  $A_{em}$ , c)  $\Pi_{E_{em}/p}$  and d)  $\Pi_{dE/dX}$ . On the four plots, the white histograms represent electrons produced in  $\tau$  decays. The grey histograms are on a)  $\pi$ 's or  $K$ 's with  $E_{em} > 0$ , on b) and on c)  $\pi$ 's from the  $\rho$  or  $a_1$  resonances with  $E_{em} > 0$  and no detected neutral particle in the same hemisphere, on d) any  $\pi$ 's or  $K$ 's. All histograms are normalised to unity.

Particles emitted within  $2^\circ$  of the  $90^\circ$   $\theta$  dead zone of the TPC, caused by the presence of the cathode plane (see section 3.2), were excluded from the analysis because their track parameters (track curvature,  $dE/dX$ ) could not be optimally determined. Also particles traversing other regions of the TPC where  $dE/dX$  could not be correctly estimated, were rejected. This occurred mostly in the boundary regions of the TPC sectors where less than 30 ionisation measurements were possible. The absence of the  $dE/dX$  information does not only decrease the identification efficiency, but it implies also poorer precision on the particle momentum used for the polarisation measurement.

## 5.1.2 Muon identification

In order to exploit the results on the muon identification performed by the dedicated algorithm of the MUFLAG package (see section 3.2.3), a cut at 3 GeV on the energy of the charged particles was applied<sup>4</sup>. Charged particles are flagged by the MUFLAG algorithm as “very loose”, “loose”, “standard” or “tight” muons. This information was fed into an input variable called  $\mu$ -flag, by digitalisation of the MUFLAG decision. It was 0 for the particles to which no MUC signal was associated. This is most often the case for pions because they are stopped before or inside the HCAL and cannot reach the muon detectors. Figures 5.3, a), b) and c) show the simulated distributions of the variable  $\mu$ -flag for electrons, muons and hadrons of at least 3 GeV.

In the regions not covered by the muon detectors ( $\theta \sim 50^\circ$  and  $\theta \sim 130^\circ$ ), the separation between muons and pions had to rely on the HCAL response (see figure 5.3, d) ). Indeed, the muons lose a constant amount of energy by ionisation in the iron and in the gas in the various active layers of the HCAL. On the contrary, the hadrons which reach the HCAL (they can be stopped before, at the level of the HPC or in the RICH) most often lose the whole of their energy in the first two layers by generating hadronic showers. Consequently, the following two variables were introduced for the muon-pion separation when no MUC information was available:

- $E_{hlay}$ , which is the averaged energy deposition in the HCAL layers:

$$E_{hlay} = \frac{E_{HCAL} \cdot \sin^2 \theta}{N_{layer}}, \quad (5.3)$$

where  $E_{HCAL}$  is the total hadronic energy associated to the track of the particle,  $N_{layer}$  is the number of layers where some energy was deposited, and the factor  $\sin^2 \theta$  takes into account the angular dependence of the energy loss,

- $A_{had}$ , which is the fraction of energy deposited in the third and fourth layers:

$$A_{had} = \frac{E_{HCAL}^3 + E_{HCAL}^4}{E_{HCAL}}, \quad (5.4)$$

where  $E_{HCAL}^3$  and  $E_{HCAL}^4$  are the energy deposits in respectively the third and fourth layers.

The spectrum of the variable  $E_{hlay}$  is shown for muons and pions on figure 5.3, e) and f), respectively for tracks without and with a positive muon identification ( $\mu$ -flag = 0 or  $\mu$ -flag > 0), and figure 5.3, g) gives the distributions of  $A_{had}$  for muons and pions when they were not identified as muons with  $0 \text{ GeV} < E_{hlay} < 2 \text{ GeV}$ , where the variable  $E_{hlay}$  is not discriminant.

---

<sup>4</sup>Indeed, muons having an energy lower than 3 GeV are stopped before reaching the muon chambers. They can then be hardly distinguished from pions.

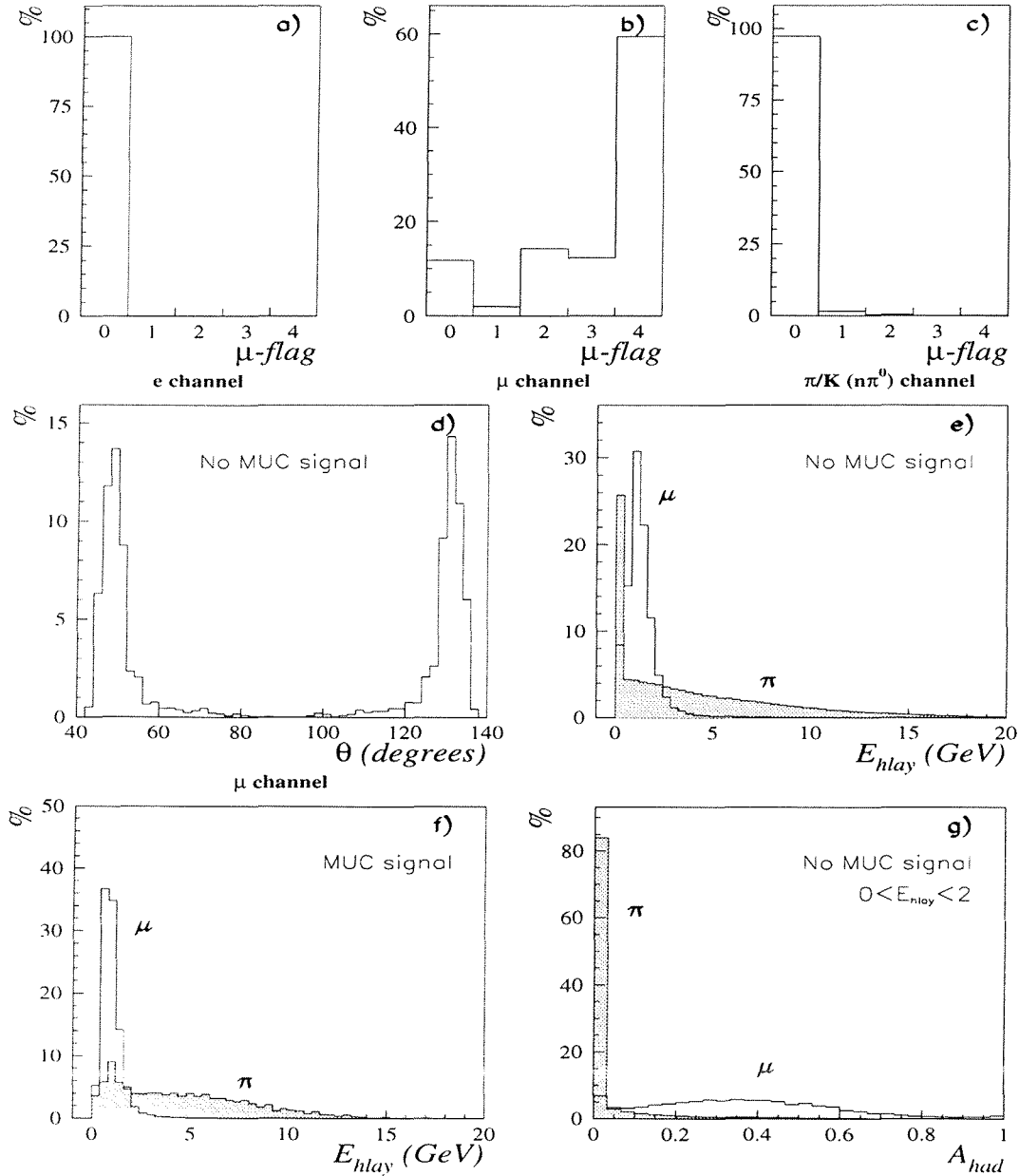


Figure 5.3: Simulated distributions of  $\mu$ -flag for respectively a) electrons, b) muons and c) pions, produced in  $\tau$  decays. The values 1, 2, 3 and 4 were attributed to  $\mu$ -flag when the particle was flagged by the MUFLAG algorithm as respectively a “very loose”, “loose”, “standard” or “tight” muon. d) Track polar angle for muons with no associated MUC signals, (i.e. mainly the  $\theta$  range not covered by the muon detectors in the barrel region of DELPHI), e) and f)  $E_{hlay}$  for muons (white) and pions (grey) respectively without and with associated MUC signals, g)  $A_{had}$  for muons (white) and pions (grey) when the variables  $\mu$ -flag and  $E_{hlay}$  are not discriminant (i.e. when there was no MUC signal associated to the track, together with  $0 \text{ GeV} < E_{hlay} < 2 \text{ GeV}$ .)

### 5.1.3 Hadron identification

The hadronic final states of the  $\tau$  decays of the classes 3, 4 and 5 described in the introduction, had also to be identified. The problem was essentially the determination of the number of  $\pi^0$ 's originating from the  $\tau$  decay, and hence the number of photons:

$$\begin{aligned} \text{Class 3: } \tau &\rightarrow \pi/K\nu_\tau && : 0 \text{ photon,} \\ \text{Class 4: } \tau &\rightarrow \rho\nu_\tau \rightarrow \pi\pi^0\nu_\tau \quad \rightarrow \pi\gamma\gamma\nu_\tau && : 2 \text{ photons,} \\ \text{Class 5: } \tau &\rightarrow a_1\nu_\tau \rightarrow \pi\pi^0\pi^0\nu_\tau \quad \rightarrow \pi\gamma\gamma\gamma\nu_\tau && : 4 \text{ photons.} \end{aligned}$$

This determination is difficult in a detector like DELPHI for the following reasons:

- the presence of background photons emitted by bremsstrahlung and by secondary hadronic interactions,
- the photon conversions before the HPC,
- the superposition of electromagnetic showers one with another or with the shower generated by the charged particle,
- the loss of photons (or of electrons from conversions) in the dead zones of the detector or because of energy threshold effects.

A part of the background photons could be rejected using the following criteria to define "good" photons:

1. The profile of the electromagnetic shower had to be recognised by the ELEPHANT package as being compatible with the one of a photon shower (see section 3.2.2). Photons converted in front of the TPC and identified by ELEPHANT were also accepted, as well as the "merged"  $\pi^0$ 's (where the two photons produced overlapping showers). Showers identified by ELEPHANT as being radiated photons were not counted as "good" photons and, as explained in section 3.2.2, they were taken into account in the re-estimation of the momentum of the radiating particle. Electromagnetic showers of more than 6 GeV which did not satisfy these criteria but were not identified as radiated photons, were also counted as "good" photons (see reference [40]).
2. In order to reject photons produced in secondary hadronic interactions, it was required, according to reference [40], that:
  - the energy of the shower was larger than 0.5 GeV,
  - the angle between the directions at the origin of the track of the charged particle and of the neutral particle was larger than  $1^\circ$  and smaller than  $10^\circ$ .
  - the squared angle between the neutral shower and the track extrapolation, multiplied by the energy of the shower to take into account the larger dispersion of low energy particles, had to be smaller than  $10 \text{ degree}^2 \text{ GeV}$ .

The number of final state photons,  $N_\gamma$ , was used as input variable. It was defined as follows:

$$\begin{aligned} N_\gamma &= \text{Number of "good" photons} \\ &+ 2 \times \text{Number of identified } \pi^0\text{'s} \\ &+ \text{Number of non-identified converted photons}^5 \end{aligned}$$

Figures 5.4, a) to e) give the simulated distributions of  $N_\gamma$  respectively for the electron, muon, pion,  $\rho$  and  $a_1$  decay channels of the  $\tau$ . It is clear that this variable is not sufficient for distinguishing  $\rho$ 's from  $a_1$ 's: in more than 10% of the  $\rho$  productions, no neutral particle was reconstructed and nearly half of the  $a_1$  final states were presenting less than three photon candidates.

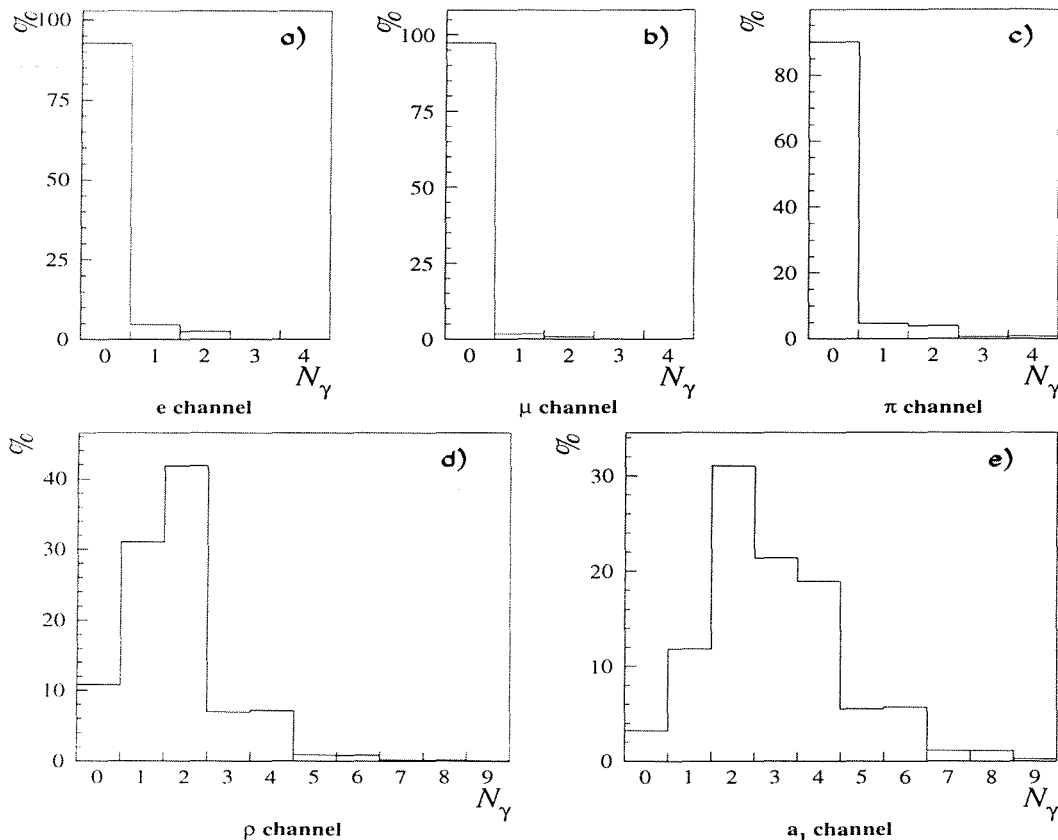


Figure 5.4: Simulated distributions of the number of final state photons ( $N_\gamma$ ) for the a) electron, b) muon, c) pion, d)  $\rho$ , e)  $a_1$  decay channels of the  $\tau$ .

When no neutral was found ( $N_\gamma = 0$ ), the variables  $A_{em}$  and  $\Pi_{E_{em}/p}$  gave some indications in the case where the electromagnetic energy of one final state photon was associated to the track of the charged particles (see figures 5.2, a), b) and c) ). The separation between the  $\pi$  channel and the  $\rho$  or  $a_1$  channels was then possible.

When at least one neutral was reconstructed ( $N_\gamma > 0$ ), the invariant mass,  $M_{inv}$ , of the final state made of the charged and of the neutral electromagnetic particles, could inform about the nature of the resonance. However, there is a large overlapping of the  $M_{inv}$  distributions because of the natural widths of the  $\rho$  and of the  $a_1$  resonances [2]:  $m_\rho = 768.5 \pm 0.6 \text{ MeV}/c^2$ ,  $\Gamma_\rho = 150.7 \pm 1.3 \text{ MeV}/c^2$  and  $m_{a_1} = 1230 \pm 40 \text{ MeV}/c^2$ ,  $\Gamma_{a_1} = 185 \pm 20 \text{ MeV}/c^2$ . The widths

<sup>5</sup>After our selection of the inclusive 1-prong  $\tau$  decays, the charged particles which had less than two VD signals associated to their track, were assumed to be electrons originating from photon conversions which were not identified by the ELEPHANT algorithm. If only one (three) such particle(s) was found, the contribution to  $N_\gamma$  was +1 (+2): the second electron of the  $e^+e^-$  pair was assumed to have been lost.

of the reconstructed distributions are even larger due to the detector resolution effects (see figure 5.5, a) ).

When more than one neutral was reconstructed ( $N_\gamma > 1$ ), the invariant mass,  $M_{neutral}$ , of the neutral electromagnetic particles, could indicate whether the neutrals were issued from a  $\pi^0$  ( $M_{neutral} \sim m_{\pi^0} = 135 \text{ MeV}/c^2$ ) for the  $\rho$  channel (see figure 5.5, b) ).

In addition to these three variables, the momentum of the charged particle,  $p$ , and the total neutral energy,  $E_{neutral}$ , were used as input variables. The variable  $E_{neutral}$  was defined as the sum of the energies of the electromagnetic showers of the “good” photons and the momentum of the electrons from non-identified conversions. Since those two variables ( $p$  and  $E_{neutral}$ ) are sensitive to the  $\tau$  polarisation, we took care to train the neural network with a non-polarised sample of  $\tau$  decays ( $\mathcal{P}_\tau = 0$ ).

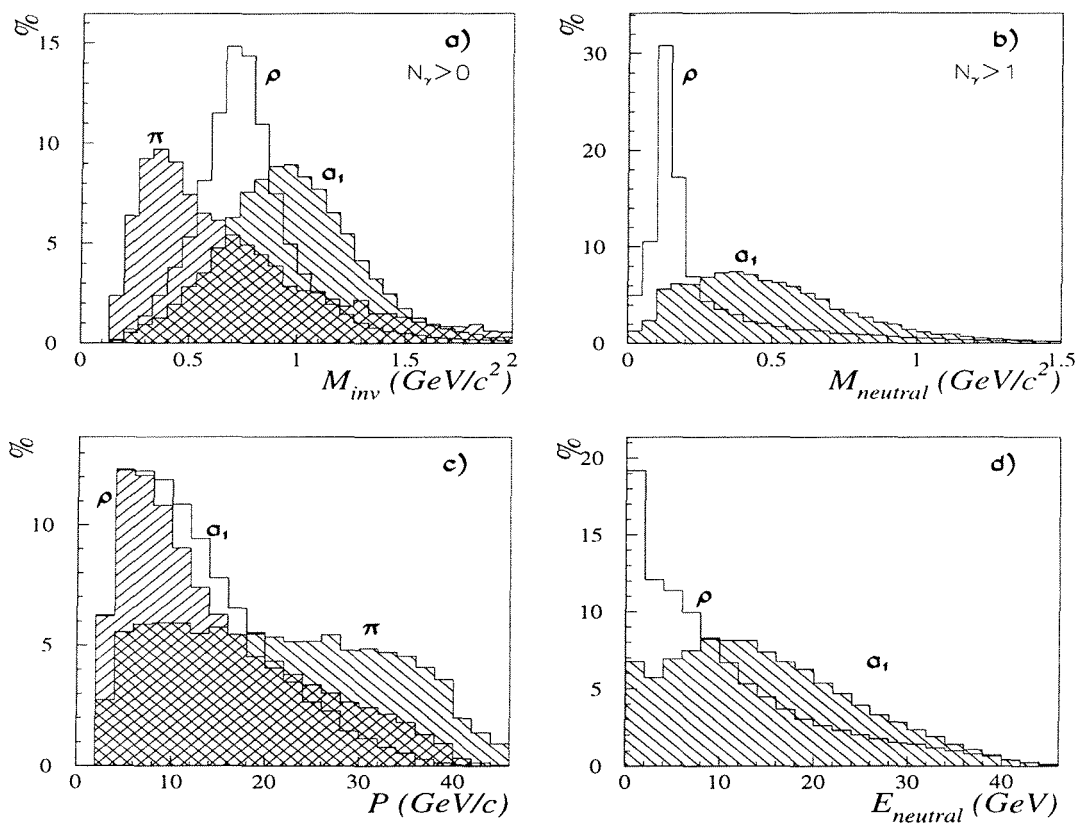


Figure 5.5: Simulated distributions of a) the invariant mass ( $M_{inv}$ ) of the neutral and charged decay products when  $N_\gamma > 0$ , b) the invariant mass ( $M_{neutral}$ ) of the reconstructed neutral decay products when  $N_\gamma > 1$ , c) the momentum of the charged particle ( $p$ ), d) the total reconstructed neutral energy ( $E_{neutral}$ ), in  $\tau$  decays through the  $\pi$ ,  $\rho$  and  $a_1$  channels as indicated on the figures. For the figures c) and d)  $\mathcal{P}_\tau$  is 0.



### 5.1.4 Summary

We have selected a set of 11 physical quantities which had a good discriminant power for the present classification problem.

They are:

- the momentum  $p$  of the charged particle,
- for the  $e$ - $\pi$  separation:  $\Pi_{E_{em}/p}$ ,  $A_{em}$ ,  $\Pi_{dE/dX}$ ,
- for the  $\mu$ - $\pi$  separation:  $\mu$ -flag,  $E_{hlay}$ ,  $A_{had}$ ,
- for the  $\pi$ - $\rho$ - $a_1$  separation:  $N_\gamma$ ,  $M_{inv}$ ,  $M_{neutral}$ ,  $E_{neutral}$ .

For a better identification of the charged particles, we have limited our analysis to the decays where the charged particle was satisfying:

- $p > 3 \text{ GeV}/c$ ,
- $\theta \in [43^\circ, 88^\circ] \cup [92^\circ, 137^\circ]$ ,
- $dE/dX$  measured.

As seen in table 5.1, this reduced the statistics of the pre-selected 1-*prong* samples by a factor of the order of 20%. The factors depend on the  $\tau$  polarisation because of the cut on  $p$ . They are given here for a polarisation of 0.14. The momentum cut affects less the kaons than the pions since the momentum spectrum of the kaons is displaced towards higher momenta because of the important Lorentz boosts of the larger mass of the kaon. The larger reduction of statistics for the non-1-*prong*  $\tau$  decays with respects to the 1-*prong* modes, is due to the requirement on  $dE/dX$ : non-1-*prong*  $\tau$  decays are selected as 1-*prong* decays when tracks are overlapping along the total track length. In that case, no ionisation signal is used for the  $dE/dX$  estimation (see section 3.2).

(%)	1993	1994	1995
$\tau \rightarrow e\nu_e\nu_\tau$	$79.4 \pm 0.1$	$78.5 \pm 0.1$	$79.4 \pm 0.1$
$\tau \rightarrow \mu\nu_\mu\nu_\tau$	$82.7 \pm 0.1$	$82.4 \pm 0.1$	$82.6 \pm 0.1$
$\tau \rightarrow \pi\nu_\tau$	$84.5 \pm 0.1$	$84.1 \pm 0.1$	$84.2 \pm 0.1$
$\tau \rightarrow K\nu_\tau$	$91.3 \pm 0.4$	$90.4 \pm 0.3$	$90.1 \pm 0.4$
$\tau \rightarrow \rho\nu_\tau$	$78.2 \pm 0.1$	$77.7 \pm 0.1$	$78.4 \pm 0.1$
$\tau \rightarrow a_1\nu_\tau$	$74.7 \pm 0.2$	$74.0 \pm 0.1$	$75.0 \pm 0.2$
$\tau \rightarrow$ 1- <i>prong</i>	$79.80 \pm 0.05$	$79.21 \pm 0.04$	$79.81 \pm 0.04$
$\tau \rightarrow$ > 1- <i>prong</i>	$40.4 \pm 0.3$	$40.4 \pm 0.3$	$41.4 \pm 0.4$

Table 5.1: *Effects on the statistics of the cuts on the momentum ( $p > 3 \text{ GeV}/c$ ), on  $\theta$  ( $\theta \in [43^\circ, 88^\circ] \cup [92^\circ, 137^\circ]$ ) and on the determination of  $dE/dX$ , for the 93, 94 and 95 simulated  $\tau$  decays selected as 1-*prong* decays.*

This set of variables is of course not unique. We tried to find a minimal number of inputs allowing to reach satisfactory performances for the classification, by presenting to the network variables which were combinations of more basic quantities: for example, we used  $A_{em}$  instead of the  $E_{em}^l$  for each HPC layer separately. In addition, we tried to find input variables which

were independent one from another as far as possible, i.e. information provided by different submodules of detection (TPC, HPC, HCAL, MUC), and which were if possible independent of the detector calibration (ratio of HPC layer energies, ratio of HCAL layer energies), in order to minimise the systematic effect in case where the simulation would not reproduce correctly the experimental distributions.

## 5.2 Test-samples

Since the performances (classification efficiencies) of the neural network, after training, are estimated on the basis of simulated events, it had to be verified that the simulated distributions of the input variables were correctly representing the experimental distributions. For this comparison, and for an eventual re-calibration (section 5.2.1), test-samples of real  $\tau$  decays into electrons ( $\tau \rightarrow e\nu_e\nu_\tau$ ), muons ( $\tau \rightarrow \mu\nu_\mu\nu_\tau$ ), and pions or kaons ( $\tau \rightarrow \pi/Kn\pi^0\nu_\tau, n \geq 0$ ) were selected using severe criteria in order to obtain relatively pure samples. As far as possible, these criteria were chosen to be independent of the variable to be studied. After that, the selection criteria were relaxed in order to check that the applied corrections were still valid for samples of events covering larger ranges of the variables, and with larger contamination levels (section 5.2.2).

### 5.2.1 Re-calibration of some variables

Two variables were found to be incorrectly simulated (see figures 5.6 a) and 5.8 d) ):  $N_{layer}$  (which is used in the estimation of the variable  $E_{hlay}$ , and is also reflected in the distributions of the variables  $A_{had}$  and  $E_{HCAL}^i$ ), due to a bad simulation of the “punch-through” of pions, and  $E_{em}^{5-9}$  (which is used in the estimation of the variable  $A_{em}$ ). We have tempted to fix them by the procedures described below.

#### Correction to $N_{layer}$

A clean sample of hadrons was selected using the cuts below:

- the track of the charged particle had to cross a region of the detector covered by both the HPC and the MUB modules:

$$\theta \in [52^\circ, 66^\circ] \cup [68^\circ, 88^\circ] \cup [92^\circ, 112^\circ] \cup [114^\circ, 128^\circ], \text{ and}$$

$$\phi|_{15^\circ} \notin [6.5^\circ, 8.5^\circ];$$

- the charged particle of both hemispheres were not identified as muon candidates by MUFLAG, for the rejection of dimuons events and of  $\tau \rightarrow \mu\nu_\mu\nu_\tau$  decays;
- for the rejection of electrons, the electromagnetic energy associated to the charged particle had to be smaller than half its momentum, and smaller than 0.5 GeV in the first four layers of the HPC:

$$E_{em}/p < 0.5 \text{ and } E_{em}^1 + E_{em}^2 + E_{em}^3 + E_{em}^4 < 0.5 \text{ GeV.}$$

The selection efficiency was of the order of 56.5% inside the geometrical acceptance, and the purities of the samples were found to be  $(96.23 \pm 0.06)\%$ ,  $(96.52 \pm 0.04)\%$ , and  $(96.42 \pm 0.05)\%$  respectively for the 93, 94 and 95 simulations.

The number of HCAL layers where some energy had been deposited by the selected particles ( $N_{layer}$ ) was found to be under-evaluated in the simulation for the three years 93, 94 and 95.

Since the simulated distribution of the total HCAL energy ( $E_{HCAL}$ ) was however in good agreement with the experimental distribution, the observed discrepancy at the level of  $N_{layer}$  was attributed to an incorrect simulation of the penetration depth of the pions into the HCAL material (what is called the punch-through of the pions). After checking that there was no significant dependence on  $p$ ,  $\theta$  or  $\phi$ , the disagreement between real and simulated data was corrected by giving to the first layer where the energy was zero ( $E_{HCAL}^l = 0$ ) an arbitrary value of energy equal to a random fraction of  $0.5 \cdot E_{HCAL}^{l-1}$ . This was done for simulated  $\tau \rightarrow \pi/Kn\pi^0\nu_\tau$  ( $n \geq 0$ ) events taken at random, in a proportion estimated to be  $23\% \pm 1\%$  for the 93 and 94 data, and  $25\% \pm 1\%$  for the 95 data. The corrected distributions are shown on figure 5.7. Since also a slight discrepancy was observed for  $N_{layer}=0$ , an additional correction was applied: in 2% of the simulated  $\tau \rightarrow \pi/Kn\pi^0$  events,  $E_{HCAL}$  was put to zero.

### Correction to $A_{em}$

A clean sample of electrons was selected using the cuts below:

- the track of the charged particle had to cross a region of the detector covered by both the HPC and the MUB modules:

$$\theta \in [52^\circ, 66^\circ] \cup [68^\circ, 88^\circ] \cup [92^\circ, 112^\circ] \cup [114^\circ, 128^\circ], \text{ and}$$

$$\phi|_{15^\circ} \notin [6.5^\circ, 8.5^\circ]:$$

- for the rejection of  $\tau \rightarrow \pi/Kn\pi^0\nu_\tau$  decays ( $n \geq 0$ ):

there had to be a non-zero electromagnetic energy associated to the charged particle and no detected photon:

$$E_{em} > 0 \text{ GeV and } N_\gamma = 0;$$

the ionisation energy loss of the particle had to be compatible with the one of an electron:

$$\Pi_{dE/dX} > -1;$$

and there had to be no energy associated to the particle in the last three layers of the HCAL:

$$E_{HCAL}^2 + E_{HCAL}^3 + E_{HCAL}^4 = 0 \text{ GeV};$$

- the particle was not identified as a muon candidate by MUFLAG, for the rejection of  $\tau \rightarrow \mu\nu_\mu\nu_\tau$  decays.

The selection efficiency of the electron test-sample was of the order of 69% inside the geometrical acceptance, and the purities of the samples were found to be  $(96.79 \pm 0.08)\%$ ,  $(95.83 \pm 0.07)\%$ , and  $(96.17 \pm 0.08)\%$  respectively for the 93, 94 and 95 simulations.

The simulated distributions of  $E_{em}^{5-9} = \sum_{l=5}^9 E_{em}^l$  was not reproducing the experimental distributions, while the agreement was satisfactory for  $E_{em}^{1-4} = \sum_{l=1}^4 E_{em}^l$  (see figure 5.8 for the 93 data). Similar discrepancies were observed for the 93, 94 and 95 data with no clear  $\theta$ ,  $\phi$  or  $p$  dependence of these differences. The reason for these disagreements comes most probably from the fact that all the HPC energy calibrations performed by ELEPHANT are focused on the total energy  $E_{em}$  and not on the layer energies  $E_{em}^l$  individually. To fix that problem, we have corrected the simulated distributions of  $E_{em}^{5-9}$  in a way to reproduce its experimental  $p$  dependence. The result of the correction is shown at the bottom of figure 5.8 but there is still some disagreement. This will be taken into account in the study of the systematic effects.

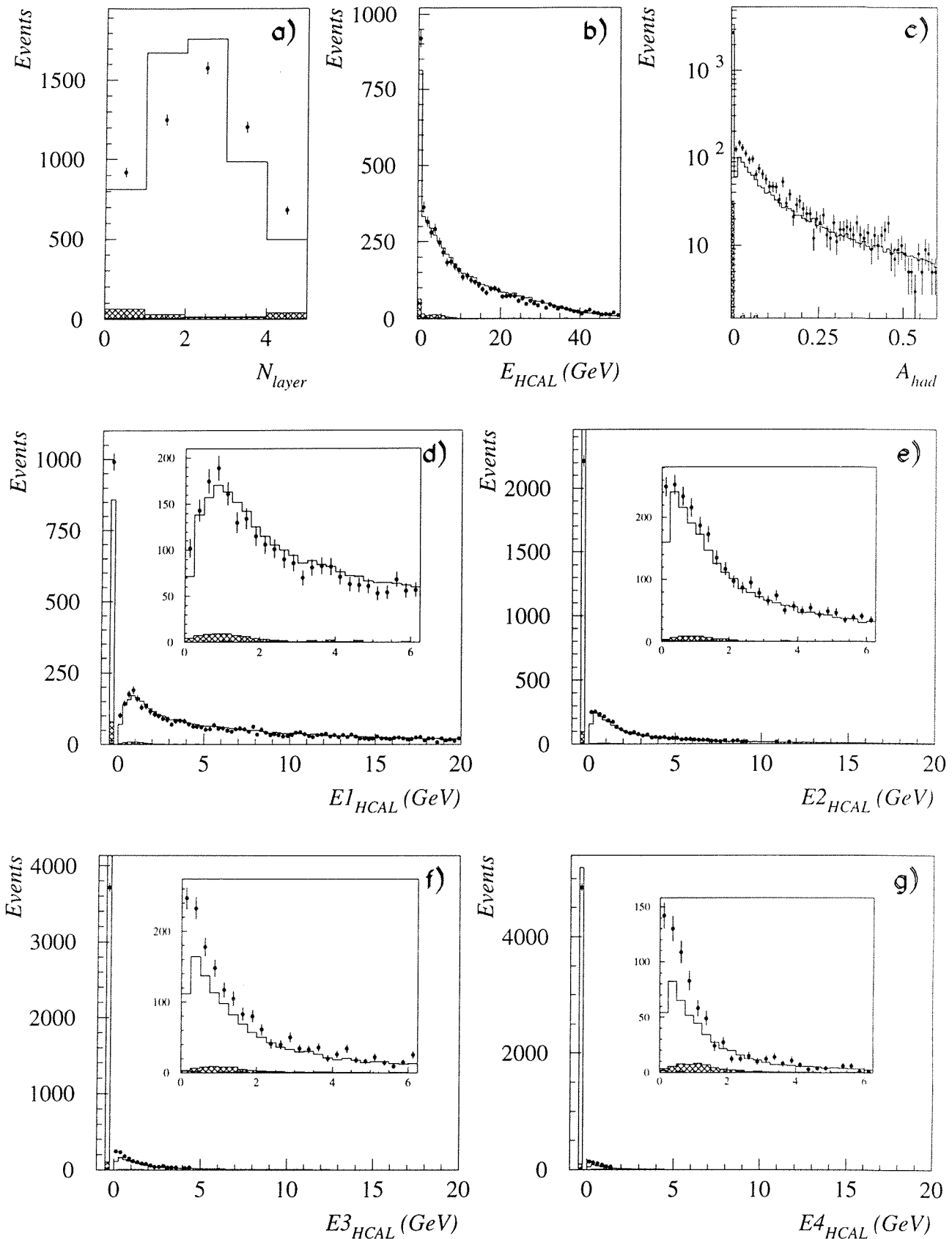


Figure 5.6: Distributions of a)  $N_{layer}$ , b)  $E_{HCAL}$ , c)  $A_{had}$ , d)  $E_{HCAL}^1$ , e)  $E_{HCAL}^2$ , f)  $E_{HCAL}^3$ , g)  $E_{HCAL}^4$ , with a zoom on the range  $E_{HCAL}^1 \in ]0, 6]$  GeV, for real 93 data (points with error bars) and simulation without any correction, normalised to  $\mathcal{L}_{int}$  and the world-average  $\tau$  branching ratios (solid line); the hatched areas represent the  $\tau \rightarrow e\nu_e\nu_\tau$  and  $\tau \rightarrow \mu\nu_\mu\nu_\tau$  contamination to the selected test-sample of  $\tau \rightarrow \pi/Kn\pi^0\nu_\tau$  decays ( $n \geq 0$ ).

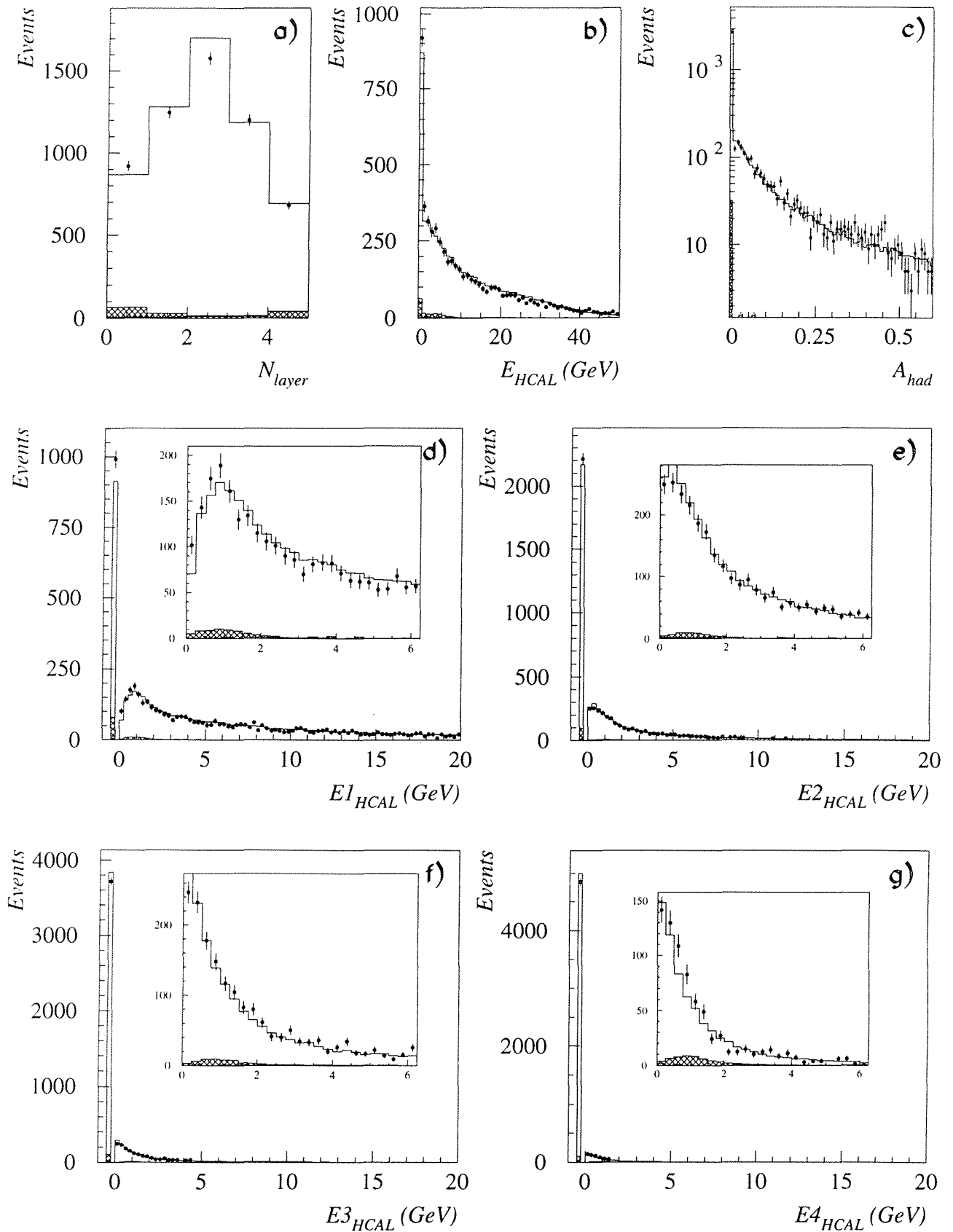


Figure 5.7: Same distributions as on figure 5.6, but a correction for the “punch-through” of  $\pi/K$ 's in the HCAL has been applied to the simulated  $\tau \rightarrow \pi/K n \pi^0 \nu_\tau$  decays ( $n \geq 0$ ) (see text).

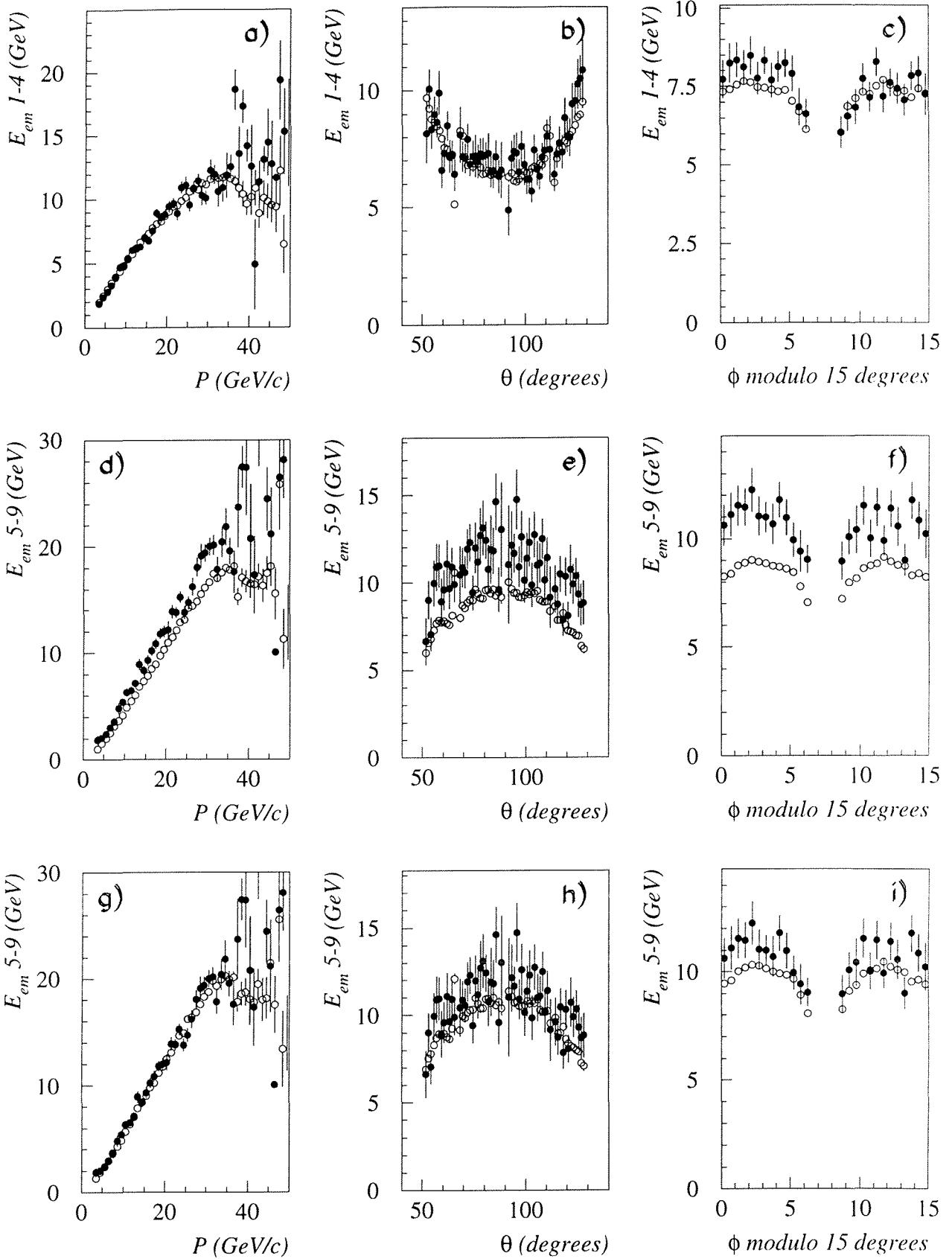


Figure 5.8: a), b) and c): Average  $E_{em}^{1-4}$  versus respectively  $p$ ,  $\theta$ , and  $\phi$ ; d), e) and f): Average  $E_{em}^{5-9}$  versus respectively  $p$ ,  $\theta$ , and  $\phi$ , for selected electrons in the 93 real data sample (closed circles) and in the simulated events (open circles), before any correction. The correction to  $E_{em}^{5-9}$  is applied to the simulated data in figures g), h) and i).

## 5.2.2 Selection criteria for the test-samples

After application of the corrections introduced in the previous section, new test-samples of electrons, muons and hadrons were selected which were covering larger domains of the spectrum of the input variables. No more restriction was applied on  $\theta$  and  $\phi$  except the adopted limitation to  $\theta \in [43^\circ, 88^\circ] \cup [92^\circ, 137^\circ]$ . The following criteria were applied to the pre-selected 1-prong  $\tau$  decay candidates:

- **Criteria for the selection of an electron test-sample:**

1. A non-zero electromagnetic energy was associated to the track of the charged particle:  
 $E_{em} > 0$  GeV;
2. The energy lost by the particle by ionisation of the TPC gas was compatible with the energy loss of an electron:  
 $\Pi_{dE/dX} > -1$ ;
3. No “good photon” having an energy larger than 1 GeV was detected;
4. There was no MUC signal associated to the track of the particle;
5. A maximum energy of 2 GeV was lost by the particle beyond the first HCAL layer:  
 $E_{HCAL}^2 + E_{HCAL}^3 + E_{HCAL}^4 < 2$  GeV.

- **Criteria for the selection of a muon test-sample:**

1. In case where there was no MUC signals associated to the track of the charged particle, some energy had to have been deposited in the last HCAL layer :  
 $E_{HCAL}^4 > 0$  GeV,
2. The average energy lost per layer of the HCAL had to be smaller than 2 GeV:  
 $E_{hlay} < 2$  GeV
3. An energy deposition in the electromagnetic calorimeter of maximum 1 GeV could have been associated to the track of the particle:  
 $E_{em} < 1$  GeV

- **Criteria for the selection of a pion test-sample:**

1. There was no MUC signal associated to the track of the particle;
2. No energy was deposited by the particle in the last HCAL layer:  
 $E_{HCAL}^4 = 0$  GeV
3. The particle could have lost some energy inside the third HCAL layer only when the total amount of HCAL energy associated to its track was larger than 7.5 GeV:  
 $E_{HCAL}^3 = 0$  GeV or  $E_{HCAL} > 7.5$  GeV
4. If the particle had lost some electromagnetic energy, the amount of that energy was not compatible with what an electron of the same momentum would have lost:  
 $\Pi_{E_{em}/p} < -2$ .

The test-samples were selected with the efficiencies and purities given in table 5.2. The large fraction of electrons selected in the pion test-samples ( $\simeq 16\%$ ) corresponds to the particles which enter the dead zones between the HPC modules.

A general good agreement was observed for all the variables for all three years. Their distributions are shown on figures 5.9, 5.10, and 5.11 for the selected test-samples for the 93 data.

Selected as ↓	Selection percentage				Purity (%)
	$\tau$ decay to:				
	e	$\mu$	$hn\pi^0$ ( $h = \pi/K, n \geq 0$ )	> 1-prong	
1993 Simulation					
e	78.6±0.1	0.06±0.01	1.97±0.03	2.6±0.2	93.30±0.08
$\mu$	0.00±0.01	86.5±0.1	1.31±0.02	0.6±0.1	96.29±0.06
$hn\pi^0$	14.3±0.1	1.96±0.04	74.50±0.08	39.3±0.6	91.25±0.06
1994 Simulation					
e	80.68±0.09	0.061±0.005	2.69±0.02	2.4±0.1	91.53±0.07
$\mu$	0.000±0.005	86.44±0.07	1.47±0.02	3.3±0.2	95.77±0.05
$hn\pi^0$	16.0±0.1	1.92±0.03	75.13±0.06	30.8±0.4	91.03±0.04
1995 Simulation					
e	81.1±0.1	0.06±0.01	2.52±0.03	2.2±0.2	92.07 ±0.09
$\mu$	0.00±0.01	86.3±0.1	1.47±0.02	2.8±0.2	95.77 ±0.06
$hn\pi^0$ $hn\pi^0$	17.4±0.1	1.96±0.04	74.98±0.08	31.3±0.6	90.50±0.06

Table 5.2: *Efficiencies and purities of the selection of electron, muon and pion test-samples used for the verification of the input variable distributions.*



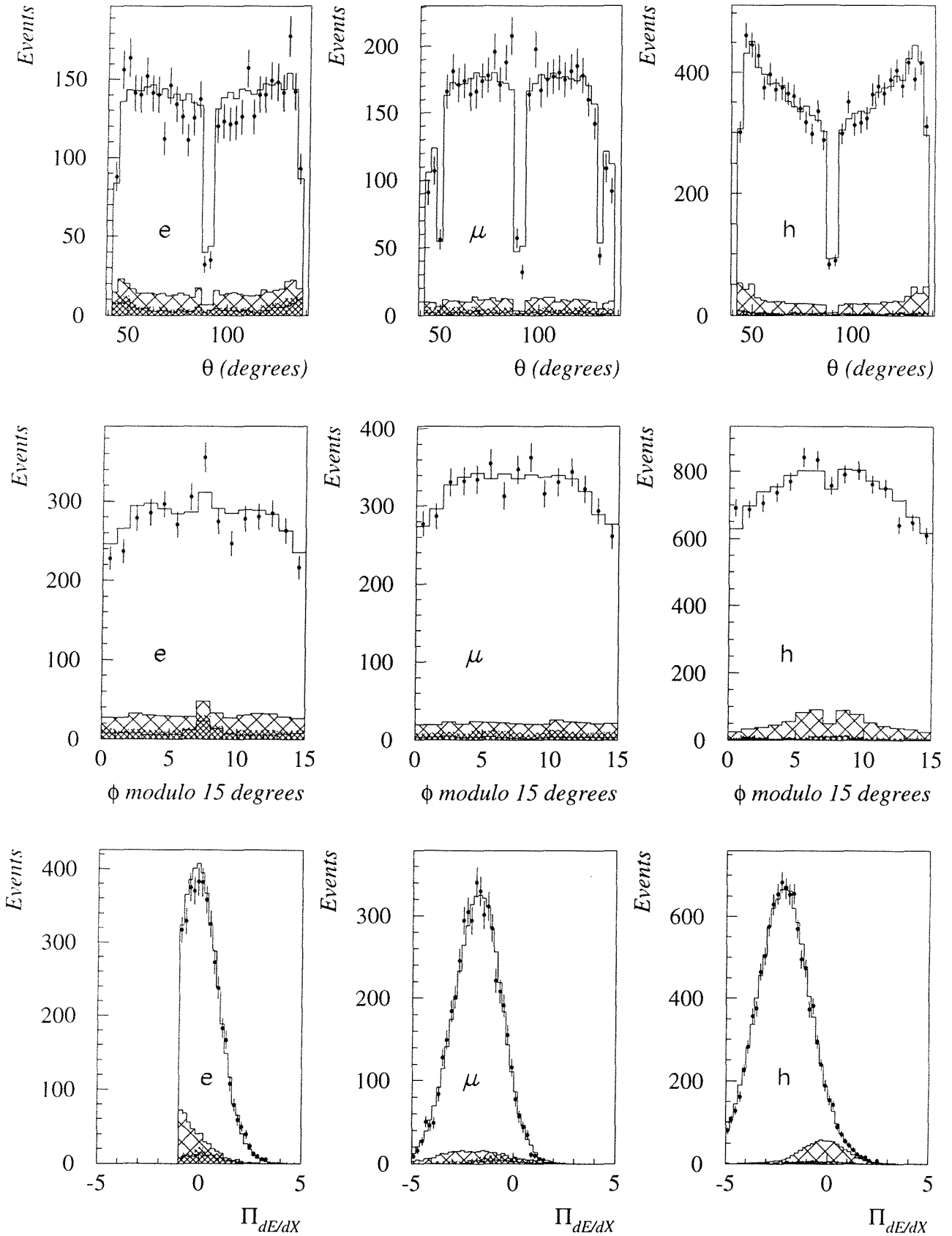


Figure 5.9: Distributions of  $\theta$ ,  $\phi$  and  $\Pi_{dE/dX}$  for the 93 real data (points with error bars) and simulated events (solid line), selected as test-samples of  $\tau \rightarrow e\nu_e\nu_\tau$  (e),  $\tau \rightarrow \mu\nu_\mu\nu_\tau$  ( $\mu$ ),  $\tau \rightarrow \pi/Kn\pi^0\nu_\tau$  (h) decays. The cross-hatched areas represent the simulated contamination from the other  $\tau$  decays, and the tight-hatched areas represent the simulated external background ( $e^+e^-$ ,  $\mu^+\mu^-$ ,  $q\bar{q}$ ,  $e^+e^-f\bar{f}$ ). The normalisation of the simulated data is done using  $\mathcal{L}_{int}$  and the world-average values of the  $\tau$  branching ratios.

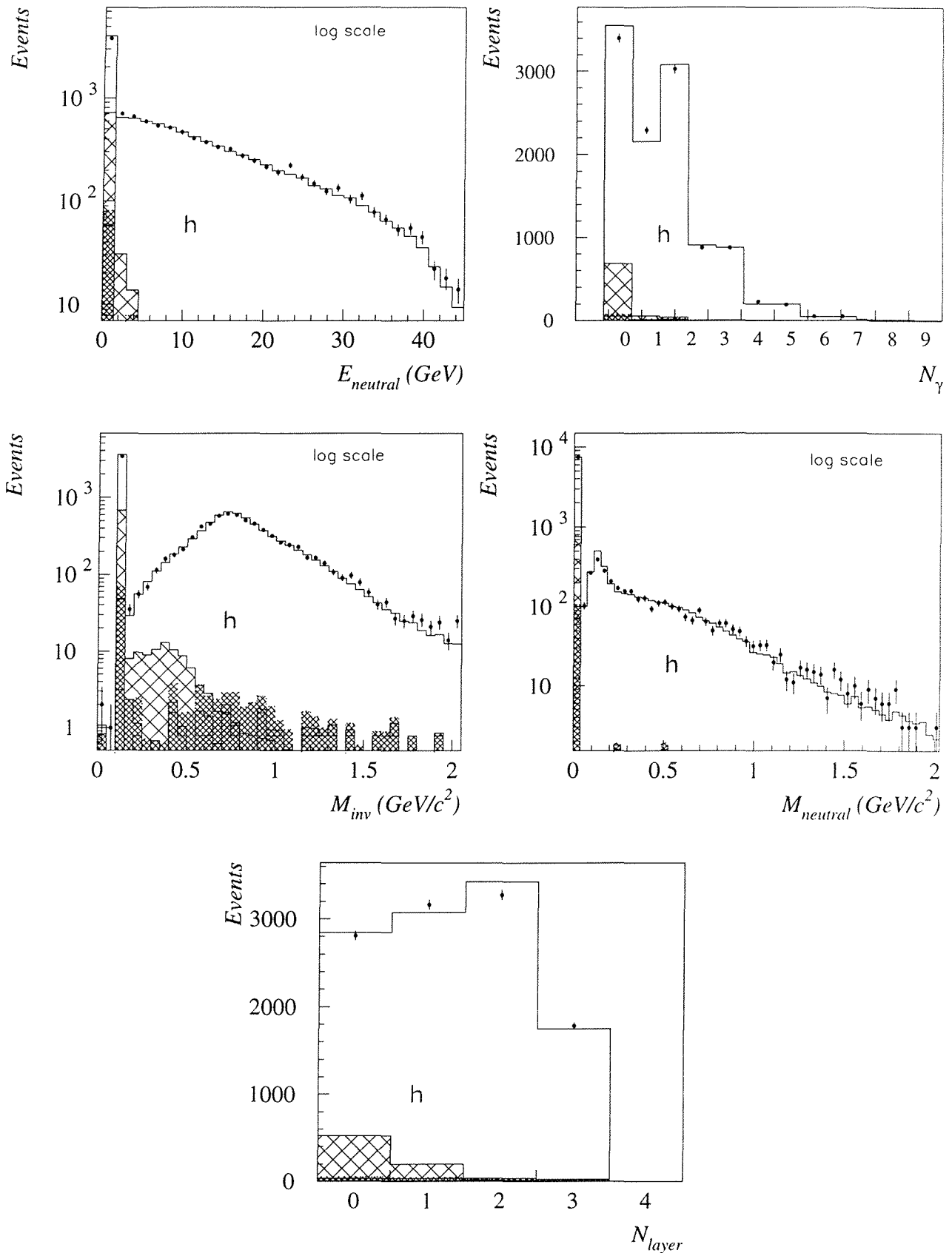


Figure 5.10: Distributions of  $E_{neutral}$ ,  $N_\gamma$ ,  $M_{inv}$ ,  $M_{neutral}$  and  $N_{layer}$  for the 93 real data (points with error bars) and simulated events (solid line), selected as test-samples of  $\tau \rightarrow \pi/K n \pi^0 \nu_\tau$  (**h**) decays. The cross-hatched areas represent the simulated contamination from the other  $\tau$  decays, and the tight-hatched areas represent the simulated external background ( $e^+e^-$ ,  $\mu^+\mu^-$ ,  $q\bar{q}$ ,  $e^+e^-f\bar{f}$ ). The normalisation of the simulated data is done using  $\mathcal{L}_{int}$  and the world-average values of the  $\tau$  branching ratios.

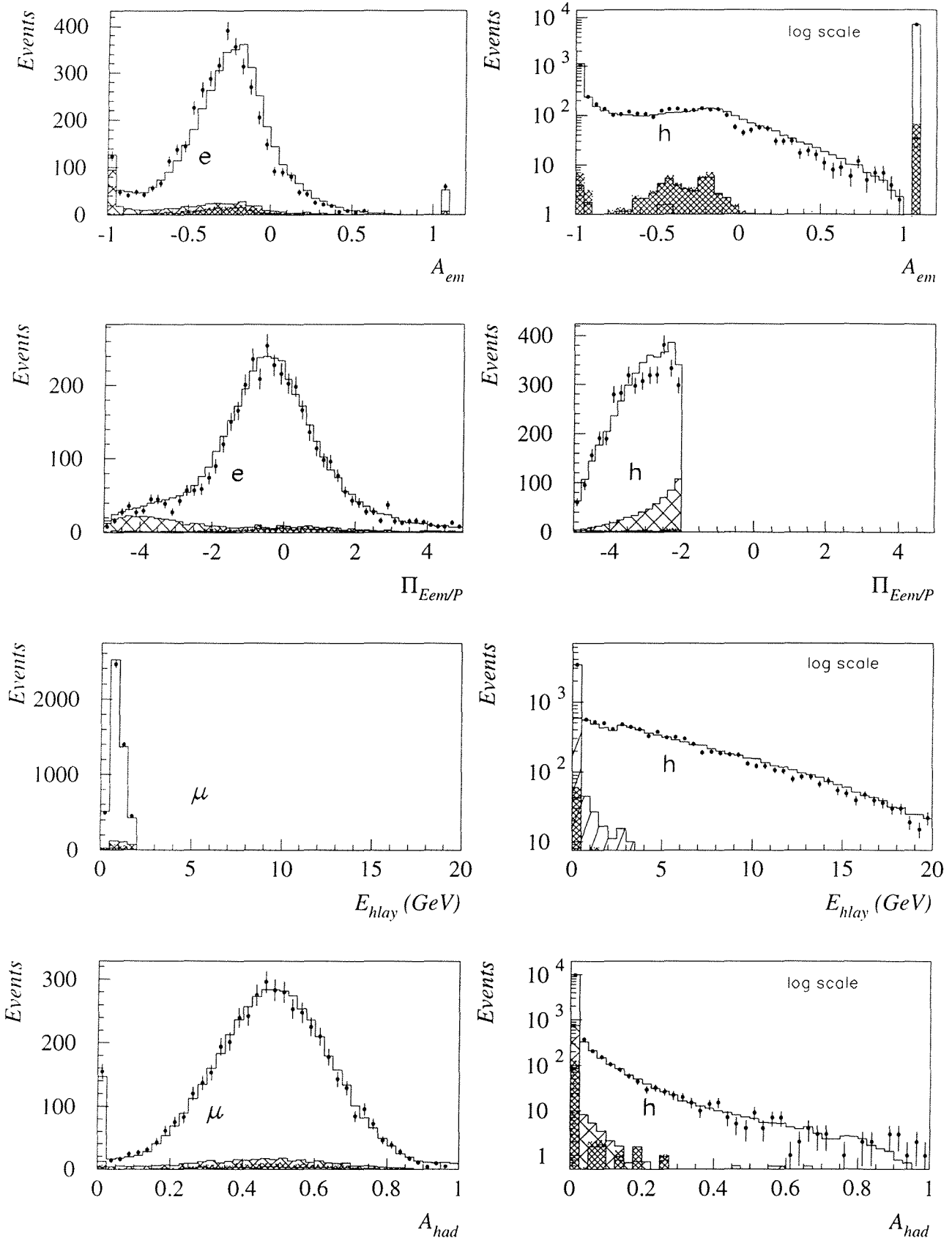


Figure 5.11: Distributions of  $A_{em}$ ,  $\Pi_{E_{em}/p}$ ,  $E_{hlay}$  and  $A_{had}$  for the 93 real data (points with error bars) and simulated events (solid line), selected as test-samples of  $\tau \rightarrow e\nu_e\nu_\tau$  (**e**),  $\tau \rightarrow \mu\nu_\mu\nu_\tau$  ( **$\mu$** )  $\tau \rightarrow \pi/Kn\pi^0\nu_\tau$  (**h**) decays. For clarity, a value of 1.1 was given to  $A_{em}$  when  $E_{em}$  was zero. Only events with  $E_{em} > 0$  enter the histograms of  $\Pi_{E_{em}/p}$ . The cross-hatched areas represent the simulated contamination from the other  $\tau$  decays, and the tight-hatched areas represent the simulated external background ( $e^+e^-$ ,  $\mu^+\mu^-$ ,  $q\bar{q}$ ,  $e^+e^-f\bar{f}$ ). The normalisation of the simulated data is done using  $\mathcal{L}_{int}$  and the world-average values of the  $\tau$  branching ratios.

## 5.3 Performances of the neural network classification

### 5.3.1 Neural network architecture and training

Using the SNN software package 3.4, a neural network was build with

- 1 input layer containing 11 units corresponding to the 11 discriminant variables which were chosen in the previous section;
- 1 hidden layer containing 7 units;
- 1 output layer containing 5 units corresponding to the 5 classes in which we had to classify the pre-selected 1-prong  $\tau$  decays.

The network was a feed-forward network fully connected (i.e. there were  $11 \times 7 + 7 \times 5 = 112$  connections)(see figure 5.12), initialised using random weights and threshold values. For the training, the Standard Backpropagation learning function was used with a learning factor  $\eta$  of 0.2, and the activation function ( $g(x)$ ) was the Logistic function.

The training of the networks was made using simulated events. The detail of the composition of the training sample is given in table 5.3 with the corresponding target values for each class. The same amount of decays from  $\tau$ 's of right helicity and of left helicity were used for the training in order not to bias *a priori* the network response in function of the  $\tau$  polarisation.

Class n°	$\tau$ decay mode	# of patterns		Target values				
		$\mathcal{P}_\tau = +1$	$\mathcal{P}_\tau = -1$	$o_1$	$o_2$	$o_3$	$o_4$	$o_5$
1	$e\nu_e\nu_\tau$	1500	1500	1	0	0	0	0
2	$\mu\nu_\mu\nu_\tau$	1500	1500	0	1	0	0	0
3	$\pi/K\nu_\tau$	1500	1500	0	0	1	0	0
4	$\rho\nu_\tau$	2000	2000	0	0	0	1	0
5	$a_1\nu_\tau$	1500	1500	0	0	0	0	1

Table 5.3: Number of simulated  $\tau$  decays used for the training of the neural network. The target values are given for the 5 ouput units for each class.

All classes were equally represented in the training sample, except the  $\rho$  channel which has the largest branching ratio: it was favoured in order to force the neural network to be more efficient in the  $\rho$  channel identification. The over-representation of the  $\rho$  channel in the training sample with respect to the other channels (classes), gave a larger weight to that class in the estimation of the error function and the convergence was oriented towards a better  $\rho$  identification (to the detriment of the most similar class: the  $a_1$  channel.) This was done in order to reduce the  $\rho$  contamination to the other channels.

Neural networks were trained separately for each year of data taking with the corresponding simulated events (93, 94 and 95 data), in order to obtain the network the best adapted to the experimental data which have to be submitted to the network. However, due to the generalisation power of neural networks, the differences between the training samples generated for each year should not affect the final result of the classification (e.g. the network trained with the 93 simulation can be applied to the 94 data) in the limit where the estimation of the network performances (efficiencies, migration matrices) is made with testing patterns generated with the same processing than the one of the analysed real data. As a cross-check, the  $\tau$  polarisation

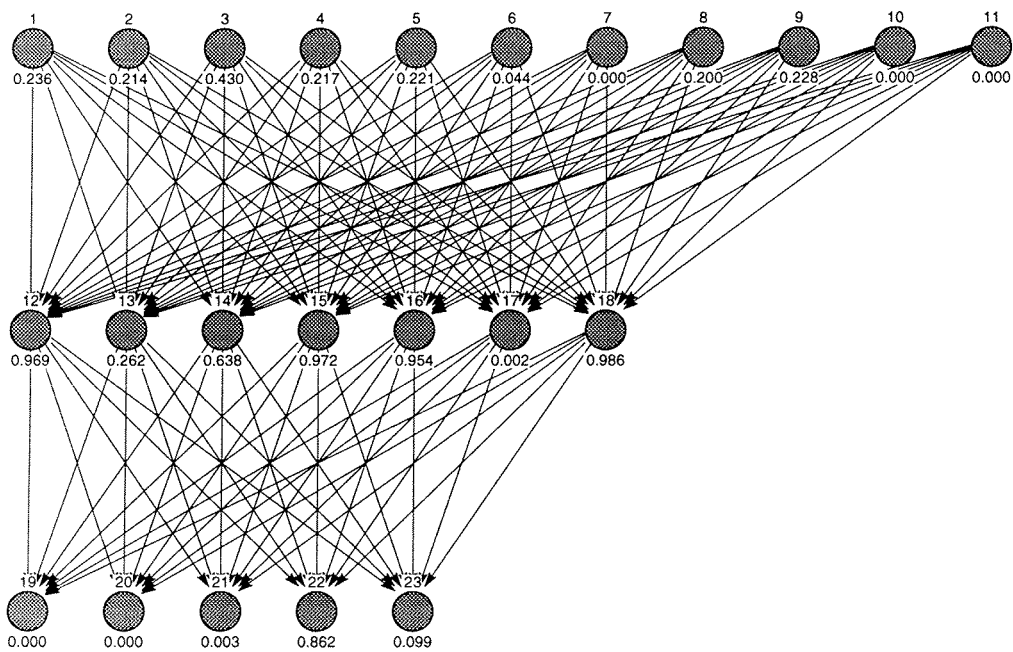


Figure 5.12: Architecture of the neural network used for the classification of the 1-prong  $\tau$  decays into 5 classes: it contains one input layer for the 11 input variables (units 1 to 11), one hidden layer with 7 units numbered 12 to 18, and one output layer of 5 units numbered 19 to 23. The arrows represent the connections between the units. This network is fully connected. The numbers written under each unit are the activation values for a given pattern. In this example, the pattern has clearly been classified into Class 4 since the activation of the 4<sup>th</sup> output unit (unit 22) is close to 1 and it is close to 0 for the other output units. For cases which are more ambiguous, a classification rule has to be defined (see text).

was measured using, for the 94 and the 95 data, the neural network trained for the 93 data. A relative change of +3% for the 94 result and -2% for the 95 result, was observed, i.e. an error a factor 6 smaller than the statistical error.

The neural networks converged relatively quickly and the trainings were stopped after 500 cycles over the full sample of training patterns read in a random order. After that, the error function starts oscillating around its minimum value. An example of the evolution of the error function is given on figure 5.13.

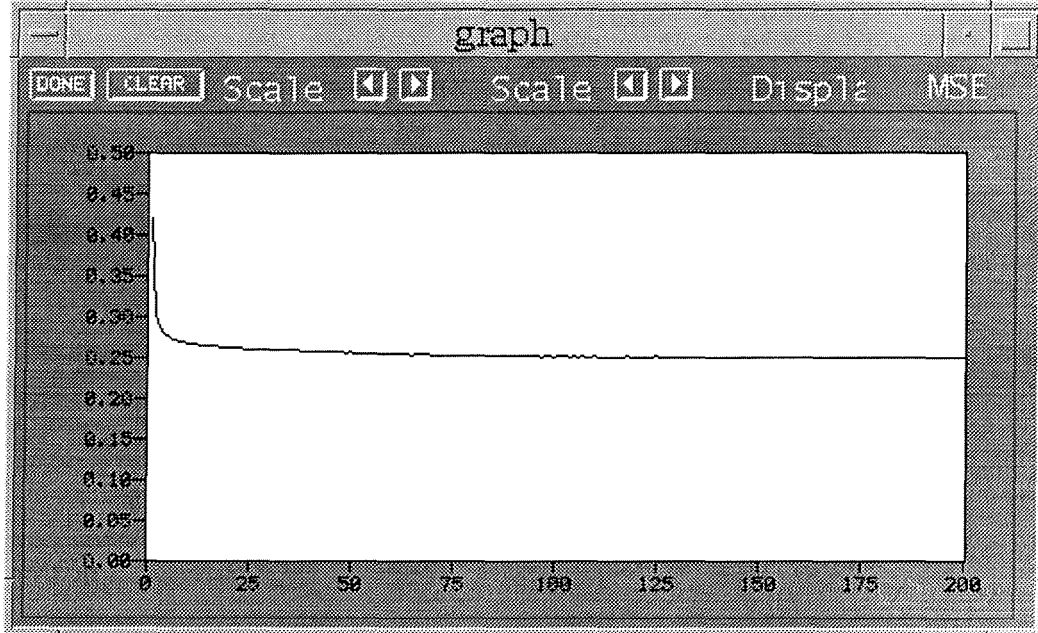


Figure 5.13: *Evolution of the error function during the training of the network: the ordinate is the total error per training pattern and the abscissa is the number of cycles. The evolution is very quick at the start of the training and then it stabilizes slowly.*

When the training procedure is completed, it is possible to estimate the power of discrimination of the input variables: figure 5.14 shows the sensitivity of the input variables to the different classes of events. The sensitivity  $S_{ij}$  of the input  $I_i$  for the class  $j$  (to which corresponds the output  $o_j$ ) is estimated by:

$$S_{ij} = \sum_{k=1}^H w_{ik} \cdot w_{kj}, \quad (5.5)$$

where  $w_{lm}$  is the weight of the connection between unit  $l$  and unit  $m$  (it can be positive or negative), and  $H$  is the number of units in the hidden layer<sup>6</sup>. Although it is far from trivial to interpret the values of the sensitivities because of the complex correlations which exist between the units inside a given class and between different classes, some expected behaviour are however observable: for example, the sensitivity of the variables introduced for the electron identification ( $\Pi_{E_{em}/p}$ ,  $A_{em}$  and  $\Pi_{dE/dX}$ ), are indeed positive (the connections are excitatory) for the output 1 ( $o_1$ ) and are negative (the connections are inhibitory) for the other outputs.

<sup>6</sup>For the training, the input variables were normalised to the range [0, 1].

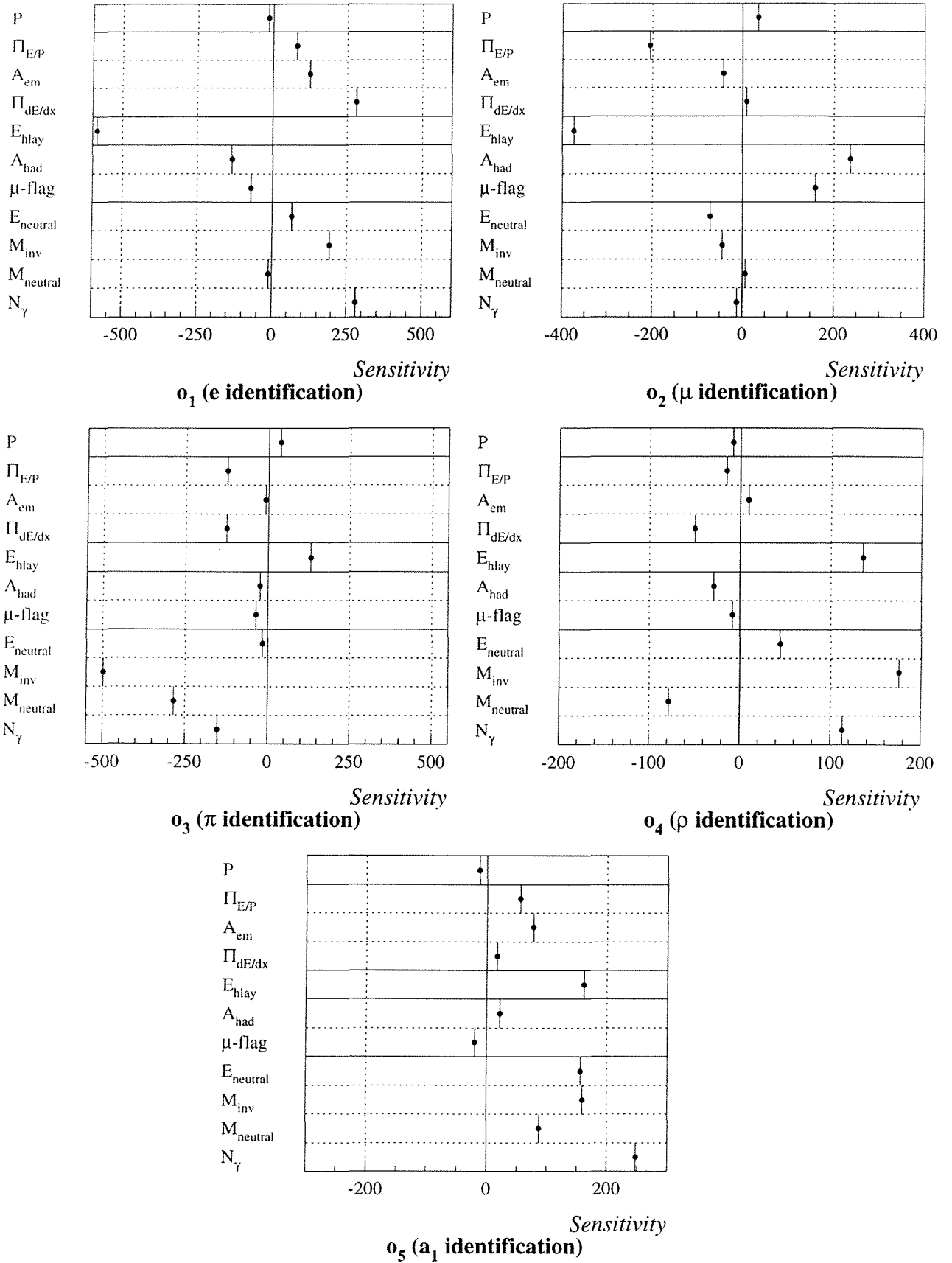


Figure 5.14: Sensitivity of the input variables for the classification of 1-prong  $\tau$  decays into the 5 following classes:  $\tau \rightarrow e\nu_e\nu_\tau$ ,  $\tau \rightarrow \mu\nu_\mu\nu_\tau$ ,  $\tau \rightarrow \pi/K\nu_\tau$ ,  $\tau \rightarrow \rho\nu_\tau$ , and  $\tau \rightarrow a_1\nu_\tau$ .

In the same way, the sensitivity of the input  $E_{hlay}$  is highly negative for the outputs 1 and 2 (no HCAL energy is associated to electrons, and muons lose a little amount of energy in the HCAL) and is positive for the output 3, 4 and 5 (hadrons usually lose a lot of energy in the first layers of the HCAL). A last example: events with a non-zero neutral mass ( $M_{neutral} > 0$ ) are preferably classified as  $a_1$  (sensitivity positive for  $o_5$ ) than as  $\pi$ 's or  $\rho$ 's (sensitivity negative for  $o_3$  and  $o_4$ ).

### 5.3.2 Neural network performances

#### Choice of a classification method

The classification of the events, based on the values of the output units ( $o_1, o_2, o_3, o_4$  and  $o_5$ ) was done using the so-called "Winner Rule". The pattern  $\lambda$  was classified in the class  $c$  for which the output  $o_c^\lambda$  was the maximum of the five outputs. In that way, all patterns are classified into one of the 5 classes; there is no ambiguous case and no loss of statistics. Figure 5.15 presents the distributions of the 5 output values for the real data (point with error bars) and the simulated events (solid line) which were used to estimate the network performances (see next section). A good agreement is observed between the simulation and the experimental data. The hatched areas represent the simulated events which belong to the class corresponding to the output unit of the respective figures. The tight-hatched surfaces are the simulated events not originating from  $\tau$  decays ( $e^+e^-$ ,  $\mu^+\mu^-$ ,  $q\bar{q}$  and  $e^+e^-f\bar{f}$  interactions). It is well visible that the electron, muon and pion channels were more clearly identified than the  $\rho$  and the  $a_1$  channels: their respective outputs are accumulating towards values close to 1 while it is not the case for the last two classes. For that reason, another classification rule which would consist in cutting on the output values instead of using the "Winner Rule", would result in much lower efficiencies. As a cross-check of the effect of the choice of the classification method, the polarisation measurements were however repeated classifying the events according to the following rule: the pattern  $\lambda$  was classified in the class  $c$  when the output  $o_c^\lambda$  was greater than 0.5 and all other outputs were lower than 0.5, implying that some events could remain unclassified. The effect on the results are given in the next chapter where the systematic effects are studied.

#### Classification efficiencies

The classification efficiencies were estimated by submitting to the trained networks the full simulation statistics, except the events which were used for the training of the networks (see table 4.2). The migration matrices are given in tables 5.4, 5.5 and 5.6 for the networks trained for the 93, 94 and 95 data respectively. The diagonal elements of the matrices correspond to the identification efficiencies, and the off-diagonal elements are the probabilities of misidentification. For information, the selection efficiencies are given separately for the  $\tau \rightarrow \pi\nu_\tau$  channel and for the  $\tau \rightarrow K\nu_\tau$  channel. It is also given for the other final states:  $\tau \rightarrow X\nu_\tau$  where  $X$  can be  $\pi 3\pi^0, \pi 2K^0, KK^0, \pi\pi^0 K^0, \eta\pi\pi^0, \gamma\pi\pi^0, KK^0\pi^0, K2\pi^0, K^*, \pi 2K, K2\pi, 3\pi, 3\pi\pi^0, 3\pi 2\pi^0, 3\pi 3\pi^0, 5\pi, 5\pi\pi^0$ . The quoted errors are the errors due to the finite statistics of simulated events used for testing the networks.

Several trainings were performed for each year, and we chose the network which was the most efficient to classify the  $\pi$  and the  $\rho$  channels, because these two decay modes are the most sensitive for the  $\tau$  polarisation measurement. The convergence could indeed sometimes lead to a minimum of energy (error) for a very good  $a_1$  recognition and a poorer  $\rho$  classification power.

Other configurations of the neural network were tried: with two hidden layers instead of one, or with more hidden units in the hidden layer. In all cases, the computation time was of course



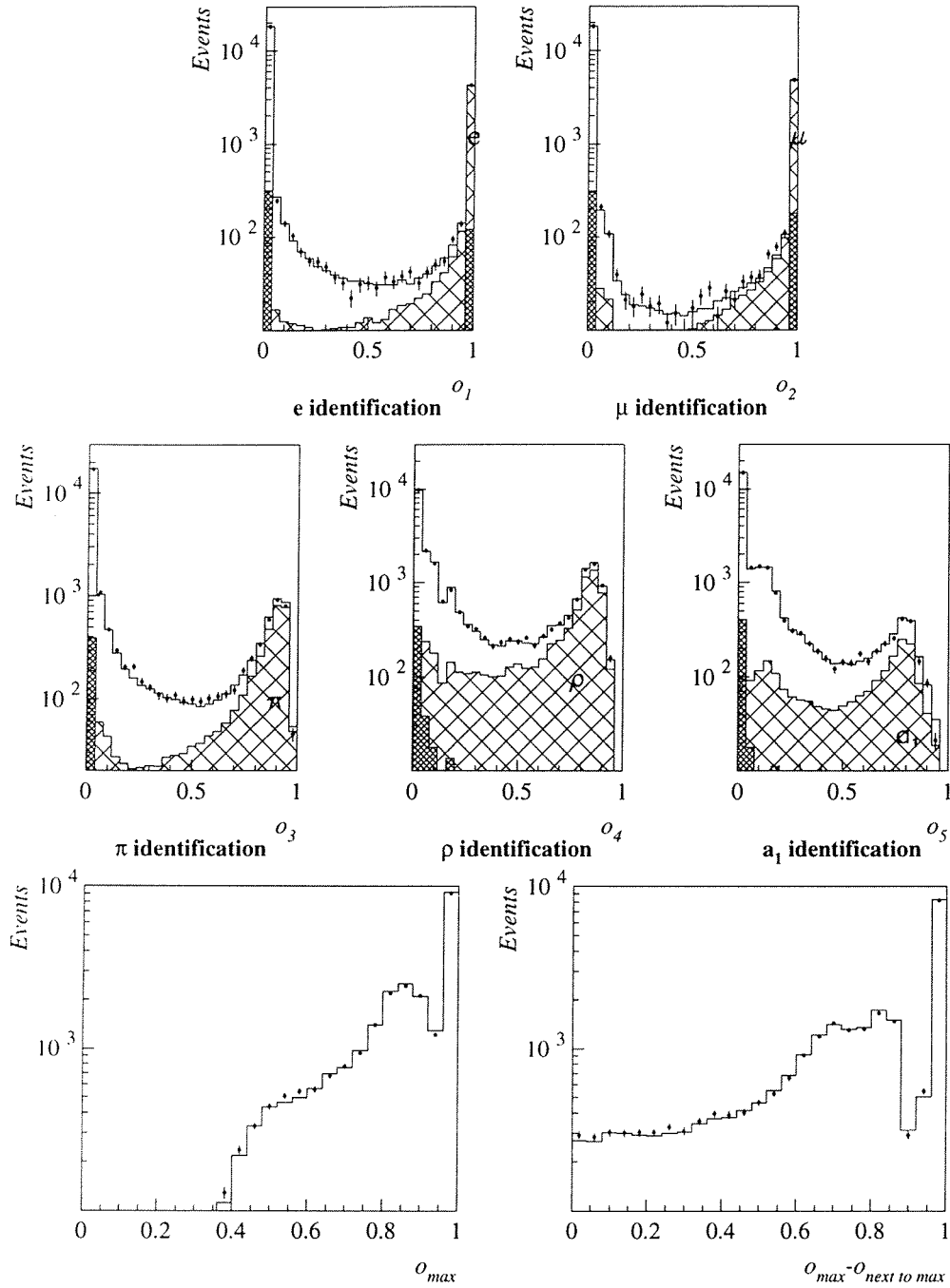


Figure 5.15: Output activation values obtained by the neural network after training for the classification of the 1-prong  $\tau$  decays into the five following classes:  $\tau \rightarrow e\nu_e\nu_\tau$ ,  $\tau \rightarrow \mu\nu_\mu\nu_\tau$ ,  $\tau \rightarrow \pi/K\nu_\tau$ ,  $\tau \rightarrow \rho\nu_\tau$ , and  $\tau \rightarrow a_1\nu_\tau$  (logarithmic scales). The points with error bars are the real 93 data, the solid line represent the simulated events normalised to  $\mathcal{L}_{int}$  using the world-average  $\tau$  branching ratios. The hatched areas represent the simulated events which belong to the class corresponding to the output unit of the respective figures. The tight-hatched surfaces are the simulated events not originating from  $\tau$  decays ( $e^+e^-$ ,  $\mu^+\mu^-$ ,  $q\bar{q}$  and  $e^+e^-f\bar{f}$  interactions). The last two plots represent respectively the distribution of the maximum output ( $o_{max}$ ) and the difference between the maximum output and the maximum of the other outputs ( $o_{max} - o_{next\ to\ max}$ ), for data and simulation.

to the class: for the decay ↓	Probability of classification (%)				
	$\tau \rightarrow e\nu_e\nu_\tau$	$\tau \rightarrow \mu\nu_\mu\nu_\tau$	$\tau \rightarrow \pi/K\nu_\tau$	$\tau \rightarrow \rho\nu_\tau$	$\tau \rightarrow a_1\nu_\tau$
$\tau \rightarrow e\nu_e\nu_\tau$	<b>96.14±0.06</b>	0.0±0.01	2.71±0.05	0.99±0.03	0.16±0.01
$\tau \rightarrow \mu\nu_\mu\nu_\tau$	0.23±0.02	<b>96.57±0.06</b>	2.86±0.05	0.31±0.02	0.03±0.01
$\tau \rightarrow \pi\nu_\tau$	2.66±0.07	1.79±0.05	<b>86.66±0.14</b>	7.96±0.11	0.94±0.04
$\tau \rightarrow \rho\nu_\tau$	1.74±0.04	0.42±0.02	7.75±0.08	<b>81.37±0.11</b>	8.72±0.08
$\tau \rightarrow a_1\nu_\tau$	0.97±0.05	0.14±0.02	1.77±0.07	39.56±0.25	<b>57.56±0.25</b>
$\tau \rightarrow K\nu_\tau$	0.26±0.08	4.46±0.32	86.85±0.52	7.86±0.42	0.57±0.12
$\tau \rightarrow X\nu_\tau$	1.97±0.10	0.63±0.06	17.09±0.27	40.40±0.35	39.91±0.35

Table 5.4: Migration matrix for the neural network classification of the 93 data

to the class: for the decay ↓	Probability of classification (%)				
	$\tau \rightarrow e\nu_e\nu_\tau$	$\tau \rightarrow \mu\nu_\mu\nu_\tau$	$\tau \rightarrow \pi/K\nu_\tau$	$\tau \rightarrow \rho\nu_\tau$	$\tau \rightarrow a_1\nu_\tau$
$\tau \rightarrow e\nu_e\nu_\tau$	<b>95.86±0.05</b>	0.09±0.01	2.34±0.04	1.56±0.03	0.15±0.01
$\tau \rightarrow \mu\nu_\mu\nu_\tau$	0.07±0.01	<b>97.05±0.04</b>	2.56±0.04	0.29±0.01	0.03±0.01
$\tau \rightarrow \pi\nu_\tau$	3.73±0.05	2.81±0.05	<b>84.79±0.10</b>	7.46±0.07	1.21±0.03
$\tau \rightarrow \rho\nu_\tau$	1.68±0.03	0.60±0.02	8.16±0.05	<b>79.91±0.08</b>	9.65±0.06
$\tau \rightarrow a_1\nu_\tau$	1.05±0.04	0.19±0.02	1.83±0.05	40.79±0.17	<b>56.14±0.17</b>
$\tau \rightarrow K\nu_\tau$	0.25±0.05	2.38±0.16	88.90±0.34	7.59±0.28	0.87±0.10
$\tau \rightarrow X\nu_\tau$	1.89±0.07	0.90±0.05	17.04±0.19	39.66±0.25	40.50±0.25

Table 5.5: Migration matrix for the neural network classification of the 94 data

to the class: for the decay ↓	Probability of classification (%)				
	$\tau \rightarrow e\nu_e\nu_\tau$	$\tau \rightarrow \mu\nu_\mu\nu_\tau$	$\tau \rightarrow \pi/K\nu_\tau$	$\tau \rightarrow \rho\nu_\tau$	$\tau \rightarrow a_1\nu_\tau$
$\tau \rightarrow e\nu_e\nu_\tau$	<b>94.61±0.07</b>	0.02±0.01	3.42±0.06	1.45±0.04	0.51±0.02
$\tau \rightarrow \mu\nu_\mu\nu_\tau$	0.11±0.01	<b>96.14±0.06</b>	3.36±0.05	0.34±0.02	0.04±0.01
$\tau \rightarrow \pi\nu_\tau$	2.49±0.06	1.75±0.05	<b>86.72±0.13</b>	8.01±0.10	1.03±0.04
$\tau \rightarrow \rho\nu_\tau$	1.06±0.03	0.39±0.02	8.27±0.07	<b>79.97±0.11</b>	10.30±0.08
$\tau \rightarrow a_1\nu_\tau$	0.67±0.04	0.13±0.02	1.95±0.06	38.60±0.23	<b>58.66±0.23</b>
$\tau \rightarrow K\nu_\tau$	0.32±0.08	1.94±0.20	88.65±0.46	8.10±0.40	0.99±0.14
$\tau \rightarrow X\nu_\tau$	1.23±0.07	0.42±0.04	17.29±0.26	39.57±0.33	41.49±0.33

Table 5.6: Migration matrix for the neural network classification of the 95 data

longer. The total error function was also slightly decreased. It means that the obtained output values were closer to the target values. However, since we have chosen the “Winner Rule” for the reasons given above, there was no improvement concerning the selection efficiencies in the way we computed them: the output unit presenting the maximum value was still the same one.

Table 5.7 gives the global selection efficiencies, taking into account the losses induced by the  $\tau^+\tau^-$  selection and the inclusive 1-prong selection (see table 4.10), the cuts on  $p$ ,  $\theta$  and  $dE/dX$  (see table 5.1), and the neural network efficiency. Also the purities of the selected samples are given, as well as the number of real events selected for each year in each class.

	Neural network classification			Classical method
	1993	1994	1995	
<b>Simulation</b>				
$\tau$ decay mode	Global 1-prong sel. efficiency (%)			
$\tau \rightarrow e\nu_e\nu_\tau$	$39.84 \pm 0.11$	$39.80 \pm 0.07$	$39.87 \pm 0.10$	$34.96 \pm 0.20$ (93+94)
$\tau \rightarrow \mu\nu_\mu\nu_\tau$	$44.80 \pm 0.11$	$45.22 \pm 0.08$	$44.86 \pm 0.10$	$46.20 \pm 0.05$ (93+94+95)
$\tau \rightarrow \pi/K\nu_\tau$	$38.21 \pm 0.13$	$37.62 \pm 0.09$	$38.52 \pm 0.12$	$23.66 \pm 0.06$ (95)
$\tau \rightarrow \rho\nu_\tau$	$33.97 \pm 0.09$	$33.22 \pm 0.06$	$33.65 \pm 0.08$	$23.13 \pm 0.05$ (93+94+95)
$\tau \rightarrow a_1\nu_\tau$	$22.76 \pm 0.13$	$21.85 \pm 0.11$	$23.32 \pm 0.13$	-
$\tau$ decay mode	Purity of the selected samples (%)			
$\tau \rightarrow e\nu_e\nu_\tau$	$90.4 \pm 0.1$	$89.4 \pm 0.1$	$90.3 \pm 0.1$	$94.63 \pm 0.35$
$\tau \rightarrow \mu\nu_\mu\nu_\tau$	$94.4 \pm 0.1$	$94.3 \pm 0.1$	$94.3 \pm 0.1$	$96.10 \pm 0.04$
$\tau \rightarrow \pi/K\nu_\tau$	$73.3 \pm 0.2$	$73.2 \pm 0.1$	$71.3 \pm 0.2$	$89.40 \pm 0.01$
$\tau \rightarrow \rho\nu_\tau$	$75.8 \pm 0.1$	$75.4 \pm 0.1$	$75.8 \pm 0.1$	$80.31 \pm 0.08$
$\tau \rightarrow a_1\nu_\tau$	$55.4 \pm 0.3$	$53.2 \pm 0.2$	$52.8 \pm 0.3$	-
<b>Real data</b>				
$\tau$ decay mode	Number of selected $\tau$ decays			
$\tau \rightarrow e\nu_e\nu_\tau$	5034	9194	4206	
$\tau \rightarrow \mu\nu_\mu\nu_\tau$	5332	9821	4658	
$\tau \rightarrow \pi/K\nu_\tau$	3943	7200	3707	
$\tau \rightarrow \rho\nu_\tau$	7287	12974	6287	
$\tau \rightarrow a_1\nu_\tau$	2417	4692	2337	

Table 5.7: Global selection efficiency (i.e. with respect to the  $4\pi$  solid angle), and purity (estimated using the world-average values for the  $\tau$  decay branching ratios), for the selection of the exclusive 1-prong  $\tau$  decay channels. Number of real events selected for each channel, for the 1993, 1994 and 1995 data.

The efficiencies obtained by classical selection methods using linear cuts [43][44][45], dedicated to each channel individually, are also given in table 5.7 for the analysis of the same data sample recorded by the DELPHI detector. The neural network method appears to be much more efficient for the identification of the  $\tau \rightarrow \rho\nu_\tau$  decays, while it reached comparable efficiencies and purities for the  $\tau \rightarrow e\nu_e\nu_\tau$  and the  $\tau \rightarrow \mu\nu_\mu\nu_\tau$  decay modes. For the  $\tau \rightarrow \pi/K\nu_\tau$  decays the neural network is 14% more efficient but the background level (mainly  $\rho$ 's) is also much higher. The selection of the  $\tau \rightarrow a_1\nu_\tau \rightarrow \pi\pi^0\pi^0\nu_\tau$  was not performed in DELPHI using classical methods because the difficulties to identify both  $\pi^0$ 's lead to a very low selection efficiency.

Figure 5.16, a) shows how the identification efficiency of the electrons depends on the azimuthal direction of the particle. It decreases when the track enters a boundary region

of the HPC modules which are situated every  $15^\circ$  in  $\phi$ : there, the electromagnetic energy of the showers is under-estimated and the electrons are misidentified as pions. Because of the action of the magnetic field, the charged particles are deviated towards larger or smaller  $\phi$  angles according to their electrical charge.

Figure 5.16, b) shows how the identification efficiency of the muons decreases in the region not covered by the MUC. The probability for the muons to be classified as pions increases accordingly.

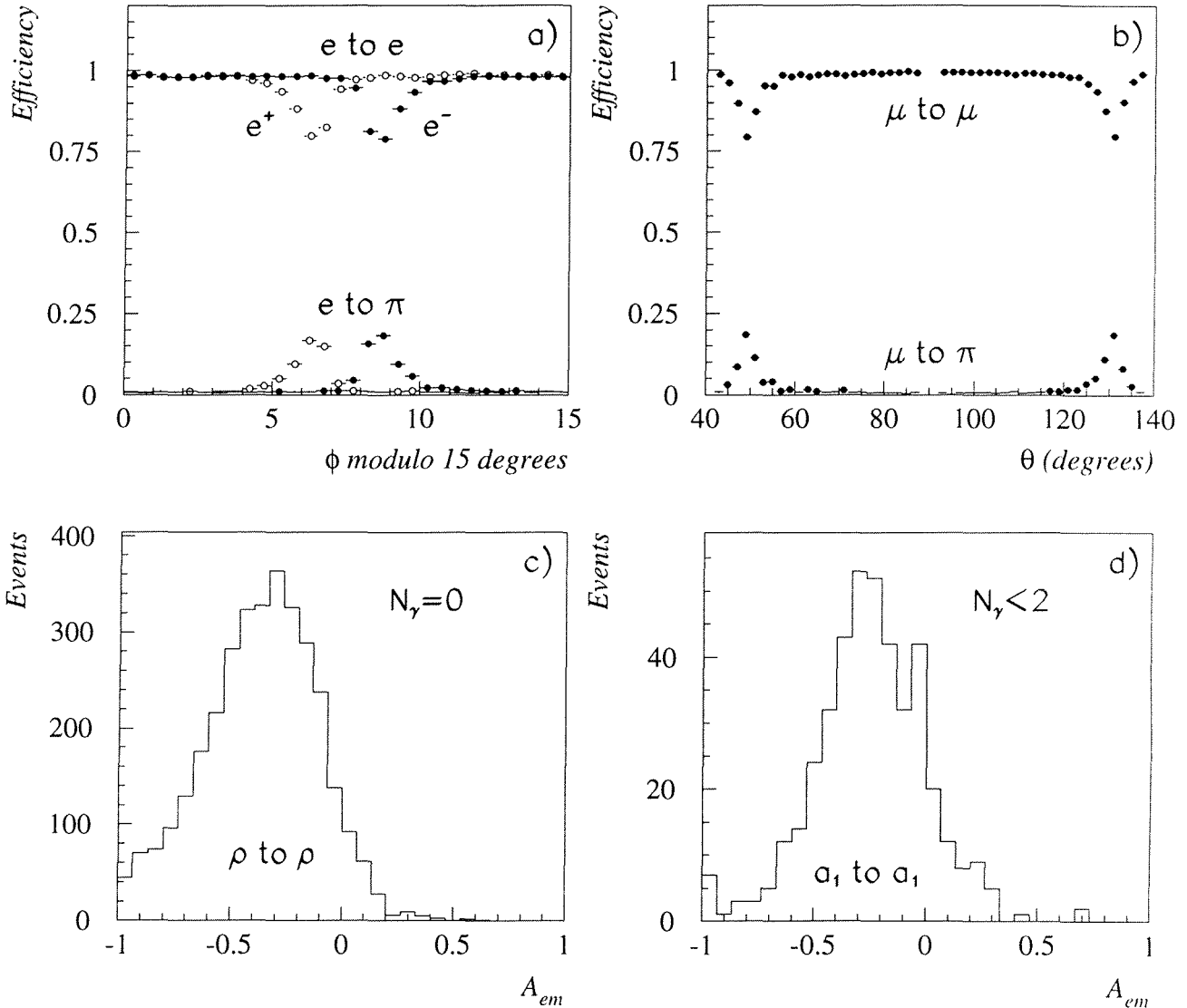


Figure 5.16: a) Probability of identification by the neural networks of electrons as electrons or pions in function of the azimuthal direction and of the electric charge of the particle. b) Probability of identification by the neural networks of muons as muons or pions in function of the polar angle of the particle. c) and d) Distribution of  $A_{em}$  for correctly identified  $\rho$ 's and  $a_1$ 's when there was respectively zero or less than two reconstructed neutral particles in the hemisphere of the charged particle.

Figure 5.16, c) and d) show that the neural network has recognised the correlation between the loss of neutral particle and a large value of  $A_{em}$  which has been emphasised in section 5.1:  $\rho$  events with no reconstructed neutral particle, and  $a_1$  events with less than two reconstructed neutrals were still correctly identified by the neural networks.

Figures 5.17, a) to d) show how the probability for correct and incorrect identification of the  $\rho$  and  $a_1$  by the neural networks varies with the reconstructed invariant mass ( $M_{inv}$ ) and the reconstructed neutral mass ( $M_{neutral}$ ).

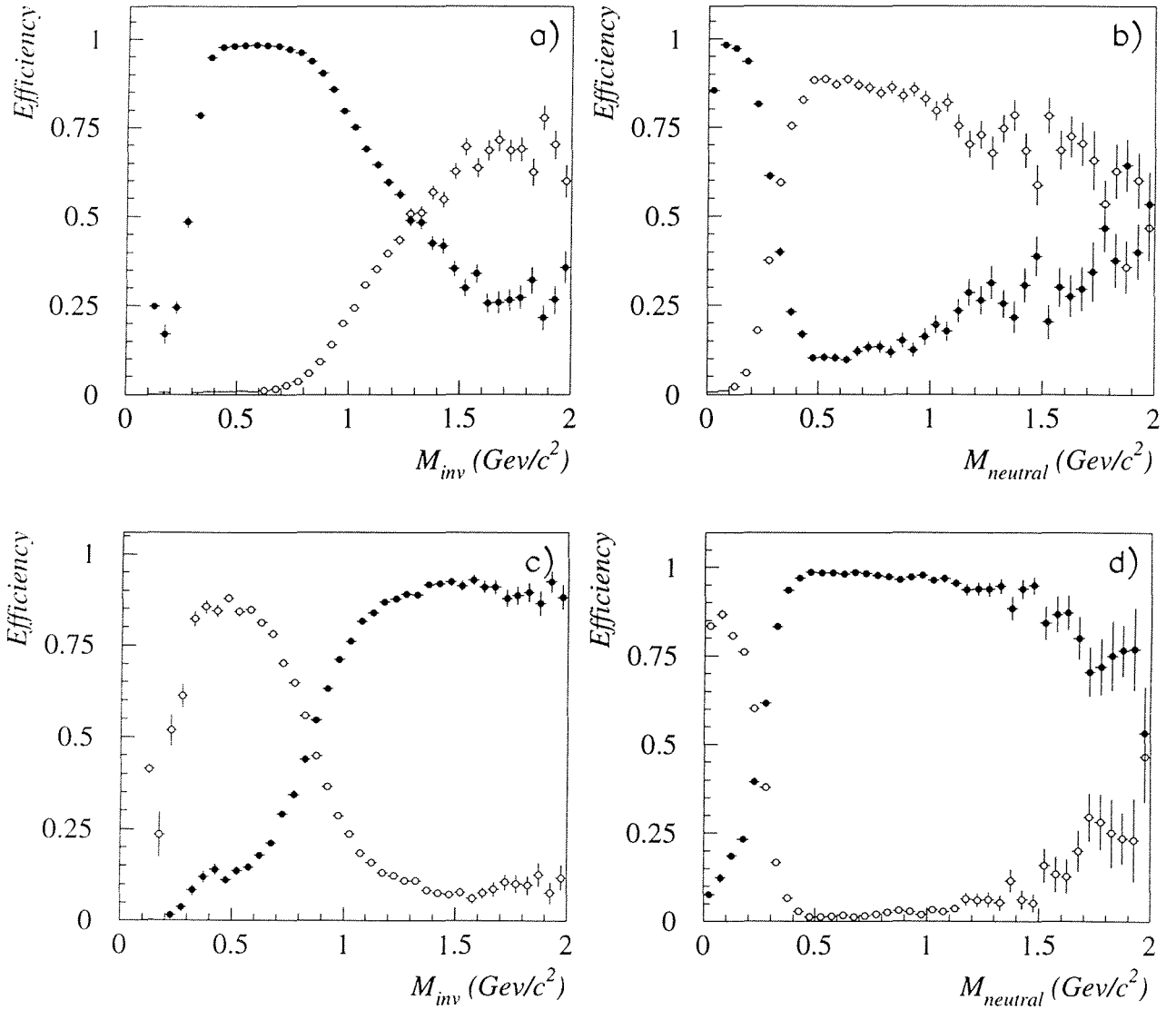


Figure 5.17: Probability for the neural network to identify a  $\rho$  as a  $\rho$  (closed circles) or as an  $a_1$  (open circles) in function of a) the total invariant mass ( $M_{inv}$ ), b) the neutral mass ( $M_{neutral}$ ). Probability for the neural network to identify an  $a_1$  as an  $a_1$  (closed circles) or as a  $\rho$  (open circles) in function of c) the total invariant mass ( $M_{inv}$ ), d) the neutral mass ( $M_{neutral}$ ).

On figures 5.18, 5.19, 5.20, the distributions of the total neutral energy  $E_{neutral}$ , of  $M_{inv}$  and of  $M_{neutral}$  are presented for the real and simulated data for the 93, 94 and 95 data respectively. A good agreement is observed. Some discrepancies appear for the distribution of the variable  $\mu$ -flag. They are taken into account for the systematic effects on the polarisation measurement.

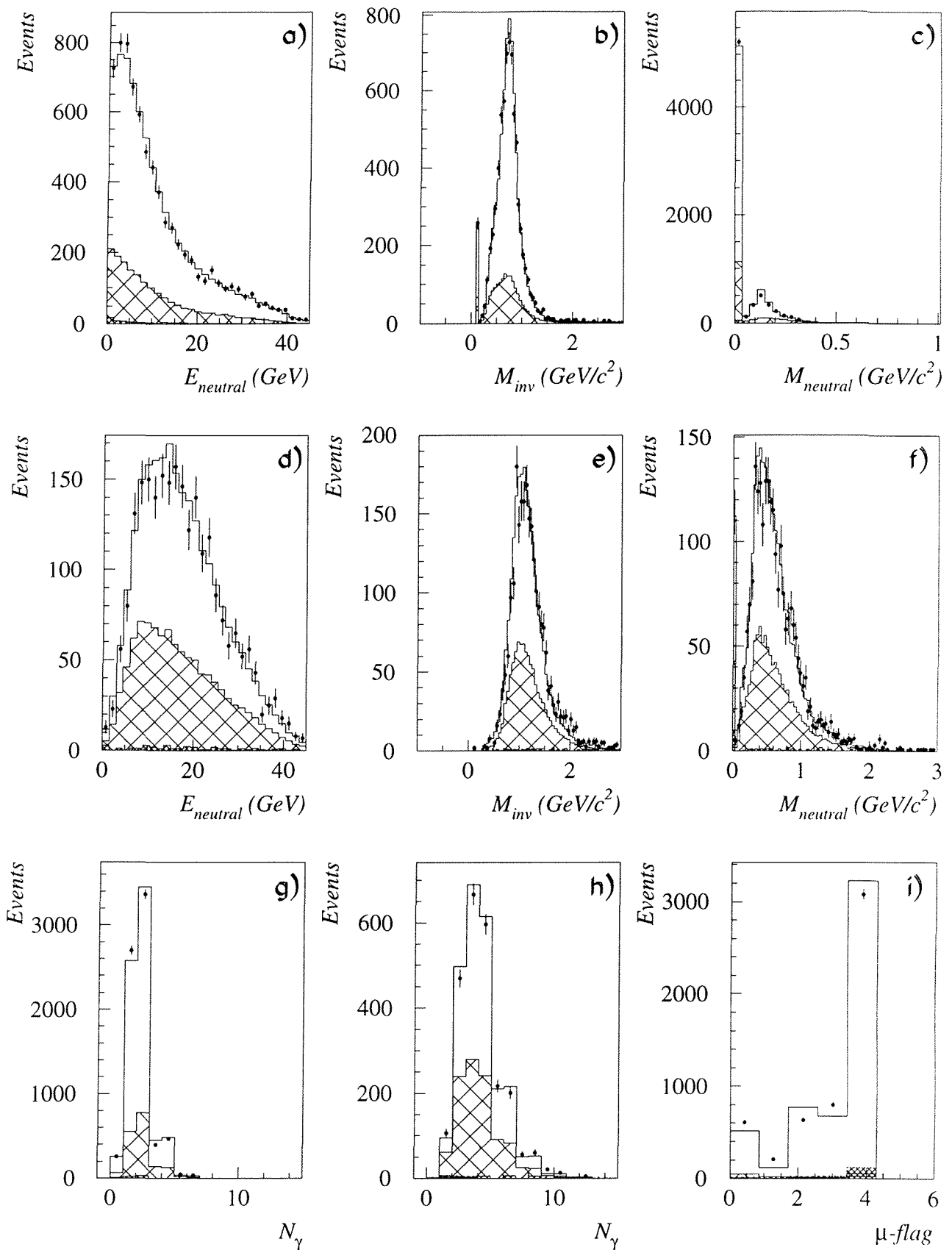


Figure 5.18: 93 data: a), b), c): Distributions of  $E_{neutral}$ ,  $M_{inv}$  and  $M_{neutral}$  of  $\tau \rightarrow \rho\nu_\tau$  decays identified by the neural network. d), e), f): Distributions of  $E_{neutral}$ ,  $M_{inv}$  and  $M_{neutral}$  of selected  $\tau \rightarrow a_1\nu_\tau$  decays. g) and h): Distribution of  $N_\gamma$  for respectively selected  $\rho$ 's and  $a_1$ 's. i) Distribution of  $\mu$ -flag for selected  $\tau \rightarrow \mu\nu_\mu\nu_\tau$  decays. The points represent the real data, the solid line histograms are the simulated events, normalised to  $\mathcal{L}_{int}$  and to the world-average values of the  $\tau$  branching ratios. The hatched-areas represent the total background originating from other  $\tau$  decay channels. The tight-hatched areas represent the total external contamination.

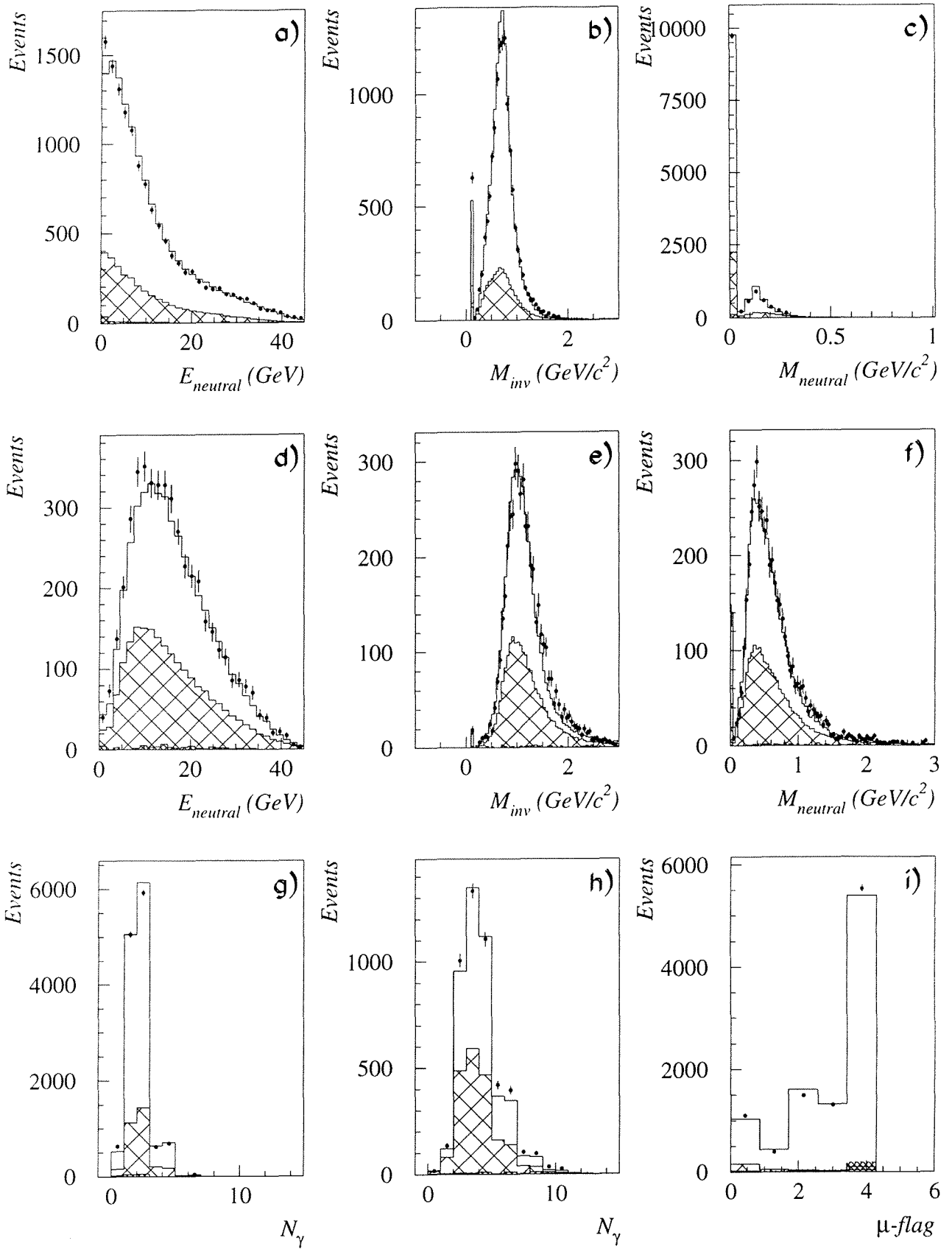


Figure 5.19: Same as figure 5.18 for the 94 data.

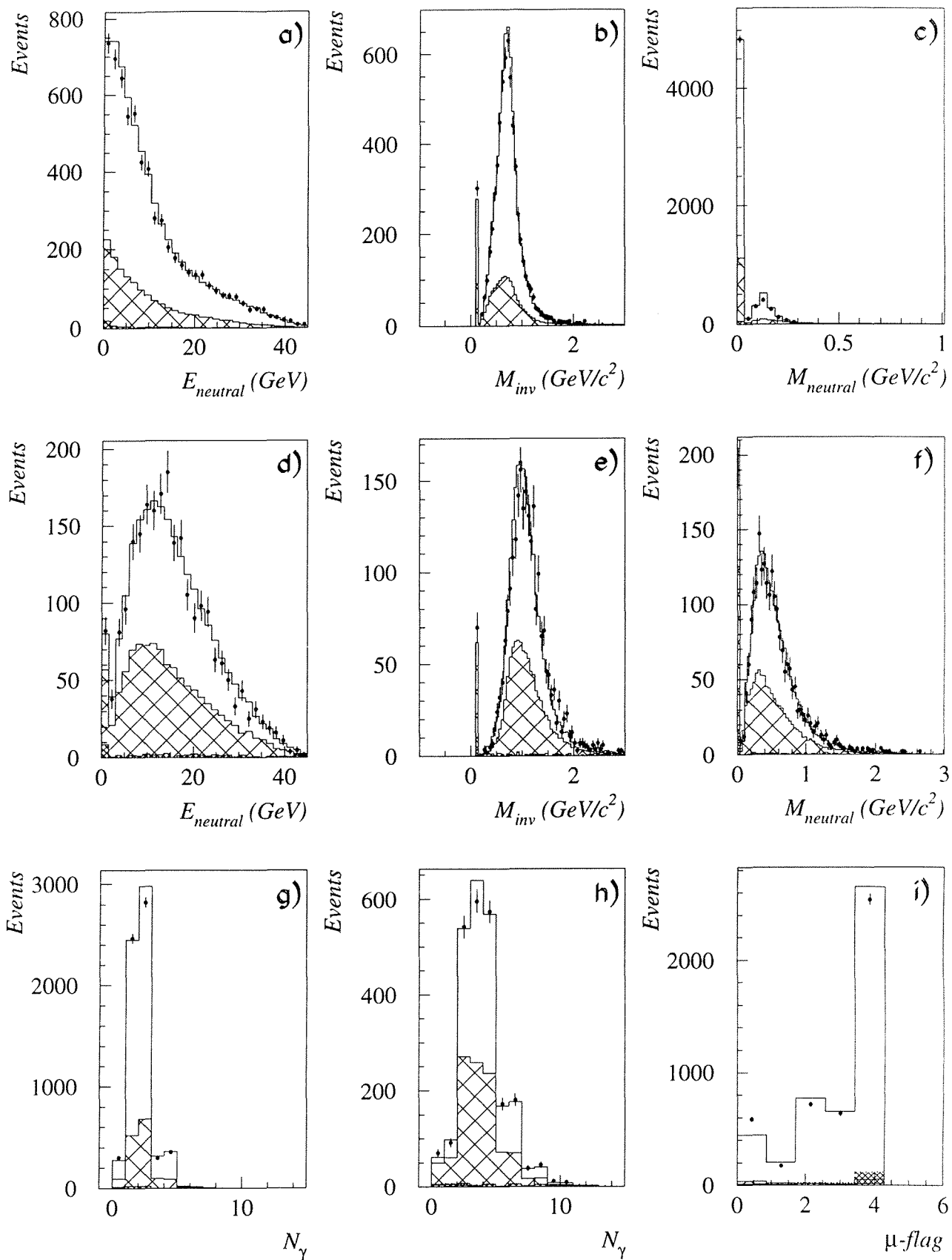


Figure 5.20: Same as figure 5.18 for the 95 data.



## 5.4 Summary

With a view to the  $\mathcal{P}_\tau$  measurement, the preselected 1-*prong*  $\tau$  decays had to be identified according to the  $\tau$  decay mode. They were classified into the five following classes:  $\tau \rightarrow e\nu_e\nu_\tau$ ,  $\tau \rightarrow \mu\nu_\mu\nu_\tau$ ,  $\tau \rightarrow \pi/K\nu_\tau$ ,  $\tau \rightarrow \rho\nu_\tau \rightarrow \pi\pi^0\nu_\tau$ ,  $\tau \rightarrow a_1\nu_\tau \rightarrow \pi\pi^0\pi^0\nu_\tau$ . The last three classes differ from one another by the number of  $\pi^0$ 's produced in the final state and by the total invariant mass of the hadronic system. Because of experimental difficulties to identify efficiently the neutral particles and to reconstruct precisely their energy, we have chosen to use the neural network technique for this classification problem, which we have then extended to the identification of the leptonic  $\tau$  decay modes. For each year of data taking, one neural network was trained for the simultaneous identification of the five classes of events, giving the possibility to estimate one global migration matrix which took into account all the correlations of contaminations from one class to the other.

A set of 11 variables was chosen for their discriminant power to recognise the final state products: they were based on the kinematical, ionisation and calorimetric information provided by several detector modules separately (TPC, HPC, HCAL, MUC) and, as far as possible, the information was transferred to the neural network in a way such that it did not depend on the detector calibration. The neural network performance being estimated on the basis of the simulated data, some variables needed to be re-calibrated in order to get a better agreement between the experimental distributions and the simulation, and to get a less biased estimation of the migration matrices.

For the  $\tau \rightarrow e\nu_e\nu_\tau$ ,  $\tau \rightarrow \mu\nu_\mu\nu_\tau$ , and  $\tau \rightarrow \pi/K\nu_\tau$  channels, the identification efficiencies obtained by the neural networks were comparable to the ones reached by classical methods usually devoted to the selection of only one  $\tau$  decay mode. They were respectively of the order of 96%, 97% and 85% inside the geometrical acceptance. For the  $\rho$  channel, an efficiency of the order of 80% was reached, i.e. about 10% higher than in the classical analysis, for a background level 5% percents higher. This was possible thanks to the ability of the neural network to take into account all correlations existing between the physical quantities describing the final state products (i.e. the input variables). This technique allowed also a relatively efficient selection of the  $\tau \rightarrow a_1\nu_\tau \rightarrow \pi\pi^0\pi^0\nu_\tau$  channel (56% of efficiency), which was not done using classical methods.

A very good agreement between data and simulation was found concerning the distributions of the neural network output values. The systematic effects due to the imperfect simulation of the input variables are estimated in the next chapter where the physical measurements ( $\mathcal{P}_\tau$ , exclusive branching ratios) are performed on the basis of this  $\tau$  decay mode classification.

# Chapter 6

## Measurement of the $\tau$ polarisation

The first section of this chapter describes the experimental method adopted for the measurement of the  $\tau$  polarisation. The results are given in the second section for the three years of data taking (93, 94 and 95 data). The systematic errors are estimated in the third section. In section 6.4, the Michel parameters are introduced for a preliminary test of the V–A Lorentz structure of the charged current assumed in what follows. Results are combined and discussed in the next chapter (Chapter 7).

### 6.1 Method for the experimental measurement of the $\tau$ polarisation

The mean polarisation of the  $\tau$  lepton ( $\langle \mathcal{P}_\tau \rangle$ ) can be statistically estimated from the energy spectrum of the  $\tau$  decay products (see section 2.3.2):

- for the  $\tau \rightarrow e\nu_e\nu_\tau$  and  $\tau \rightarrow \mu\nu_\mu\nu_\tau$  channels, the variable used is:

$$x_l = E_l/E_\tau, \quad l = e, \mu, \quad (6.1)$$

- for the  $\tau \rightarrow \pi/K\nu_\tau$  channel, it is:

$$\cos \theta^* = 2x_\pi - 1, \quad x_\pi = E_\pi/E_\tau, \quad (6.2)$$

- for the  $\tau \rightarrow \rho\nu_\tau$  and  $\tau \rightarrow a_1\nu_\tau$  channels, the 2-dimensional spectrum of the energy of the charged particle and of the total neutral energy is needed, using the variables:

$$\cos \theta^* = \frac{2x_h - 1 - (m_h/m_\tau)^2}{1 - (m_h/m_\tau)^2}, \quad x_h = \frac{E_h}{E_\tau} \quad (6.3)$$

and

$$\cos \psi = \frac{m_h}{\sqrt{m_h^2 - 4m_\pi^2}} \frac{E_{charged} - E_{neutral}}{E_{charged} + E_{neutral}}, \quad h = \rho, a_1 \quad (6.4)$$

where  $E_{charged}$  is the energy of the final state charged particle (a  $\pi^\pm$ ) and  $E_{neutral}$  is the total energy of the final state neutral particles (one or two  $\pi^0$ 's). The hadron energy  $E_h$  is reconstructed by taking the norm of the vectorial sum of the momentum of the detected charged and neutral particles. The  $\tau$  energy  $E_\tau$  is approximated by the beam energy.

Figure 6.1 shows how these variables are sensitive to the  $\tau$  helicity: the solid-line and dashed-line histograms represent the distributions of the variables for decay products of  $\tau$ 's of respectively right-handed helicity ( $h_\tau = +1$ ) and left-handed helicity ( $h_\tau = -1$ ), for simulated events which have been selected as 1-prong  $\tau$  decay candidates (see Chapter 4). Two-dimensional distributions are also shown for the  $\rho$  and for the  $a_1$  channels (figure 6.2). The displayed distributions are made using the *true* quantities, i.e. the momentum or energy without any detector effect, as it has been produced at the generator level. It can be observed that the sensitivity of the variable  $\cos\theta^*$  to the  $\tau$  helicity is lower for the  $\rho$  channel than for the  $\pi$  channel because of the different spins of the hadrons, and that it decreases from the  $\rho$  channel to the  $a_1$  channel because of the larger mass of the  $a_1$ . The introduction of the variable  $\cos\psi$  allows to regain some sensitivity, however more efficiently for the  $\rho$  channel than for the  $a_1$  channel. Indeed, the  $a_1$  decay being a three body decay, the expression of  $\cos\psi$  given above is not optimal for that decay mode. The expression of  $\cos\psi$  which describes more exactly the  $a_1$  decay, given for example in reference [16], can be used in the case of the  $a_1$  decay into three charged pions because the kinematical information of all decay products can be measured with a much greater precision than in the case where two of the three final state particles are neutral pions. The  $a_1$  decay mode into three charged pions was analysed, for the  $\tau$  polarisation measurement, in two other works, using the DELPHI data ([46] and [47]).

It is not possible to directly determine  $\langle\mathcal{P}_\tau\rangle$  from a fit of the theoretical expression of the spectra (2.43, 2.44, 2.47) to the experimental distributions, because of the distortion of the spectra due to several causes:

- the selection inefficiencies
- the contamination from background sources
- the resolution of the detector which smears the energies
- other detector effects: loss of tracks or of neutral electromagnetic showers

Figures 6.3 and 6.4 present the distributions of the *true* momentum<sup>1</sup> and neutral energy (solid line) and of the reconstructed momentum and neutral energy (dashed line) for simulated electrons, muons, pions,  $\rho$ 's and  $a_1$ 's, and the ratios of the reconstructed quantity to the *true* quantity. An important smearing of the electron momentum is observed. It is caused by the loss of energy due to multiple scattering and bremsstrahlung, the rate of which is higher for the electron because of its very small mass, and increases with increasing energy of the particle. The momentum spectrum of the pions is slightly affected by secondary hadronic interactions. The momentum resolution of the hadrons  $\rho$  and  $a_1$  is mainly determined by the precision on the reconstruction of the energy of the neutral particles. The neutral energy can be totally or partially lost because of dead zones of the detector or because of threshold effects at low energy. Both effects affect more the  $a_1$  channels than the  $\rho$  channel because of the larger number of photons present in the final state products of the  $a_1$  decay.

All the effects listed above lead to a reduction of the sensitivity of the variables to  $\langle\mathcal{P}_\tau\rangle$  and of the statistical weight of each decay mode used for the determination of  $\langle\mathcal{P}_\tau\rangle$  (see table 5.14): normalising to the weight of the pion channel (after reduction of the sensitivity), the weight of the  $\rho$  decay mode decreases from 1.6 to 1.1, the electron mode from 0.2 to 0.1, and the relative weight of the muon and  $a_1$  modes remain respectively at 0.2 and 0.1.

---

<sup>1</sup>Neglecting the particle mass, the momentum of the charged particle  $p_l$  is equivalent to its energy  $E_l$ .

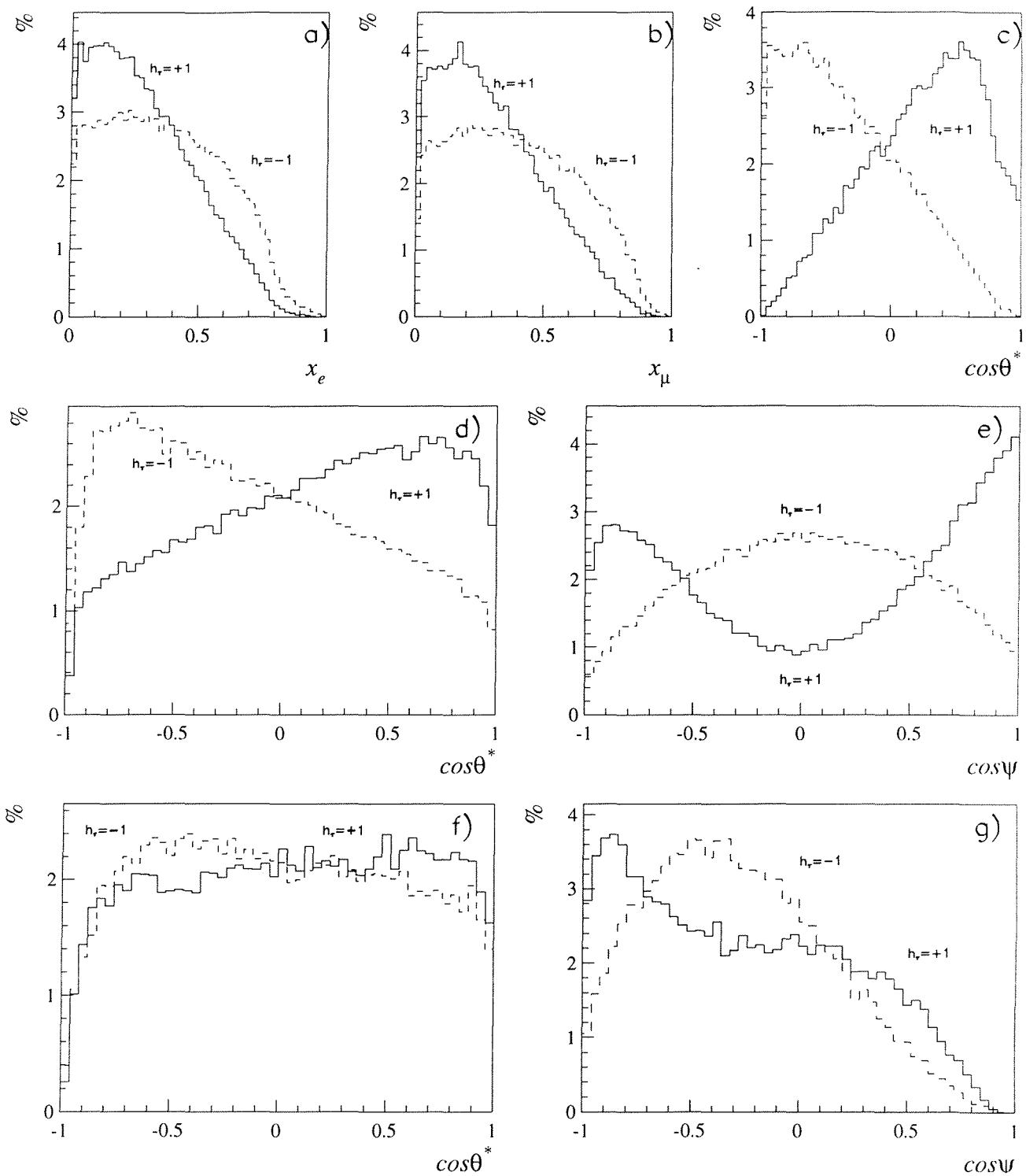


Figure 6.1: Distributions of the kinematical variables of the  $\tau$  decay products, which are sensitive to the  $\tau$  helicity state  $h_\tau = \pm 1$ , for simulated events: a)  $x_e = E_e/E_\tau$  for the  $\tau \rightarrow e\nu_e\nu_\tau$  channel, b)  $x_\mu = E_\mu/E_\tau$  for the  $\tau \rightarrow \mu\nu_\mu\nu_\tau$  channel, c)  $\cos\theta^*$  for the  $\tau \rightarrow \pi\nu_\tau$  channel, d) and e)  $\cos\theta^*$  and  $\cos\psi$  for the  $\tau \rightarrow \rho\nu_\tau$  channel, f) and g)  $\cos\theta^*$  and  $\cos\psi$  for the  $\tau \rightarrow a_1\nu_\tau$  channel. The distributions are made with the true values of the variables, where no detector effect has been introduced. (Only events satisfying the  $\tau^+\tau^-$  selection enter the histograms.)

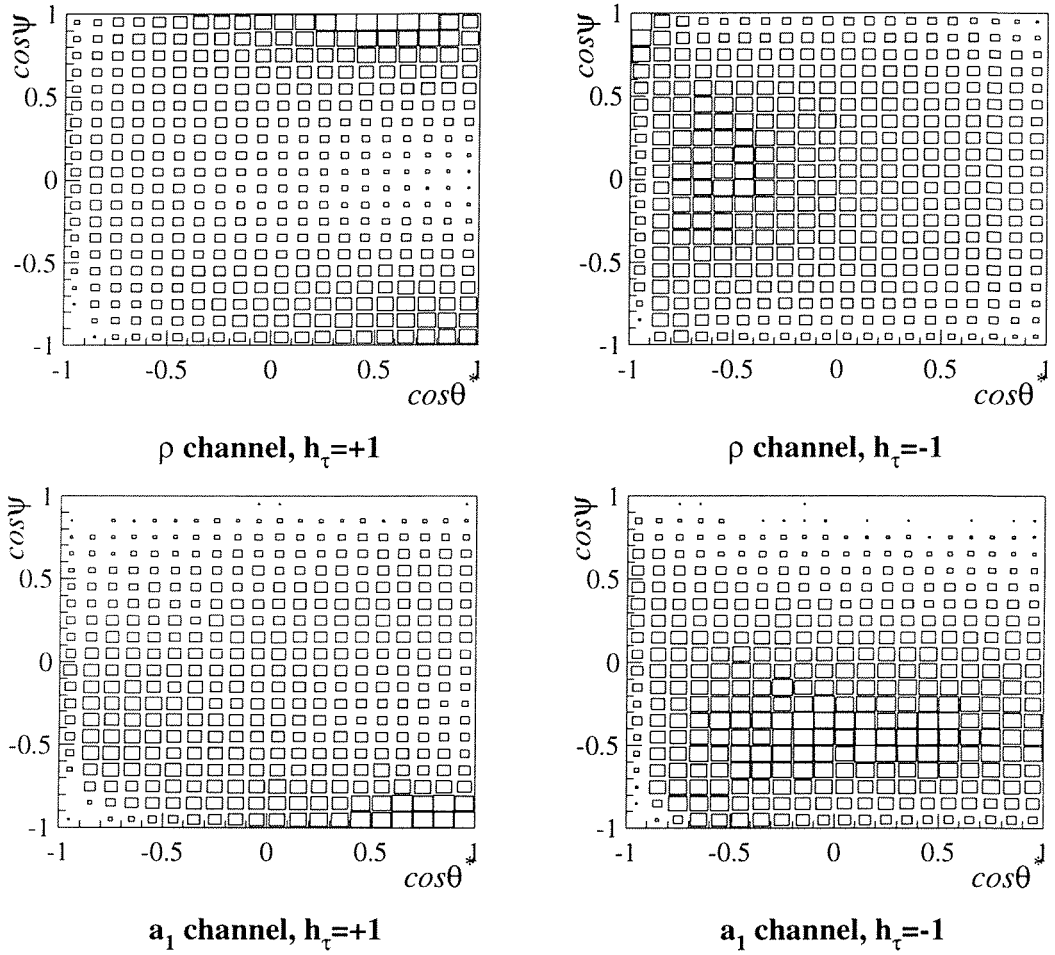


Figure 6.2: *Two-dimensional distributions corresponding to the figures 6.1, d) to g): the surfaces of the boxes are proportional to the number of events entering the corresponding range of the distribution.*

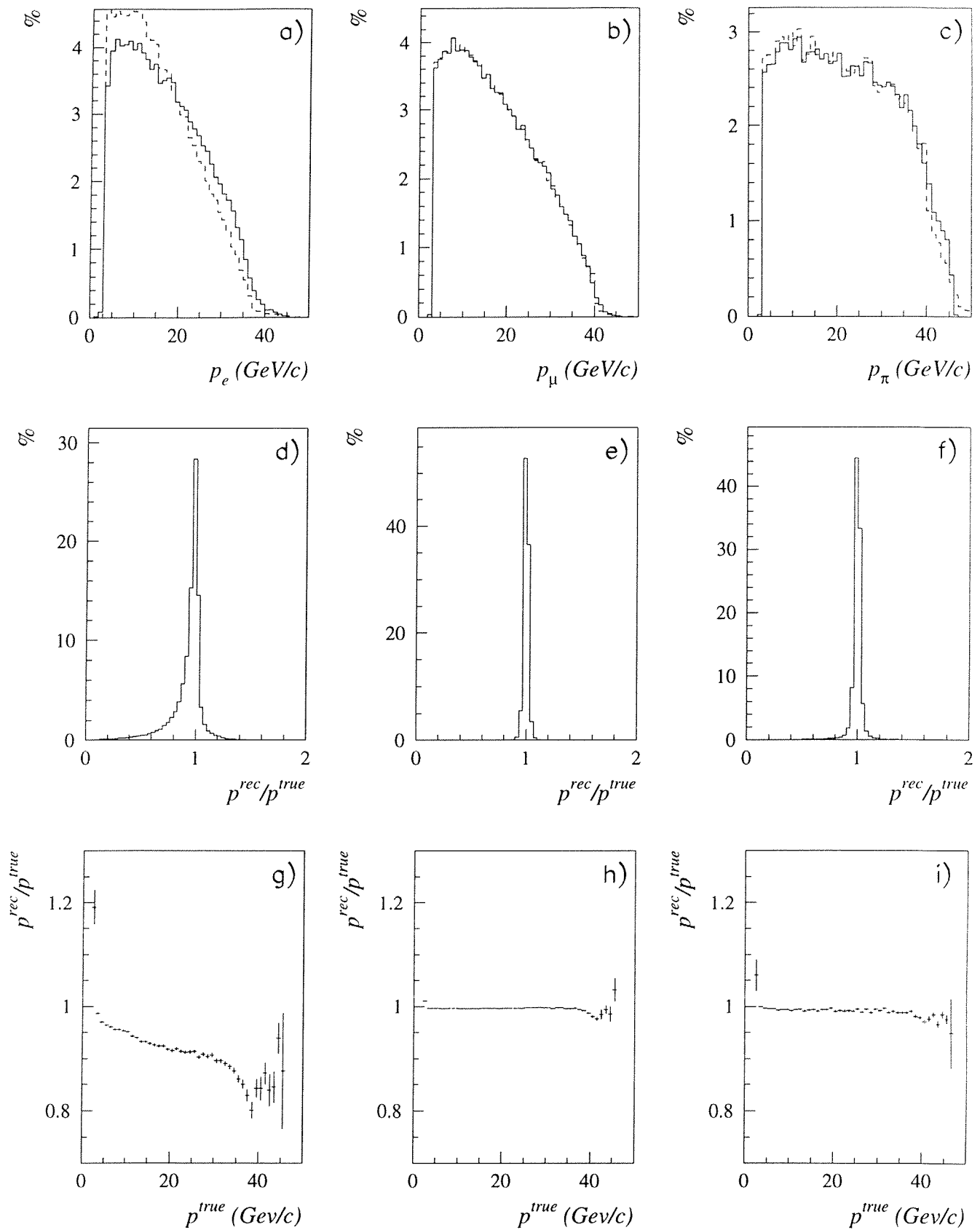


Figure 6.3: Distribution of the momentum of charged particles produced in simulated  $\tau$  decay events: a) electron momentum ( $p_e$ ), b) muon momentum ( $p_\mu$ ), c) pion momentum ( $p_\pi$ ). The solid line corresponds to the true momentum (no detector effect) ( $p^{\text{true}}$ ) and the dashed line corresponds to the reconstructed momentum ( $p^{\text{rec}}$ ). Histograms d), e), and f) give the distribution of the ratio of  $p^{\text{rec}}/p^{\text{true}}$  respectively for the electrons, muons and pions. Figures g), h) and i) show the average ratio  $p^{\text{rec}}/p^{\text{true}}$  in function of  $p^{\text{true}}$ , respectively for the electrons, muons and pions.

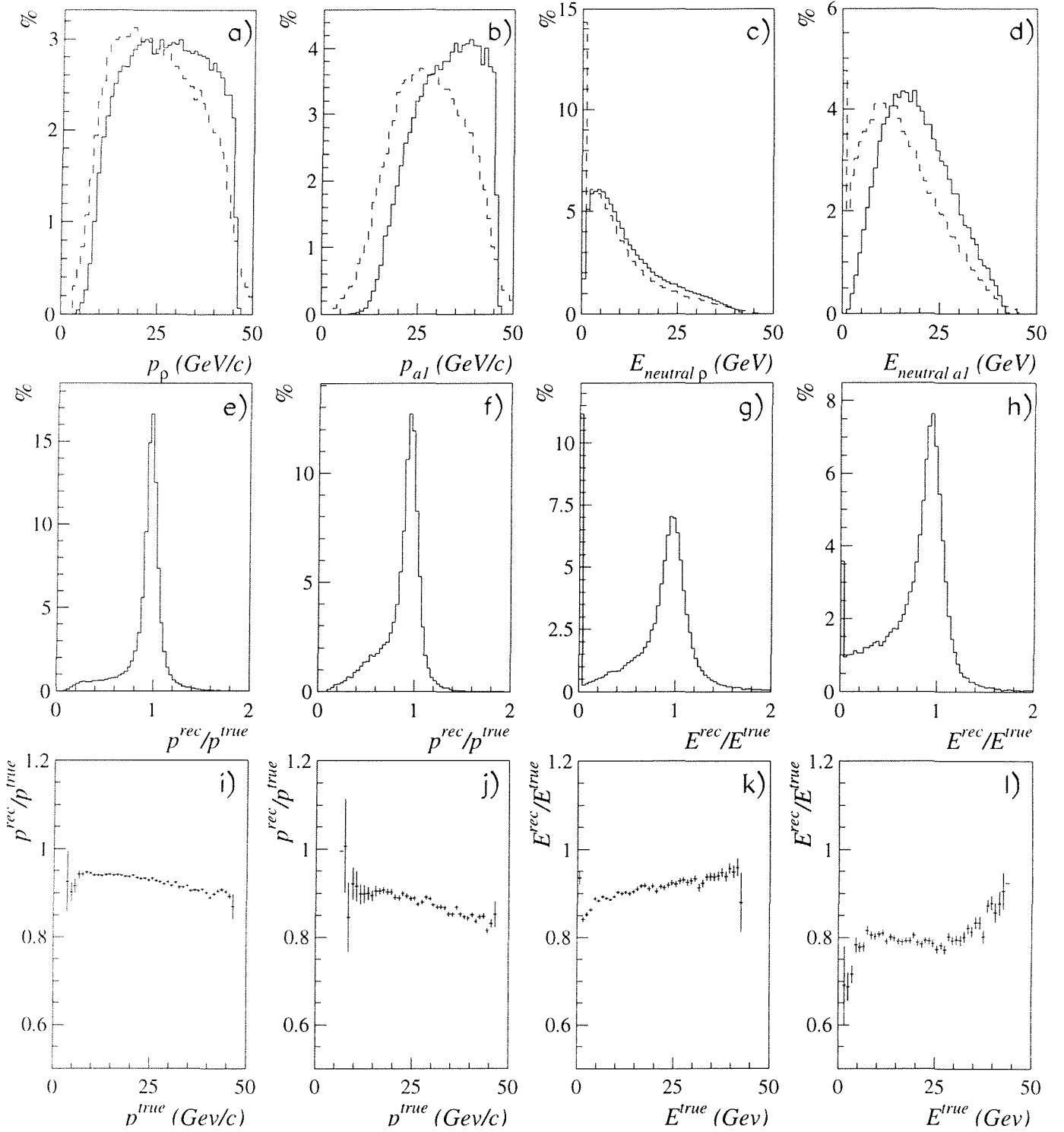


Figure 6.4: Distribution of the momentum and of the energy of particles produced in simulated  $\tau$  decay events: a)  $\rho$  momentum ( $p_\rho$ ), b)  $a_1$  momentum ( $p_{a_1}$ ), c)  $\rho$  neutral energy ( $E_{neutral \rho}$ ), d)  $a_1$  neutral energy ( $E_{neutral a_1}$ ). The solid line corresponds to the true momentum or energy (no detector effect) ( $p^{true}$ ,  $E^{true}$ ) and the dashed line corresponds to the reconstructed momentum or energy ( $p^{rec}$ ,  $E^{rec}$ ). Histograms e), f), g) and h) give the distribution of the ratio of  $p^{rec}/p^{true}$  and  $E^{rec}/E^{true}$  respectively for the  $\rho$  and the  $a_1$  channels. Figures i), j), k) and l) show the average ratios  $p^{rec}/p^{true}$  and  $E^{rec}/E^{true}$  (excluding events for which  $E^{rec} = 0$ ) in function of  $p^{true}$  or  $E^{true}$ , respectively for the  $\rho$  and the  $a_1$  channels.

The method for the determination of  $\langle \mathcal{P}_\tau \rangle$  consists in fitting to the experimental distributions, a linear combination of the simulated distributions of the relevant reconstructed variables  $\{\vec{x}\}$  ( $\{\vec{x}\} = \{x_l\}$ ,  $\{\cos \theta^*\}$ , or  $\{\cos \theta^*, \cos \psi\}$ ) obtained for decay products from  $\tau$ 's of helicity  $+1$  and from  $\tau$ 's of helicity  $-1$ . The simulated distributions include all the effects listed above when the contamination of external background sources ( $e^+e^-$ ,  $\mu^+\mu^-$ ,  $q\bar{q}$ ,  $e^+e^-f\bar{f}$ ) are properly taken into account in addition to the  $\tau$  events. The value of  $\langle \mathcal{P}_\tau \rangle$  is introduced in the fit procedure as a free parameter, weighting the contributions of the  $h_\tau = +1$  and  $h_\tau = -1$  simulated  $\tau$  decay events.

Using the maximum likelihood method for the adjustment<sup>2</sup> of  $\langle \mathcal{P}_\tau \rangle$ , the likelihood function  $\mathcal{L}(\langle \mathcal{P}_\tau \rangle)$  is computed as follows:

$$\mathcal{L} = \prod_i \prod_b \frac{N_{ib}^{mc}(\langle \mathcal{P}_\tau \rangle)^{N_{ib}^r} e^{-N_{ib}^{mc}(\langle \mathcal{P}_\tau \rangle)}}{N_{ib}^r!} \quad (6.5)$$

where

- $i$  designates the  $\tau$  decay channel ( $e$ ,  $\mu$ ,  $\pi/K$ ,  $\rho$  or  $a_1$  channel) on which the fit is performed,
- $b$  loops over the number of bins into which the spectrum of the variable  $\{\vec{x}\}$  has been divided.
- $N_{ib}^r$  is the number of real events classified into class  $i$ , having  $\{\vec{x}\} \in \text{bin } b$ ,
- $N_{ib}^{mc}(\langle \mathcal{P}_\tau \rangle)$  is the expected number of events selected in class  $i$  and having  $\{\vec{x}\} \in \text{bin } b$ , for a given value of  $\langle \mathcal{P}_\tau \rangle$ . It is evaluated as:

$$\begin{aligned} N_{ib}^{mc}(\langle \mathcal{P}_\tau \rangle) = & N_{norm} \sum_j Br_j \left( \frac{1 + \langle \mathcal{P}_\tau \rangle}{2} f_j^+(b) \epsilon_{j \rightarrow i, b}^+ + \frac{1 - \langle \mathcal{P}_\tau \rangle}{2} f_j^-(b) \epsilon_{j \rightarrow i, b}^- \right) \\ & + 2\mathcal{L}_{int} \sum_{j'} \sigma_{j'} f_{j'}(b) \epsilon_{j' \rightarrow i, b} \end{aligned} \quad (6.6)$$

In this expression:

- $N_{norm}$  is the normalisation factor that constraints the total number of simulated events to be equal to the total number of real events ( $\sum_i \sum_b N_{ib}^{mc} = \sum_i \sum_b N_{ib}^r$ ).
- $j$  loops over all possible  $\tau$  decay final states, of respective branching ratios  $Br_j$ , i.e. the signal decay modes ( $e$ ,  $\mu$ ,  $\pi/K$ ,  $\rho$  or  $a_1$  channel) plus, inclusively, the other possible final states  $\tau \rightarrow X\nu_\tau$ <sup>3</sup>. The world-average value of  $Br_X$  is computed as  $1 - Br_e - Br_\mu - Br_{\pi/K} - Br_\rho - Br_{a_1}$  and is equal to  $(18.29 \pm 0.28)\%$ . The world-average values of  $Br_e$ ,  $Br_\mu$ ,  $Br_{\pi/K}$ ,  $Br_\rho$  and  $Br_{a_1}$  are respectively:

$$\begin{aligned} Br_e &= (17.83 \pm 0.08) \% \\ Br_\mu &= (17.35 \pm 0.10) \% \\ Br_{\pi/K} &= (12.03 \pm 0.14) \% \\ Br_\rho &= (25.24 \pm 0.16) \% \\ Br_{a_1} &= (9.27 \pm 0.14) \% \end{aligned}$$

<sup>2</sup>The minimisation of  $-\log \mathcal{L}$  was performed using the dedicated program MINUIT [48] provided by the CERN software library.

<sup>3</sup> $X$  can be  $\pi 3\pi^0$ ,  $\pi 2K^0$ ,  $KK^0$ ,  $\pi\pi^0 K^0$ ,  $\eta\pi\pi^0$ ,  $\gamma\pi\pi^0$ ,  $KK^0\pi^0$ ,  $K2\pi^0$ ,  $K^*$ ,  $\pi 2K$ ,  $K2\pi$ ,  $3\pi$ ,  $3\pi\pi^0$ ,  $3\pi 2\pi^0$ ,  $3\pi 3\pi^0$ ,  $5\pi$ ,  $5\pi\pi^0$ .



- $\mathcal{L}_{int}$  is the integrated luminosity corresponding to the sample of the analysed experimental data,
- $j'$  loops over the external sources of backgrounds ( $e^+e^-$ ,  $\mu^+\mu^-$ ,  $q\bar{q}$ ,  $e^+e^-ff$ ) of production cross-section  $\sigma_{j'}$
- $f_j^\pm(b)$  is the probability that a  $\tau$  of helicity  $h = \pm 1$ , decays through the decay mode of type  $j$ , producing final state particles which have  $\{\vec{x}\} \in \text{bin } b$ .
- $\epsilon_{j \rightarrow i, b}^\pm$  is the probability that, for a given value of  $\{\vec{x}\}$ , a  $\tau$  decay final state product of type  $j$  is selected as a  $\tau$  decay final state product of type  $i$ , when the decaying  $\tau$  is of helicity  $h = \pm 1$ .
- $f_{j'}(b)$  is the probability that a particle is produced with  $\{\vec{x}\} \in \text{bin } b$  through the interaction process of type  $j'$ .
- $\epsilon_{j' \rightarrow i, b}$  is the probability that, a particle produced through an external background process type  $j'$ , with  $\{\vec{x}\} \in \text{bin } b$ , is selected as a  $\tau$  decay final state product of type  $i$ .

The products  $f_j^\pm(b) \cdot \epsilon_{j \rightarrow i, b}^\pm$ , or  $f_{j'}(b) \cdot \epsilon_{j' \rightarrow i, b}$  are directly obtained from the relevant spectra after the complete selection of the simulated events (1-prong  $\tau$  selection and identification by the neural networks of the  $\tau$  decay mode).

The expression 6.6 takes into account the possible polarisation dependence of the internal backgrounds (i.e. migration of events from the  $\tau$  decay mode  $j$  to the  $\tau$  decay mode  $i$ ). As shown in [49], the fact that both  $\tau$  decays of a same event are sometimes used for the polarisation determination while they are completely correlated leads to a negligible under-estimation of the statistical error of the result.

The exclusive branching ratios of the  $\tau \rightarrow e\nu_e\nu_\tau$  ( $Br_e$ ),  $\tau \rightarrow \mu\nu_\mu\nu_\tau$  ( $Br_\mu$ ),  $\tau \rightarrow \pi/K\nu_\tau$  ( $Br_{\pi/K}$ ),  $\tau \rightarrow \rho\nu_\tau$  ( $Br_\rho$ ), and  $\tau \rightarrow a_1\nu_\tau$  ( $Br_{a_1}$ ) channels can also be determined from the experimental data by keeping the  $Br_i$ 's as free parameters of the fit, together with  $\langle \mathcal{P}_\tau \rangle$ . In that case, the sum of the exclusive branching ratios was constraint to add up to 1 by defining  $Br_{a_1}$  as  $1 - Br_e - Br_\mu - Br_{\pi/K} - Br_\rho - Br_X$ .

## 6.2 Results

The  $\tau$  polarisation  $\langle \mathcal{P}_\tau \rangle$  was determined for the three samples of experimental data (93, 94 and 95), fitting simultaneously the 1-dimensional spectra of  $x_e$ ,  $x_\mu$  and  $\cos\theta^*$  for respectively the  $\tau \rightarrow e\nu_e\nu_\tau$ ,  $\tau \rightarrow \mu\nu_\mu\nu_\tau$  and  $\tau \rightarrow \pi/K\nu_\tau$  channels, and the 2-dimensional spectra of  $\cos\theta^* \times \cos\psi$  for the  $\tau \rightarrow \rho\nu_\tau$  and the  $\tau \rightarrow a_1\nu_\tau$  channels. The distributions of  $x_e$ ,  $x_\mu$  were divided into 17 bins between 0. and 1.1,  $\cos\theta^*$  into 17 bins between -1 and 1.3, and  $\cos\theta^* \times \cos\psi$  into  $10 \times 10$  bins for the ranges  $[-1, 1.3] \times [-1, 1.1]$ . Unphysical values of  $x_l$ ,  $\cos\theta^*$  and  $\cos\psi$  ( $> 1$ ) resulted from the experimental distortion of the momentum and energy reconstruction.

Because of the definitions of  $\cos\theta^*$  and  $\cos\psi$  (equations 6.3 and 6.4), the events classified into the  $\rho$  and  $a_1$  decay modes and having a reconstructed invariant mass ( $M_h = M_{inv}$ ) smaller than  $2m_\pi$  or larger than  $m_\tau$  (see figures 5.18, e) 5.19, e) and 5.20, e) ), were not included in the fit procedure (i.e.  $13.3\% \pm 0.4\%$  of the  $\rho$  candidates and  $24\% \pm 1\%$  of the  $a_1$  candidates). A systematic error was estimated to take into account possible discrepancies between the kinematical distributions for the rejected events in the simulated and the experimental samples (see next section).

The results of the fits are:

$$\begin{aligned}
\langle \mathcal{P}_\tau \rangle &= -0.140 \pm 0.024 \text{ (stat)} & (\chi^2/ndf = 1.3) & \text{for the 93 data,} \\
\langle \mathcal{P}_\tau \rangle &= -0.113 \pm 0.018 \text{ (stat)} & (\chi^2/ndf = 1.3) & \text{for the 94 data,} \\
\langle \mathcal{P}_\tau \rangle &= -0.164 \pm 0.025 \text{ (stat)} & (\chi^2/ndf = 1.1) & \text{for the 95 data.}
\end{aligned}$$

with a combined result of:

$$\langle \mathcal{P}_\tau \rangle = -0.133 \pm 0.012 \text{ (stat)}$$

The fitted distributions are represented on figures 6.5 and 6.6 for the global sample of the 93, 94 and 95 data. The points with error bars are the real data, the solid line histograms represent the total number of simulated events estimated using the fitted value of  $\langle \mathcal{P}_\tau \rangle$ . The dashed line shows the contribution of  $\tau$  decays of helicity +1 and the dotted line shows the contribution of  $\tau$  decays of helicity -1. The hatched areas represent the total external background. The 2-dimensional distributions of  $\cos \theta^* \times \cos \psi$  are displayed in the 10 slices of the  $\cos \theta^*$  spectrum. The values of  $\langle \mathcal{P}_\tau \rangle$ , fitted individually to each spectrum, are given in table 6.1.

Channel	$\langle \mathcal{P}_\tau \rangle$		
	1993	1994	1995
$\tau \rightarrow e\nu_e\nu_\tau$	$-0.43 \pm 0.10$	$-0.37 \pm 0.08$	$-0.28 \pm 0.11$
$\tau \rightarrow \mu\nu_\mu\nu_\tau$	$-0.15 \pm 0.08$	$-0.29 \pm 0.06$	$-0.28 \pm 0.08$
$\tau \rightarrow \pi/K\nu_\tau$	$-0.17 \pm 0.04$	$-0.13 \pm 0.03$	$-0.17 \pm 0.04$
$\tau \rightarrow \rho\nu_\tau$	$-0.09 \pm 0.04$	$-0.03 \pm 0.03$	$-0.12 \pm 0.04$
$\tau \rightarrow a_1\nu_\tau$	$+0.05 \pm 0.11$	$-0.05 \pm 0.09$	$-0.14 \pm 0.12$
$\tau \rightarrow \pi/K/\rho/a_1\nu_\tau$	$-0.12 \pm 0.02$	$-0.08 \pm 0.02$	$-0.14 \pm 0.03$

Table 6.1: Results of the measurement of  $\langle \mathcal{P}_\tau \rangle$  with the statistical error, for each  $\tau$  decay channel individually, and for the three hadronic decay modes inclusively.

When the exclusive branching ratios were left as free parameters, the results given in table 6.2 were obtained. No significant change of the results of  $\langle \mathcal{P}_\tau \rangle$  was observed.

Data	$\langle \mathcal{P}_\tau \rangle$	$Br_e(\%)$	$Br_\mu(\%)$	$Br_{\pi/K}(\%)$	$Br_\rho(\%)$	$Br_{a_1}(\%)$
93	$-0.141 \pm 0.024$	$17.75 \pm 0.25$	$17.84 \pm 0.23$	$11.81 \pm 0.25$	$26.10 \pm 0.43$	$8.21 \pm 0.35$
94	$-0.114 \pm 0.018$	$17.62 \pm 0.19$	$17.67 \pm 0.17$	$12.10 \pm 0.19$	$25.15 \pm 0.33$	$9.17 \pm 0.27$
95	$-0.167 \pm 0.026$	$17.00 \pm 0.26$	$17.71 \pm 0.25$	$12.57 \pm 0.28$	$25.36 \pm 0.46$	$9.07 \pm 0.39$
Comb.	$-0.134 \pm 0.013$	$17.49 \pm 0.13$	$17.73 \pm 0.12$	$12.12 \pm 0.13$	$25.47 \pm 0.23$	$8.88 \pm 0.19$
$\chi^2/2$	1.5	2.5	0.2	2.0	1.6	2.5
w.-a.		$17.83 \pm 0.08$	$17.35 \pm 0.10$	$12.03 \pm 0.14$	$25.24 \pm 0.16$	$9.27 \pm 0.14$

Table 6.2: Results of the measurement of  $\langle \mathcal{P}_\tau \rangle$  adjusted to the real data together with the  $\tau$  decay branching ratios (%). The errors are statistical only.

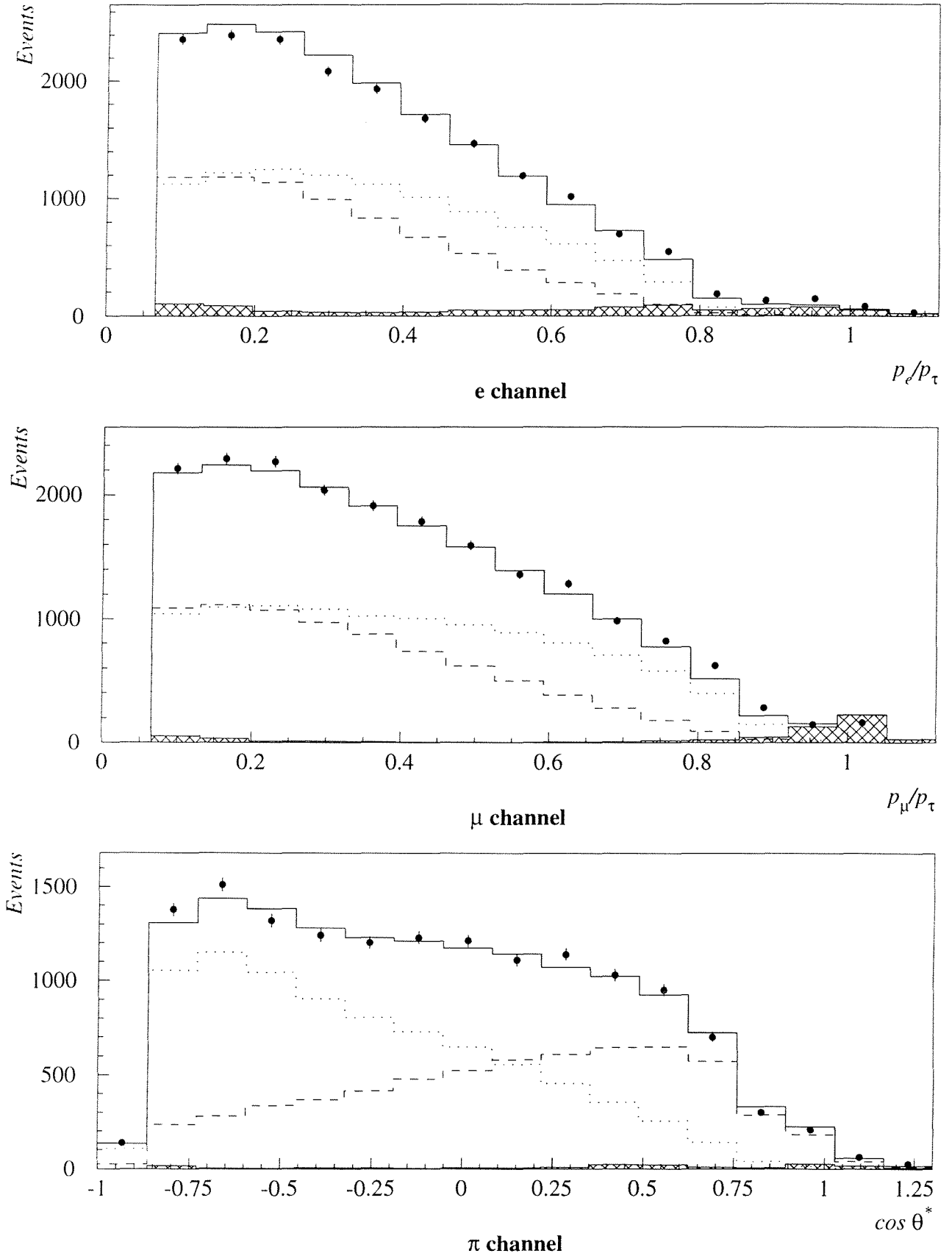


Figure 6.5: Distributions of the variables sensitive to  $\langle \mathcal{P}_\tau \rangle$ , after a fit to the 93, 94 and 95 real data (points with error bars), for the  $\tau \rightarrow e\nu_e\nu_\tau$ ,  $\tau \rightarrow \mu\nu_\mu\nu_\tau$  and  $\tau \rightarrow \pi/K\nu_\tau$  channels: the solid line histograms represent the total number of simulated events, the dashed (dotted) lines show the contribution of  $\tau$  decays of helicity +1 (-1); the hatched areas represent the total external background.

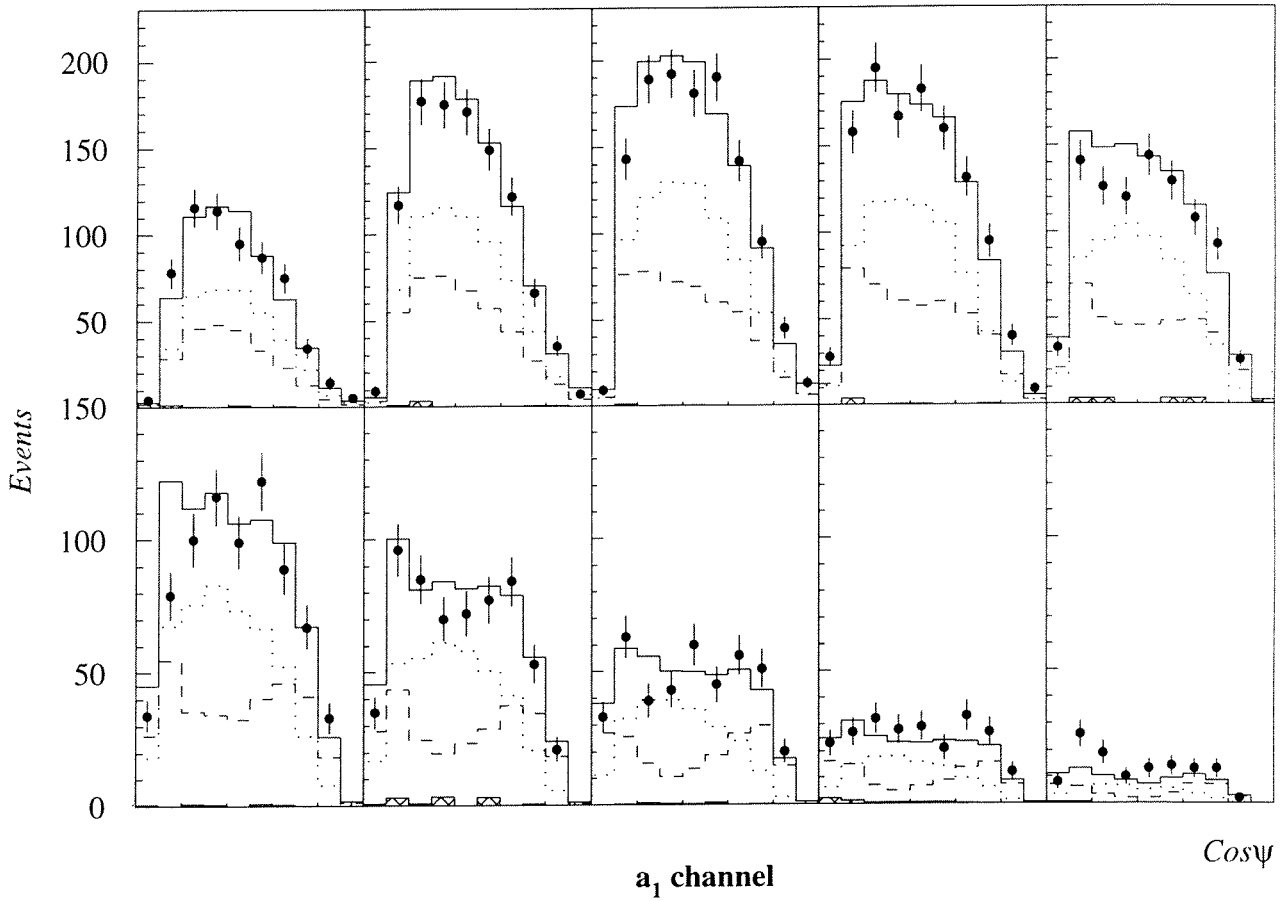
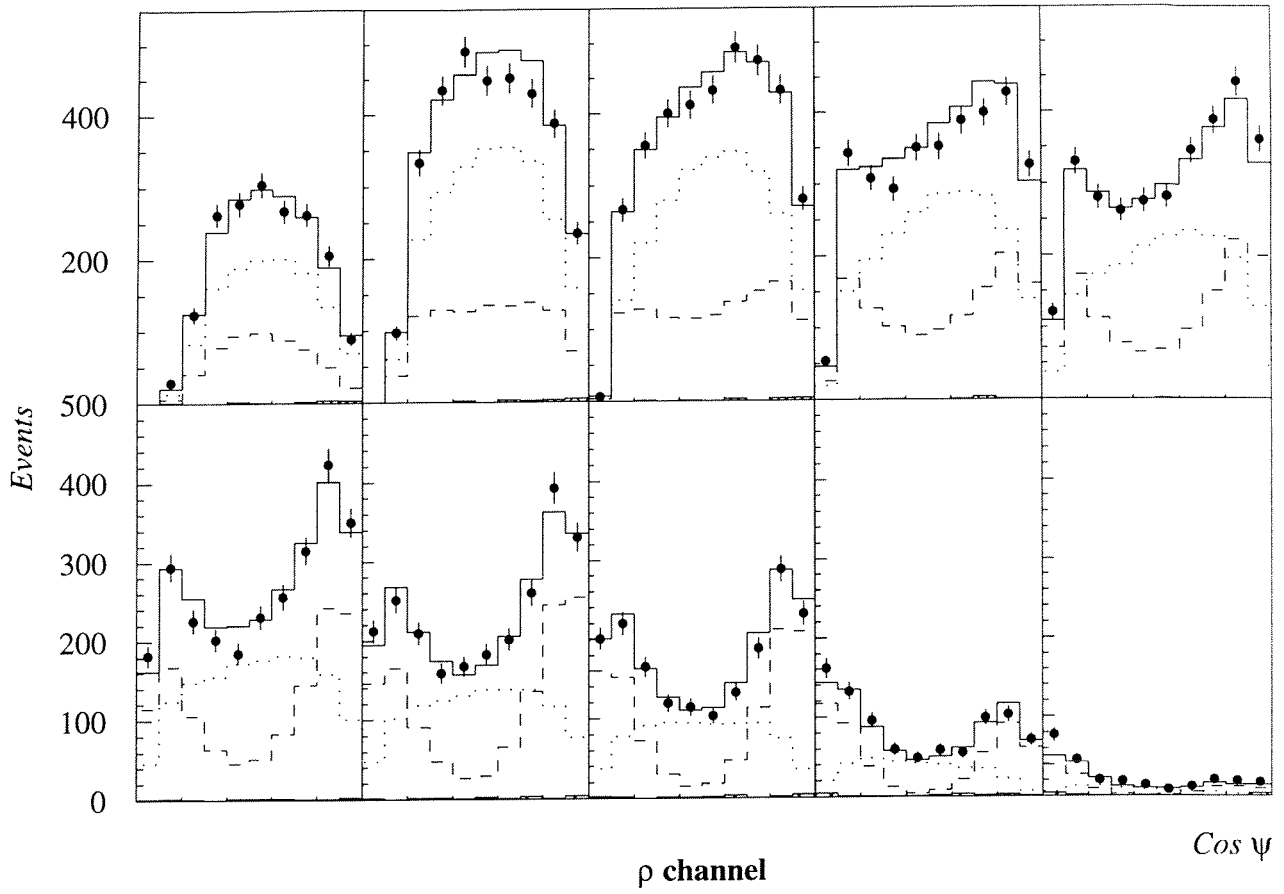


Figure 6.6: Same as 6.5 for the  $\tau \rightarrow \rho\nu_\tau$  and  $\tau \rightarrow a_1\nu_\tau$  channels. The 2-dimensional distributions of  $\cos \theta^* \times \cos \psi$  are displayed by representing the  $\cos \psi$  distribution (10 bins on the range  $[-1, 1.1]$ ) for the 10 slices of the  $\cos \theta^*$  spectrum ( $[-1, 1.3]$ ).

The correlations between the parameters are illustrated on figure 6.7. A strong correlation between  $Br_\rho$  and  $Br_{a_1}$  is observed as expected because of the large migrations from one channel to the other. No important correlations is observed between the parameter  $\langle \mathcal{P}_\tau \rangle$  and the branching ratios.

For the measurement of the  $\theta_{\tau^-}$  dependence of the  $\tau$  polarisation,  $\mathcal{P}_\tau(\cos \theta_{\tau^-})$ , the mean  $\tau$  polarisation was estimated for six domains of the polar angle of the  $\tau^-$  lepton (see table 6.3). The charge of the decaying  $\tau$  was estimated from the charge of the final state particle and its direction ( $\theta_{\tau^-}$ ) was approximated by the thrust axis direction. The obtained results are given in table 6.3.

$\mathcal{P}_\tau(\cos \theta_{\tau^-})$	1993	1994	1995	Combined
$-0.731 < \cos \theta_{\tau^-} < -0.488$	$+0.0001 \pm 0.055$	$+0.008 \pm 0.040$	$-0.094 \pm 0.059$	$-0.018 \pm 0.028$
$-0.488 < \cos \theta_{\tau^-} < -0.244$	$-0.043 \pm 0.057$	$-0.057 \pm 0.042$	$-0.026 \pm 0.060$	$-0.046 \pm 0.029$
$-0.244 < \cos \theta_{\tau^-} < 0$	$-0.050 \pm 0.065$	$-0.116 \pm 0.049$	$-0.043 \pm 0.068$	$-0.080 \pm 0.034$
$0 < \cos \theta_{\tau^-} < 0.244$	$-0.172 \pm 0.064$	$-0.184 \pm 0.049$	$-0.185 \pm 0.069$	$-0.181 \pm 0.034$
$0.244 < \cos \theta_{\tau^-} < 0.488$	$-0.309 \pm 0.051$	$-0.180 \pm 0.040$	$-0.214 \pm 0.057$	$-0.225 \pm 0.028$
$0.488 < \cos \theta_{\tau^-} < 0.731$	$-0.207 \pm 0.050$	$-0.198 \pm 0.039$	$-0.342 \pm 0.053$	$-0.237 \pm 0.027$

Table 6.3: Results of the measurement of  $\mathcal{P}_\tau$  with the statistical error, for six ranges of the  $\tau^-$  polar angle.

The theoretical  $\theta_{\tau^-}$  dependence of the  $\tau$  polarisation (see section 2.3.2) was then fitted to the experimental results of table 6.3:

$$\mathcal{P}_\tau(\cos \theta_{\tau^-}) = \frac{(1 + \cos^2 \theta_{\tau^-})\langle \mathcal{P}_\tau \rangle + 2 \cos \theta_{\tau^-} \mathcal{P}_Z}{(1 + \cos^2 \theta_{\tau^-}) + 2 \cos \theta_{\tau^-} \langle \mathcal{P}_\tau \rangle \mathcal{P}_Z}, \quad (6.7)$$

allowing the determination of  $\langle \mathcal{P}_\tau \rangle$  and  $\mathcal{P}_Z$  (2 parameters fit) or of  $\langle \mathcal{P}_\tau \rangle = \mathcal{P}_Z$ , assuming lepton universality (1 parameter fit). The results of the fit are given in table 6.4. They are represented graphically on figure 6.8 and are in very good agreement with the expected  $\cos \theta_{\tau^-}$  dependence of  $\mathcal{P}_\tau$ .

Data	$\langle \mathcal{P}_\tau \rangle$	$\mathcal{P}_Z$	$\chi^2/(6-2)$	$\langle \mathcal{P}_\tau \rangle = \mathcal{P}_Z$	$\chi^2/(6-1)$
93	$-0.134 \pm 0.023$	$-0.153 \pm 0.034$	1.0	$-0.140 \pm 0.019$	0.9
94	$-0.118 \pm 0.017$	$-0.111 \pm 0.026$	0.4	$-0.116 \pm 0.015$	0.3
95	$-0.157 \pm 0.025$	$-0.153 \pm 0.036$	1.1	$-0.156 \pm 0.020$	0.9
Comb.	$-0.131 \pm 0.012$	$-0.133 \pm 0.018$		$-0.133 \pm 0.010$	

Table 6.4: Results of the adjustments of  $\langle \mathcal{P}_\tau \rangle$  and  $\mathcal{P}_Z$  to the 93, 94 and 95 data, without and with assumption of lepton universality, and combined result for the three samples.

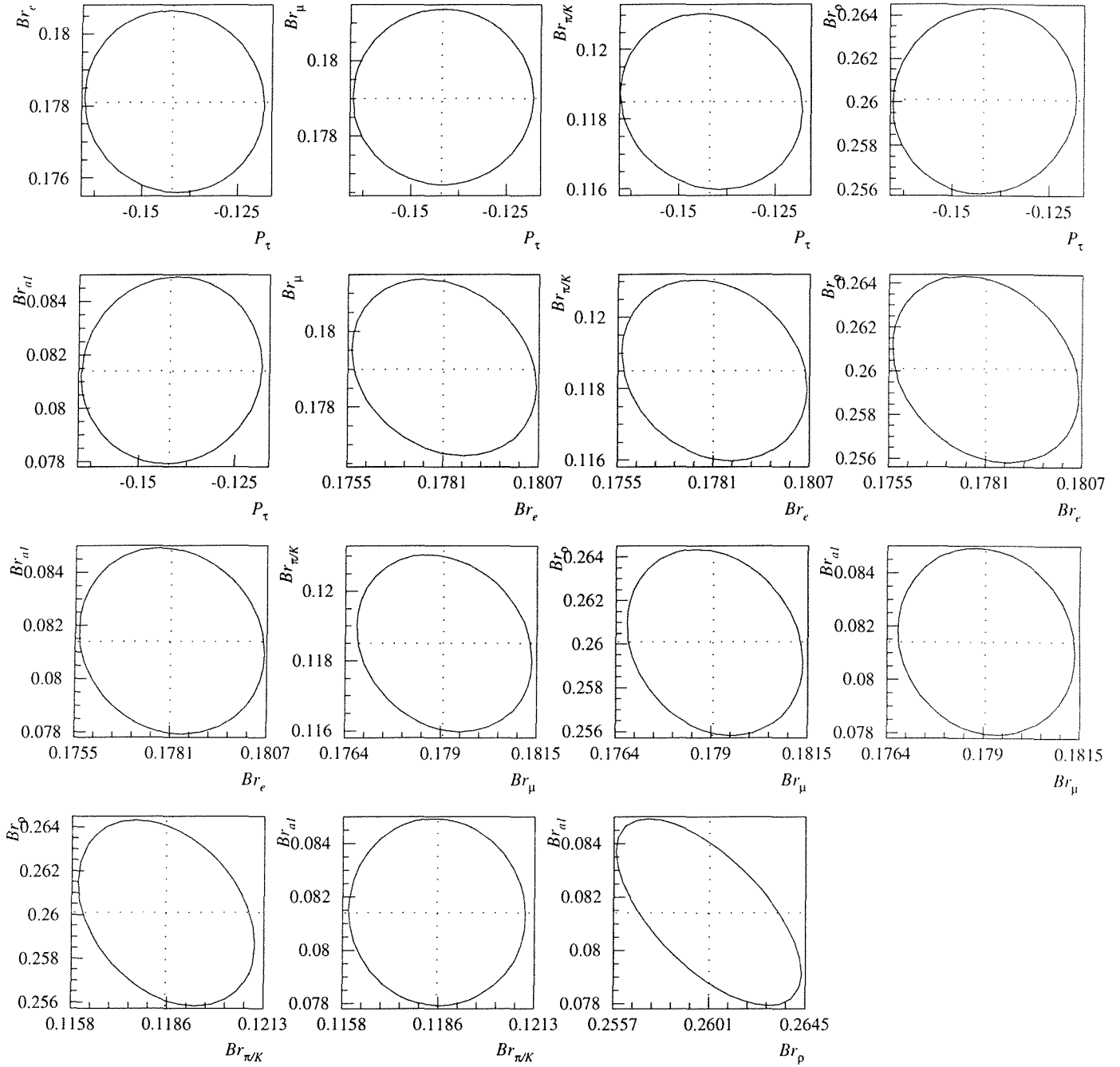


Figure 6.7: Contours for the confidence level corresponding to one standard deviation of the individual results, for pairs of the fitted parameters.

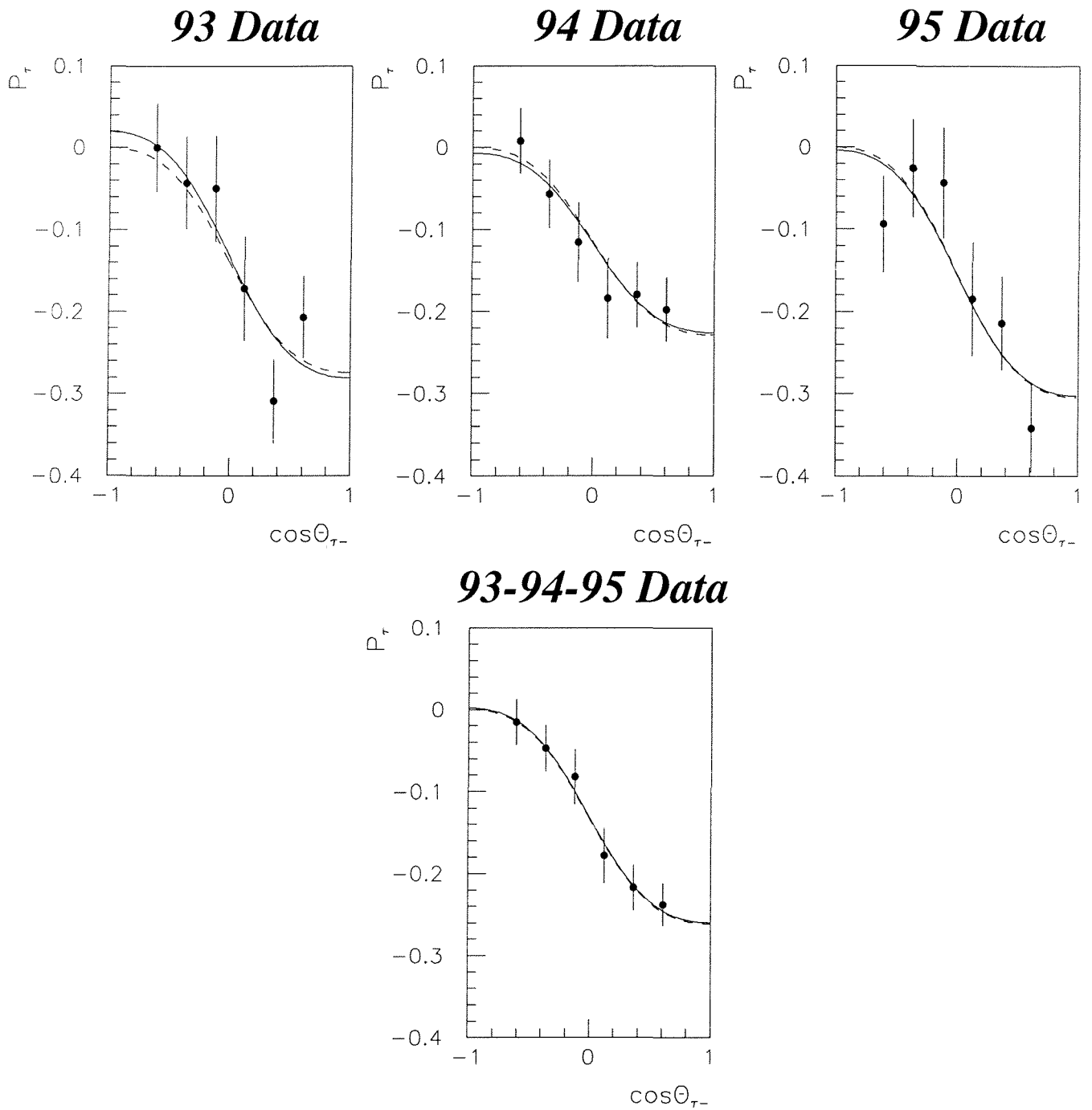


Figure 6.8: Results of the  $\mathcal{P}_{\tau}$  measurement as a function of  $\cos\theta_{\tau^-}$  (points with error bars) for the 93, 94 and 95 data, and for the combination of the three data samples. The solid (dashed) lines represent the fit results of the Standard Model expression of  $\mathcal{P}_{\tau^-}(\cos\theta_{\tau^-})$  to the data, without (with) the assumption of the universality of the Z coupling constants.

## 6.3 Study of the systematic effects

The influence on the results of  $\langle \mathcal{P}_\tau \rangle$ ,  $\mathcal{P}_Z$ , and on the measurement of the exclusive branching ratios  $Br_i$ , of several possible sources of systematical effects were studied and quantified. The estimated systematic errors are given in tables 6.5, 6.6, 6.7, 6.8 and 6.9, 6.10 and 6.11. The following sources were examined:

- **HCAL response:**

To estimate the effects of the incorrect simulation of the HCAL response, the measurements were repeated without the application of the corrections introduced in the previous chapter, and the variation of the results were taken as systematic errors.

- $E_{em}^{5-9}$  **calibration:**

In the previous chapter, it was shown that there was an incorrect simulation of the variable  $E_{em}^{5-9}$ , the electromagnetic energy deposited by the particle in the last five layers of the HPC, which was indirectly used for the particle identification. The variable had to be recalibrated for the simulated electrons. However, a discrepancy of the order of 10% was still observed after the correction. In order to take into account any possible effect of that disagreement and of the correction itself, the measurements were repeated, increasing  $E_{em}^{5-9}$  by 10% for the simulated electrons. The variation of the results were considered as systematic errors.

- **MUFLAG efficiency:**

After the classification of the events by the neural network, a slight discrepancy was observed concerning the distributions of the input variable  $\mu$ -flag (the muon identification flag provided by the MUFLAG package) for the events identified as  $\tau \rightarrow \mu\nu_\mu\nu_\tau$  decays, which was compatible with an over-estimation of the MUFLAG efficiency by 2 to 3 %, in the simulation. The measurements were then repeated, after forcing  $\mu$ -flag to zero for simulated muons, at random in 2% of the cases for the 93 and 94 data, and 3% for the 95 data, according to the observed disagreements. The variations of the results were considered as systematic errors.

- **dE/dX calibration:**

A global shift of  $\pm 0.02$  was applied to the pull of dE/dX for all simulated events. This variation corresponds to the uncertainty on the calibration of the variable. The average effect was taken as systematic errors. It affects mainly the estimation of  $Br_e$  and  $Br_{\pi/K}$ .

- $N_\gamma$ :

A disagreement was observed concerning the distributions of the variable  $N_\gamma$ : for the 1994 data there was a significant deficit of simulated events classified as  $\rho$ 's for the events with no reconstructed neutral particle ( $N_\gamma=0$ ). The effect of that discrepancy was estimated by repeating the measurements, forcing all simulated and real events of that category (i.e. classified as  $\rho$  and with  $N_\gamma=0$ ) to migrate to the  $\pi$  class. Half the effect on the results was taken as systematic error.

- $a_1$  **mass:**

Analysis studying the  $a_1$  decay mode into three charged pions (which allow a precise reconstruction of the  $a_1$  mass) have observed that the  $a_1$  mass value used in the Monte Carlo generator was a factor 1.024 lower than the experimental data [50]. To estimated the



systematic error due to that discrepancy, the measurements were repeated after scaling by 1.024 the reconstructed invariant mass used as input variable of the neural networks, for the simulated  $\tau \rightarrow a_1\nu_\tau$  decays. The variations in the results were taken as systematic error.

- **HPC energy calibration:**

As explained in section 4.2, the HPC energy had to be re-calibrated for the simulated events. The scaling factor applied for this re-calibration was varied within one standard deviation and the measurement were repeated. The average variations of the results were taken as systematic errors. Note that the HPC calibration affects both the classification of the events and the measurement of the parameters through the reconstruction of  $\cos\theta^*$  and  $\cos\psi$ .

- **Photon conversions:**

In the same way as what was done for the determination of the 1-*prong* topological branching ratio  $B_1$ , the selection efficiencies had to be corrected according to the factor  $1.36 \pm 0.02$  (stat) which quantifies the deficit of unreconstructed photon conversions in the simulated data. This correction was taken into account in the results presented here. The measurements were repeated without this correction and half the variation of the results were taken as systematic errors.

- **$\pi/K$  proportion:**

The pions and kaons present slightly different energy spectra and selection efficiencies. Their relative proportions in the simulated samples were varied within the one standard deviation on the world-average value of  $Br_K$  and the effects on the measurement of the parameters were estimated. The average variations of the results were taken as systematic errors.

- **Classification method:**

The classification method (“Winner Rule”) was changed as explained in the previous chapter to a cut on the neural network output values at 0.5 (see section 5.3.2). This implied a global loss of efficiency of 3.5% with an increase in the purity of the selected sample of 1.5% for the electrons, 0.7% for the muons, 2.8% for the pions, 2.4% for the  $\rho$ 's and 6.6% for the  $a_1$ 's. The measurement were repeated with that classification rule and half the variations of the results were taken as an estimation of the systematic error due to the imperfect generalisation power of the neural network. However, that error was not included in the computation of the total systematic errors since it is highly correlated to all effects estimated above, related to the discrepancies between the simulated and the experimental distributions of the input variables.

- **Branching fractions:**

The estimation of the influence of the value of the exclusive branching ratios on the measured quantities  $\langle\mathcal{P}_\tau\rangle$  and  $\mathcal{P}_Z$  was made by varying by plus and minus one standard deviation the world-average value of each exclusive branching fraction. The estimated error was found to be identical for the three years. It is dominated by the variation of  $Br_{\pi/K}$ .

For the measurement of the exclusive branching ratios themselves, the world-average value of  $Br_X$  was varied by plus or minus one standard deviation.

- **External background:**

The proportion of the total external background was varied by 10%. This is larger than the statistical error on the background, but we wanted to be conservative because of the uncertainty on the HPC energy calibration (which affects mainly the Bhabha background). The effect was found to be negligible.

- **$p_e$  and  $p_\mu$  reconstruction:**

In order to have an estimation of the influence of possible differences between real data and simulation concerning the electron and muon momentum reconstruction, the momentum of the simulated electrons and muons were scaled by a factor (after classification of the events by the neural networks) and the measurement were repeated. The factor applied to the momentum of the electrons and muons was estimated from the ratio of the experimental to simulated mean track momentum of respectively Bhabha and dimuon event candidates. For the three years, they were found to be respectively 0.9963, 0.9973 and 0.9998 for the electrons, and 1.004, 1.001 and 1.004 for the muons. The variation of the results were taken as systematic errors.

- **$\rho$  and  $a_1$  rejection:**

As explained in the previous section, about 13% of the  $\rho$  candidates and 24% of the  $a_1$  candidates were not used for the polarisation measurement because they had an unphysical reconstructed mass. In order to have an estimation of the effect of a possible discrepancy between the simulated and the real rejected events which would bias the efficiencies or the  $\cos\theta^* \times \cos\psi$  spectra, or both, the measurements were repeated, attributing those events to an additional bin of the  $\cos\theta^*$  versus  $\cos\psi$  distributions. Half the variations of the results, taking into account the statistical fluctuations, were taken as systematic errors.

- **$\theta_{\tau^-}$ :**

The approximation of direction of the  $\tau$  emission by the thrust axis direction generates a smearing of  $\cos\theta_{\tau^-}$ . The effect on the determination of  $\mathcal{P}_Z$  was estimated by fitting simulated events, using the true  $\tau$  polar angle and using the thrust direction. The shift on the results were taken as systematic error.

- **$\tau$  charge:**

The charge of the  $\tau$  was considered to be the charge of the final state particle. In case of a wrong charge determination, events were classified into the wrong  $\cos\theta_{\tau^-}$  bin. In order to estimate how much that could affect the determination of  $\mathcal{P}_Z$ , the fits were performed on simulated events, using the true  $\tau$  charge and using the reconstructed  $\tau$  charge. The shift on the results were taken as systematic error.

	1993	1994	1995
$\langle \mathcal{P}_\tau \rangle$	$-0.140 \pm 0.023$	$-0.113 \pm 0.018$	$-0.164 \pm 0.025$
MC statistics	0.0054	0.0038	0.0051
Systematic errors:			
HCAL response	0.0019	0.0024	0.0017
$E_{em}^{5-9}$ Calibration	0.0006	0.0003	0.0003
MUFLAG efficiency	0.0007	0.0007	0.0025
dE/dX Calibration	0.0002	0.0007	0.0009
$N_\gamma$ simulation	0.0015	0.0025	0.0014
$a_1$ mass	0.0005	0.0001	0.0002
HPC energy calibration	0.0017	0.0011	0.0011
Photon conversions	0.0006	0.0006	0.0006
$\pi/K$ proportions	0.0001	0.0001	0.0001
(Classification method)	(0.0034)	(0.0007)	(0.0043)
$Br$ 's	0.0017	0.0017	0.0017
External background	0.00003	0.00025	0.00005
$p_e, p_\mu$ reconstruction	0.0022	0.0003	0.0035
$\rho$ and $a_1$ rejection	0.0060	0.0015	0.0016
Total:	0.0073	0.0045	0.0056

Table 6.5: Results of the measurement of  $\langle \mathcal{P}_\tau \rangle$  with the statistical error, and estimation of the systematic errors. The error “Classification method” was not included in the total error (see text).

1993 Data	$\langle \mathcal{P}_\tau \rangle$	$\mathcal{P}_Z$	$\langle \mathcal{P}_\tau \rangle = \mathcal{P}_Z$
	$-0.134 \pm 0.023$	$-0.153 \pm 0.034$	$-0.140 \pm 0.019$
MC Statistics	0.0052	0.0076	0.0043
Systematic errors:			
HCAL response	0.0019	0.0017	0.0019
$E_{em}^{5-9}$ Calibration	0.0038	0.0073	0.0002
MUFLAG efficiency	0.0006	0.0006	0.0002
dE/dX Calibration	0.0003	0.0002	0.0001
$N_\gamma$ simulation	0.0019	0.0029	0.0022
$a_1$ mass	0.0010	0.0001	0.0007
HPC energy calibration	0.0012	0.0010	0.0011
Photon conversions	0.0006	0.0001	0.0004
$\pi/K$ proportions	0.0003	0.0005	0.0001
(Classification method)	(0.0053)	(0.0003)	(0.0035)
$B\tau$ 's	0.0017	0.0000	0.0012
External background	0.0000	0.0003	0.0001
$p_e, p_\mu$ reconstruction	0.0019	0.0006	0.0015
$\rho$ and $a_1$ rejection	0.0060	0.0023	0.0030
$\theta_{\tau^-}$	0.0005	0.0009	0.0005
$\tau$ charge	0.0000	0.0005	0.0000
Total:	0.0082	0.0085	0.0048

Table 6.6: Results of the measurement of  $\langle \mathcal{P}_\tau \rangle$  and  $\mathcal{P}_Z$ , without and with assumption of lepton universality, for the 93 data, with the statistical error. The error due to the limited statistics of simulated events (MC) and the estimation of the systematic errors are given separately. The error "Classification method" was not included in the total error (see text).

1994 Data	$\langle \mathcal{P}_\tau \rangle$	$\mathcal{P}_Z$	$\langle \mathcal{P}_\tau \rangle = \mathcal{P}_Z$
	$-0.118 \pm 0.017$	$-0.111 \pm 0.026$	$-0.116 \pm 0.015$
MC Statistics	0.0037	0.0055	0.0031
Systematic errors:			
HCAL response	0.0010	0.0011	0.0011
$E_{em}^{5-9}$ Calibration	0.0004	0.0000	0.0002
MUFLAG efficiency	0.0006	0.0006	0.0002
dE/dX Calibration	0.0009	0.0002	0.0005
$N_\gamma$ simulation	0.0024	0.0002	0.0016
$a_1$ mass	0.0005	0.0001	0.0003
HPC energy calibration	0.0014	0.0009	0.0012
Photon conversions	0.0006	0.0001	0.0004
$\pi/K$ proportions	0.0004	0.0002	0.0002
(Classification method)	(0.0010)	(0.0007)	(0.0004)
$B\tau$ 's	0.0017	0.0000	0.0012
External background	0.0007	0.0012	0.0009
$p_e, p_\mu$ reconstruction	0.0003	0.0010	0.0005
$\rho$ and $a_1$ rejection	0.0015	0.0004	0.0005
$\theta_{\tau^-}$	0.0005	0.0009	0.0005
$\tau$ charge	0.0000	0.0005	0.0000
Total:	0.0041	0.0025	0.0030

Table 6.7: Same as table 6.6 for the 94 data.

1995 Data	$\langle \mathcal{P}_\tau \rangle$	$\mathcal{P}_Z$	$\langle \mathcal{P}_\tau \rangle = \mathcal{P}_Z$
	$-0.157 \pm 0.025$	$-0.153 \pm 0.036$	$-0.156 \pm 0.020$
MC Statistics	0.0050	0.0073	0.0041
Systematic errors:			
HCAL response	0.0027	0.0029	0.0028
$E_{em}^{5-9}$ Calibration	0.0005	0.0004	0.0002
MUFLAG efficiency	0.0025	0.0001	0.0017
dE/dX Calibration	0.0008	0.0005	0.0005
$N_\gamma$ simulation	0.0002	0.0025	0.0006
$a_1$ mass	0.0003	0.0005	0.0003
HPC energy calibration	0.0004	0.0012	0.0005
Photon conversions	0.0006	0.0001	0.0004
$\pi/K$ proportions	0.0002	0.0001	0.0001
(Classification method)	(0.0036)	(0.0011)	(0.0021)
$Br$ 's	0.0017	0.0000	0.0012
External background	0.0002	0.0002	0.0001
$p_e, p_\mu$ reconstruction	0.0032	0.0000	0.0022
$\rho$ and $a_1$ rejection	0.0016	0.0022	0.0003
$\theta_{\tau^-}$	0.0005	0.0009	0.0005
$\tau$ charge	0.0000	0.0005	0.0000
Total:	0.0056	0.0048	0.0043

Table 6.8: Same as table 6.6 for the 95 data.

1993 Data	Exclusive $\tau$ branching ratios (%)				
	$Br_e$	$Br_\mu$	$Br_{\pi/K}$	$Br_\rho$	$Br_{a_1}$
	$17.75 \pm 0.25$	$17.84 \pm 0.23$	$11.81 \pm 0.25$	$26.10 \pm 0.43$	$8.21 \pm 0.35$
MC Statistics	0.041	0.038	0.041	0.069	0.058
Systematic errors:					
HCAL response	0.050	0.060	0.090	0.050	0.060
$E_{em}^{5-9}$ Calibration	0.030	0.000	0.020	0.050	0.050
MUFLAG efficiency	0.000	0.040	0.040	0.000	0.000
dE/dX Calibration	0.035	0.005	0.030	0.010	0.000
$N_\gamma$ simulation	0.000	0.000	0.010	0.005	0.000
$a_1$ mass	0.000	0.000	0.000	0.040	0.040
HPC energy calibration	0.010	0.000	0.005	0.020	0.050
Photon conversions	0.030	0.030	0.020	0.045	0.035
$\pi/K$ proportions	0.000	0.000	0.000	0.010	0.000
(Classification method)	(0.030)	(0.010)	(0.060)	(0.015)	(0.035)
$Br_X$	0.050	0.050	0.040	0.070	0.070
External Backgd.	0.050	0.010	0.010	0.040	0.010
Total:	0.103	0.093	0.115	0.115	0.128

Table 6.9: Results of the measurement of the exclusive branching ratios of the  $\tau$  1-prong decay channels, for the 93, with the error due to the real events statistics. The error due to the limited statistics of simulated events (MC) and the estimation of the systematic errors are given separately. The error "Classification method" was not included in the total error (see text).

1994 Data	Exclusive $\tau$ branching ratios (%)				
	$Br_e$	$Br_\mu$	$Br_{\pi/K}$	$Br_\rho$	$Br_{a_1}$
	$17.62 \pm 0.19$	$17.67 \pm 0.17$	$12.10 \pm 0.19$	$25.15 \pm 0.33$	$9.17 \pm 0.27$
MC Statistics	0.028	0.026	0.029	0.050	0.042
Systematic errors:					
HCAL response	0.040	0.060	0.090	0.030	0.060
$E_{em}^{5-9}$ Calibration	0.010	0.000	0.010	0.040	0.030
MUFLAG efficiency	0.000	0.040	0.040	0.000	0.000
dE/dX Calibration	0.030	0.005	0.040	0.020	0.010
$N_\gamma$ simulation	0.030	0.030	0.085	0.035	0.025
$a_1$ mass	0.000	0.000	0.000	0.020	0.020
HPC energy calibration	0.010	0.000	0.000	0.030	0.030
Photon conversions	0.030	0.030	0.025	0.045	0.035
$\pi/K$ proportions	0.010	0.010	0.010	0.000	0.010
(Classification method)	(0.015)	(0.015)	(0.030)	(0.040)	(0.025)
$Br_X$	0.050	0.050	0.040	0.070	0.070
External Backgd.	0.050	0.000	0.005	0.030	0.015
Total:	0.098	0.098	0.145	0.115	0.114

Table 6.10: Same as table 6.9 for the 94 data.

1995 Data	Exclusive $\tau$ branching ratios (%)				
	$Br_e$	$Br_\mu$	$Br_{\pi/K}$	$Br_\rho$	$Br_{a_1}$
	$17.00 \pm 0.26$	$17.71 \pm 0.25$	$12.57 \pm 0.28$	$25.36 \pm 0.46$	$9.07 \pm 0.39$
MC Statistics	0.038	0.035	0.039	0.066	0.055
Systematic errors:					
HCAL response	0.010	0.060	0.030	0.040	0.070
$E_{em}^{5-9}$ Calibration	0.020	0.010	0.010	0.010	0.010
MUFLAG efficiency	0.000	0.070	0.070	0.000	0.000
dE/dX Calibration	0.030	0.005	0.040	0.010	0.000
$N_\gamma$ simulation	0.015	0.015	0.070	0.025	0.010
$a_1$ mass	0.000	0.000	0.000	0.030	0.030
HPC energy calibration	0.010	0.000	0.030	0.030	0.060
Photon conversions	0.030	0.030	0.020	0.040	0.040
$\pi/K$ proportions	0.000	0.000	0.010	0.000	0.000
(Classification method)	(0.035)	(0.015)	(0.010)	(0.010)	(0.050)
$Br_X$	0.045	0.045	0.045	0.075	0.070
External Backgd.	0.055	0.015	0.010	0.045	0.010
Total:	0.088	0.109	0.126	0.116	0.127

Table 6.11: Same as table 6.9 for the 95 data.

## 6.4 Introduction of the Michel parameters and $h_{\nu_\tau}$ in the $\langle \mathcal{P}_\tau \rangle$ measurement

The measurement of the  $\tau$  polarisation performed in the previous section, was done assuming a pure V–A Lorentz structure of the charged current interaction describing the  $\tau$  lepton decay. In this section, we propose to take into account the possibility of a violation of the V–A rule, by allowing the Michel parameters  $\rho_l$ ,  $\delta_l$  and  $\xi_l$  as well as the  $\tau$ -neutrino helicity  $h_{\nu_\tau}$ , to be different from their standard values  $3/4$ ,  $3/4$ ,  $1$  and  $-1$  respectively (see chapter 2.3.1). These parameters were thus introduced as free parameters of the adjustment described below. The fourth Michel parameter  $\eta_l$  was fixed to its Standard Model value  $0$ .

The analysis presented in this section is a first approach of the measurement of the Michel parameters and  $h_{\nu_\tau}$ : only combinations of the  $\tau \rightarrow e\nu_e\nu_\tau$ ,  $\tau \rightarrow \mu\nu_\mu\nu_\tau$  and  $\tau \rightarrow \pi/K\nu_\tau$  decay modes were used (called  $ee$ ,  $e\mu$ ,  $e\pi$ ,  $\mu\mu$ ,  $\mu\pi$  and  $\pi\pi$  combinations), resulting in a reduced statistics so that only the statistical errors were estimated, since they are expected to dominate with respect to the systematic errors which are probably of the same order as the ones affecting the polarisation results presented in the previous section.

In order to let the Michel parameters vary (they are fixed to their Standard Model values in the Monte Carlo generator), the adjustment was performed starting from the semi-analytical expressions of the spectra provided in reference [51], which correct the spectra of reduced energy  $x_i = E_i/E_\tau$  of equations 2.39 and 2.43 for the final state radiations.

As explained in chapter 2.3.1, it is necessary to keep the information of the correlation between the  $\tau^+$  and the  $\tau^-$  decays because  $\langle \mathcal{P}_\tau \rangle$  is multiplied by  $\xi_l$  or by  $h_{\nu_\tau}$  in the expression of the energy distribution of the charged decay product.

The procedure was then the following: for a binning into  $N \times N$  intervals of the two-dimensional spectra  $x_i \times x_j \in [0, 1] \times [0, 1]$  of each combination  $ab$  ( $ab=ee, e\mu, e\pi, \mu\mu, \mu\pi$  or  $\pi\pi$ ),

- the correlated spectra  $R_{ab}(x_i, x_j) = \frac{d^2\Gamma_{ab}}{\Gamma_{ab}dx_idx_j}$  (see equation 2.40) were computed for the  $(N + 1) \times (N + 1)$  points.  $R_{ab}(x_i, x_j)$  is a sum of terms bilinear in the parameters  $p_k$  ( $p_k = h_{\nu_\tau}, \xi_e, \xi_\mu, \rho_e, \rho_\mu, \delta_e, \delta_\mu$ ):

$$R_{ab}(x_i, x_j) = \sum p_k p_l r_{abkl}(x_i, x_j) + \langle \mathcal{P}_\tau \rangle \sum p_m p_n r_{abmn}(x_i, x_j) ; \quad (6.8)$$

- each function  $r_{abmn}(x_i, x_j)$  was convoluted by the initial state radiation probability function (see equation 2.15):

$$\hat{r}_{abmn}(x_i, x_j) = \int_0^{v_{max}} dv \rho(v) \sigma_{f\bar{f}}^0(s(1-v)) r_{abmn}(x_i, x_j) ; \quad (6.9)$$

- the value of the functions  $\hat{r}_{abmn}(i, j)$  for the bin  $(i, j) = [x_{i-1}, x_i] \times [x_{j-1}, x_j]$  of the two-dimensional spectrum, was approximated by the average

$$\hat{r}_{abmn}(i, j) = \frac{1}{4} [\hat{r}_{abmn}(x_{i-1}, x_{j-1}) + \hat{r}_{abmn}(x_{i-1}, x_j) + \hat{r}_{abmn}(x_i, x_{j-1}) + \hat{r}_{abmn}(x_i, x_j)] ; \quad (6.10)$$

- the spectra were corrected for the detector effects and for the selection efficiencies and migrations, by applying a resolution  $\times$  migration matrix  $\mathcal{RM}(i, j, i', j', ab, a'b')$  estimated from simulated events. The matrix gives the probability that the charged particle of reduced energy  $x_i$  ( $x_j$ ) produced through the  $a$  (the  $b$ )  $\tau$  decay mode was identified as being produced through the  $a'$  (the  $b'$ )  $\tau$  decay mode, with a reconstructed reduced energy  $x_{i'}$  ( $x_{j'}$ );



- the spectra were normalised to the number of selected events after correction for the external background  $E_{a'b'}(i', j')$  and the other  $\tau$  decay combinations  $T_{a'b'}(i', j')$ . The set of parameters  $\vec{p}$  was determined by an adjustment, based on the maximum likelihood method, of the expected number of events  $N_{a'b'}^{exp}(i', j'; \vec{p})$  computed as:

$$N_{a'b'}^{exp}(i', j'; \vec{p}) = \sum_{i,j,ab} \hat{R}_{ab}(i, j; \vec{p}) \mathcal{R}\mathcal{M}(i, j, i', j', ab, a'b') + E_{a'b'}(i', j') + T_{a'b'}(i', j'), \quad (6.11)$$

to the number of experimental events  $N_{a'b'}^{real}(i', j')$  selected in the combination  $a'b'$  and the bin  $(i', j')$ .

The analysis was performed with a  $10 \times 10$  binning (square bins) of the two-dimensional spectra on the ranges  $[\frac{3GeV}{E_\tau}, 1] \times [\frac{3GeV}{E_\tau}, 1]$ , folded along the diagonal for the symmetric combinations (ee,  $\mu\mu$  and  $\pi\pi$ ).

For a verification of our computation of the theoretical spectra and of our fitting procedure, the parameters were fitted to the six simulated two-dimensional distributions, in each of the following steps:

1. fit the generated spectra (no detector effect, no selection effect, no background effect);
2. introduce the resolution and efficiency matrix;
3. introduce the internal migrations;
4. introduce the other  $\tau$  decay contaminations ( $T_{a'b'}(i', j')$ ).

The results are given in table 6.12 (the simulated value of  $\langle \mathcal{P}_\tau \rangle$  was -0.14). The  $\chi^2/ndf$  of the first fit result was 1.03 (=475/(465-5)) and the obtained values were statistically compatible with the expected values. The lepton universality was assumed for all steps. The step 4 was repeated without this assumption.

Step	$\langle \mathcal{P}_\tau \rangle$ (-0.14)	$h_{\nu\tau}$ (-1)	$\rho_l$ (0.75)	$\xi_l$ (1)	$\delta_l$ (0.75)
1	$-0.159 \pm 0.008$	$-1.03 \pm 0.02$	$0.75 \pm 0.01$	$1.04 \pm 0.06$	$0.76 \pm 0.06$
2	$-0.141 \pm 0.016$	$-1.01 \pm 0.04$	$0.78 \pm 0.02$	$1.03 \pm 0.12$	$0.66 \pm 0.13$
3	$-0.152 \pm 0.018$	$-0.95 \pm 0.04$	$0.77 \pm 0.02$	$1.05 \pm 0.13$	$0.64 \pm 0.13$
4	$-0.170 \pm 0.019$	$-1.00 \pm 0.05$	$0.76 \pm 0.02$	$1.01 \pm 0.13$	$0.70 \pm 0.15$
4	$-0.166 \pm 0.019$	$-1.00 \pm 0.05$	$\rho_e = 0.77 \pm 0.035$ $\rho_\mu = 0.76 \pm 0.027$	$\xi_e = 0.99 \pm 0.21$ $\xi_\mu = 1.09 \pm 0.17$	$\delta_e = 0.84 \pm 0.27$ $\delta_\mu = 0.56 \pm 0.15$

Table 6.12: Results of the fit of the parameters to simulated spectra (the expected values are given in brackets).

The correlation matrix for the Step 1 fit was:

	$\langle \mathcal{P}_\tau \rangle$	$h_{\nu\tau}$	$\rho_l$	$\xi_l$	$\delta_l$
$\langle \mathcal{P}_\tau \rangle$	1	-0.256	0.493	0.156	-0.184
$h_{\nu\tau}$		1	-0.293	0.199	-0.047
$\rho_l$			1	-0.227	0.107
$\xi_l$				1	-0.873
$\delta_l$					1

The procedure was then applied to the experimental distributions resulting from the combination of the three samples of data (93, 94 and 95). The number of selected events in the six categories  $ee$ ,  $e\mu$ ,  $e\pi$ ,  $\mu\mu$ ,  $\mu\pi$  and  $\pi\pi$  were respectively 1268, 2518, 1991, 1649, 2155 and 799. The results are given in table 6.13 for different conditions imposed on the parameters. Line 1 corresponds to the fit of  $\langle \mathcal{P}_\tau \rangle$  alone, fixing all other parameters to their Standard Model values. Taking into account that the events analysed here are a subsample of the events used to determine  $\langle \mathcal{P}_\tau \rangle$  in the previous chapter, the present result of  $\langle \mathcal{P}_\tau \rangle = -0.159 \pm 0.033$  is found to be compatible with the first one, i.e.  $\langle \mathcal{P}_\tau \rangle = -0.133 \pm 0.012$ . The other lines of the table give the result of different fits where some parameters have been fixed to their Standard value, with or without the hypothesis of lepton universality for the electron and the muon. When the assumption of universality was not done (lines 4, 6, and 8), the results were in agreement with the hypothesis. All results were found to be in agreement with the Standard Model. The fitted distributions corresponding to the fit of line 9 are presented on figure 6.9.

	$\langle \mathcal{P}_\tau \rangle$	$h_{\nu\tau}$ (-1)	$\rho_l$ (0.75)	$\xi_l$ (1)	$\delta_l$ (0.75)	$\chi^2/ndf$
1	$-0.159 \pm 0.033$	-	-	-	-	1.05
2	$-0.178 \pm 0.039$	$-0.81 \pm 0.13$	-	-	-	1.07
3	$-0.162 \pm 0.040$	-	$0.74 \pm 0.05$	-	-	1.05
4	$-0.162 \pm 0.040$	-	$\rho_e = 0.73 \pm 0.07$ $\rho_\mu = 0.75 \pm 0.06$	-	-	1.05
5	$-0.149 \pm 0.041$	-	-	$1.1 \pm 0.3$	$0.6 \pm 0.3$	1.05
6	$-0.157 \pm 0.050$	-	-	$\xi_e = 1.2 \pm 0.7$ $\xi_\mu = 1.0 \pm 0.4$	$\delta_e = 0.9 \pm 0.8$ $\delta_\mu = 0.5 \pm 0.3$	1.05
7	$-0.152 \pm 0.046$	-	$0.74 \pm 0.05$	$1.1 \pm 0.3$	$0.6 \pm 0.3$	1.05
8	$-0.162 \pm 0.052$	-	$\rho_e = 0.69 \pm 0.08$ $\rho_\mu = 0.77 \pm 0.06$	$\xi_e = 1.3 \pm 0.7$ $\xi_\mu = 1.0 \pm 0.4$	$\delta_e = 0.9 \pm 0.6$ $\delta_\mu = 0.5 \pm 0.3$	1.05
9	$-0.28 \pm 0.12$	$-0.6 \pm 0.2$	$0.6 \pm 0.2$	$1.3 \pm 0.3$	$0.8 \pm 0.2$	1.07

Table 6.13: Results of the fit of the parameters to the experimental spectra. The sign “-” indicates that the parameter was fixed to its Standard Model value (given in brackets).

Introducing the  $\rho$  decay channel would increase the statistics by a factor of more than 2, increasing the sensitivity to the polarisation and reducing the statistical error in such a way that the systematical errors would become significant. However, since the expression of the matrix elements of the  $\rho$  decay itself (which depends on models) are then also necessary, simulated events are needed and we are back to the experimental method used in the previous chapter for the  $\langle \mathcal{P}_\tau \rangle$  measurement. That partially redundant analysis could then not be used as a cross-check of our results.

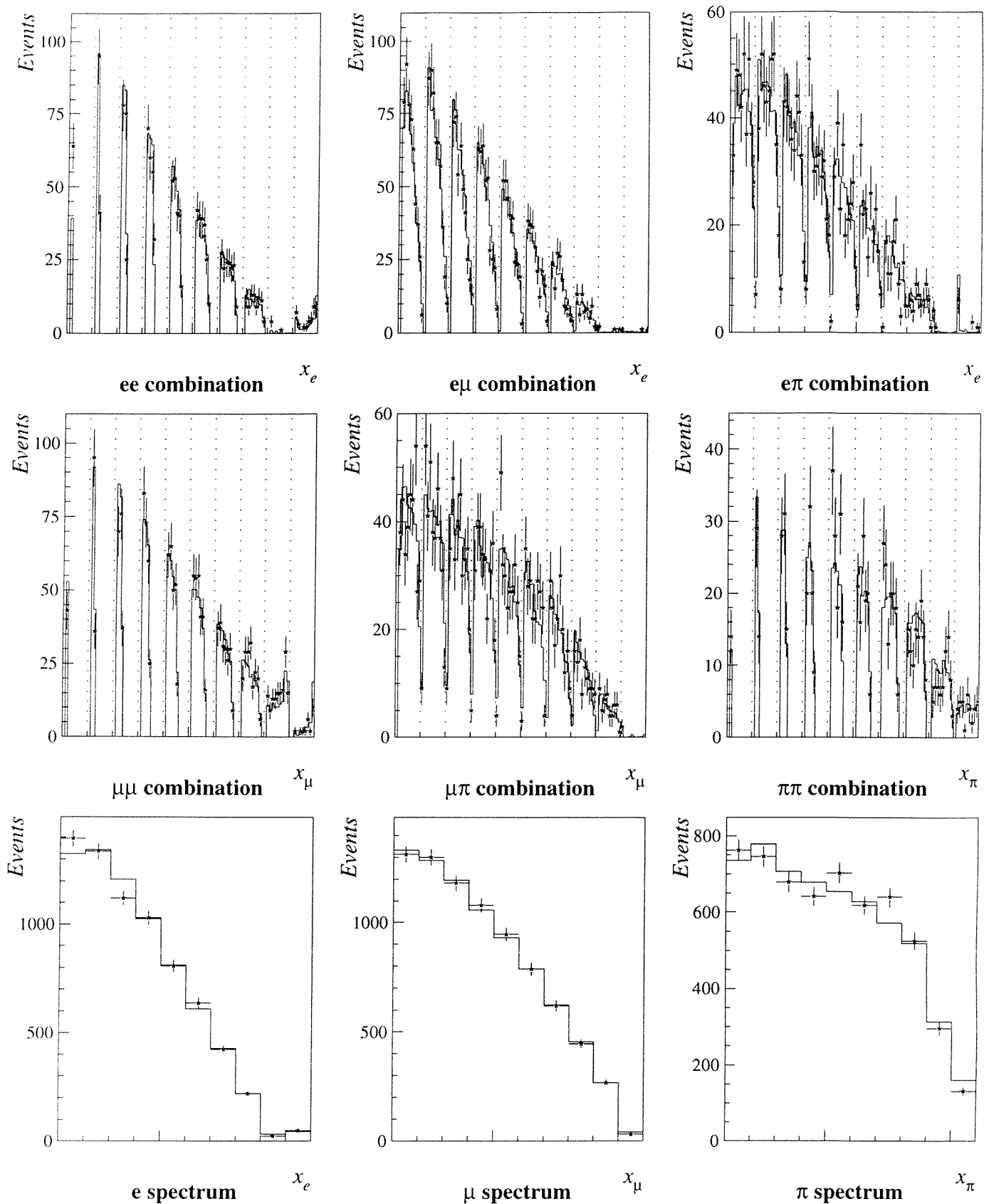


Figure 6.9: Distributions of the experimental two-dimensional spectra (points with error bars) used for the simultaneous adjustment of  $\langle \mathcal{P}_\tau \rangle$ ,  $h_{\nu\tau}$ ,  $\rho_l$ ,  $\xi_l$ , and  $\delta_l$ . The solid line represents the fitted histograms. For each combination  $ab$  ( $ab = ee, e\mu, e\pi, \mu\mu, \mu\pi$  and  $\pi\pi$ ), the data are displayed for the 10 slices of the spectrum of  $b$ . For all histograms, the ranges of  $x_e$ ,  $x_\mu$  and  $x_\pi$  have been divided into 10 bins of equal width, between  $3 \text{ GeV}/E_\tau$  and 1, as was done for the fitting procedure. The last three histograms represent the global projected spectra of the electrons, muons and pions candidates respectively.

# Chapter 7

## Discussion of the results

### 7.1 Combination of the 93, 94 and 95 results

In the previous chapter, we have performed the measurement of the mean  $\tau$  polarisation  $\langle \mathcal{P}_\tau \rangle$  and of the  $Z$  polarisation  $\mathcal{P}_Z$  for the data recorded by the DELPHI detector in 1993, 1994 and 1995, corresponding to respectively 30710, 56288 and 27504 selected  $\tau$  decays. The results obtained assuming a pure V-A Lorentz structure of the charged current for the  $\tau$  decay, are combined and discussed here.

First, we have measured  $\langle \mathcal{P}_\tau \rangle$  alone, using the current world-average values of the  $\tau$  branching ratios [2]. The results obtained with the data samples of the three years were found to be compatible with each other. The combined result and the  $\chi^2$  of the combination are:

$$\langle \mathcal{P}_\tau \rangle = -0.133 \pm 0.012 \text{ (stat)} \pm 0.0055 \text{ (syst)} \quad (\chi^2/ndf = 2.72/2)$$

where the first error is purely statistical (*stat*) and the second (*syst*) combines in quadrature the Monte Carlo statistical error and the systematic.

The  $\tau$  branching ratios could also be determined when fitting  $\langle \mathcal{P}_\tau \rangle$ , without significant loss of accuracy on the  $\langle \mathcal{P}_\tau \rangle$  determination. In that case the value of

$$\langle \mathcal{P}_\tau \rangle = -0.134 \pm 0.013 \text{ (stat)}$$

was obtained, in excellent agreement with the first result. The combined results for the branching ratios are given below. They are compatible with the world-average values (w.a.), although the  $B(\tau^- \rightarrow e^- \bar{\nu}_e \nu_\tau)$  was found to be quite small for the 1995 data (see previous chapter):

$B(\tau^- \rightarrow e^- \bar{\nu}_e \nu_\tau)$	$= (17.49 \pm 0.13 \pm 0.10) \%$	$(-1.9 \sigma \text{ from } (17.83 \pm 0.08) \%)$ ;
$B(\tau^- \rightarrow \mu^- \bar{\nu}_\mu \nu_\tau)$	$= (17.73 \pm 0.12 \pm 0.10) \%$	$(+2.0 \sigma \text{ from } (17.35 \pm 0.10) \%)$ ;
$B(\tau^- \rightarrow \pi^- / K^- \nu_\tau)$	$= (12.12 \pm 0.13 \pm 0.13) \%$	$(+0.4 \sigma \text{ from } (12.03 \pm 0.14) \%)$ ;
$B(\tau^- \rightarrow \rho^- \nu_\tau)$	$= (25.47 \pm 0.23 \pm 0.12) \%$	$(+0.3 \sigma \text{ from } (25.24 \pm 0.16) \%)$ ;
$B(\tau^- \rightarrow a_1^- \nu_\tau \rightarrow \pi^- \pi^0 \pi^0 \nu_\tau)$	$= (8.88 \pm 0.19 \pm 0.12) \%$	$(-1.5 \sigma \text{ from } (9.27 \pm 0.14) \%)$ .

The measurement of the variation of  $\mathcal{P}_\tau$  as a function of the direction of the  $\tau$  lepton with respect to the momentum of the incident electron provides in addition the determination of  $\mathcal{P}_Z$ .

The results for the three years of data were found to be compatible with each other:

	$\langle \mathcal{P}_\tau \rangle$			$\mathcal{P}_Z$		
93 data:	$-0.134 \pm 0.023$	$\pm 0.005$	$\pm 0.008$	$-0.153 \pm 0.034$	$\pm 0.008$	$\pm 0.009$
94 data:	$-0.118 \pm 0.017$	$\pm 0.004$	$\pm 0.004$	$-0.111 \pm 0.026$	$\pm 0.006$	$\pm 0.003$
95 data:	$-0.157 \pm 0.025$	$\pm 0.005$	$\pm 0.006$	$-0.153 \pm 0.036$	$\pm 0.007$	$\pm 0.005$
	<i>(stat)</i>	<i>(MC)</i>	<i>(syst)</i>	<i>(stat)</i>	<i>(MC)</i>	<i>(syst)</i>

The combined values are:

$$\begin{aligned} \langle \mathcal{P}_\tau \rangle &= -0.131 \pm 0.012 \text{ (stat)} \pm 0.005 \text{ (syst)} & (\chi^2/ndf = 1.58/2) \\ \mathcal{P}_Z &= -0.133 \pm 0.018 \text{ (stat)} \pm 0.006 \text{ (syst)} & (\chi^2/ndf = 1.28/2) \end{aligned}$$

which are fully in agreement with the lepton universality hypothesis for the electron and the  $\tau$  leptons as were the individual results.

Assuming lepton universality, the fit gave:

$$\begin{aligned} \langle \mathcal{P}_\tau \rangle &= \mathcal{P}_Z \\ 93 \text{ data: } & -0.140 \pm 0.019 \text{ (stat)} \pm 0.004 \text{ (MC)} \pm 0.005 \text{ (syst)} \\ 94 \text{ data: } & -0.116 \pm 0.015 \text{ (stat)} \pm 0.003 \text{ (MC)} \pm 0.003 \text{ (syst)} \\ 95 \text{ data: } & -0.156 \pm 0.020 \text{ (stat)} \pm 0.004 \text{ (MC)} \pm 0.004 \text{ (syst)} \end{aligned}$$

leading to the combined result

$$\langle \mathcal{P}_\tau \rangle = \mathcal{P}_Z = -0.133 \pm 0.010 \text{ (stat)} \pm 0.004 \text{ (syst)} \quad (\chi^2/ndf = 2.61/2) .$$

This value is identical to the above result obtained from the measurement of  $\langle \mathcal{P}_\tau \rangle$  alone, but is affected by smaller errors.

## 7.2 Determination of the coupling constants of the Z boson

Before deriving the coupling constants of the Z boson from the above results via the relation

$$\mathcal{A}_l \equiv \frac{2g_v^l g_a^l}{g_v^{l2} + g_a^{l2}} = \frac{2g_v^l / g_a^l}{1 + (g_v^l / g_a^l)^2} = \frac{2(1 - 4 \sin^2 \theta_w)}{1 + (1 - 4 \sin^2 \theta_w)^2} \quad (l = e, \tau) \quad (7.1)$$

a correction has to be introduced in order to obtain the ratio of the effective coupling constants  $g_v^l / g_a^l(s = M_Z^2)$  and  $\sin^2 \theta_w(s = M_Z^2)$ , i.e. for a centre-of-mass energy equal to the Z boson mass, and after removing QED effects: photon exchange and QED radiative corrections. The program ZFITTER [41], based on the Standard Model prediction and the world-average values of the Z mass  $M_Z = (91.186 \pm 0.002)$  GeV/c<sup>2</sup>, the top mass  $M_{top} = (175 \pm 6)$  GeV/c<sup>2</sup> and the limits on the Higgs mass  $M_{Higgs} = (300_{-240}^{+700})$  GeV/c<sup>2</sup>, was used to determine the expected relation between the measured quantity and the corrected result, for the beam energies and the integrated luminosities corresponding to the analysed samples of events. The following relations were obtained:  $\mathcal{A}_\tau(s = M_Z^2) = -1.0047 \langle \mathcal{P}_\tau \rangle + 0.0019$ , and  $\mathcal{A}_e(s = M_Z^2) = -1.0082 \mathcal{P}_Z + 0.0019$ , with an uncertainty of  $10^{-4}$  on the proportional factors due to  $\Delta M_Z$  (the errors on  $M_{top}$  and  $M_{Higgs}$  have negligible effects), leading to the final results of:

Lepton universality not assumed

$$\mathcal{A}_\tau = 0.134 \pm 0.012 \text{ (stat)} \pm 0.005 \text{ (syst)}$$

$$\mathcal{A}_e = 0.136 \pm 0.018 \text{ (stat)} \pm 0.006 \text{ (syst)}$$

Lepton universality assumed

$$\mathcal{A}_l = 0.135 \pm 0.010 \text{ (stat)} \pm 0.004 \text{ (syst)}$$

from which the ratios of the vector to axial coupling constants of the Z boson to the electron and to the  $\tau$  leptons, estimated for  $s = M_Z^2$ , can be extracted:

Lepton universality not assumed

$$g_v^\tau/g_a^\tau = 0.067 \pm 0.006 \text{ (stat)} \pm 0.003 \text{ (syst)}$$

$$g_v^e/g_a^e = 0.068 \pm 0.009 \text{ (stat)} \pm 0.003 \text{ (syst)}$$

Lepton universality assumed

$$g_v^l/g_a^l = 0.068 \pm 0.005 \text{ (stat)} \pm 0.002 \text{ (syst)}$$

$$\sin^2 \theta_w = 0.2330 \pm 0.0013 \text{ (stat)} \pm 0.0005 \text{ (syst)}$$

Our results are in agreement with those previously obtained from the data recorded in 1991 and 1992 by the DELPHI detector [52]:

$$\mathcal{A}_\tau = 0.148 \pm 0.017 \pm 0.014 ;$$

$$\mathcal{A}_e = 0.136 \pm 0.027 \pm 0.003 ;$$

$$\sin^2 \theta_w = 0.2320 \pm 0.0021 .$$

The systematic error on  $\mathcal{A}_\tau$  is a factor three smaller in our analysis. The one affecting  $\mathcal{A}_e$  is found however to be a factor two larger in the present analysis. This is due to the fact that, for the 91-92 results, the simulation statistics were folded for bins of positive and negative  $\cos \theta$ , reducing statistical fluctuations. On the other hand, for the 91-92 results, only systematic sources were studied which were expected to affect  $\mathcal{A}_e$  ( $\tau$  charge and polar angle determination), while here, all effects studied for the estimation of the systematic error on  $\mathcal{A}_\tau$  were also investigated for the determination of  $\mathcal{A}_e$ , so that possible asymmetric effects of the detector response could be traced.

Using the results presented here, and the values of reference [52], the DELPHI estimation of  $\sin^2 \theta_w$  is:

$$\text{DELPHI 91-95:} \quad \sin^2 \theta_w = 0.2327 \pm 0.0012$$

Results obtained by the other LEP experiments listed below [53]<sup>1</sup> are also in good agreement with our results:

	data	$\cos \theta_\tau$ range	$\mathcal{A}_\tau$	$\mathcal{A}_e$	$\sin^2 \theta_w$
ALEPH	90-92	26° – 154°	$0.136 \pm 0.012 \pm 0.009$	$0.129 \pm 0.016 \pm 0.005$	$0.2332 \pm 0.0014$
L3	90-93	23° – 157°	$0.150 \pm 0.013 \pm 0.009$	$0.157 \pm 0.020 \pm 0.005$	$0.2309 \pm 0.0016$
OPAL	90-94	47° – 133°	$0.134 \pm 0.009 \pm 0.010$	$0.129 \pm 0.014 \pm 0.005$	$0.2334 \pm 0.0012$

The global LEP average for  $\sin^2 \theta_w$  determined from the  $\tau$  polarisation measurement is then (figure 7.1):

$$\text{LEP average from } \mathcal{P}_\tau: \quad \sin^2 \theta_w = 0.2327 \pm 0.0007.$$

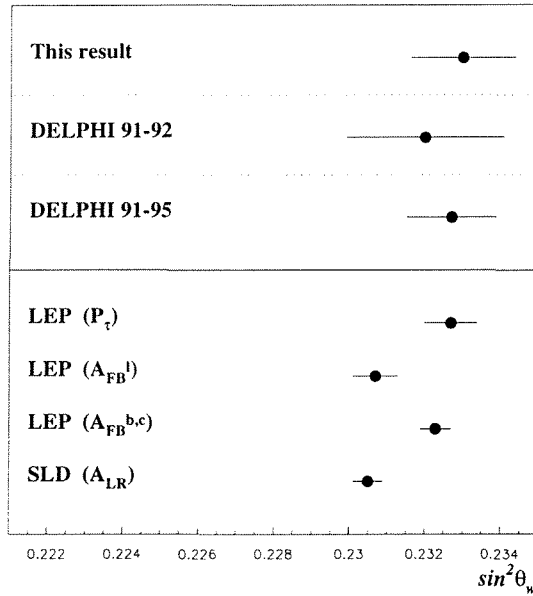


Figure 7.1: Results from the measurement of  $\sin^2 \theta_w(s = M_Z^2)$  by the LEP and SLD experiments

This result is compatible within 2.4 standard deviations with the average value obtained by the four LEP experiments from the measurement of the forward-backward asymmetry  $A_{FB}^l$  performed using the  $e^+e^-$ ,  $\mu^+\mu^-$  and  $\tau^+\tau^-$  final states ( $l = e, \mu, \tau$ ) [54]:

$$\text{LEP average from } A_{FB}^l: \quad \sin^2 \theta_w = 0.2307 \pm 0.0006.$$

A good agreement is also observed with the results obtained from the quark charge asymmetry  $A_{FB}^b$  and  $A_{FB}^c$  which average to [54]:

$$\text{LEP average from } A_{FB}^{b,c}: \quad \sin^2 \theta_w = 0.2323 \pm 0.0004.$$

Results from left-right asymmetry measurements performed by SLD using polarised beams are also found to be compatible within 2.6 standard deviations with the LEP ( $\mathcal{P}_\tau$ ) value [54]:

$$\text{SLD result from } A_{LR}: \quad \sin^2 \theta_w = 0.2305 \pm 0.0004.$$

<sup>1</sup>All experiments have analysed the  $e, \mu, \pi/K, \rho$  and  $a_1$   $\tau$  decay modes with the  $a_1$  decay into three charged pions except L3 which analysed the 1-prong  $a_1$  decay.

### 7.3 Test of lepton universality for weak neutral current interactions

As already mentioned, the measurement of the angular dependence of the  $\tau$  polarisation gives the opportunity to test the hypothesis of lepton universality for the electron and the  $\tau$  leptons in neutral current weak interactions. The determination of  $\mathcal{A}^l$  for  $l=e$  and  $l=\tau$  allowed the estimation of the ratio of the vector and axial coupling constants of the Z boson for both lepton types,  $g_v^\tau/g_a^\tau = 0.067 \pm 0.007$  and  $g_v^e/g_a^e = 0.068 \pm 0.010$ . The ratio of these two quantities gives an estimation of the validity of the lepton universality hypothesis<sup>2</sup>:

$$\frac{g_v^\tau/g_a^\tau}{g_v^e/g_a^e} = 0.98 \pm 0.18.$$

The combination of cross-section and asymmetry measurements allows the determination of the individual coupling constants  $g_v^l$  and  $g_a^l$ . The values obtained by the LEP and SLD experiments confirm more precisely that the lepton universality hypothesis holds, not only for  $e-\tau$  but also for  $e-\mu$  [54]:

$$\begin{aligned} g_v^\mu/g_v^e &= 0.939 \pm 0.087; \\ g_v^\tau/g_v^e &= 0.954 \pm 0.045; \\ g_a^\mu/g_a^e &= 0.9994 \pm 0.0017; \\ g_a^\tau/g_a^e &= 0.9996 \pm 0.0019. \end{aligned}$$

Better precisions are obtained on the results of  $g_a^l$  than of  $g_v^l$  because the former are mainly determined from the measurements of cross-sections which are more accurate than the ones of asymmetries. The information available on  $g_v^\tau$  is more precise than the one on  $g_v^\mu$  due to the possibility to determine  $\mathcal{A}_\tau$  from the measurement of the  $\tau$  polarisation in addition to the forward-backward charge asymmetry. The present values of the coupling constants  $g_v^l$  and  $g_a^l$  are presented on figure 7.2

### 7.4 Test of the V–A structure of the charged current in $\tau$ decays

In the second part of the previous chapter we have envisaged the possibility of a non-standard V–A structure of the charged current which had been assumed for all measurements presented above. A preliminary measurement of the Michel parameters and the  $\nu_\tau$  helicity was performed using the selected lepton and pion  $\tau$  decays  $\tau \rightarrow l\nu_l\nu_\tau, \pi\nu_\tau$ . Our best determination was:

$$\begin{aligned} \rho_l &= 0.74 \pm 0.05 \\ \xi_l &= 1.1 \pm 0.3 \\ \delta_l &= 0.6 \pm 0.3 \\ h_{\nu_\tau} &= -0.8 \pm 0.1 \end{aligned}$$

in agreement with the Standard Model values of 0.75, 1, 0.75 and  $-1$  respectively. The CLEO experiment has recently obtained very precise results using  $\tau$  decays produced in  $e^+e^-$  collisions at  $\sqrt{s}=10.6$  GeV in the CESR storage ring [55]. At these lower energies, the interaction proceeds mainly through photon exchange. There is then a zero average polarisation of the  $\tau$ 's. The

<sup>2</sup>The error on the ratio is computed assuming no correlation between the systematic errors of the two results.



# Preliminary

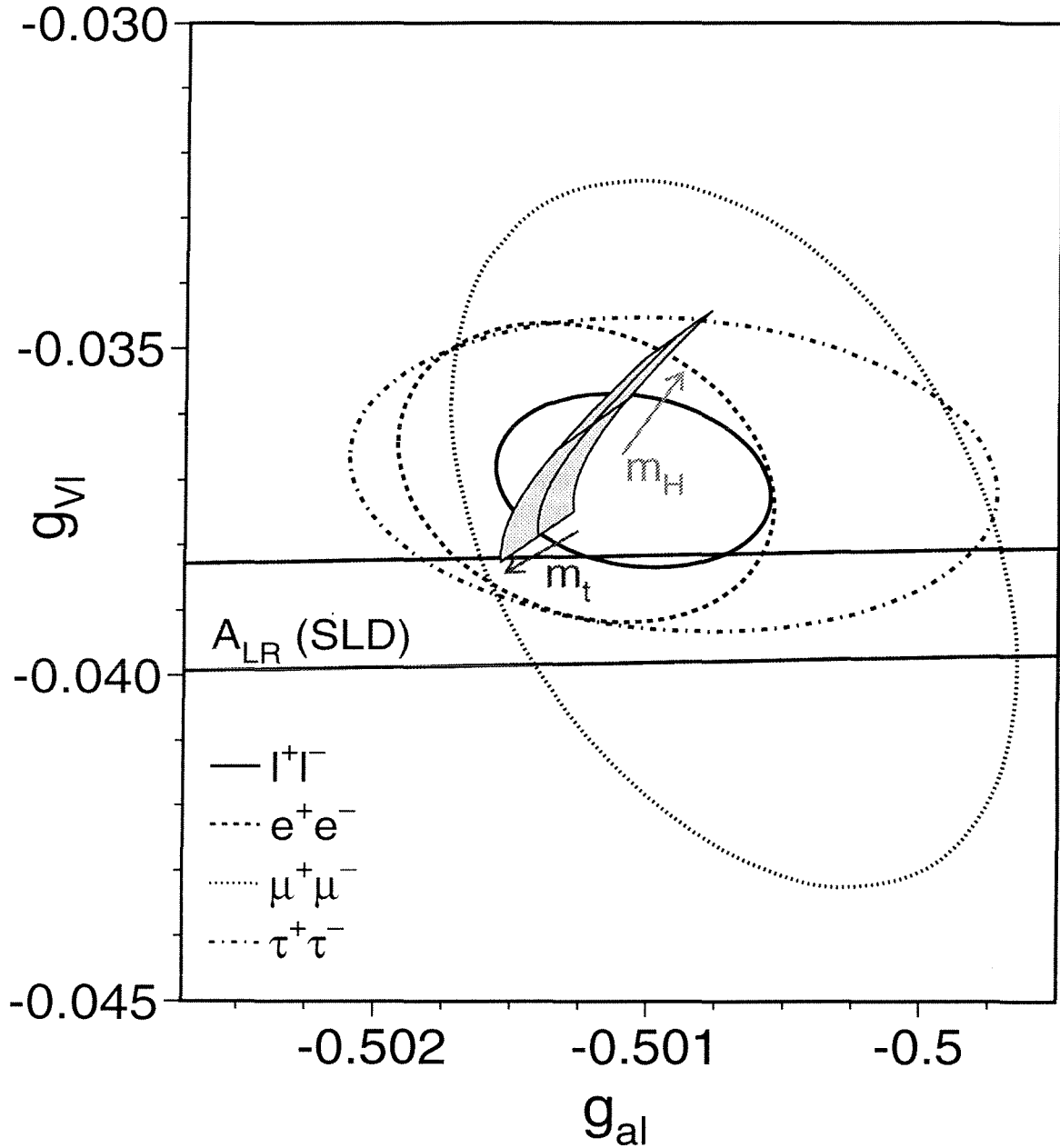


Figure 7.2: Contours of 68% probability in the  $g_v^l - g_a^l$  plane from LEP measurements. The solid contour results from a fit assuming lepton universality. Also shown is the one standard deviation band resulting from the  $A_{LR}$  measurement of SLD. The shaded region corresponds to the Standard Model prediction for  $m_{top} = (175.6 \pm 5.5) \text{ GeV}/c^2$  and  $m_{Higgs} = (300_{-240}^{+700}) \text{ GeV}/c^2$ . The arrows point in the direction of increasing values of  $m_{top}$  and  $m_{Higgs}$ .

Lorentz structure parameters can still be determined since there is a spin-spin correlation between the two  $\tau$  leptons, leading to correlations between the kinematical properties of the decay products. The following decay channels were used:  $\tau^+\tau^- \rightarrow (l^\pm\nu\bar{\nu})(\pi^\mp\pi^0\nu)$  with  $l = e$  and  $\mu$ , and  $\tau^+\tau^- \rightarrow (\pi^\pm\pi^0\nu)(\pi^\mp\pi^0\nu)$ , with a total statistics of 3 million  $\tau$  pairs. They obtained the following results, in full agreement with the Standard Model, validating the assumption of a pure V-A used for our measurement of the  $\tau$  polarisation:

$$\begin{aligned}\rho_l &= 0.747 \pm 0.010 \pm 0.006 \\ \xi_l &= 1.007 \pm 0.040 \pm 0.015 \\ \xi_l\delta_l &= 0.745 \pm 0.026 \pm 0.009 \\ h_{\nu\tau} &= -0.995 \pm 0.010 \pm 0.003\end{aligned}$$

An independent analysis performed by CLEO was devoted to the  $\eta_l$  measurement [56] giving  $\eta_l = -0.015 \pm 0.061 \pm 0.062$  and  $\rho_l = 0.735 \pm 0.013 \pm 0.008$ . All results were confirming e- $\mu$  lepton universality for the weak charged current.



# Chapter 8

## Conclusions

The object of this thesis was a precise determination of the coupling constants of both the Z boson to the e and  $\tau$  leptons and the weak mixing angle  $\sin^2 \theta_w$ , via the measurement of the  $\tau$  polarisation using  $\tau$  decays into one charged particle and any number of neutrals (called *1-prong* decays), produced in  $e^+e^-$  interactions. Our experimental approach of the problem allowed to tackle several other aspects of the  $\tau$  physics at LEP, leading to additional physics results in the domain of the weak neutral and charged current interactions: the experimental results concerning the selection of the  $e^+e^- \rightarrow \tau^+\tau^-$  interactions were found to be in a very good agreement with the Standard Model predictions for the cross-section of the process; the results obtained on the coupling constants of the Z boson gave the opportunity to test the hypothesis of the lepton universality for the e and  $\tau$  leptons, which was indeed verified; a precise determination of the topological  $\tau \rightarrow 1\text{-prong}$  branching ratio was performed; the branching ratio of the exclusive *1-prong*  $\tau$  decay modes were also estimated for the channels  $\tau^- \rightarrow e^-\bar{\nu}_e\nu_\tau$ ,  $\mu^-\bar{\nu}_\mu\nu_\tau$ ,  $\pi^-/K^-\nu_\tau$ ,  $\rho^-\nu_\tau \rightarrow \pi^-\pi^0\nu_\tau$ ,  $a_1^-\nu_\tau \rightarrow \pi^-\pi^0\pi^0\nu_\tau$  selected for the measurement of the  $\tau$  polarisation; finally, preliminary results concerning the test of the V–A Lorentz structure of the charged current were obtained with the measurement of the Michel parameters and the  $\nu_\tau$  helicity.

The procedure for the selection of the *1-prong*  $\tau$  decay candidates was the following. Firstly, the interactions  $e^+e^- \rightarrow \tau^+\tau^-$  were isolated from other final states. The selection criteria were carefully chosen in order to minimise the loss of high energetic pions produced by the  $\tau$  decays through the channel  $\tau^- \rightarrow \pi^-\nu_\tau$ . This was done with a view to the polarisation measurement which relies on the high sensitivity to  $\langle P_\tau \rangle$  of this decay mode. The rejection of the  $e^+e^- \rightarrow e^+e^-$  and  $e^+e^- \rightarrow \mu^+\mu^-$  events was based on the electromagnetic properties of the respective final state charged particles and on their topological characteristics (two back to back energetic charged particles). Since photon conversions into  $e^+e^-$  pairs modify the charged particle multiplicity of the events, they are of fundamental importance in the identification of  $\tau$  decay events (where at least one  $\pi^0$  is produced in 30% of the cases) and the rejection of  $e^+e^- \rightarrow e^+e^-$  final states (energetic electrons have a high probability to radiate a photon through bremsstrahlung). A detailed comparison of the photon conversion probability for experimental and simulated data was thus performed. A deficit of  $36\% \pm 2\%$  of conversions was observed in the simulated data, indicating an incorrect evaluation of the repartition of the detector material. Therefore, the selection efficiencies and background levels being estimated on the basis of the simulated data, an adequate reconstruction of the event topology was necessary in order to have minimum bias. This imperfect simulation of the photon conversions affected mainly the  $e^+e^- \rightarrow e^+e^-$  rejection and the *1-prong*  $\tau$  decay mode selection. A sample of 68600  $\tau^+\tau^-$  pairs was selected, with an efficiency 88% within the geometrical acceptance region and

a residual background level of 3.5%. The number of selected experimental events was found to be in a very good agreement with the value predicted from the Standard Model (given the present world-average value of  $M_Z$ ) and the integrated luminosity of the analysed data: their ratio  $N^{real}/N^{pred}$  was evaluated to be

$$\frac{N^{real}}{N^{pred}} = 1.002 \pm 0.004 (stat) \pm 0.003 (syst).$$

Among the retained  $e^+e^- \rightarrow \tau^+\tau^-$  candidates, 114502  $\tau \rightarrow 1\text{-prong}$  decays were then selected with an efficiency of 99% and a purity of 96%. This selection allowed an accurate determination of the topological 1-prong  $\tau$  branching ratio:

$$B(\tau \rightarrow 1\text{-prong}) = 85.30\% \pm 0.10\%(stat) \pm 0.09\%(syst),$$

consistent with the present world-average value of  $85.53\% \pm 0.14\%$ .

For the determination of the decay modes of the preselected  $\tau \rightarrow 1\text{-prong}$  events, the five main decay channels to be identified were  $\tau \rightarrow e\nu_e\nu_\tau$ ,  $\tau \rightarrow \mu\nu_\mu\nu_\tau$ ,  $\tau \rightarrow \pi/K\nu_\tau$ ,  $\tau \rightarrow \rho\nu_\tau \rightarrow \pi\pi^0\nu_\tau \rightarrow \pi\gamma\gamma\nu_\tau$ , and  $\tau \rightarrow a_1\nu_\tau \rightarrow \pi\pi^0\pi^0\nu_\tau \rightarrow \pi\gamma\gamma\gamma\nu_\tau$ . The  $e$  and  $\mu$  channels offered relatively clear signatures. Due to detector effects, this was not the case for the three hadronic channels which, in ideal conditions, could be distinguished simply on the basis of the number of the primary photons and the invariant mass of the hadronic system. Experimentally the situation was not so clear. On one hand, photons could be lost due to detector threshold effects or dead zones, or because the electromagnetic showers they generate could be merged either with the shower of another photon or with the energy deposition associated to a charged particle. On the other hand, secondary photons, not easily distinguished from the primary ones, could be produced in hadronic interactions of the charged pions in the detector material, or by final state radiation or bremsstrahlung. All these effects require, for classical selection methods, complex selection criteria for the identification of the  $\tau \rightarrow \rho\nu_\tau$  decay mode to take into account all the correlations and lead to relatively low selection efficiencies. Using those methods, the exclusive channel  $\tau \rightarrow \pi\pi^0\pi^0\nu_\tau$  has even never been analysed with the DELPHI detector. We have hence chosen to make use of the neural network technique as a new approach for the treatment of that classification problem. The technique turned out to be very powerful: using only eleven well chosen discriminant variables as inputs to the neural network, the classification of the above five exclusive  $\tau$  decay modes was performed in one step with efficiencies and contamination levels similar to the results obtained by classical analysis methods for the  $e$ ,  $\mu$  and  $\pi$  channels, and with 10% more efficiency for the  $\rho$  channel. In addition, it was possible to isolate relatively efficiently the  $\tau \rightarrow \pi\pi^0\pi^0\nu_\tau$  decays. A fully connected feed-forward architecture was used for the neural networks which were trained with the standard back-propagation learning procedure, using simulated events. The input variables were based on the information provided by the various modules of the detector concerning the ionisation, electromagnetic and penetration properties of the charged particles, and on the kinematics and the number of detected neutral particles. For the estimation of the migration matrices, the neural networks were tested with large samples of simulated events. The good reproduction of the experimental distributions of the input variables by the simulation was carefully checked using a subsample of non-ambiguous events. Some variables needed to be recalibrated using data test samples. The average selection efficiencies and sample purities obtained using the neural networks were respectively

$$\begin{aligned} (95.66 \pm 0.04)\% & \quad \text{and} \quad (90.03 \pm 0.06)\% & \quad \text{for the } \tau \rightarrow e\nu_e\nu_\tau \text{ channel,} \\ (96.72 \pm 0.03)\% & \quad \text{and} \quad (94.33 \pm 0.06)\% & \quad \text{for the } \tau \rightarrow \mu\nu_\mu\nu_\tau \text{ channel,} \\ (85.79 \pm 0.07)\% & \quad \text{and} \quad (72.90 \pm 0.08)\% & \quad \text{for the } \tau \rightarrow \pi\nu_\tau \text{ channel,} \\ (80.30 \pm 0.06)\% & \quad \text{and} \quad (75.67 \pm 0.06)\% & \quad \text{for the } \tau \rightarrow \rho\nu_\tau \text{ channel,} \\ (57.15 \pm 0.12)\% & \quad \text{and} \quad (53.62 \pm 0.14)\% & \quad \text{for the } \tau \rightarrow a_1\nu_\tau \text{ channel.} \end{aligned}$$

After classification, a very good agreement was observed between experimental and simulated data for the distributions of the input and output variables.

The Z and  $\tau$  polarisations were determined on the basis of this classification. The kinematics of the  $\tau$  decay products were used as polarimeter. In order to take into account the detector effects and the selection efficiencies, the  $\tau$  polarisation was measured using simulated distributions which were fitted to the experimental data. The Z polarisation was determined from the angular dependence of the  $\tau$  polarisation. After correction for the radiative effects and the photon exchange, the following results were obtained:

$$\begin{aligned} \mathcal{A}_\tau &= 0.134 \pm 0.012 \text{ (stat)} \pm 0.005 \text{ (syst)} ; \\ \mathcal{A}_e &= 0.136 \pm 0.018 \text{ (stat)} \pm 0.006 \text{ (syst)} , \end{aligned}$$

implying

$$\begin{aligned} g_v^\tau/g_a^\tau &= 0.067 \pm 0.006 \text{ (stat)} \pm 0.003 \text{ (syst)} ; \\ g_v^e/g_a^e &= 0.068 \pm 0.009 \text{ (stat)} \pm 0.003 \text{ (syst)} , \end{aligned}$$

for the ratios of the vector to axial coupling constants of the Z boson. These results show an excellent agreement with the e- $\tau$  lepton universality hypothesis and lead to the determination of the weak mixing angle,

$$\sin^2 \theta_w = 0.2330 \pm 0.0013 \text{ (stat)} \pm 0.0005 \text{ (syst)} ,$$

in agreement with the results obtained by other experiments.

In addition, a simultaneous fit of  $\langle \mathcal{P}_\tau \rangle$  and the exclusive  $\tau$  decay branching ratios gave:

$$\begin{aligned} B(\tau^- \rightarrow e^- \bar{\nu}_e \nu_\tau) &= (17.49 \pm 0.13 \pm 0.10) \% ; \\ B(\tau^- \rightarrow \mu^- \bar{\nu}_\mu \nu_\tau) &= (17.73 \pm 0.12 \pm 0.10) \% ; \\ B(\tau^- \rightarrow \pi^- / K^- \nu_\tau) &= (12.12 \pm 0.13 \pm 0.13) \% ; \\ B(\tau^- \rightarrow \rho^- \nu_\tau) &= (25.47 \pm 0.23 \pm 0.12) \% ; \\ B(\tau^- \rightarrow a_1^- \nu_\tau \rightarrow \pi^- \pi^0 \pi^0 \nu_\tau) &= (8.88 \pm 0.19 \pm 0.12) \% . \end{aligned}$$

Finally, making use of the selected  $\tau^- \rightarrow e^- \bar{\nu}_e \nu_\tau$ ,  $\mu^- \bar{\nu}_\mu \nu_\tau$  and  $\pi^- / K^- \nu_\tau$  decays, a measurement of the Michel parameters and of the  $\nu_\tau$  helicity was performed, providing the following results:

$$\begin{aligned} \rho_l &= 0.74 \pm 0.05 \text{ (stat)} ; \\ \xi_l &= 1.1 \pm 0.3 \text{ (stat)} ; \\ \delta_l &= 0.6 \pm 0.3 \text{ (stat)} ; \\ h_{\nu_\tau} &= -0.8 \pm 0.1 \text{ (stat)} , \end{aligned}$$

in agreement with the Standard Model expectations of respectively 0.75, 1, 0.75 and  $-1$ .

The results obtained in this thesis open new perspectives in this type of analysis:

- Concerning the particle identification: the efficiency for the identification of the  $\tau$  decay modes was found to be limited by the relatively poor reconstruction of the neutral particle kinematics due to a difficult treatment of the information provided, in the central part of the detector, by the electromagnetic calorimeter HPC. This aspect of the particle identification problem could certainly be improved by applying the neural network technique for a direct identification of the photons and  $\pi^0$ 's in DELPHI.

- Concerning the  $\tau$  polarisation measurement: the extension of the analysis to a larger geometrical acceptance, i.e. larger values of  $|\cos \theta_\tau|$ , would increase the precision obtained on  $\mathcal{A}_e$ . This would necessitate the use of the information provided by the end-cap modules of the detector, requiring either the elaboration of a new set of input variables for the neural network classification, or the adaptation of the variables presented here so that they would not depend on the physical characteristics of the detection modules such as the number of active layers in the calorimeters.
- Concerning the Michel parameter determination: the results presented here are preliminary: no study of the systematic effects was performed, and, more specifically, introducing the  $\tau \rightarrow \rho\nu_\tau$  events will increase the statistics by a factor 2, reducing the statistical error and increasing the precision of the measurement of  $h_{\nu_\tau}$ .

# Appendix A

## A.1 The simple perceptron

The threshold unit can be used to solve linearly separable problems. Let the number of input units  $N$  be equal to 2 and the inputs  $I_j$  ( $j = 1, 2$ ) be continuous-valued: events (or patterns)  $\mathcal{E}^p$  are represented by two coordinates in the plane ( $\vec{\mathcal{E}}^p = (I_1^p, I_2^p)$ ), as in the example given in figure A.1 where solid circles represent events belonging to class A and open circles are events of class B.

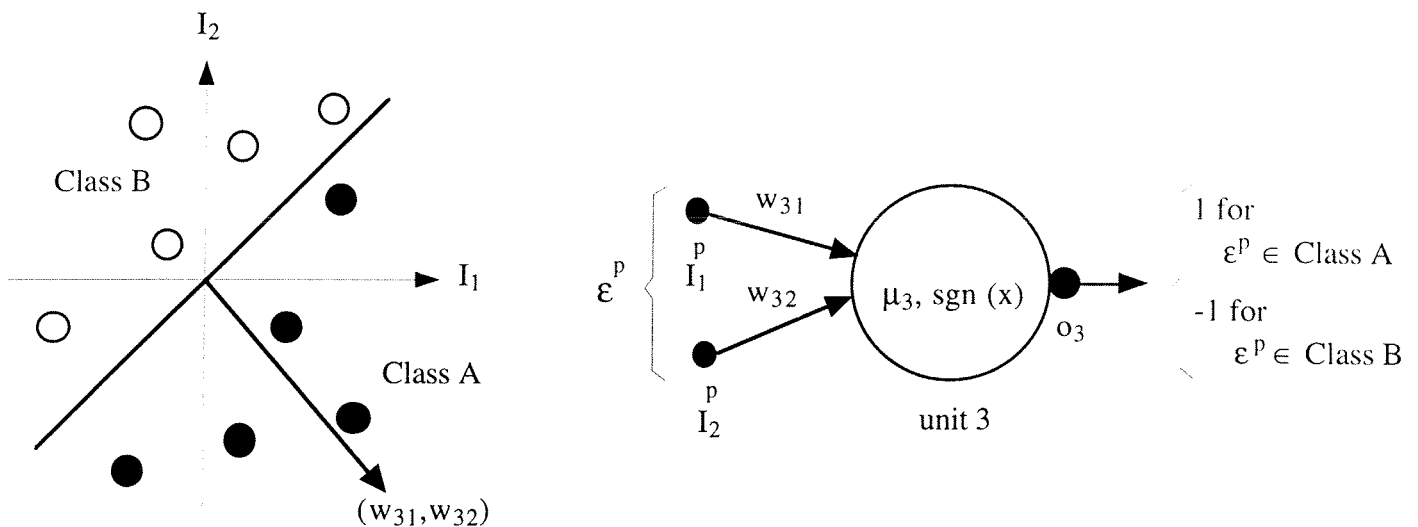


Figure A.1: *Example of a linearly separable problem.*

For example, using the sign function  $sgn(x)$ , we demand that the output  $o_3^p$  be equal to the following target values  $t^p$ :

$$t^p \equiv \begin{cases} 1 & \text{when } \mathcal{E}^p \text{ belongs to class A,} \\ -1 & \text{when } \mathcal{E}^p \text{ belongs to class B.} \end{cases} \quad (\text{A.1})$$

The problem is to find the appropriate set of  $w_{ij}$ 's ( $(w_{31}, w_{32}) = \vec{w}$ ) and  $\mu_3$ , such that the output  $o_3^p$ , given by the threshold unit for each event  $\mathcal{E}^p$ , corresponds the class of the events. The set of solutions  $\{\vec{w}\}$  correspond to all straight lines (or planes or hyper-planes for higher dimensions  $N > 2$ ) satisfying:

$$t^p \cdot \vec{\mathcal{E}}^p \cdot \vec{w} > 0$$



for all  $\mathcal{E}^p$ . The threshold  $\mu_3$  is different from 0 when the straight line separating the 2 classes does not pass through the origin. In that case, equation (3.1) can be re-written:

$$o_i = g\left(\sum_{j=0}^N w_{ij} I_j\right), \quad (\text{A.2})$$

with  $w_{i0} = -1$  and  $I_0$  is fixed at the value  $\mu_i$ .

The Boolean AND function can be executed by a threshold unit. Table A.1 gives the four possible input patterns and the result of the AND function in each case, which can be taken as target values if the threshold function  $\theta(x)$  is used. The geometrical representation of the function shows that the problem is linearly separable (see figure A.2). A solution is given on the right side of the figure.

$p$	$I_1^p$	$I_2^p$	$t^p$
1	0	0	0
2	1	0	0
3	0	1	0
4	1	1	1

Table A.1: The AND function: 4 possible input patterns ( $I_1^p, I_2^p$ ) and the target values  $t^p$

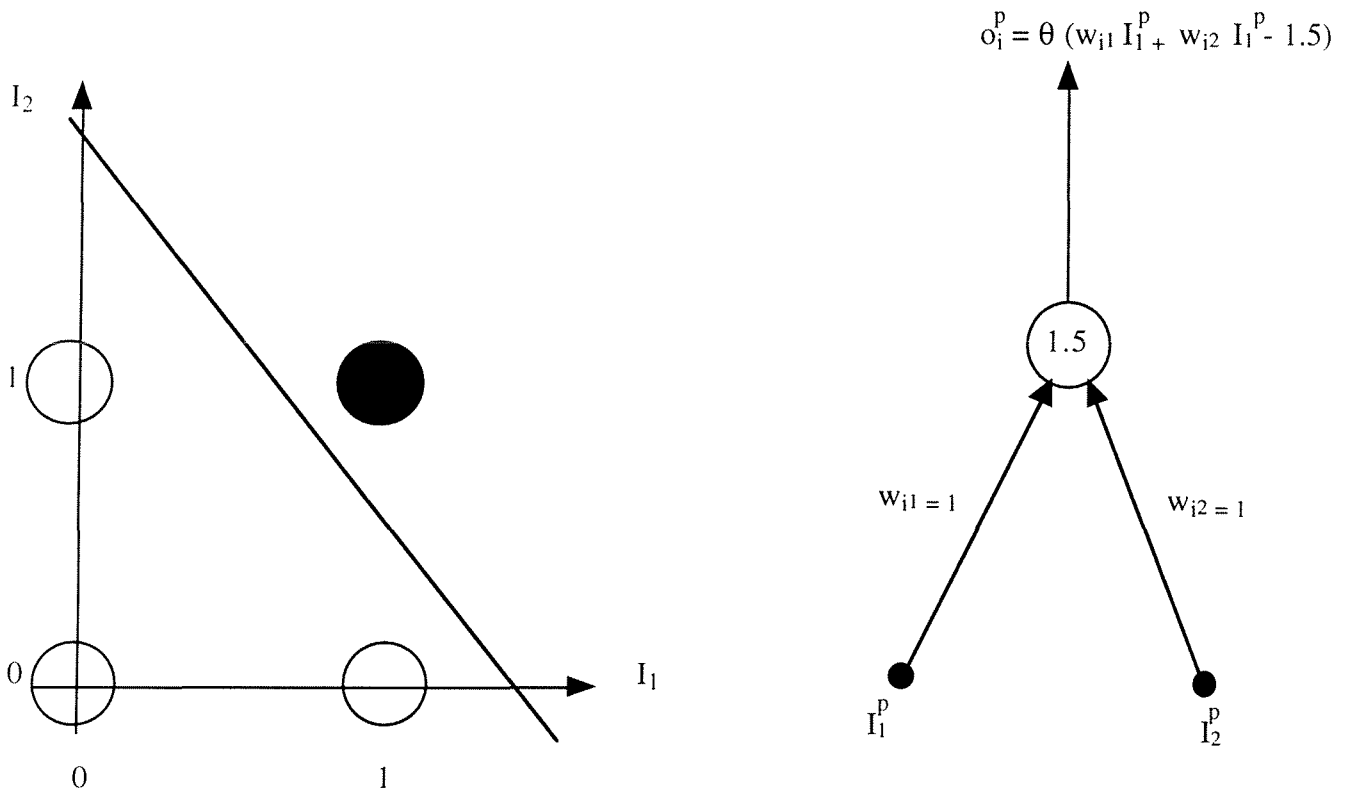


Figure A.2: Schematic representation of the AND function.

When patterns have to be classified into more than two classes, additional units are needed. They are then organised into layer of neurons, called perceptrons. All inputs are fed to all units. For  $M$  units,  $N \times M$  weights  $w_{ij}$  are needed ( $i = 1, \dots, M; j = 1, \dots, N$ ), and  $2M$  classes can be delimited.

## A.2 The multi-layer perceptron

Non-linearly separable problems cannot be solved with the help of the simple perceptron. A simple illustration is given by the boolean XOR function. Table A.2 gives the four possible input patterns and the result of the XOR function in each case. The geometrical representation

$p$	$I_1^p$	$I_2^p$	$t^p$
1	0	0	0
2	1	0	1
3	0	1	1
4	1	1	0

Table A.2: *The XOR function: 4 possible input patterns ( $I_1^p, I_2^p$ ) and the target values  $t^p$*

shows that patterns 2 and 3 cannot be isolated from patterns 1 and 4 by using a single threshold unit (i.e. by drawing a single straight line). At least two units (1 and 2) have to be used for delimiting the plane into three regions I, II, and III. In addition, it has to be specified that points lying in the regions I and III are belonging to the same class. The solution is to use the output space of these two units as input space of a third unit (3) by constructing a two-layer perceptron (see figure A.3).

For example, with

$$\begin{aligned}
 o_1^1 = 0 & \quad \text{and} \quad o_2^1 = 0 \\
 o_1^2 = 1 & \quad \text{and} \quad o_2^2 = 0 \\
 o_1^3 = 0 & \quad \text{and} \quad o_2^3 = 1 \\
 o_1^4 = 1 & \quad \text{and} \quad o_2^4 = 1,
 \end{aligned}
 \tag{A.3}$$

unit 3 should map

$$\begin{aligned}
 (o_1^1, o_2^1) = (0, 0) & \quad \text{on} \quad o_3^1 = 0 \\
 (o_1^2, o_2^2) = (1, 0) & \quad \text{on} \quad o_3^2 = 1 \\
 (o_1^3, o_2^3) = (0, 1) & \quad \text{on} \quad o_3^3 = 1 \\
 (o_1^4, o_2^4) = (1, 1) & \quad \text{on} \quad o_3^4 = 0.
 \end{aligned}
 \tag{A.4}$$

This is realised by the neural network of figure A.3.

The intermediate units (1 and 2) are called *hidden* units and constitute the *hidden* layer, while the *output* layer is made, in this example, of one single *output* unit (unit 3).

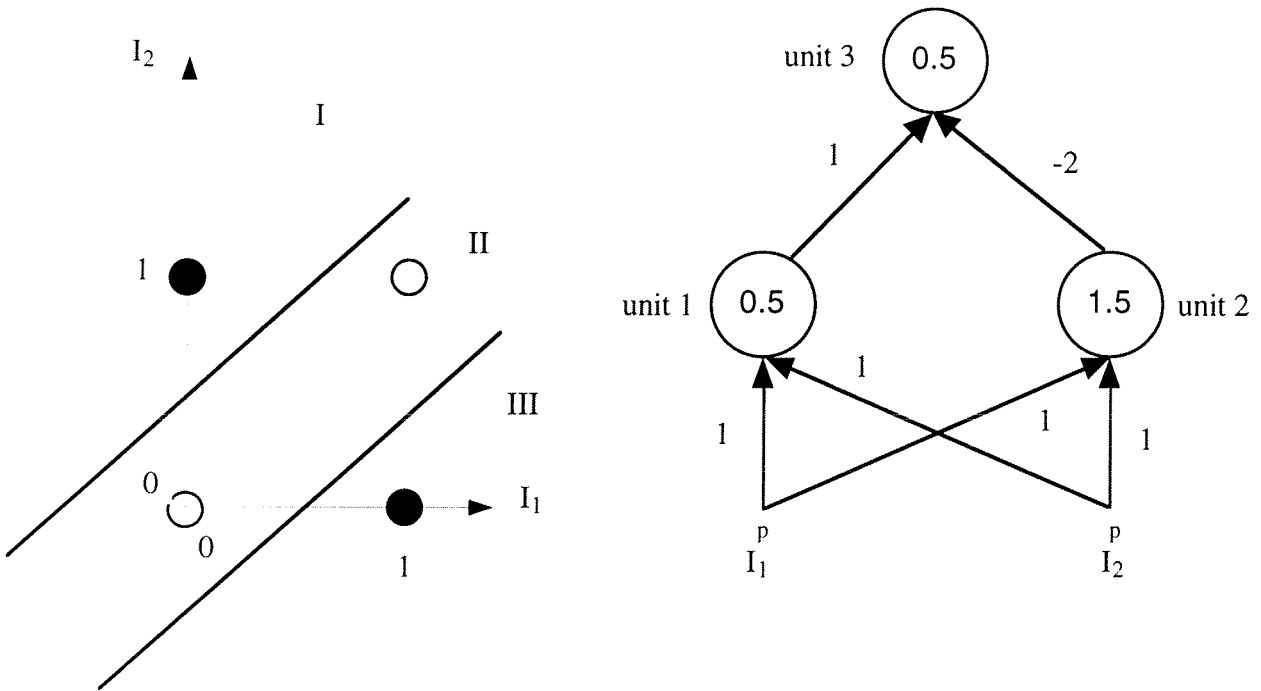


Figure A.3: Schematic representation of the XOR function.

# Bibliography

- [1] CDF Coll., Phys. Rev. Lett. 74(1995) 2626;  
D0 Coll., Phys. Rev. Lett. 74(1995) 2632
- [2] R.M. Barnett et al., Phys. Rev. 54 D(1996) 1
- [3] S.L. Glashow, Nucl. Phys. 22 B(1961) 579;  
S. Weinberg, Phys. Rev. Lett. 19(1967) 1264;  
A. Salam, in Proc. of the 8th Nobel Symp., p. 367, ed. N. Svartholm, Almqvist and Wiksell, Stockholm, 1968
- [4] P.W.Higgs, Phys. Lett. 12 (1964) 132
- [5] F.J. Hasert et al., Phys. Lett. 46 B(1973) 138, Nucl.Phys 73 B(1974) 1
- [6] G. Arnison et al., UA1 Coll., Phys. Lett. 122 B(1983) 103;  
M. Banner et al., UA2 Coll., Phys. Lett. 122 B(1983) 476;  
C. Rubbia, Nobel Lecture, Rev. Mod. Phys. 57(1985) 699
- [7] M. Kobayashi and T. Maskawa, Prog. Theor. Phys. 49 (1973) 652
- [8] D. Decamp et al., ALEPH Coll., Z. Phys. 53 C(1992) 1;  
P. Abreu et al., DELPHI Coll., Nucl. Phys. 367 B(1992) 511;  
B. Adeva et al., L3 Coll., Z. Phys. 51 C(1991) 179;  
G. Alexander et al., OPAL Coll., Z. Phys. 52 C(1991) 175
- [9] "Z Physics at LEP 1", M.Consoli and W.Hollik, CERN 89-08 p7
- [10] G. Burgers, "The shape and size of the Z resonance", CERN report 88-06 (1988)
- [11] SLD Coll., Phys. Rev. Lett. 73 (1994) 25
- [12] MARK I Coll., M.L.Perl et al., Phys. Rev. Lett. 35(1975) 1489
- [13] Y.S.Tsai, Phys. Rev. 4 D(1971) 2821
- [14] "New tensor interaction in  $\mu$  decay", M.V.Chizhov, Modern Phys. Lett. A Vol. 9, 32 (1994) 2979
- [15] L.Michel, Proc. Phys. Soc. London A 63 (1950) 514
- [16] K. Hagiwara, A.D. Martin and D. Zeppenfeld Phys. Lett. 235 B(1990) 198;  
A. Roug e , Z. Phys. 48 C(1990) 75;  
J.H. K uhn and F. Wagner, Nucl. Phys. 236 B(1984) 16
- [17] M.Davier, L.Duflot, F.Le Diberder and A.Roug e, Phys. Lett. 306 B(1993) 411

- [18] Annual Reports to the CERN Council, John Adams, 1979 and 1980 referred to in 'Excerpts from The John Adams Memorial Lecture' delivered at CERN on 26 November 1990 by S.Myers.
- [19] P.Aarnio et al., DELPHI Coll., Nucl. Instr. and Meth. A303(1991) 233
- [20] DELPHI Collaboration, P. Aarnio et al., CERN-PPE/95-194
- [21] DELANA User Guide, DELPHI 89-44/PROG 137, 1989
- [22] ELEPHANT reference manual, M.Feindt, C.Kreuter, O.Podobrin, DELPHI 96-82 PROG217 17 June, 1996;  
PXPHOT - Third stage pattern recognition for DELPHI, M.Feindt, O.Podobrin, DELPHI 93-xxx;  
W.Adam et al., DELPHI Coll., Z. Phys. 69 C(1996) 561
- [23] Performance of muon identification in DELPHI for 93 and 94 data, F.Stichelbaut, G.R.Wilkinson, DELPHI 95-140 PHYS 565
- [24] Architecture and performances of the DELPHI trigger system, V.Bocci et al., Nucl. Instr. and Meth. A362 (1995) 361.
- [25] DELANA Tags for 1991 Data, J.Wickens, DELPHI 91-20 PHYS 91 - PROG 160
- [26] S.Jadach et al., CERN-TH/96-158, June 1996
- [27] DELSIM User Manual, DELPHI 87-96/PROG 99, 1989  
DELSIM Reference Manual, DELPHI 87-98/PROG 100,1989
- [28] T.Sjöstrand, Comp. Phys. Comm. 82 (1994) 74
- [29] F.A.Berends, W.Hollik and R.Kleiss, Nucl. Phys. 304 B(1988) 712
- [30] J.E.Campagne and R.Zitoun, Z. Phys. 43 C(1989) 469
- [31] S. Jadach et al. Comp. Phys. Comm. 79 (1994) 503
- [32] F.A.Berends, P.H.Daverveldt, R.Kleiss, Comp. Phys. Comm. 40 (1986) 285
- [33] "Introduction to the theory of neural computation", J.Hertz, A.Krogh, R.G.Palmer;  
"Neural computing, an introduction", R.Beale, T.Jackson.
- [34] "A logical calculus of ideas immanent in nervous activity", W.S.McCulloch and W.Pitts, Bulletin of Mathematical Biophysics 5 (1943) 115
- [35] "Design of the SNNS neural network simulator", A.Zell et al., in Österreichische Artificial-Intelligence-Tagung, pp.93-102, Wien 1991. Informatik-Fachberichte 287, Springer Verlag.  
Networks Conference, SPIE volume 1469, pp. 708-719, Orlando Florida 1991  
"The SNNS Neural Network Simulator", A.Zell et al. , in GWAI - 91, 15. Fachtagung für künstliche Intelligenz, pp 254-263. Informatik-Fachbericht 285, Springer Verlag, 1991.  
SNNS User manual, Version 4.0, A.Zell et al., Report N° 6/95. University of Stuttgart.  
Institute for parallel and distributed high performance systems.
- [36] Charged particle multiplicity distributions in  $Z^0$  hadronic decays, DELPHI Collaboration, P.Abreu et al., Z.Phys. C50 (1991) 185

- [37] DELPHI cosmic runs, J.M Benlloch and Tz. Spasoff, DELPHI 90-6 GEN 104 TRACK 60
- [38] On the possibility of the calibration of the DELPHI forward detectors with LEP halo muons, S.I.Bityukov et al., DELPHI 89-90 TRACK 59
- [39] Physics Team Tagging Criteria in PXTAG, J.Wickens, DELPHI 92-44 PROG 184
- [40]  $\gamma$  and  $\pi^0$  identification in  $\tau$  decays, J.M.Lopez and F.Matorras, DELPHI note in preparation
- [41] ZFITTER - an analytical program for fermion pair production in  $e^+e^-$  annihilation, D. Bardin et al., CERN-TH.6443/92 (March 1992)
- [42] Proceedings of the 28<sup>th</sup> International Conference on High Energy Physics, Warsaw, Poland, 25-31 July 1996, Z.Ajduk and A.K.Wroblewski, World Scientific
- [43] M.McCubbin, B.Stugu, DELPHI 96-117 CONF 44, ICHEP'96 Ref. pa07-0012
- [44] S.Amato, L.De Paula, DELPHI note in preparation
- [45] J.R.P.Mahon, M.E.Pol, DELPHI note in preparation
- [46] "Study of the decay  $\tau \rightarrow 3\pi(n\gamma)\nu_\tau$  with the DELPHI detector at LEP", Privitera P., Thesis, Univ. Karlsruhe (1992)
- [47] "The decay of the heavy lepton  $\tau$  to three charged mesons", De Brabandere S., Thesis, Univ. Antwerpen (1997)
- [48] "MINUIT Function Minimization and Error Analysis" Version 92.1 (March 1992)
- [49] "Tau decays as polarization analyser", A.Rougé, Workshop on  $\tau$  Lepton Physics, Orsay, France, September 24-27, 1990.
- [50] Private communication
- [51] "Z Physics at LEP 1", S.Jadach and Z.Was, CERN 89-08 p235-265
- [52] "Measurements of the  $\tau$  polarisation in Z decays", DELPHI Coll., Z.Phys. C67,183(1995)
- [53] "Improved  $\tau$  polarisation measurement", ALEPH Coll., Z.Phys. C69,183(1996);  
 "A measurement of  $\tau$  polarisation at LEP", L3 Coll., Phys.Lett. B341, 245(1994);  
 "A precise measurement of the  $\tau$  polarisation and its forward-backward asymmetry at LEP", OPAL Coll., Z.Phys. C72,365 (1996)
- [54] "A combination of preliminary electroweak measurements and constraints on the Standard Model", Contributions from the LEP and SLD experiments to the 1997 winter conferences, LEPEWWG/97-01
- [55] "Determination of the Michel parameters and the  $\tau$  neutrino helicity in  $\tau$  decays", CLEO Coll., CLNS 97/1480
- [56] "A measurement of the Michel parameters in leptonic decays of the tau", CLEO Coll., CLNS 96/1429



# Acknowledgements

Je tiens à remercier le Professeur Jean Sacton pour m'avoir donné goût à la physique expérimentale des hautes énergies lors de mes études de licence, pour m'avoir encouragée à présenter mon mémoire dans ce domaine et enfin pour m'avoir accueillie dans son service durant les quatre années consacrées à la préparation de cette thèse.

Je remercie également Daniel Bertrand qui fut un promoteur hors pair. Ses compétences scientifiques exemplaires, son esprit critique et son souci de perfection m'ont guidée tout au long de la réalisation de cette thèse. Sa bonne humeur quotidienne et ses nombreux encouragements m'ont bien souvent aidée. Ce fut un réel plaisir de travailler avec lui.

Merci aussi au Professeur Jacques Lemonne pour ses remarques et suggestions concernant mon analyse, ainsi que pour m'avoir accompagnée et soutenue lors de presque toutes mes présentations orales.

Thanks a lot to Duncan Reid and Francisco Matorras for having worked with me at CERN. Thanks for the very interesting discussions we had together, and for the countless advice and enlightenments.

Thanks to all of them, as well as to Jean-Marie Frère and Catherine De Clercq, for having read the first versions of this work and provided me with precious remarks and advice. Thanks also to John Wickens who could always provide me with untraceable information.

Merci à Luc Pape pour son excellent "drill" lors de la préparation de ma première interview I.R.S.I.A.

Merci à Danielle Peymans et Myriam Pins pour leur aide à la réalisation de plusieurs illustrations, ainsi qu'à Monique Garnier.

Met dank ook aan Sabine De Brabandere, met wie ik de aangename en minder aangename kanten van de experimentele fysica gedeeld heb.

Merci aussi à tous les autres chercheurs, techniciens et doctorants de l'IIHE avec qui j'ai principalement partagé les bons côtés de la physique expérimentale, au laboratoire et en dehors. Merci en particulier à Pascal pour son Harrap's, à Muriel, Jacqueline, Sophie, Kathy, Ann, Barbara, Patrio, Othmane, Mourad, Caofang, Chen, Arnaud, Patrick, Yves et Arkadi (sur sa demande ;-)).

Un très grand merci à Isabelle G. pour s'être spontanément proposée pour une dernière relecture de ma thèse.

Merci enfin à toute ma famille et future belle-famille, et à Olivier, pour leur soutien moral généreux autant qu'indispensable.



